Nonlinear Energy Transfer and Nonlinear Estimation in Turbulent Channel Flows

by

Jitong Ding

ORCID ID: 0000-0003-3646-8441

Submitted in total fulfilment of the requirements
of the degree of Doctor of Philosophy

April, 2024

Department of Mechanical Engineering

UNIVERSITY OF MELBOURNE

Abstract

Turbulent flows exhibit chaotic and unpredictable motions. Nevertheless, coherent structures are prevalent in turbulent flows near a solid wall. Energy transfer occurs among these structures and is governed by the nonlinear Navier-Stokes equations. Channel flow as one of the simple canonical geometries has been widely studied in wall turbulence. This thesis focuses on the nonlinear energy transfer physics and a flow estimation problem in turbulent channel flows.

This thesis comprises three parts. In the first part, we quantify the energy transfer between any pair of modes in spectral space where a mode characterises structures of a specific size. This is achieved by examining the triadic interactions of the nonlinear terms in the Navier-Stokes equations in the streamwise-spanwise wavenumber space. We quantify the net energy transfer gain and loss due to nonlinear interactions for each mode. We focus on the energy transfer gain and loss of streamwise streaks, obliques waves and Tollmien–Schlichting waves which are crucial for sustaining turbulence in wall-bounded flows. In addition, we quantify the forward and inverse cascades between resolved scales (large scales) and subgrid scales (small scales) in the spirit of large-eddy simulations.

In the second part, we extract the coherent structures linked to positive and negative nonlinear energy transfer events in physical space using conditional averaging. Positive nonlinear energy transfer events are characterised by significant energy transfer gain while negative nonlinear energy transfer events are characterised by significant energy transfer loss. We extract similar velocity fields, nonlinear energy transfer fields and vortical fields for both positive and negative nonlinear energy transfer events. The main distinction is that positive and negative nonlinear energy transfers occur at different locations around the vortical structures.

In the third part, we consider a flow estimation problem in which we use limited velocity measurements at one location to predict the unknown velocities at other locations. We design a velocity estimator by combining a linear Kalman filter and a nonlinear relationship described by the nonlinear terms in the Navier-Stokes equations. The designed nonlinear estimator outperforms the purely linear estimator in terms of predicting velocity magnitudes, structures and energy transfer at the low Reynolds number considered. However, a linear estimator embedded with a simple eddy viscosity outperforms the designed nonlinear estimator in terms of estimation performance and stability at the high Reynolds number considered, implying that eddy viscosity is a favourable model for flow estimation and control in high-Reynolds-number wall-bounded flows.

Declaration of Authorship

This is to certify that:

- the thesis comprises only my original work towards the PhD,
- due acknowledgement has been made in the text to all other material used,
- the thesis is fewer than 100, 000 words in length, exclusive of tables, maps, bibliographies and appendices.

Signed: Jitong Ding

Date: 30/09/2024

觀山難越關山越

聞水易覓紊水覓

I saw the high mountains and I passed every one of them.
I heard the flowing water and I found turbulence.

Acknowledgements

I would like to express my sincere gratitude to my principal supervisor, Dr. Simon Illingworth, for mentoring me on how to 'think globally and act locally'; allowing me to pursue topics that I am interested in; providing guidance on my academic writing and communication; and your continuous patience over the years. I have gained confidence in conceptualising a giant research question bravely and decomposing it into small components systematically. In addition, I have benefited and will continue to benefit from developing the ability to present my research findings in a concise and accessible story. I would also like to extend my gratitude to my co-supervisor A/Prof. Daniel Chung for your detailed comments on my paper drafts and for sharing your DNS datasets; to my committee members Prof. Richard Sandberg and A/Prof. Jimmy Philip for your feedback on my progress review meetings. Acknowledgement is also due to my colleagues and friends in Boat Lab for the research inspirations over the office conversations, genuine laughter during the COVID-19 lockdown, gatherings at the PA and the memorable trip during the 2022 Sydney conference. I also appreciate my stay at Newman College during the final year of my PhD journey. I was fortunate to be surrounded by chilled friends and kind staff.

Engaging in research in the past four years has given me an invaluable opportunity to self-reflect on who I am and what I want to achieve. Nevertheless, it would have been incomplete without the wonderful times spent outside the uni.

I cherish the running training sessions with Mike and Bill who motivated me from a 3km run to participating in a half-marathon event in 2022. Life resembles a long-distance running, full of challenges, uncertainties and aspirations. I look forward to joining you guys in a full marathon in the near future.

I will definitely miss the exhilarating swimming squad training sessions organised by Baden, Wilson and Hugo on Tuesday and Thursday nights. Not only have I honed my swimming skills but I have established a consistent swimming routine which steadily promotes my physical and mental well-being.

Michael, your companionship during the final months of my PhD brought me joy, calmness and determination to tackle my studies and life's challenges. Hard to forget the lovely and relaxing hours we spent together in Brimbank Park, You Yang, Lorne and many places we will explore in future.

Bo, our regular meet-ups for chats, meals and hikes have been refreshing and enjoyable. Particularly our stay with Lulu (the cat) in December 2023, which evoked a sense of home in Melbourne. I think the magical fate builds a bridge between Parkville and Werribee, and I deeply believe this fate will shape both of us into better persons.

Lastly, I would like to thank my parents for their unwavering care and support. This thesis is dedicated to you. I wish you both good health and hope to see you often.

Contents

List of Figures

List of Tables

Nomenclature

Symbols

ΔT_m	measurement sampling time
ΔT_s	simulation time step
ε	error
η	wall-normal vorticity
λ_x, λ_y	streamwise wavelength, spanwise wavelength
λ_{ci}	swirling strength
$\lambda_{xC}, \lambda_{yC}$	streamwise cutoff wavelength, spanwise cutoff wavelength
corr	correlation
i	imaginary number unit, $\mathrm{i} = \sqrt{-1}$
ν	kinetic viscosity
ν_T	eddy viscosity
ρ	flow density
τ_w	mean shear stress at the wall
f_x, f_y, f_z	streamwise, spanwise and wall-normal nonlinear forcing
h	half channel height
k_x, k_y	streamwise wavenumber, spanwise wavenumber
k_{xC}, k_{yC}	streamwise cutoff wavenumber, spanwise cutoff wavenumber
p	fluctuation pressure
P_b	bulk production
Re	Reynolds number
Re_τ	Reynolds number based on friction velocity
t	time
U	streamwise mean (time-averaged) velocities
u, v, w	streamwise, spanwise and wall-normal fluctuation velocities
u_τ	friction velocity
x, y, z	streamwise, spanwise and wall-normal directions

Fourier Space Symbols

(k_x, k_y)	2-D Fourier mode with streamwise wavenumber k_x and spanwise wavenumber k_y
(s_x, s_y)	2-D Fourier mode with streamwise wavenumber s_x and spanwise wavenumber s_y
$\hat{D}(k_x, k_y)$	dissipation at mode (k_x, k_y)
$\hat{M}_{(s_x,s_y)(k_x,k_y)}$	nonlinear energy transfer from mode (a, b) to mode (k_x, k_y)
$\hat{M}_{(s_x,s_y)\to obwaves}$	nonlinear energy transfer of oblique waves
$\hat{M}_{(s_x,s_y)\to streaks}$	nonlinear energy transfer of streamwise streaks
$\hat{M}_{(s_x,s_y)\to TSwaves}$	nonlinear energy transfer of TS waves
$\hat{N}(k_x, k_y)$	net nonlinear energy transfer at mode (k_x, k_y)
$\hat{N}^+(k_x, k_y)$	net nonlinear energy transfer gain at mode (k_x, k_y)
$\hat{N}_F^+(k_x, k_y)$	net nonlinear energy transfer gain at mode (k_x, k_y) for forward cascade
$\hat{N}_I^+(k_x, k_y)$	net nonlinear energy transfer gain at mode (k_x, k_y) for inverse cascade
$\hat{N}^-(k_x, k_y)$	net nonlinear energy transfer loss at mode (k_x, k_y)
$\hat{N}_F^-(k_x, k_y)$	net nonlinear energy transfer loss at mode (k_x, k_y) for forward cascade
$\hat{N}_I^-(k_x, k_y)$	net nonlinear energy transfer loss at mode (k_x, k_y) for inverse cascade
$\hat{P}(k_x, k_y)$	production at mode (k_x, k_y)
$\hat{u}^{(k_x,k_y)}$	the Fourier coefficient of u at mode (k_x, k_y)

Other Symbols

u_i	fluctuation velocity in tensor notation, $i = 1, 2, 3$
$\frac{1}{2}u_i u_i$	fluctuation kinetic energy in tensor notation, Einstein summation rule applies to the repeated index.
$\hat{u}^*$	complex conjugate of $\hat{u}$
$\langle c_1, c_2 \rangle$	scalar product, $\langle c_1, c_2 \rangle = c_1^* c_2$
$\langle c_1, c_2 \rangle_I$	inner product, $\langle c_1, c_2 \rangle = \frac{1}{2}\int_{-1}^{1} c_1^* c_2 \mathrm{d}z$
$\tilde{u}$	conditionally averaged streamwise velocity
z^+	wall-normal distance to the wall in viscous unit, $z^+ = z u_\tau / \nu$

Set Symbols

$\mathbb{R}$	real number set
$\mathbb{R}^+$	non-negative real number set
$\mathbb{C}$	complex number set
$\mathbb{R}$, $\mathbb{S}$	large-scale (resolved-scale) region, small-scale (subgrid-scale) region

Abbreviations

1-D	One-Dimensional
2-D	Two-Dimensional
3-D	Three-Dimensional
DNS	Direct Numerical Simulation
KF	Kalman Filter
LE	Linear Estimator
LEe	Linear Estimator with Eddy Viscosity
LES	Large-Eddy Simulation
NE	Nonlinear Estimator
RMS	Root Mean Square
ROM	Reduced-Order Model
SSP	Self-Sustaining Process
SSROM	State-Space Reduced-Order Model
SVD	Singular Value Decomposition
TKE	Turbulent Kinetic Energy
TS	Tollmien-Schlichting

Chapter 1

Introduction

1.1 Motivation

Turbulence, characterised by chaotic and unpredictable fluid motions, is found in various natural and engineered systems. However, turbulent flows are far from being comprehensively understood because the momentum equations governing the dynamics of turbulence, the Navier-Stokes equations, are nonlinear.

Wall-bounded flows that occur near a solid surface are an important class of flows. Wall turbulence is closely related to a wide variety of applications, such as air flowing over the surface of an aircraft, oil transportation inside a pipe and cloud pattern formation in the atmospheric boundary layer. Since studying wall turbulence in a complex geometry is both more challenging and less generalisable, researchers in the fluid mechanics community study wall turbulence using canonical flow geometries. Examples include channels, pipes and boundary layers. A full understanding of wall turbulence in simple geometries would make it possible to unravel the mysteries of wall turbulence, though investigating wall turbulence in a simple canonical flow geometry is already a difficult problem.

A common strategy to tackle a nonlinear system is to use the linearised Navier-Stokes equations. For wall turbulence, the linearised Navier-Stokes equations are able to explain transient energy growth, where an infinitesimal perturbation could grow temporarily triggering turbulence even in the absence of unstable eigenvalues (Trefethen et al., 1993; Reddy & Henningson, 1993). In addition, the linearised Navier-Stokes equations are able to explain the formation of streamwise streaks from streamwise vortices via the lift-up mechanism (Landahl, 1980). Both streamwise streaks and streamwise vortices are prevalent in wall turbulence.

Linear analysis only solves parts of the puzzle of wall turbulence leaving other parts to be answered by nonlinear analysis. For example, the energy cascade from large scales

to small scales is achieved through nonlinear interactions and the formation of streamwise vortices in the self-sustaining process (SSP) is related to nonlinear mechanisms (Hamilton et al., 1995). In addition, embedding knowledge of the nonlinearity into the linearised Navier-Stokes models recovers more accurate turbulence features (Zare et al., 2017; Illingworth et al., 2018; Madhusudanan et al., 2019). Therefore, it is worthwhile to investigate nonlinear energy transfer among different structures and ways to embed knowledge of the nonlinear dynamics into linear models for wall turbulence.

1.2 Thesis outline

This thesis focuses on the nonlinear energy transfer and nonlinear estimation of turbulent channel flows using direct numerical simulation (DNS) datasets.

We start with a literature review covering two main topics in chapter 2: energy transfer and structures in wall turbulence, and linearised models for wall turbulence and applications. These two main topics are closely related to the studies presented in the following chapters.

A brief description and validation of the DNS datasets is presented in chapter 3.

In chapter 4, we discuss the nonlinear energy transfer in spectral space. Specifically, we investigate three aspects of the nonlinear energy transfer among different modes, where each mode is characterised by a streamwise wavelength and a spanwise wavelength because channel flows are homogeneous in these two directions. First, we quantify the dual feature of nonlinear energy transfer: how much energy each mode gains and loses nonlinearly. Second, we investigate the nonlinear energy transfer of structures which are important in sustaining turbulence and providing guidance for numerical simulation. Third, we quantify the forward and inverse cascades between the resolved scales and subgrid scales in the spirit of large-eddy simulation (LES).

Having looked at the nonlinear energy transfer in spectral space, we proceed to discuss the nonlinear energy transfer in physical space in chapter 5. We extract significant positive and negative nonlinear energy transfer events using conditional averaging. Based on the conditionally averaged events, we look at the conditionally averaged velocity fields, nonlinear energy transfer fields and vorticity fields. We further explore the relationship between nonlinear energy transfer and the detected vortical coherent structures. The similarities and differences between positive and negative nonlinear energy transfer events are discussed. Since nonlinear energy transfer in physical space is often termed turbulent convection, we use the phrase turbulent convection in chapter 5.

In chapter 6, we consider the estimation problem for channel flows. Given a single velocity measurement at one wall-normal height, we design an estimator to predict the

velocity fluctuations at other wall-normal heights. Illingworth et al. (2018) found that including a simple eddy viscosity model which considers the nonlinear effect of the small scales on the large scales in the linear estimator (based on the linearised Navier-Stokes equations) improves the estimation performance compared to the purely linear estimator, indicating the importance and benefits of embedding knowledge of the nonlinear dynamics in a linear model. Inspired by this, we embed knowledge of the nonlinear terms into the linear estimator using a different approach by explicitly calculating the remaining nonlinear terms in the Navier-Stokes equations. The estimation performance of the designed nonlinear estimator is discussed and compared with the estimators presented in Illingworth et al. (2018) and Oehler et al. (2018).

We summarise the present study and propose possible future work in chapter 7.

1.3 Contributions

The contributions of this thesis are summarised as follows:

- The early findings in chapter 4 were published in the following conference proceeding: Ding, J., Illingworth, S., & Chung, D. (2022, December). Nonlinear energy transfer in channel flow at $Re_\tau = 180$. In *23rd Australian Fluid Mechanics Conference (Sydney, Australia)*.

- The early findings in chapter 6 were published in the following workshop: Ding, J., Illingworth, S., & Chung, D. (2022, June). Nonlinear estimation in channel flow at $Re_\tau = 180$. In *14th ERCOFTAC SIG 33 Workshop, Progress in Flow Instability, Transition and Control (Cádiz, Spain)*.

Chapter 2

Literature review

This chapter provides a brief literature review on two broad areas of wall turbulence: the first is energy transfer and structures; the second is linearised models and applications. It gives a general background for the discussions in the following chapters. The review is mainly about wall-bounded flows, though other types of flows are discussed where appropriate.

2.1 Energy transfer and structures in wall turbulence

2.1.1 Turbulent kinetic energy budget

Inhomogeneity in the wall-normal direction

Because of the no-slip boundary condition at the wall, velocity statistics change significantly in the wall-normal direction z, leading to the inhomogeneity associated with different physical characteristics across the wall-normal height. In the near-wall region, often called the 'inner layer', viscous forces dominate (Prandtl, 1925). The characteristic length is the viscous unit ν/u_τ where ν is the kinetic viscosity and u_τ is the friction velocity. In the region far away from the wall and often called the 'outer layer', viscous forces are no longer important and the fluid is mainly affected by the bulk flow. The characteristic length is then the size of the flow geometry. For channel flow, it is the half channel height h; for boundary layer flow, it is the boundary layer thickness δ; for pipe flow, it is the pipe radius r. An intermediate region linking the inner and outer regions exists and the mean streamwise velocity follows the well-known logarithmic law (Millikan, 1938). While the extent of the logarithmic region is not completely settled, one sensible definition is $30\nu/u_\tau < z < 0.15\delta$ for $Re_\tau > 2000$ (Smits et al., 2011). Figure 2.1 schematically shows the categorisation of different regions in the wall-normal direction for wall turbulence (Pope, 2000).

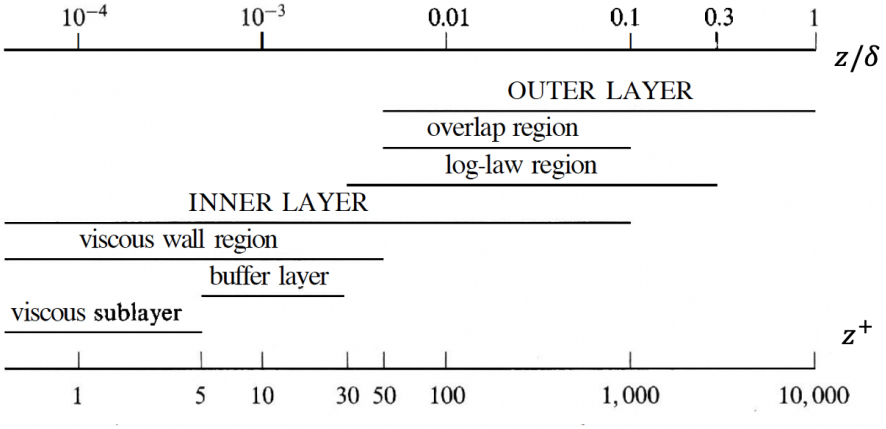

Figure 2.1: Different regions in the wall-normal direction z for wall turbulence. This figure is taken from Pope (2000).

Spectral turbulent energy transfer budget for channel flow

Turbulence can be regarded as fluctuations based on the time-averaged flow. The Reynolds decomposition divides instantaneous quantities into time-averaged quantities and fluctuation quantities. Turbulent kinetic energy (TKE) equation is used to describe energy transfer concerning the fluctuations in physical space (Moin & Kim, 1982; Mansour et al., 1988; Pope, 2000):

$$\frac{\mathrm{D}}{\mathrm{D}t}\left(\frac{1}{2}u_i u_i\right) = \overbrace{-u_i u_j \frac{\partial U_i}{\partial x_j}}^{\text{production}} \underbrace{-\frac{1}{Re}\frac{\partial u_i}{\partial x_j}\frac{\partial u_i}{\partial x_j}}_{\text{dissipation}} \overbrace{-u_j \frac{\partial\left(\frac{1}{2}u_i u_i\right)}{\partial x_j}}^{\text{turbulent convection}} \underbrace{-u_i \frac{\partial p}{\partial x_i}}_{\text{pressure diffusion}} + \overbrace{\frac{1}{Re}\frac{\partial^2\left(\frac{1}{2}u_i u_i\right)}{\partial x_j \partial x_j}}^{\text{viscous diffusion}} \tag{2.1}$$

First consider energy transfer *locally*, TKE (2.1) reveals that different types of energy transfer involving both linear and nonlinear mechanisms contribute to sustaining turbulence. If we integrate equation (2.1) across the whole flow domain Ω, either with periodic or no-turbulence boundary condition, we arrive at the Reynolds-Orr equation (Schmid & Henningson, 2001):

$$\int_\Omega \frac{\mathrm{D}}{\mathrm{D}t}\left(\frac{1}{2}u_i u_i\right)\mathrm{d}\Omega = \underbrace{\int_\Omega -u_i u_j \frac{\partial U_i}{\partial x_j}\mathrm{d}\Omega}_{\text{production}} + \underbrace{\int_\Omega -\frac{1}{Re}\frac{\partial u_i}{\partial x_j}\frac{\partial u_i}{\partial x_j}\mathrm{d}\Omega}_{\text{dissipation}} \tag{2.2}$$

Now consider energy transfer *globally*, the Reynolds-Orr equation (2.2) tells us that the true source of turbulence is production from mean shear and the true sink of turbulence is dissipation to heat, both of which involve only linear mechanisms. The nonlinear term $u_j \frac{\partial u_i}{\partial x_j}$ in the Navier-Stokes equations is conservative: it neither adds nor drains energy when considered over the entire flow. Rather, it plays the role of energy redistribution.

For most turbulent flows, energy transfer happens across a wide range of scales. A scale refers to structures with certain dimension(s) in specific direction(s). However, equation (2.1) does not relate energy transfer with scales. For channel flows that are homogeneous in the streamwise and spanwise directions, we can arrive at the spectral turbulent kinetic energy equation for a single scale with streamwise wavenumber k_x and spanwise wavenumber k_y (Bolotnov et al., 2010):

$$\frac{\partial \hat{e}}{\partial t} = \overbrace{-\langle \hat{u}_i, \widehat{u_j \frac{\partial U_i}{\partial x_j}} \rangle}^{\text{production}} \underbrace{-\frac{1}{Re} \langle \widehat{\frac{\partial u_i}{\partial x_j}}, \widehat{\frac{\partial u_i}{\partial x_j}} \rangle}_{\text{dissipation}} \overbrace{-\langle \hat{u}_i, \widehat{u_j \frac{\partial u_i}{\partial x_j}} \rangle}^{\substack{\text{nonlinear} \\ \text{energy} \\ \text{transfer}}} \underbrace{-\langle \hat{u}_i, \widehat{\frac{\partial p}{\partial x_i}} \rangle}_{\substack{\text{pressure} \\ \text{diffusion}}} + \overbrace{\frac{1}{Re} \frac{\partial^2 \hat{e}}{\partial x_j \partial x_j}}^{\substack{\text{viscous} \\ \text{diffusion}}} \tag{2.3}$$

For each term, the contribution from the streamwise and spanwise velocities is termed 'in-plane' (or 'spatial') energy transfer and the contribution from the wall-normal velocity is termed 'inter-plane' (or 'interscale') energy transfer (Bolotnov et al., 2010; Mizuno, 2016; Andrade et al., 2018; Lee & Moser, 2019). In-plane energy transfer refers to energy transfer in the homogeneous directions and inter-plane energy transfer refers to energy transfer in the wall-normal direction. Energy transfer is usually plotted in terms of premultiplied energy transfer spectrum. In this case, the energy transfer contributed from certain scales is easily determined by looking at the area delineated by the corresponding energy transfer curve. For example, production $\hat{P}$ is visualised in the form of $k_x k_y \hat{P}$. However, one drawback of using premultiplied spectra is that scales with zero wavenumbers cannot be visualised since the corresponding premultiplied energy transfer is zero.

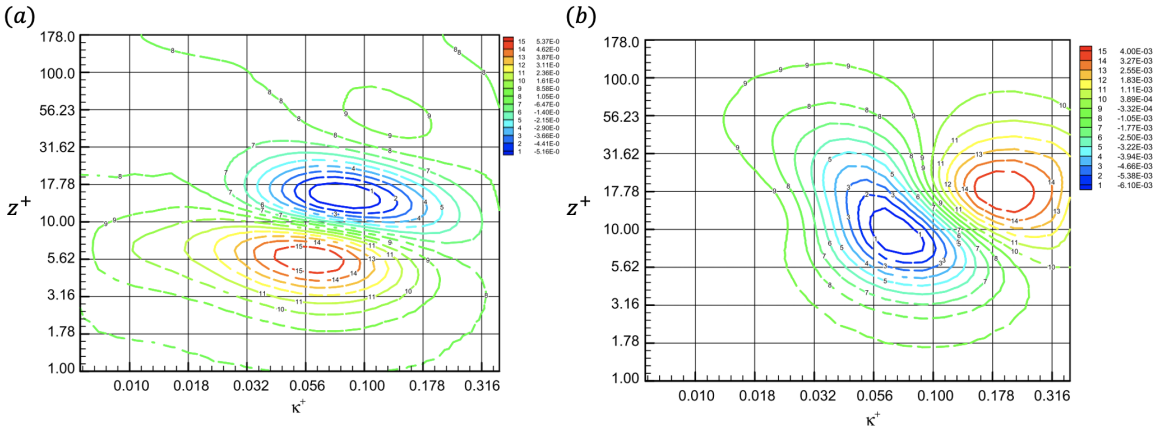

Figure 2.2: (a) Inter-plane nonlinear energy transfer. (b) In-plane nonlinear energy transfer. k is the polar wavenumber defined as $k = \sqrt{k_x^2 + k_y^2}$. This figure is taken from Bolotnov et al. (2010).

Lumley (1964) first analytically investigated the spectral budget (2.3) and proposed that an inverse cascade could appear because of the presence of the wall. As DNS data has become available, Bolotnov et al. (2010); Mizuno (2016); Cho et al. (2018); Andrade et al. (2018); Lee & Moser (2019) investigated the statistical properties of energy transfer in channel flows for both low and high Reynolds number datasets. Discussions relating to the energy cascade, self-similarity in the wall-normal direction, the effect of Reynolds number, velocity components and physical mechanisms are provided. For example, figure 2.2 shows the inter-plane and in-plane nonlinear energy transfer contributed by the nonlinear terms (Bolotnov et al., 2010). Figure 2.2(a) shows that the logarithmic region where the maximum production occurs is responsible for transferring energy nonlinearly to the near-wall region and the outer layer region. Figure 2.2(b) shows that energy is transferred nonlinearly from large scales to small scales. In recent years, Lee & Moser (2019) used the 'polar' coordinates to visualise the energy transfer spectra and two main advantages were explained.

There are other ways to investigate the spectral energy budget apart from using equation (2.3). For example, Dunn & Morrison (2003, 2005) used orthogonal wavelets which give a dual space-scale description of the energy transfer; Cimarelli et al. (2013, 2016) use the second-order structure function and two physical mechanisms of near-wall turbulence regeneration cycle and outer self-sustaining mechanism were explained.

For channel flows, similar to the derivation of the Reynolds-Orr equation (2.2), integrating spectral energy budget (2.3) across the flow domain for each scale gives (Symon et al., 2021):

$$\int_\Omega \frac{\partial \hat{e}}{\partial t} \mathrm{d}\Omega = \underbrace{\int_\Omega -\langle \hat{u}_i, u_j \widehat{\frac{\partial U_i}{\partial x_j}} \rangle \mathrm{d}\Omega}_{\text{production}} + \underbrace{\int_\Omega -\langle \widehat{\frac{\partial u_i}{\partial x_j}}, \widehat{\frac{\partial u_i}{\partial x_j}} \rangle \mathrm{d}\Omega}_{\text{dissipation}} + \underbrace{\int_\Omega -\langle \hat{u}_i, u_j \widehat{\frac{\partial u_i}{\partial x_j}} \rangle \mathrm{d}\Omega}_{\substack{\text{nonlinear} \\ \text{energy} \\ \text{transfer}}} \tag{2.4}$$

The pressure diffusion term and viscous diffusion term disappear because of the no-slip and the impermeability boundary conditions at the walls. Equation (2.4) describes the wall-normal integrated spectral energy transfer for a single spatial scale.

Nonlinear energy transfer from triadic interactions

It is generally understood that turbulence transfers energy from large scales to small scales (Richardson, 1922; Kolmogorov, 1941). Large scales are effective in extracting energy from the mean shear (Ellingsen & Palm, 1975; Landahl, 1980), while small scales are effective in dissipating kinetic energy isotropically into heat (Vassilicos, 2015). The ratio of the largest scale to the smallest scale becomes large as the Reynolds number increases.

As indicated in equation (2.4), nonlinear energy transfer bridges the gap between large scales that gain more energy from production than they can dissipate; and small scales that dissipate more than they gain from production.

The following discussion focuses on the nonlinear energy transfer term in equation (2.3) and (2.4) which can be written in a convolution form as:

$$-\hat{u}_i^{-\boldsymbol{k}}\left(\widehat{u_j\frac{\partial u_i}{\partial x_j}}^{\boldsymbol{k}}\right) = -\hat{u}_i^{-\boldsymbol{k}}\left(\sum_{\boldsymbol{q}}\hat{u}_j^{\boldsymbol{k}-\boldsymbol{q}}\widehat{\frac{\partial u_i}{\partial x_j}}^{\boldsymbol{q}}\right) = \sum_{\boldsymbol{p},\boldsymbol{q}}\left(-\hat{u}_i^{\boldsymbol{k}}\hat{u}_j^{\boldsymbol{p}}\widehat{\frac{\partial u_i}{\partial x_j}}^{\boldsymbol{q}}\right) \tag{2.5}$$

The superscript represents the Fourier mode under consideration. The nonlinear energy transfer term is a convolution composed of all possible wavenumber-compatible triadic interactions (Domaradzki & Rogallo, 1990). It represents the net energy mode $\boldsymbol{k}$ received from the nonlinear interactions between mode $\boldsymbol{k}$ and all the other modes. However, with a loss of information about details of the nonlinear energy transfer within individual triads, this nonlinear energy transfer term in equations (2.3) and (2.4) cannot reveal the nonlinear energy transfer from a specific mode to a specific mode.

In equation (2.5), a single triadic interaction involving wavenumber vector $\boldsymbol{k},\boldsymbol{p},\boldsymbol{q}$ satisfies $\boldsymbol{k}+\boldsymbol{p}+\boldsymbol{q}=\boldsymbol{0}$. This single triadic interaction could be interpreted as the energy transferred nonlinearly from the source mode $\boldsymbol{q}$ to the recipient mode $\boldsymbol{k}$ with the help of the advective mode $\boldsymbol{p}$ (Domaradzki & Rogallo, 1990; Smyth, 1992; Dar et al., 2001; Webber et al., 2002; Alexakis et al., 2005; Jin et al., 2021).

Works related to the triadic interactions of this nonlinear energy transfer term in equation (2.5) started in homogeneous isotropic turbulence (HIT) (Domaradzki & Rogallo, 1990; Waleffe, 1992; Brasseur & Wei, 1994). Main discussions fall into two aspects: first, whether scales involved in a triad are of similar sizes (local) or quite different sizes (distant); second, whether energy is transferred from large scales to small scales (forward energy cascade) or from small scales to large scales (reverse energy cascade). Energy is transferred mainly locally, and both forward and inverse cascades exist. Triadic interactions are inherently related to energy cascade as Cheung & Zaki (2014) derived the $-5/3$ energy spectrum law from the Navier-Stokes equations using nonlinear triad interactions.

As for wall-bounded flows, Domaradzki et al. (1994) was the first to explore the triadic interactions in channel flows and he found that the nonlinear energy transfer in channel flows is similar to that in homogeneous isotropic turbulence. In recent years, a few studies have looked at the energy cascade mechanisms in channel flows by characterising triadic interactions (Cho et al., 2018; Karban et al., 2023). However, research on triadic interactions in wall-bounded flows remains limited compared to homogeneous isotropic flows.

Apart from homogeneous isotropic turbulence and wall turbulence, nonlinear triadic

interactions have been explored in other flow geometries. For example, magnetohydrodynamic turbulence (Dar et al., 2001) and cylinder flows (Jin et al., 2021). It has been found that inverse cascades exist in these types of flows. Table 2.1 shows that in cylinder flows, energy is not always transferred nonlinearly from the vortex shedding frequency to the higher frequencies and there exists non-negligible inverse cascade from the 2nd and 3rd harmonic frequencies to the vortex shedding frequency (Jin et al., 2021).

$\hat{\mathcal{N}}_{mn}$	Advection	Source	Recipient	Magnitude (10^{-2})	Cascade
$\hat{\mathcal{N}}_{01}$ $[\hat{P}(\omega_1)]$	1	0	1	24.2	Down
$\hat{\mathcal{N}}_{12}$	1	1	2	3.42	Down
	3	2	1	0.39	Up
$\hat{\mathcal{N}}_{23}$	1	2	3	1.73	Down
$\hat{\mathcal{N}}_{31}$	2	3	1	0.68	Up

Table 2.1: Example of nonlinear energy transfer in cylinder flow. $\hat{\mathcal{N}}_{mn}$ represents energy transferred nonlinearly from mth harmonic frequency to nth harmonic frequency. This figure is taken from Jin et al. (2021).

Implications of nonlinear energy transfer to large-eddy simulations

Large-eddy simulation (LES) resolves large energy-containing scales (resolved scales) directly affected by the boundary conditions and does not resolve small scales (subgrid scales) which are modelled instead. LES is more computationally efficient than direct numerical simulation (DNS) and more accurate than Reynolds averaged Navier-Stokes (RANS) equations. An important step in LES is the subgrid scale (SGS) model relating the energy transfer between the resolved scales and subgrid scales. The traditional modelling methodology is based on Kolmogorov's theory of energy cascade and assumes that the subgrid scales only gain energy from the resolved scales. The discovery of the inverse cascade in which energy is transferred from small scales to large scales, also known as 'backscatter' compromises the accuracy of LES, especially in near-wall regions (Piomelli et al., 1991; Härtel et al., 1994; Cimarelli et al., 2013; Cho et al., 2018). It is therefore necessary to recognise and model the inverse cascade to improve LES.

Several modelling approaches have been proposed to account for the inverse cascade. For example, Domaradzki et al. (1994) used a negative eddy viscosity to account for the energy transferred from the subgrid scales to the resolved scales; Cimarelli & De Angelis (2014) combined the classical linear formation of eddy viscosity with the nonlinear anisotropic features of the velocity increments tensor to account for the inverse cascade. The general statistics such as the mean velocities and root mean square (RMS) quantities are in good agreement with the DNS even though the LES grid is coarse.

2.1.2 Related coherent structures and physical mechanisms

Coherent structures in wall-bounded turbulence

Coherent structures characterised by high spatial or temporal correlation exist in wall-bounded flows, exhibiting regularity and simplicity in high chaotic systems governed by the nonlinear Navier-Stokes equations (Cantwell, 1981; Robinson, 1991; Jiménez, 2018).

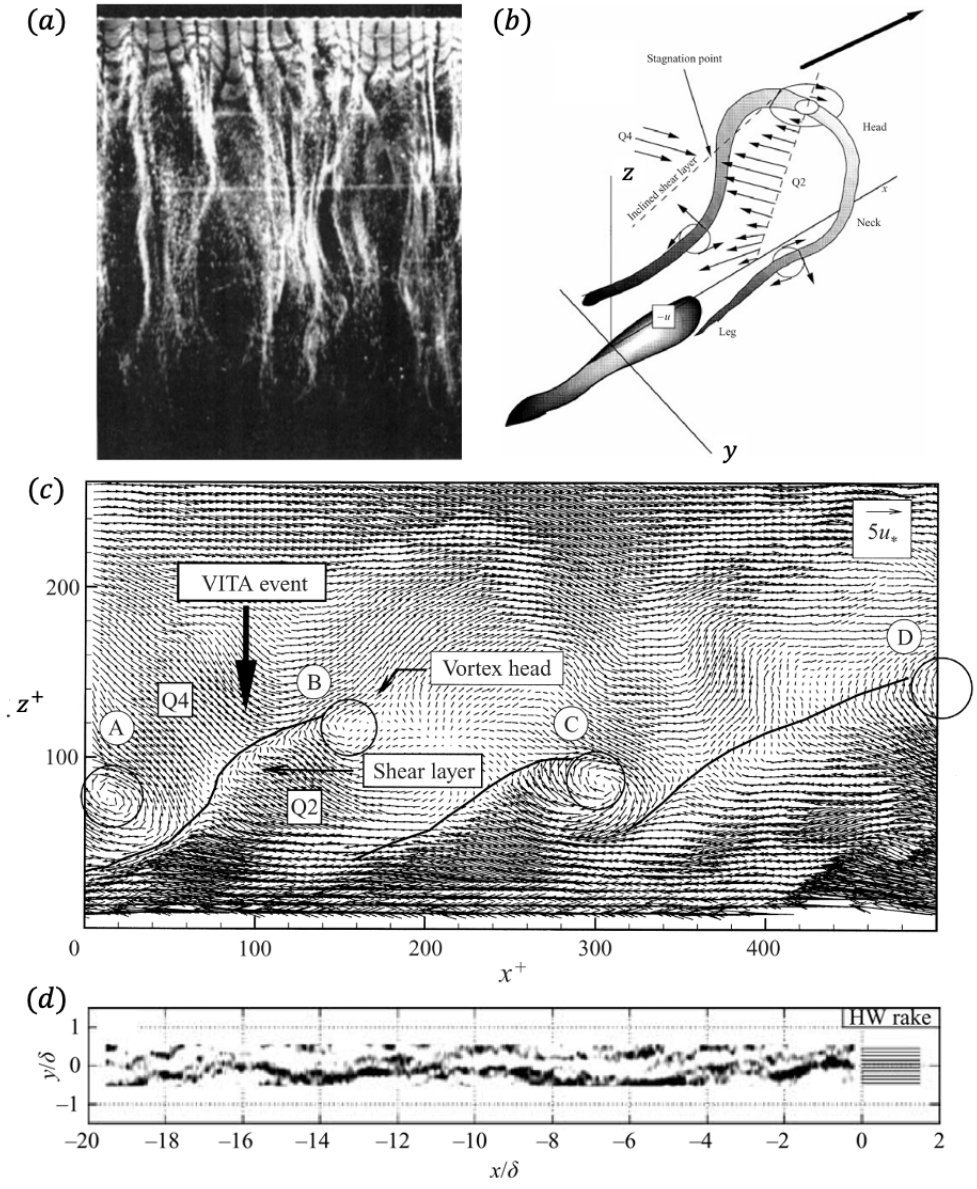

Figure 2.3: The four classes of coherent structures in wall turbulence. (a) Near-wall streaks at $z^+ = 2.7$ in the laminar sublayer. The flow is from top to bottom. Taken from Kline et al. (1967). (b) Sketch of a hairpin vortex. It is accompanied by a low-speed streak. Taken from Zhou et al. (1999). (c) LSM: a vortex packet consisting of four hairpin vortices aligned in the streamwise direction observed from the PIV experiment. Taken from Adrian et al. (2000) (d) VLSM: a regime of very long meandering positive and negative streamwise velocity fluctuations. Taken from Hutchins & Marusic (2007).

Theodorsen (1952) was the first to conceptualise the hairpin vortex structure as a basic element in boundary layer flows. Later on, experimental visualisation techniques enabled observations of coherent structures. For example, Kline et al. (1967) observed well-organised low-speed streaks in the near-wall region using a hydrogen bubble technique. Head & Bandyopadhyay (1981) observed elongated hairpin vortices at high Reynolds number and vortex loops at low Reynolds number in zero pressure gradient boundary layer flows using hot-wire anemometry and an oil-fog flow visualization technique. With the rapid development of computation, inspecting coherent structures has become easier. For example, Wu & Moin (2009) observed populated hairpin vortices in a DNS of a zero-pressure-gradient flat-plate boundary layer.

Structures scattered irregularly in flow fields could be systematically detected and analysed using conditional averaging techniques, which are the best mean-square estimation of the quantity being averaged (Antonia, 1981). Here we give two representative examples. The first is quadrant analysis initiated by Wallace et al. (1972). It classifies four types of motions that contribute to the Reynolds shear stress $-\rho\overline{uw}$: (1) Q1: outward interactions $(u>0, w>0)$; (2) Q2: ejections $(u<0, w>0)$; (3) Q3: inward interactions $(u<0, w<0)$; (4) Q4: sweeps $(u>0, w<0)$. It was found that Q2 and Q4 events make the largest contributions to the Reynolds shear stress. The second is the VITA (variable interval time average) method proposed by Blackwelder & Kaplan (1976). It was initially used to detect bursting events associated with high local rapid temporal changes. Bursting events are a series of ejections (Q2) and sweeps (Q4). It was found that bursting events make a significant contribution to turbulent production. Kim & Moin (1986) adapted the VITA technique and proposed VISA (variable interval spatial average) to detect events with lower spatial variance. Two distinct horseshoe-shaped vortical structures associated with bursting were found: one associated with ejections and the other with sweeps.

Different types of coherent structures exist in wall turbulence at different wall-normal locations. Smits et al. (2011) categorise coherent structures in wall turbulence into four classes as shown in figure 2.3. (1) near-wall streaks and quasi-streamwise vortices (Kline et al., 1967); (2) hairpin vortices spanning from the wall to the overlap region (Theodorsen, 1952); (3) large-scale motions (LSMs) referring to packets of hairpin vortices with lengths of 2-3 outer length scales in the streamwise direction (Zhou et al., 1999; Adrian et al., 2000); (4) very large-scale motions (VLSMs) referring to superstructures with lengths of 10-15 outer length scales in the streamwise direction and which contain an increasing percentage of streamwise energy and Reynolds shear stress for higher Reynolds numbers (Hutchins & Marusic, 2007).

Attached eddy model

Despite access to large datasets, models for wall turbulence are still insufficient to understand the physics. A widely acknowledged model for the logarithmic region of wall turbulence is the attached eddy model (AEM) (Marusic & Monty, 2019). The attached eddy model is based on the hypothesis that there exist hierarchies of geometrically self-similar structures that are attached to the wall (Townsend, 1976). The widths and lengths of these structures scale in proportion to their wall-normal heights, and their population densities scale inversely with their wall-normal heights, as shown in figure 2.4. Perry & Chong (1982) extended this hypothesis with Λ-shaped vortex and derived the mean flow, Reynolds stresses and energy spectra. The credibility of this model is supported by experimental observations (Head & Bandyopadhyay, 1981; Dennis & Nickels, 2011) and DNS data (Wu & Moin, 2009).

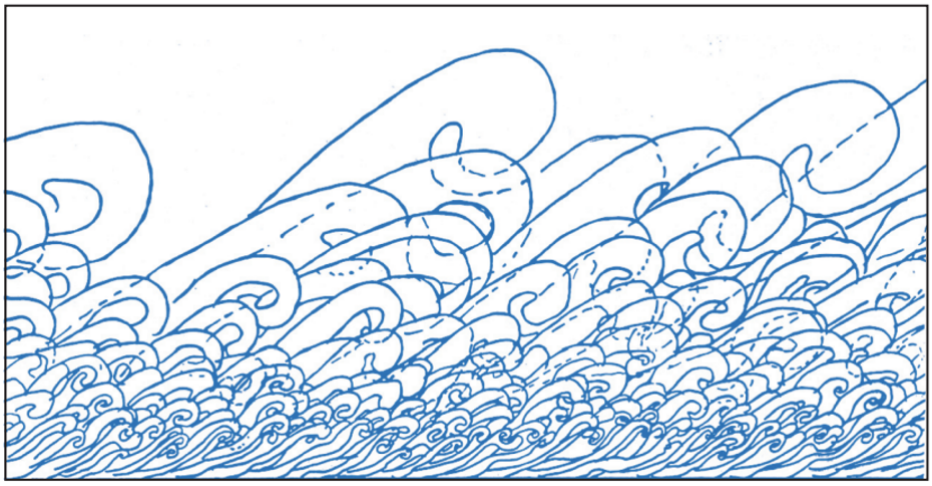

Figure 2.4: A sketch of an assemblage of hierarchies of eddies in a boundary layer with inverse-scale probability distribution in the wall-normal direction. This figure is taken from Marusic & Monty (2019).

Self-sustaining process (SSP) in the near-wall region

Evidence for a self-sustaining process for turbulence could be traced back to Jiménez & Moin (1991), who showed that turbulence could be sustained in a minimal channel box with a spanwise length of 100 wall units. The low-order turbulence statistics in this minimal channel box are correct in the near-wall region. Later, it was found that a cycle exists which is in the near-wall region and is independent of the outer flow at low Reynolds number (Jiménez & Pinelli, 1999).

Hamilton et al. (1995); Waleffe (1997) proposed the self-sustaining process in the near-wall region by investigating plane Couette flow which requires a minimal set of structures for sustaining turbulence. The SSP is composed of three distinct physical

phases and the absence of any phase will cause the relaminarisation of flow. Forward and inverse energy cascades are involved in the SSP.

The first phase is related to the lift-up effect which is a linear mechanism. During this phase, streamwise streaks are formed due to wall-normal advection by streamwise vortices (Ellingsen & Palm, 1975). Because of the mean shear $U(z)$, streamwise vortices bring the fluid with low streamwise velocity upward and the fluid with high streamwise velocity downward.

The second phase is related to streak breakdown which is also a linear mechanism. Because of the lift-up effect from the first phase, there is a change in the mean shear $U(z) \rightarrow U(y,z)$ which triggers the inflection instability in the spanwise direction (Waleffe, 1995; Schmid & Henningson, 2001). This instability breaks streamwise streaks into x-dependent structures with $k_x \approx 1$ as the most unstable mode. This stage involves a forward energy cascade from streamwise streaks (large structures) to x-dependent structures (small structures).

The third phase is related to nonlinear interactions involving nonlinear mechanisms. During this phase, streamwise vortices are regenerated. This involves an inverse energy cascade from x-dependent structures (small structures) to streamwise vortices (large structures). The dominant wavenumbers related to nonlinear interactions could be found theoretically by investigating the governing equation of streamwise vortices with x-dependent modes substituted (Jiménez & Moin, 1991; Hamilton et al., 1995; Schoppa & Hussain, 2002). Differently, Bae et al. (2021) found that spanwise rolls interacting with oblique streaks plays an important role in sustaining turbulence by restricting the formation of the nonlinear forcing in the DNS and LES.

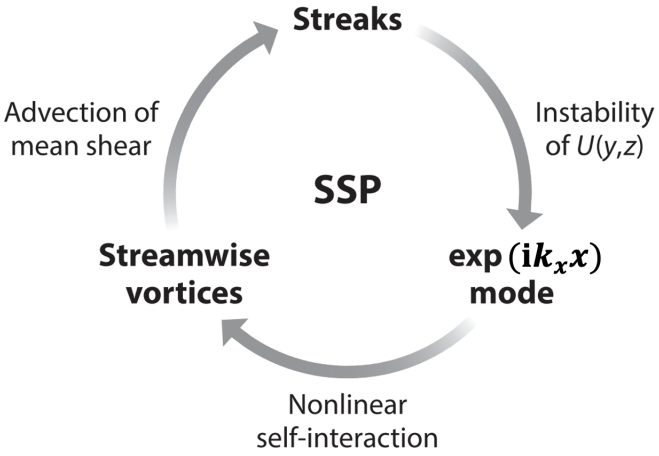

Figure 2.5: The three phases are involved in the self-sustaining process (SSP) in the near-wall region. The figure is taken from Hamilton et al. (1995).

2.2 Linearised models and applications

2.2.1 Reduced-order models for wall turbulence

One powerful strategy for tackling nonlinear high-dimensional fluid systems is to construct reduced-order models (ROMs). Reduced-order modelling not only saves computational resources and time, but also helps us extract low-dimensional coordinates related to dominant physical mechanisms and coherent structures. As indicated by Candès & Wakin (2008), 'many natural signals are sparse or compressible in the sense that they have concise representations when expressed in the proper basis'. A common categorisation divides reduced-order modelling into data-driven modelling and equation-based modelling (Rowley & Dawson, 2017; Taira et al., 2017, 2020). Table 2.2 gives several examples illustrating different reduced-order modelling techniques for wall turbulence.

ROM method		Flow type	Study
data-driven	POD	pipe	Aubry et al. (1988)
		channel	Alfonsi & Primavera (2007)
	BPOD	channel	Ilak & Rowley (2008)
		boundary layer	Bagheri et al. (2009)
	DMD	channel	Mizuno et al. (2011)
		channel	Le Clainche et al. (2022)
equation-based	Koopman analysis	boundary layer	Dotto et al. (2021)
	global stability	channel	Orszag (1971)
		boundary layer	Åkervik et al. (2008)
	resolvent analysis	pipe	McKeon & Sharma (2010)
		channel	Moarref et al. (2014)

Table 2.2: A brief summary of reduced-order modelling techniques for wall turbulence. POD represents proper orthogonal decomposition, also known as principal component analysis (PCA), Karhunen-Loève procedure. BPOD represents balanced proper orthogonal decomposition. DMD represents dynamic mode decomposition.

2.2.2 Linearised Navier-Stokes equations

Although the Navier-Stokes equations are nonlinear and the nonlinearity cannot be neglected in wall turbulence, the Navier-Stokes equations linearised around the mean velocity profile capture some important physical processes, such as transient energy growth and streamwise vortices generating streamwise streaks. The linearised Navier-Stokes equations also serve as a useful tool for flow estimation and control.

Eigenvalues and pseudospectra

From the control theory, the stability of a dynamic system could be determined by calculating the eigenvalues of the linear operator governing the dynamics (Zhou et al., 1996). If a flow system has unstable eigenvalues, then the perturbations around the laminar velocity profile will grow and lead to turbulence. Unlike wake flows which have unstable eigenvalues indicating instability (Williamson, 1996), a number of wall-bounded flows present no unstable eigenvalues. For Poiseuille flow, the first unstable mode appears when the Reynolds number reaches 5772 (Orszag, 1971) and this instability mode corresponds to Tollmien–Schlichting (TS) waves (Schmid & Henningson, 2001). For Couette flow, there are no unstable eigenvalues for all Reynolds numbers (Romanov, 1973). Apparently, these eigenvalue results contradict the experiments in which turbulence occurs at a much lower Reynolds number (Davies & White, 1928). The absence of unstable eigenvalues had haunted researchers for a long period until the proposed theory of pseudospectral analysis which concerns the sensitivity of the eigenvalues in terms of perturbations to the operator (Trefethen et al., 1993; Trefethen, 1999):

$$\Lambda_\varepsilon(A) = \{z \in \mathbb{C} : z \in \Lambda(A + \Delta A), \quad \text{where } \|\Delta A\| \leq \varepsilon\} \tag{2.6}$$

where A is the linear operator, ε is the perturbation, Λ is the symbol for eigenvalue spectra and Λ_ε represent the ε-pseudospectra of A.

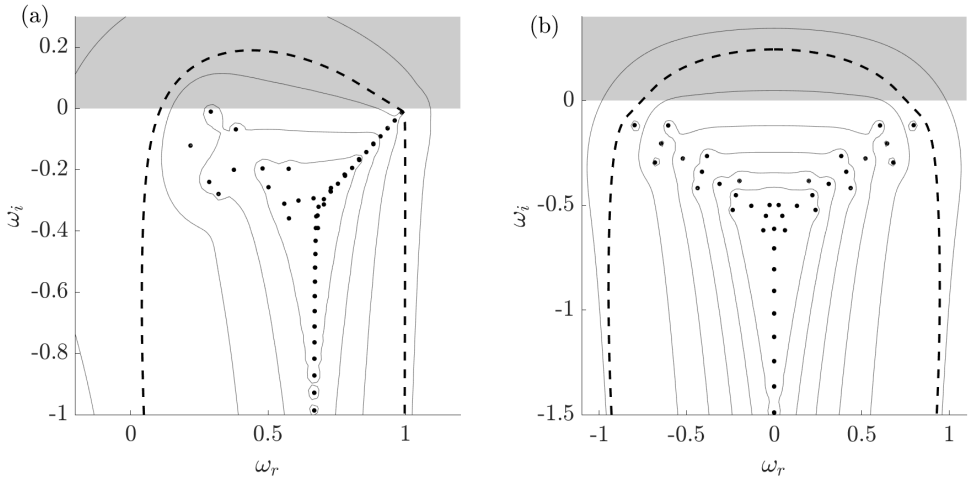

Figure 2.6: Pseudospectra of the Orr-Sommerfeld & Squire operator for (a) Poiseuille flow at $k_x = 1$, $k_y = 0$ and $Re = 3000$, thin grey lines are boundaries of the ε-pseudospectra for $\varepsilon = 10^{-1}, 10^{-2}, ..., 10^{-4}$; (b) for Couette flow at $k_x = 1$, $k_y = 0$ and $Re = 1000$, thin grey lines are boundaries of the ε-pseudospectra for $\varepsilon = 10^{-1}, 10^{-2}, ..., 10^{-6}$. The velocities are assumed as downstream travelling waves: $u_i = \hat{u}_i e^{\mathrm{i}(k_x x + k_y y - \omega t)}$. For (a)(b), solid dots are the eigenvalues and thick dashed lines are the numerical ranges. Grey patches mark the unstable regions. The figure is reproduced from Reddy & Henningson (1993).

Reddy & Henningson (1993) showed two examples illustrating the eigenvalues and pseudospectra of the Orr-Sommerfeld & Squire operator (Orr, 1907; Sommerfield, 1908; Squire, 1933), as shown in figure 2.6. Two cases all have stable eigenvalues. However, the pseudospectra intruding into the grey areas indicates that a small perturbation will trigger the flow system to enter the unstable region where the small perturbations grow and develop into turbulence.

Non-normality and transient energy growth

The transient energy growth feature is rooted in the non-normality of the linear operator (Schmid, 2007; Symon et al., 2018). A self-adjoint operator satisfies $A = A^*$, where $*$ denotes the Hermitian transpose. It has orthogonal eigenvectors and real eigenvalues. A normal operator satisfies $AA^* = A^*A$. It has orthogonal eigenvectors but may have complex eigenvalues (Strang, 1988). A non-normal operator does not have orthogonal eigenvectors and may experience transient growth before decaying.

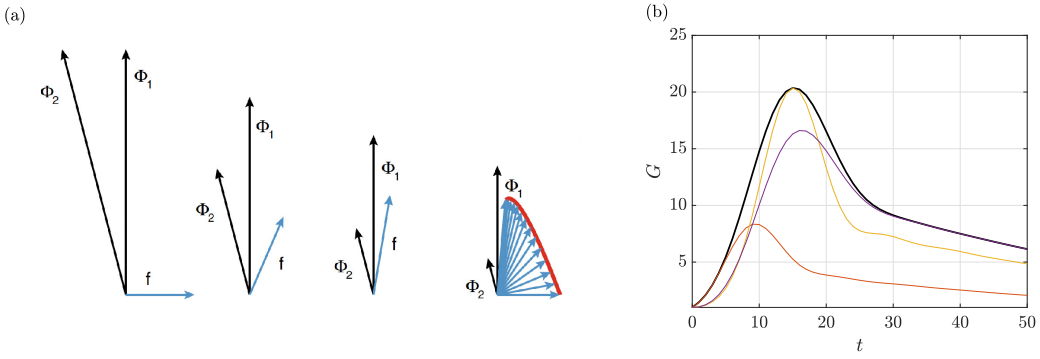

Figure 2.7: (a) A simple example of transient growth. Vector f is defined as the difference between two non-orthogonal vectors Φ_1 and Φ_2. Φ_1 has a lower shrinking rate than Φ_2. Starting on the left, vector f increases substantially in length in the direction of Φ_1 at first before decaying to zero (eventually both Φ_1 and Φ_2 decay to zero). This figure is taken from Schmid (2007). (b) Maximum amplification of initial energy defined in equation (2.7) for Poiseuille flow at $k_x = 1$, $k_y = 0$ and $Re = 3000$. The thick black line shows the maximum amplification G. Three thin coloured lines represent three energy growth cases under different initial conditions. The maximum amplification G is the envelope of any energy growth under a specific initial condition. This figure is reproduced from Reddy & Henningson (1993) with modifications.

A simple example is shown in figure 2.7(a) (Schmid, 2007). The Orr-Sommerfeld & Squire operator is non-normal because of the coupling term related to the mean shear between wall-normal velocity and wall-normal vorticity (Reddy & Henningson, 1993; Henningson & Reddy, 1994). Figure 2.7(b) shows an example of perturbation energy growth from the initial moment for Poiseuille flow at $k_x = 1$, $k_y = 0$ and $Re = 3000$,

where G is defined as the maximum amplification of initial kinetic energy $q(0)$ (Reddy & Henningson, 1993):

$$G(t) = \max_{q_0} \frac{\|q(t)\|^2}{\|q(0)\|^2}, \quad q = \frac{1}{2}\hat{u}_i^* \hat{u}_i \tag{2.7}$$

This could be linked back to the fact that its pseudospectra extrude into the unstable region as shown in figure 2.6(a).

Gustavsson (1991) was the first to apply the idea of transient energy growth in channel flows and found that the induced energy density from the wall-normal velocity greatly exceeds the initial energy density. The least-damped Orr-Sommerfeld mode as the initial condition excites the maximum energy density for structures infinitely elongated in the streamwise direction. Later, Butler & Farrell (1992, 1993) found that streamwise vortices divert the mean flow energy into streaks of streamwise velocity and enable the energy of the perturbation to grow by as much as three orders of magnitude in channel flows. Similar turbulence transient energy growth could also be found in pipe flows (Schmid & Henningson, 1994) and boundary layer flows (Andersson et al., 1999).

The dimension of optimal modes for transient energy growth could also be predicted by the linearised Navier-Stokes equations. Del Alamo & Jimenez (2006) predicted the typical widths of the near-wall streaks corresponding to two transient growth peaks: $\lambda_y^+ = 100$ in inner units and $\lambda_y/h = 3$ in outer units, by using the Orr-Sommerfeld & Squire operator with the eddy-viscosity model of Cess (1958). The two peaks separate well when the Reynolds number is large. Later, Pujals et al. (2009) used the same model and found that the optimal streaks associated with the primary peak have an optimal spacing of $\lambda_y = 4h$ in outer units and the peak increases as the Reynolds number increases. It should be noted that both studies form the linearised operators around the turbulent mean velocity profile.

Input-output model

Apart from the transient energy growth analyses, the linearised Navier-Stokes operator could be understood as a transfer function mapping an input to an output and revealing the receptivity of a flow system. The input could include contributions from free-stream turbulence, wall roughness, body forces and the neglected nonlinear forcing. The output is usually set to be the velocity field, though other outputs (for example turbulent production) have been investigated (Gong, 2021).

In terms of the unknown input mentioned above, one way is to treat it as stochastic forcing (Farrell & Ioannou, 1993, 1998; Bamieh & Dahleh, 2001; Jovanović & Bamieh, 2005; Hwang & Cossu, 2010b). The optimal modes can be obtained by solving the 2-norm of the linear operator related to the Lyapunov equation (Zhou et al., 1996). A

classic study by Jovanović & Bamieh (2005) looks at componentwise transfer functions, as shown in figure 2.8. The amplification mechanisms of TS waves, oblique waves, and streamwise streaks in subcritical transition could be explained by looking at the corresponding wavenumber regions. The streamwise-elongated structures are most amplified, followed by the oblique modes (with $k_x \neq 0$ and $k_y \neq 0$), followed by the TS waves. Jovanović & Bamieh (2005) also found that wall-normal and spanwise forces have a much stronger influence on the velocity field than streamwise force and that the impact of these forces is most powerful on the streamwise velocity component.

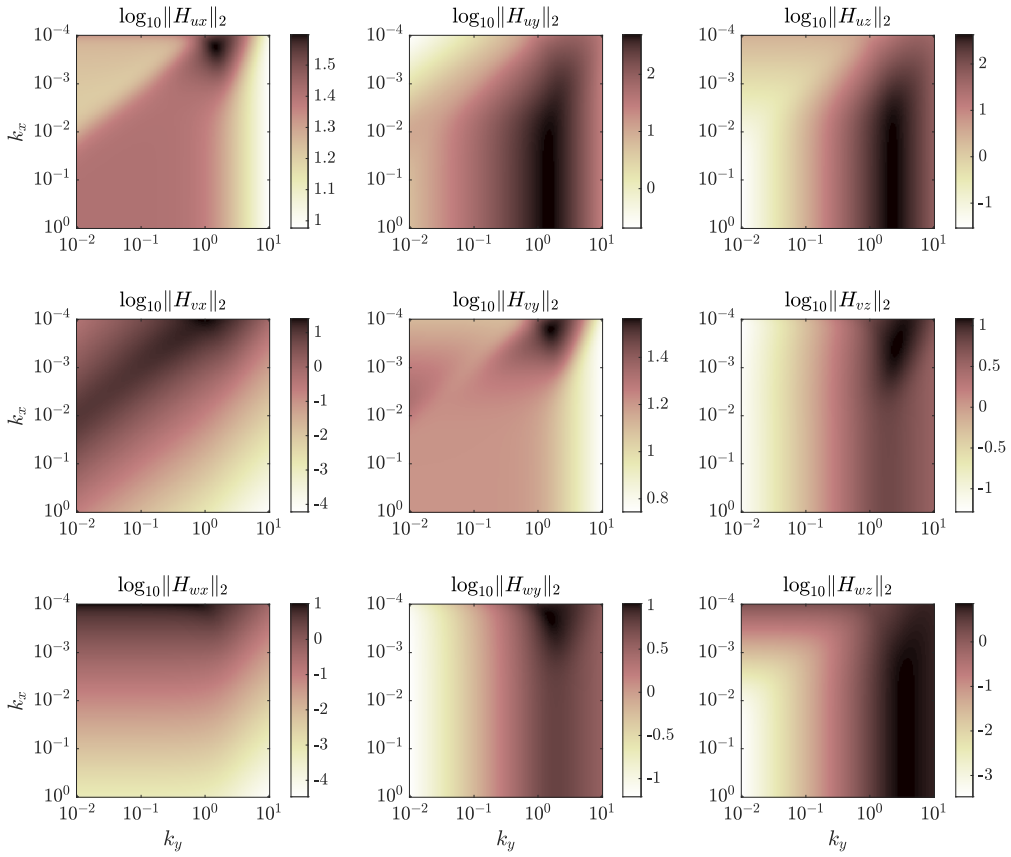

Figure 2.8: The 2-norm of the transfer function maps the forcing to the velocities componentwise at $Re = 2000$. The inputs of the first, second and third columns are the streamwise, spanwise and wall-normal forcings, respectively. The outputs of the first, second and third rows are the streamwise, spanwise and wall-normal velocities, respectively. This figure is reproduced from Jovanović & Bamieh (2005).

Another way is to treat the unknown input as harmonic forcing at a specified frequency (McKeon & Sharma, 2010; Hwang & Cossu, 2010b). The frequency could be chosen according to the characteristic time-scale in a flow or the frequency corresponding to the 'worst' case by calculating the infinity-norm of the linear operator (Zhou et al., 1996).

Interestingly, Hwang & Cossu (2010b) found that the optimal modes for channel flow (Poiseuille flow) from the initial-value, the harmonic-forcing, and the stochastic-forcing analyses are almost indistinguishable. The optimal input mode is composed of streamwise vortices and the optimal output mode is composed of streamwise streaks. It is worth mentioning that this input-output methodology was nicely further explored by McKeon & Sharma (2010) as discussed below.

Resolvent analysis[1]

The study by McKeon & Sharma (2010) uses the linearised Navier-Stokes equations of fluctuation velocities u_i around the turbulent mean velocity profile U_i and treats the nonlinear forcing terms (involving the Reynolds stress) as an input *without* assuming small perturbations:

$$\frac{\partial u_i}{\partial t} = \underbrace{-U_j\frac{\partial u_i}{\partial x_j} - u_j\frac{\partial U_i}{\partial x_j} - \frac{\partial p}{\partial x_i} + \frac{1}{Re_\tau}\frac{\partial^2 u_i}{\partial x_j^2}}_{\text{linear part}} \underbrace{-u_j\frac{\partial u_i}{\partial x_j} + \overline{u_j\frac{\partial u_i}{\partial x_j}}}_{\text{nonlinear part}} \tag{2.8}$$

The essence of resolvent analysis is shown in figure 2.9(a). The linear part in equation (2.8) maps the nonlinear forcing to the fluctuation velocities, involving energy amplification mechanisms. The nonlinear part in equation (2.8) maps the fluctuation velocities back to the nonlinear forcing, involving energy redistribution mechanisms. This feedback loop resembles the self-sustaining mechanisms in wall turbulence.

For channel flows, the time variable or the spatial variable(s) could be transformed into Fourier space:

$$\hat{\boldsymbol{u}}(z) = H(z;k_x,k_y,\omega)\hat{\boldsymbol{f}}(z) \tag{2.9}$$

where H is the resolvent operator casting the nonlinear forcing $\hat{\boldsymbol{f}}$ to the velocity $\hat{\boldsymbol{u}}$.

Fluid systems usually present low-rank features. For example, streamwise vortices generating streamwise streaks in wall-bounded flows and vortex shedding patterns in wake flows. Singular value decomposition (SVD) (Eckart & Young, 1936; Strang, 1988) is applied to the resolvent operator to extract the optimal modes:

$$H = \sum_{i=1}^{\infty} \sigma_i \phi_i^* \psi_i \tag{2.10}$$

where σ is the singular value, ϕ is the right singular vector corresponding to the input mode and ψ is the left singular vector corresponding to the output mode. If there is a

[1] In the fluid mechanics' community nowadays, resolvent analysis mostly refers to the study by McKeon & Sharma (2010). However, 'resolvent' is originally a term in mathematics and has been used for a long history (Schmid & Henningson, 2001).

great separation between the first singular value (or the first few singular values) and the rest, plus the nonlinear forcing does not present any preferential direction toward one of the suboptimal input modes, the velocities could be approximated using the leading mode from the singular value decomposition (Beneddine et al., 2016):

$$\hat{\boldsymbol{u}} \approx \sigma_1 \chi_1 \psi_1, \quad \sigma_1 \gg \sigma_2, \sigma_3 \ldots \tag{2.11}$$

where $\chi_1 = \langle \hat{\boldsymbol{f}}, \phi_1 \rangle$ is the coefficient of projection of the actual forcing onto the optimal input mode. Such condition is usually met at the critical layer for wall-bounded flows (McKeon & Sharma, 2010; Moarref et al., 2013) and at vortex shedding frequency for wake flows (Jeun et al., 2016).

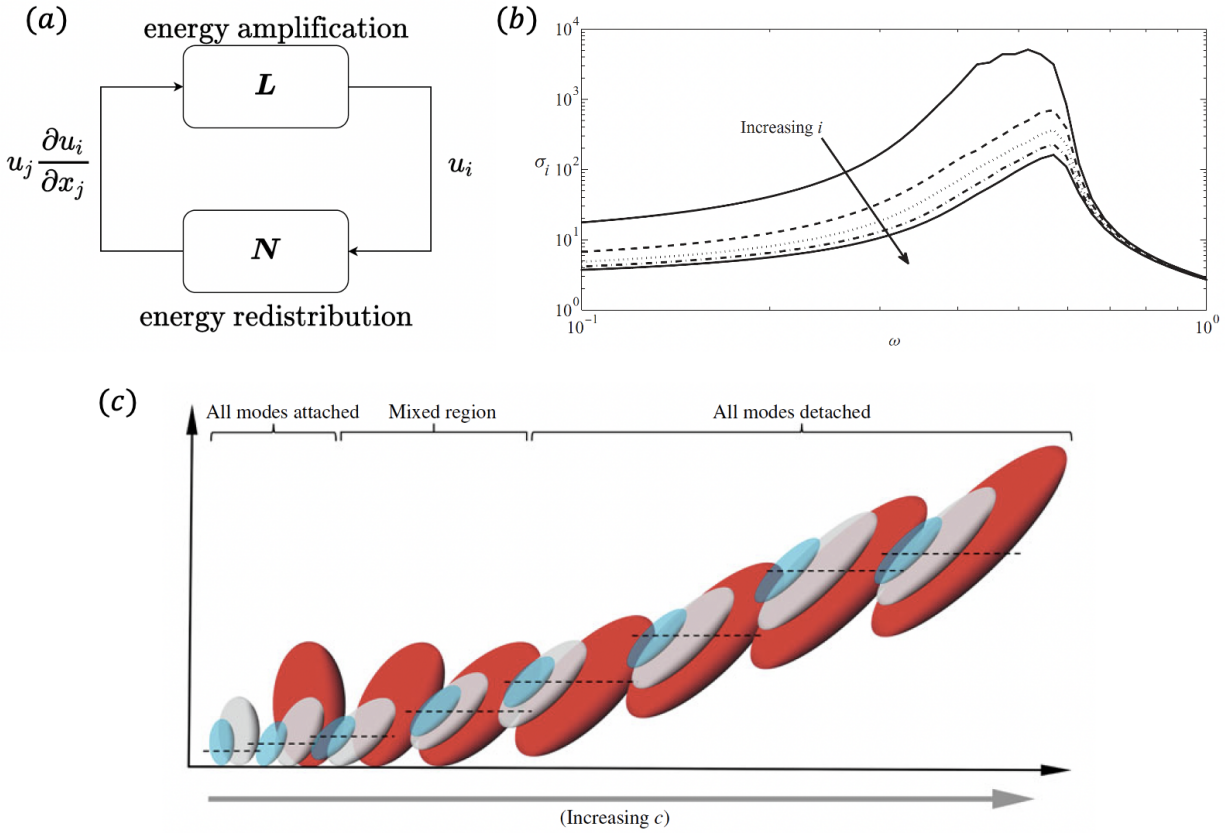

Figure 2.9: (a) The essence of resolvent analysis. $\boldsymbol{L}$ represents the linear part and $\boldsymbol{N}$ represents the nonlinear part as shown in equation (2.8). (b) Singular values for pipe flow at $(k,n) = (1,10)$ (k is the streamwise wavenumber and n is the azimuthal wavenumber) and $Re = 75 \times 10^3$. This figure is taken from McKeon & Sharma (2010). (c) A sketch for the output modes of the streamwise velocity observed with increasing c (wavespeed) for fixed (k_x, k_y) values. Three scales with decreasing streamwise wavenumber k_x are identified by blue, grey and red shading. The horizontal dashed lines mark the z-location of the critical layer for a given ω/k_x. This figure is taken from McKeon (2017).

Figure 2.9(b) shows an example of pipe flow resolvent. We can see that the first singular value is substantially greater than the rest as there is a great separation between the upper black solid line and the other lines. In this case, the first response mode (2.11) would approximate the real flow well (McKeon & Sharma, 2010).

Because of the low-rank characteristics in flows, resolvent analysis can predict the Reynolds number scaling statistics (McKeon & Sharma, 2010; Moarref et al., 2013) and relevant coherent structures, such as streaks and hairpin vortices (Sharma & McKeon, 2013). Figure 2.9(c) shows the attached modes and detached modes for the streamwise velocity predicted from resolvent analysis (McKeon, 2017).

However, for flow conditions where there is no significant separation of the leading singular values from the rest (linear mechanisms do not dominate), knowledge of the nonlinear forcing is required. The nonlinear forcing is structured (Zare et al., 2017; Morra et al., 2021; Nogueira et al., 2021) and has non-negligible projection onto the suboptimal input modes under some conditions (Symon et al., 2018; Rosenberg et al., 2019). As indicated in figure 2.9(a), the nonlinear part is essential for closing the loop for resolvent analysis. One way to achieve that is to model the nonlinear forcing (Farrell et al., 2017; Liu & Gayme, 2021; Hernández et al., 2022a,b). Another way is to link resolvent analysis with self-sustaining solutions (Park & Graham, 2015).

2.2.3 Flow estimation and control

Flow estimation

Method	Flow type	Study
stochastic estimation	boundary layer	Guezennec (1989)
extended Kalman filter	channel	Chevalier et al. (2006)
ensemble Kalman filter	channel	Colburn et al. (2011)
stochastic estimation + Kalman filter	flat plate	Tu et al. (2013)
stochastic estimation	boundary layer	Baars et al. (2016)
SINDy	cylinder	Loiseau et al. (2018)
Kalman filter	channel	Illingworth et al. (2018)
stochastic estimation	channel	Madhusudanan et al. (2019)
Kalman filter	cylinder	Gong et al. (2020)
resolvent+SPOD	channel	Towne et al. (2020)
adjoint-variational	channel	Wang et al. (2022)

Table 2.3: A brief summary of flow estimation. SINDy represents sparse identification of nonlinear dynamics. SPOD represents spectral proper orthogonal decomposition.

Flow estimation involves predicting the temporal and spatial evolution of a fluid system using noisy observations and mathematical models, as real-time measurements are limited in terms of spatial-temporal resolution. Generally speaking, there are three classes of state estimation methods: linear stochastic estimation (LSE), filtering and smoothing. Table 2.3 gives a few examples of flow estimation.

Linear stochastic estimation (LSE) uses the velocity at one location as input to predict velocity at other locations as output with prior knowledge of the two-point correlation between these two locations (Adrian & Moin, 1988). The two-point correlation could also be understood as a joint probability distribution. Spectral linear stochastic estimation is an extension in which estimation is implemented in Fourier space (Baars et al., 2016; Madhusudanan et al., 2019).

Filtering refers to using current states and measurements to predict future states using time marching. Kalman filter (Kalman, 1960) is a classic filter and was applied in laminar channel flow first by Hœpffner et al. (2005). Later, Chevalier et al. (2006) used the Kalman filter in turbulent channel flow at $Re_\tau = 100$ and treated the nonlinear forcing terms as disturbance in the Kalman filter set-up. They also showed that the extended Kalman filter outperforms the standard Kalman filter. An excellent state estimation of $Re_\tau = 100$ turbulent flow using wall information only was achieved by Colburn et al. (2011) using ensemble Kalman filter targeted for high-dimensional systems.

Smoothing (adjoint-variational approach) refers to minimising the cost function which is proportional to the difference between prediction and observation involving finding an optimal initial condition (Le Dimet & Talagrand, 1986; Wang et al., 2022). Unlike linear stochastic estimation and Kalman filtering, smoothing satisfies the government equations which are the Navier-Stokes equations for fluid systems.

Including the nonlinearity improves estimator performance since the Navier-Stokes equations are nonlinear. The nonlinearity could be incorporated into the linear models by calculating the covariance of the nonlinear forcing (Chevalier et al., 2006), calculating the cross-spectral density (CSD) tensors of the nonlinear forcing (Towne et al., 2020), using an eddy-viscosity model (Illingworth et al., 2018; Madhusudanan et al., 2019), to name a few. Figure 2.10 gives an example of channel flow estimation where the linear model is augmented with an eddy viscosity model (Cess, 1958). This estimator outperforms the pure linear model (Madhusudanan et al., 2019).

Incorporating physics into mathematical models is another way to improve estimation performance. For example, Baars et al. (2016) added a predictive model illustrating the relationship between inner and outer layers (Marusic et al., 2010) into the spectral linear stochastic estimation model and gave good estimation over a three-decade span of high Reynolds numbers.

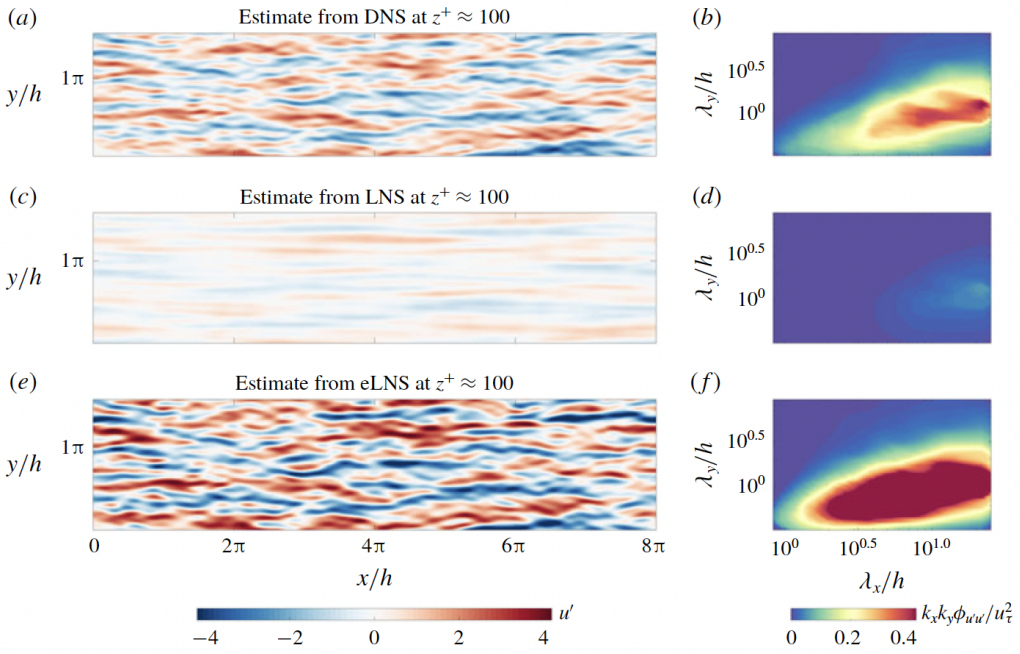

Figure 2.10: (a,c,e) The estimated instantaneous streamwise velocity field and (b,d,f) the corresponding 2-D energy spectrum obtained using (a,b) the DNS dataset, (c,d) linear Navier-Stokes equation model (LNS) and (e,f) linear Navier-Stokes equation model augmented with eddy viscosity (eLNS). The estimate is obtained at $z_1^+ \approx 100$ based on a measurement at $z_2^+ \approx 300$. The figure is taken from Madhusudanan et al. (2019).

Flow control

Method	Flow type	Study
polymer additives (experiment)	boundary layer	Lumley (1973)
blowing/suction (experiment)	boundary layer	Tardu (2001)
blowing/suction (DNS)	channel	Bewley et al. (2001)
LQG	channel	Lim (2003)
resolvent	channel	Luhar et al. (2015)
PID	channel	Kim & Choi (2017)
SINDy + MPC	F8 aircraft	Kaiser et al. (2018)
linearised NS equations	channel with riblets	Ran et al. (2021)
resolvent + POD	cylinder	Jin et al. (2022)

Table 2.4: A brief summary of flow control. LQG represents linear quadratic regulator. PID represents proportional–integral–derivative. MPC represents model predictive control.

Flow control involves manipulating flow into a desired behaviour, such as enhancing the mixing of oxygen and fuel in a combustion chamber, delaying the transition to turbulent flow, or reducing the drag of a boundary layer. Generally speaking, control strategies

could be categorised into two major groups: passive control and active control (Gad-el Hak, 1996; Kim & Bewley, 2007; Tardu, 2017). Active control could be further divided into open-loop control and closed-loop control (feedback control) (Brunton & Noack, 2015). Table 2.4 gives a few examples of flow control.

Passive control does not require energy input for flow manipulation. A typical way to achieve wall turbulence control is to change the surface condition of the wall, such as adding polymer additives (Lumley, 1973), using complaint surfaces (Luhar et al., 2015), or designing riblets (Ran et al., 2021).

Active control requires energy input for flow manipulation. Periodic blowing and suction in boundary layers is an example of open-loop control (Tardu, 2001). Closed-loop control considers the feedback from the output and is more robust in off-design situations. A classic example of closed-loop control is the proportional-integral-derivative (PID) controller in channel flows (Kim & Choi, 2017). With the increased computational power, closed-loop control of wall turbulence has been implemented in DNS (Bewley et al., 2001) or using machine learning methods (Kaiser et al., 2018).

Incorporating the wall turbulence physics into controller design is insightful. It has been shown that skin friction in turbulent boundary layers is mainly contributed by near-wall streamwise vortices which are key components in the self-sustaining process. So, cutting any phase in the self-sustaining process off leads to weakening the formation of near-wall structures (Kim, 2011). Lim (2003) designed a linear quadratic regulator (LQR) to minimise the linear coupling between the wall-normal velocity and wall-normal vorticity and 20% of drag reduction was achieved. Figure 2.11 shows an example of the drag reduction on the bottom wall owing to the reduced vorticity.

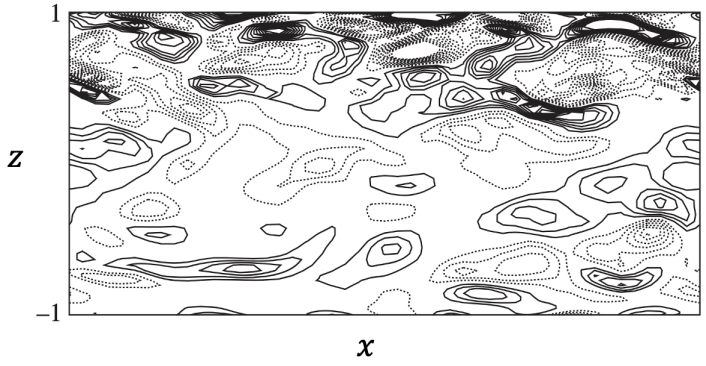

Figure 2.11: Contours of streamwise vorticity in the xz plane. A LQR controller is implemented on the bottom wall. The figure is taken from Kim (2011).

Chapter 3

Direct numerical simulation datasets

3.1 Channel flow geometry

The channel flow geometry used in the following chapters is shown in figure 3.1. The streamwise, spanwise and wall-normal directions are denoted by x, y and z, respectively. The instantaneous streamwise, spanwise and wall-normal velocities are denoted by $\mathscr{U}$, $\mathscr{V}$ and $\mathscr{W}$, respectively. The instantaneous pressure is denoted by $\mathscr{P}$. The dimensions of the channel are $2\pi h \times \pi h \times 2h$, which is sufficiently large to obtain correct turbulence statistics (Lozano-Durán & Jiménez, 2014).

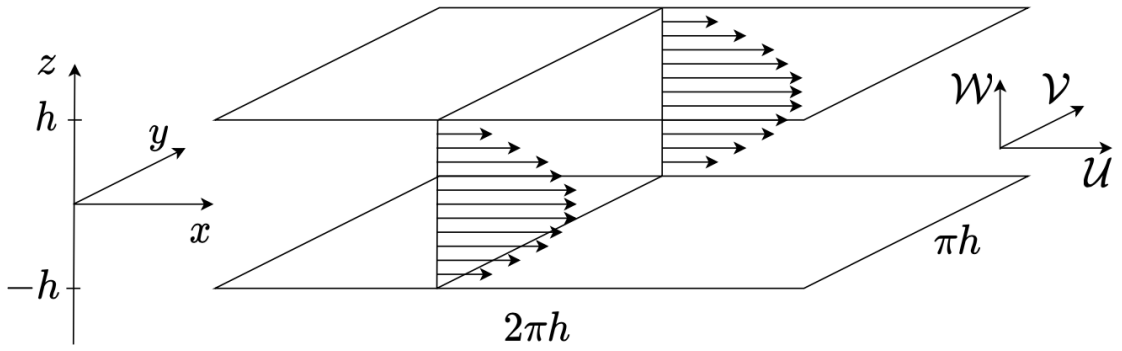

Figure 3.1: Channel flow geometry (Poiseuille flow).

We perform a Reynolds decomposition in which we decompose the instantaneous variables into time-averaged variables and fluctuation variables: $\mathscr{U}_i = U_i + u_i$, $\mathscr{P} = P + p$. $\mathscr{U}$, U and u represent the instantaneous velocity, time-averaged velocity and fluctuation velocity, respectively. Index i $(i = 1, 2, 3)$ denotes the streamwise x, spanwise y and wall-normal z direction, respectively. Most discussions in this thesis are for the fluctuation velocities.

As for the normalisation, length scales are non-dimensionalised using the channel

half-height h, and time scales are non-dimensionalised using u_τ/h, where $u_\tau = \sqrt{\tau_w/\rho}$, ρ is the density, τ_w is the mean wall shear stress and u_τ is the friction velocity. Then, the friction Reynolds number, $Re_\tau = hu_\tau/\nu$, is defined using h, u_τ and the kinematic viscosity, ν.

For incompressible Poiseuille flow (pressure-driven flow), the external input to the flow is a mean pressure gradient in the streamwise direction $\frac{dP}{dx} < 0$. The laminar analytic solution is a parabolic profile for the streamwise velocity and zero spanwise and wall-normal velocities: $U_i = (1-z^2, 0, 0)$.

3.2 DNS datasets

Direct numerical simulations of incompressible channel flows are performed using a staggered-grid fourth-order finite-difference solver (Chung et al., 2014). The staggered-grid fourth-order finite difference method has been chosen because it provides accurate turbulence statistics without being computationally demanding at low Re_τ. There are two main advantages of using a staggered grid (Ferziger et al., 2019). First, it enhances numerical stability by preventing oscillatory pressure fields. Second, it improves mass and momentum conservation accuracy as the arrangement of velocity components on cell faces and pressure at cell centres facilitates more precise flux calculations. The fourth-order finite difference method also offers significant benefits (Lele, 1992; Morinishi et al., 1998). First, it has a lower truncation error compared to lower-order methods. Second, it enables a faster convergence rate, particularly for DNS where high solution resolution is necessary. One drawback of both the staggered-grid and fourth-order methods is the increased computational time and resources required, especially at high Re_τ. However, given the low Re_τ considered in our study, DNS simulations could be efficiently executed on modern supercomputers.

Table 3.1 summarises the simulation parameters. For $Re_\tau = 180$, the minimum wavenumbers are $k_x = \pm 1$, $k_y = \pm 2$ and the maximum wavenumbers are $k_x = \pm 55$, $k_y = \pm 110$. For $Re_\tau = 590$, the minimum wavenumbers are $k_x = \pm 1$, $k_y = \pm 2$ and the maximum wavenumbers are $k_x = \pm 191$, $k_y = \pm 382$.

Re_τ	L_x	L_y	$n_x \times n_y \times n_z$	Δx^+	Δy^+	Δz^+_{max}	Δz^+_{min}	Δt^+
180	2π	π	$112 \times 112 \times 150$	10.01	5.05	3.77	0.04	0.36
590	2π	π	$384 \times 384 \times 500$	9.65	4.83	3.71	0.01	0.118

Table 3.1: Parameters for the DNS. L, domain length; n, number of grid points; Δ^+, grid-spacing in viscous units; Δt is the simulation time step.

Figure 3.2 shows the staggered grid. To calculate the values (nonlinear terms and

turbulent kinetic energy budget in this thesis) that require velocities in the three directions (u,v,w), we first linearly interpolate the velocities from the staggered grid onto a collocated grid where velocities and pressure are at the same locations. Then, we use the interpolated velocities on the collocated grid to calculate the values. The grids are evenly distributed in the streamwise and spanwise directions. In the wall-normal direction, the grid follows a Chebyshev distribution. The grid coordinate in the z direction is $z = \cos(\frac{n}{N\pi})$, $z \in [-1,1]$, where n is an integer from 0 to N and N is the total number of grid point in the z direction. $N = 129$ for the $Re_\tau = 180$ dataset and $N = 501$ for the $Re_\tau = 590$ dataset.

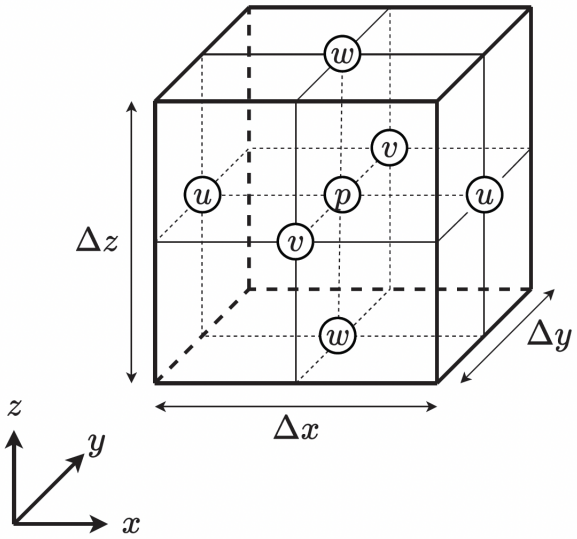

Figure 3.2: Staggered grid illustration.

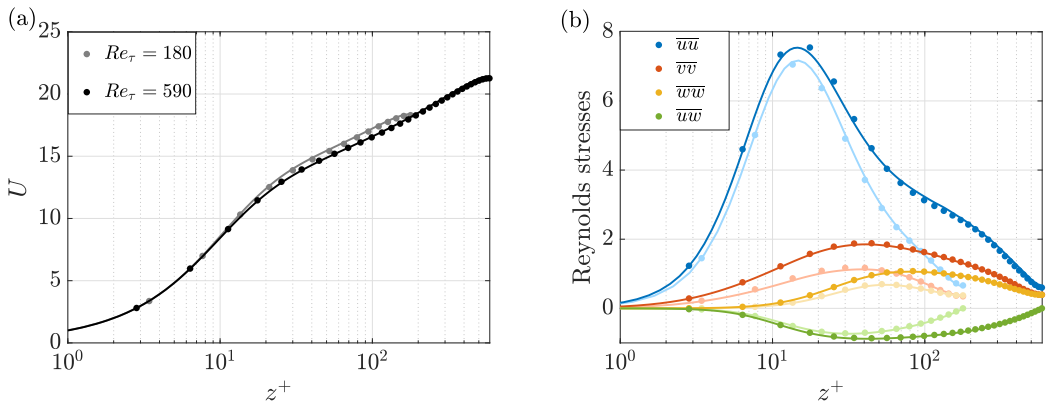

Figure 3.3: Comparison between the DNS datasets represented by solid lines and the standard DNS datasets (Moser et al., 1999) represented by discrete markers. (a) Mean streamwise velocity. (b) Reynolds stresses.

For $Re_\tau = 180$, the total simulation time is $20h/u_\tau$ with a time step of $0.002h/u_\tau$; for $Re_\tau = 590$, the total simulation time is $10h/u_\tau$ with a time step of $0.0002h/u_\tau$. h/u_τ is used as the time unit for non-dimensionalisation. The time-averaged first-order and second-order statistics of the present DNS datasets show good agreement with the Moser et al. (1999), as shown in figure 3.3.

The turbulent kinetic energy (TKE) equation with each term as a third-order statistics on the right-hand side is (Pope, 2000):

$$\frac{\mathrm{D}}{\mathrm{D}t}\left(\frac{1}{2}u_i u_i\right) = \overbrace{-u_i u_j \frac{\partial U_i}{\partial x_j}}^{\text{production}} \underbrace{-\frac{1}{Re}\frac{\partial u_i}{\partial x_j}\frac{\partial u_i}{\partial x_j}}_{\text{dissipation}} \overbrace{-u_j \frac{\partial\left(\frac{1}{2}u_i u_i\right)}{\partial x_j}}^{\text{turbulent convection}} \underbrace{-u_i \frac{\partial p}{\partial x_i}}_{\text{pressure diffusion}} \overbrace{+\frac{1}{Re}\frac{\partial^2\left(\frac{1}{2}u_i u_i\right)}{\partial x_j \partial x_j}}^{\text{viscous diffusion}} \tag{3.1}$$

$\frac{\mathrm{D}}{\mathrm{D}t} = \frac{\partial}{\partial t} + U_j \frac{\partial}{\partial x_j}$ is the material derivative operator. The Einstein summation convention applies to the repeated indices i and j. For a statistically stationary flow, the left-hand side of equation (3.1) is zero.

The time-averaged third-order statistics of the present DNS datasets show good agreement with the Moser et al. (1999), as shown in figures 3.4 and 3.5.

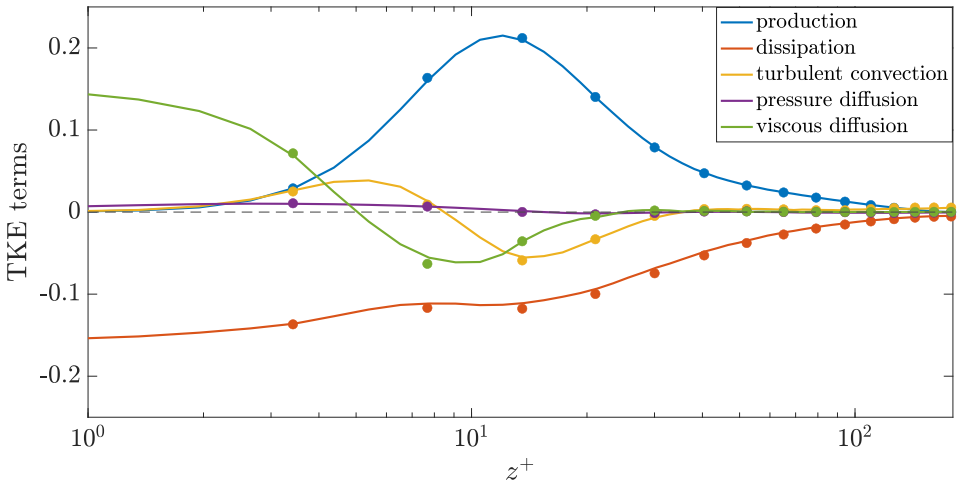

Figure 3.4: Turbulent kinetic energy budget at $Re_\tau = 180$. Solid lines are for the calculated DNS dataset and markers are for the standard DNS dataset (Moser et al., 1999).

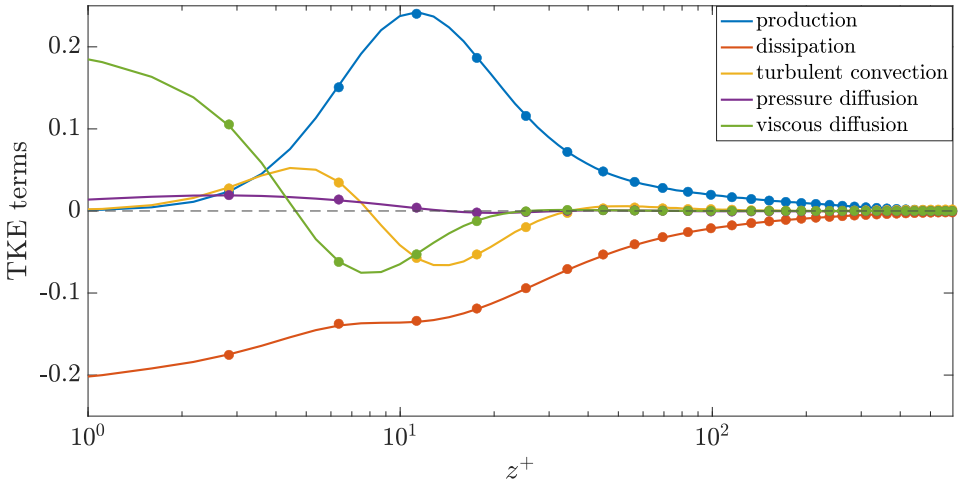

Figure 3.5: Turbulent kinetic energy budget at $Re_\tau = 590$. Solid lines are for the calculated DNS dataset and markers are for the standard DNS dataset (Moser et al., 1999).

Deviations between the current DNS data and the results of Moser et al. (1999) originate from two factors. First, the methods used to solve partial differential equations are different: Moser et al. (1999) uses spectral method (Fourier expansion in the stramwise and spanwise direction, Chebyshev-tau expansion in the wall-normal direction) and this study uses fourth-order finite difference method. Second, the domain sizes of the simulated flow are different: $4\pi h \times 4\pi h/3 \times h$ in Moser et al. (1999) and $2\pi h \times \pi h \times h$ in this study. Nevertheless, the deviations are within tolerance, and both datasets provide accurate turbulence statistics.

Chapter 4

Mode-to-mode nonlinear energy transfer in channel flows

We investigate nonlinear energy transfer for channel flows at friction Reynolds numbers of $Re_\tau = 180$ and 590. The key feature of the analysis is that we introduce a new variable, which quantifies the energy transferred from a source mode to a recipient mode through explicit examination of nonlinear triadic interactions in streamwise-spanwise wavenumber space. First, we use this variable to quantify the nonlinear energy transfer gain and loss for individual Fourier modes. The nonlinear energy transfer gain and loss cannot be directly obtained from the turbulent kinetic energy (TKE) equation. Second, we quantify the nonlinear energy transfer budgets for three types of structures: streamwise streaks, oblique waves and Tollmien-Schlichting waves. We found that a transverse cascade from streamwise-elongated modes to spanwise-elongated modes exists in all three structures. Third, we quantify the forward and inverse cascades between resolved scales and subgrid scales in the spirit of large-eddy simulation. For the cutoff wavelength range we consider, the forward and inverse cascades between the resolved scales and subgrid scales result in a net forward cascade from the resolved scales to the subgrid scales. The shape of the net forward cascade curve with respect to the cutoff wavelength resembles the net forward cascade predicted by the Smagorinsky eddy viscosity.

4.1 Introduction

Turbulence involves energy transfer across a wide range of scales and is important for many applications, such as combustion (Ertesvåg & Magnussen, 2000), ocean engineering (Hasselmann et al., 1963) and the earth's climate (Richardson, 1922). It is generally understood that energy is transferred from large scales to small scales, known as the forward cascade (Richardson, 1922; Kolmogorov, 1941). But an inverse cascade in which energy is transferred from small scales to large scales also occurs (Domaradzki et al., 1994; Dunn & Morrison, 2003; Cimarelli et al., 2013, 2016). Both forward and inverse cascades are involved in vortex regeneration in the self-sustaining process for wall-turbulence (Hamilton et al., 1995; Waleffe, 1997), as discussed in chapter 2. In large-eddy simulation (LES), the failure to account for backscatter has been proposed as a cause of inaccurate results (Piomelli et al., 1991; Härtel et al., 1994; Cimarelli & De Angelis, 2014). The above considerations are all dictated by the physics of the energy cascade across scales in wall-bounded turbulent flows.

This energy cascade can be viewed in either physical space or Fourier space. In physical space, the energy cascade is characterised by high spatio-temporal intermittency (Meneveau & Sreenivasan, 1991). In Fourier space, for flow geometries (such as channels, pipes, boundary layers) with at least one homogeneous spatial dimension, the energy cascade can be interpreted as energy redistributed among different Fourier modes, described by the nonlinear energy transfer term in the spectral turbulent kinetic energy (sTKE) equation (Tennekes & Lumley, 1972; Pope, 2000). Here, a mode refers to scales with a particular wavelength in the homogeneous direction. The nonlinear energy transfer term in the spectral energy budget represents the net energy received by a particular mode from all other modes through nonlinear interactions since the term is a convolution of all wavenumber-compatible triadic interactions. Triadic interaction refers to the energy transfer among three modes whose wavenumbers satisfy $\boldsymbol{k}+\boldsymbol{p}+\boldsymbol{q}=\boldsymbol{0}$ (Domaradzki & Rogallo, 1990; Domaradzki, 1992; Waleffe, 1992; Domaradzki et al., 1994). However, we merely know the net energy transfer for each Fourier mode but not the detailed contributions to this net value from the nonlinear energy transfer term, because the convolution hides the individual triadic interactions.

Compared to homogeneous isotropic turbulence, only a few studies have explored the triadic interactions of nonlinear energy transfer for channel flows (Domaradzki et al., 1994; Webber et al., 2002; Cho et al., 2018; Karban et al., 2023). A single wavenumber triad could be interpreted as energy transfer from a source mode to a recipient mode via an advective mode (Domaradzki & Rogallo, 1990; Smyth, 1992; Webber et al., 2002; Alexakis et al., 2005; Jin et al., 2021). To gain more insight into the energy cascade in channel flows, we expand the convolution of the nonlinear energy transfer term in

streamwise-spanwise wavenumber space. Following this, we formulate a new variable $\hat{M}_{(s_x,s_y)(k_x,k_y)}$ (defined in §4.2.2) that represents mode-to-mode nonlinear energy transfer in streamwise-spanwise wavenumber space. Compared to the convolution term which only gives us the net energy transfer for a specific Fourier mode, with this variable, we are able to quantify the energy transfer between any two Fourier modes.

We use this four-dimensional variable $\hat{M}_{(s_x,s_y)(k_x,k_y)}$ (one source mode and one recipient mode with each mode consisting of a streamwise wavenumber and a spanwise wavenumber) to explore three things using direct numerical simulation (DNS) datasets at $Re_\tau = 180$ and 590. First, since the nonlinear energy transfer term in the sTKE equations could only give us one value representing the net energy transfer for each mode previously, we use this new variable $\hat{M}_{(s_x,s_y)(k_x,k_y)}$ to obtain two additional values quantifying the net energy transfer gain and loss due to nonlinear interactions for each mode. Second, we investigate the nonlinear energy transfer budgets for three types of structures: streamwise streaks, oblique waves and Tollmien–Schlichting (TS) waves which are important in sustaining turbulence in wall-bounded flows. Third, similar to a large-eddy simulation set-up, we quantify the forward cascade and inverse cascade between resolved and subgrid scales. We further compare the forward cascade calculated using $\hat{M}$ with the forward cascade calculated using the Smagorinsky eddy viscosity. The similarities and differences between $Re_\tau = 180$ and 590 are discussed.

This chapter is organised as follows. In §4.2, the equations for spectral turbulent kinetic energy (sTKE) budget and the new variable $\hat{M}_{(s_x,s_y)(k_x,k_y)}$ representing mode-to-mode nonlinear energy transfer are derived. §4.3 presents the results. Specifically, §4.3.1 revisits the previous study from Symon et al. (2021) about the wall-normal integrated spectral energy transfer budget; §4.3.2 uses two examples to interpret the new variable and to illustrate energy transfer pathways; §4.3.3 presents the positive and negative nonlinear energy transfer spectra; §4.3.4 investigates the nonlinear energy transfer of streamwise streaks, oblique waves and TS waves; §4.3.5 quantifies the forward cascade and inverse cascade between resolved scales and subgrid scales in the spirit of LES. Conclusions are drawn in §4.4.

4.2 Methods

An introduction to the spectral turbulent kinetic energy equation integrated across the channel height is presented in §4.2.1. In §4.2.2, we introduce a four-dimensional variable quantifying mode-to-mode nonlinear energy transfer and the pertinent properties.

4.2.1 Spectral energy transfer budget

The non-dimensional incompressible Navier-Stokes equations for the fluctuation velocities are:

$$\begin{aligned} \frac{\partial u_i}{\partial x_i} &= 0 \\ \frac{\partial u_i}{\partial t} + u_j\frac{\partial U_i}{\partial x_j} + U_j\frac{\partial u_i}{\partial x_j} + \frac{\partial}{\partial x_j}(u_iu_j - \overline{u_iu_j}) &= -\frac{\partial p}{\partial x_i} + \frac{1}{Re_\tau}\frac{\partial^2 u_i}{\partial x_j \partial x_j} \end{aligned} \tag{4.1}$$

Owing to the periodic assumption in the streamwise and spanwise directions, we investigate energy transfer in two-dimensional streamwise-spanwise wavenumber space. We define the inner product $\langle c_1, c_2\rangle_I = \frac{1}{2}\int_{-1}^{1} c_1^* c_2 \,\mathrm{d}z$, where c_1 and c_2 are two complex vectors, $*$ denotes the complex conjugate. We use this inner product definition to represent the wall-normal integrated kinetic energy at mode (k_x, k_y) (Reddy & Henningson, 1993; Domaradzki et al., 1994):

$$\hat{E}(k_x,k_y) = \frac{1}{2}\langle \hat{u}^{(k_x,k_y)}, \hat{u}^{(k_x,k_y)}\rangle_I + \frac{1}{2}\langle \hat{v}^{(k_x,k_y)}, \hat{v}^{(k_x,k_y)}\rangle_I + \frac{1}{2}\langle \hat{w}^{(k_x,k_y)}, \hat{w}^{(k_x,k_y)}\rangle_I \tag{4.2}$$

where k_x is the streamwise wavenumber and k_y is the spanwise wavenumber. The superscript refers to the individual Fourier mode under consideration: $\hat{u}^{(k_x,k_y)}$ is the Fourier coefficient of u_i at wavenumber (k_x, k_y). More explanations of energy transfer in Fourier space are in Appendix A.1.

The spectral energy transfer budget can be obtained by first taking Fourier transforms of equation (4.1) in the x and y directions, and then multiplying by the conjugate mode $(\hat{u}_i^{(k_x,k_y)})^* = \hat{u}_i^{(-k_x,-k_y)}$. Then, we integrate the energy transfer budget in the wall-normal direction and obtain (Symon et al., 2021):

$$\overline{\frac{\partial \hat{E}(k_x,k_y)}{\partial t}} = \underbrace{-\overline{\langle \hat{u}, \frac{\mathrm{d}U}{\mathrm{d}z}\hat{w}\rangle_I}}_{\hat{P}(k_x,k_y)} \underbrace{- \frac{1}{Re_\tau}\overline{\langle \widehat{\frac{\partial u_i}{\partial x_j}}, \widehat{\frac{\partial u_i}{\partial x_j}}\rangle_I}}_{\hat{D}(k_x,k_y)} \underbrace{- \overline{\langle \hat{u}_i, \widehat{\frac{\partial u_i u_j}{\partial x_j}}\rangle_I}}_{\hat{N}(k_x,k_y)} \tag{4.3a}$$

$$\hat{P}(k_x,k_y) - \hat{D}(k_x,k_y) + \hat{N}(k_x,k_y) = 0 \tag{4.3b}$$

with summation implied in the coordinate directions over the repeating index i or j. Equation (4.3a) describes the wall-normal integrated energy transfer balance for a single Fourier mode. The left-hand side is the time derivative of the turbulent kinetic energy for a single Fourier mode. $\hat{P}$ represents production; $-\hat{D}$ represents (pseudo) dissipation (Pope, 2000); and $\hat{N}$ represents the net nonlinear energy transfer (the net energy that mode

(k_x, k_y) receives through nonlinear interactions with all other modes). The size of an eddy corresponding to a given Fourier mode can be defined using the isotropic wall-parallel wavelength: $\lambda_I = 2\pi/k_I$, where $k_I^2 = k_x^2 + k_y^2$ (Jiménez, 2018; Lee & Moser, 2019). However, this definition neglects the anisotropy in channel flows. For a statistically stationary flow, the left-hand side of equation (4.3a) is zero, meaning that the wall-normal integrated production, dissipation and net nonlinear energy transfer reach a balance for each mode, as shown in equation (4.3b). According to the normalisation described in §3, the energy transfer terms ($\hat{P}$, $\hat{D}$ and $\hat{N}$ in (4.3a)) are non-dimensionalised by u_τ^3/h. Strictly speaking, production, dissipation and nonlinear energy transfer in equation (4.3a) are energy transfer rates because it is the kinetic energy variation rate on the left-hand side of (4.3a).

We use non-negative wavenumbers to describe a mode (k_x, k_y), where $k_x \geq 0$ and $k_y \geq 0$. The energy transfer at mode (k_x, k_y) with $k_x > 0$ and $k_y > 0$ contains the contributions from the wavenumber pairs (k_x, k_y), $(-k_x, -k_y)$, $(-k_x, k_y)$ and $(k_x, -k_y)$. For example, production at mode (k_x, k_y) is equal to $\hat{P}(k_x, k_y) + \hat{P}(-k_x, k_y) + \text{c.c.}$, where c.c. represents complex conjugate. The energy transfer at mode $(k_x, 0)$ with $k_x > 0$ contains the contributions from the wavenumber pairs $(k_x, 0)$ and $(-k_x, 0)$. For example, production at mode $(k_x, 0)$ is equal to $\hat{P}(k_x, 0) + \text{c.c.}$. The energy transfer at mode $(0, k_y)$ with $k_y > 0$ contains the contributions from the wavenumber pairs $(0, k_y)$ and $(0, -k_y)$. For example, production at mode $(0, k_y)$ is equal to $\hat{P}(0, k_y) + \text{c.c.}$. Following this, the energy transfer $\hat{P}, \hat{D}, \hat{N}$ at one mode (k_x, k_y) with $k_x \geq 0, k_y \geq 0$ is a real number. The derivation of equation (4.3a) is in Appendix A.2.

$\hat{N}(k_x, k_y)$ in (4.3a) is conservative:

$$\int_0^\infty \int_0^\infty \hat{N}(k_x, k_y)\, \mathrm{d}k_x \mathrm{d}k_y = 0 \tag{4.4}$$

Equation (4.4) states that the sum of the net nonlinear energy transfer across all Fourier modes is zero. This implies that nonlinear energy transfer redistributes energy across scales without adding or removing energy overall. This can also be seen from the Reynolds-Orr equation: the only energy source for turbulence is production and the only energy sink for turbulence is dissipation (Schmid & Henningson, 2001).

4.2.2 Mode-to-mode nonlinear energy transfer $\hat{M}_{(s_x,s_y)(k_x,k_y)}$

$\hat{N}(k_x, k_y)$ on the right-hand side of equation (4.3a) represents the net energy received by mode (k_x, k_y) from nonlinear interactions between mode (k_x, k_y) and all other modes, without giving information about the individual contributions to this net value. To illustrate, mode (k_x, k_y) could potentially gain energy from mode (s_{x1}, s_{y1}), lose energy to mode (s_{x2}, s_{y2}), gain energy from mode (s_{x3}, s_{y3}), lose energy to mode (s_{x4}, s_{y4}), and so on. But

those mode-to-mode nonlinear energy transfer is hidden because $\hat{N}$ represents a sum over all modes.

$\hat{N}(k_x, k_y)$ in equation (4.3a) can be expressed as a convolution composed of all wavenumber-compatible triadic interactions:

$$\hat{N}(k_x, k_y) = \int_0^\infty \int_0^\infty \hat{M}_{(s_x,s_y)(k_x,k_y)} \mathrm{d}s_x \mathrm{d}s_y \tag{4.5}$$

where

$$\hat{M}_{(s_x,s_y)(k_x,k_y)} = -\hat{u}_i^{(-k_x,-k_y)} \widehat{\hat{u}_j^{(k_x-s_x,k_y-s_y)} \frac{\partial u_i}{\partial x_j}}^{(s_x,s_y)} \tag{4.6}$$

A single set of triadic interaction involving three distinct modes can be understood as the energy transferred nonlinearly from mode (s_x, s_y) to mode (k_x, k_y) with the help of mode $(k_x - s_x, k_y - s_y)$ (Domaradzki & Rogallo, 1990; Smyth, 1992; Webber et al., 2002; Alexakis et al., 2005; Jin et al., 2021). s_x is the streamwise wavenumber and s_y is the spanwise wavenumber for another mode (s_x, s_y) different from mode (k_x, k_y). Thus, the four-dimensional variable $\hat{M}_{(s_x,s_y)(k_x,k_y)}$ describes the energy transferred nonlinearly from one Fourier mode (s_x, s_y) to another Fourier mode (k_x, k_y). As mentioned before, we discuss modes composed of non-negative wavenumbers. The expressions for $\hat{M}_{(s_x,s_y)(k_x,k_y)}$ with $s_x, s_y, k_x, k_y \geq 0$ are discussed in detail in Appendix A.3. Most result discussions in this chapter centre on the mode-to-mode nonlinear energy transfer $\hat{M}$ (4.6). For the ease of reading, we sometimes omit the word 'nonlinear'. Apart from production and dissipation, energy transfer, gaining energy and losing energy in the following discussions refer to $\hat{M}$ (4.6) due to nonlinear interactions.

Furthermore, $\hat{M}$ which represents wall-normal integrated energy transfer satisfies the following identities:

$$\hat{M}_{(s_x,s_y)(k_x,k_y)} = -\hat{M}_{(k_x,k_y)(s_x,s_y)} \tag{4.7}$$

$$\hat{M}_{(k_x,k_y)(k_x,k_y)} = 0 \tag{4.8}$$

Equation (4.7) states that the nonlinear energy transfer from mode (s_x, s_y) to mode (k_x, k_y) is equal and opposite to the nonlinear energy transfer from mode (k_x, k_y) to mode (s_x, s_y). Equation (4.8) states that each mode transfers zero energy nonlinearly to itself. Equation (4.7) and equation (4.8) arise from the continuity equation and the boundary conditions at the walls (the proof can be found in Appendix A.4). Appendix A.5 discusses the number of independent $\hat{M}$ for a chosen scenario.

Energy transfer $\hat{M}$ is typically presented in its premultiplied form $k_x k_y \hat{M}$ on a logarithmic axis, as is the case for $\hat{P}$, $\hat{D}$ and $\hat{N}$. However, the premultiplied energy transfer becomes zero if the investigated mode contains a zero wavenumber. Therefore, we plot the non-premultiplied energy transfer on a linear axis when discussing modes containing

a zero wavenumber.

4.3 Results

4.3.1 Energy transfer distributions

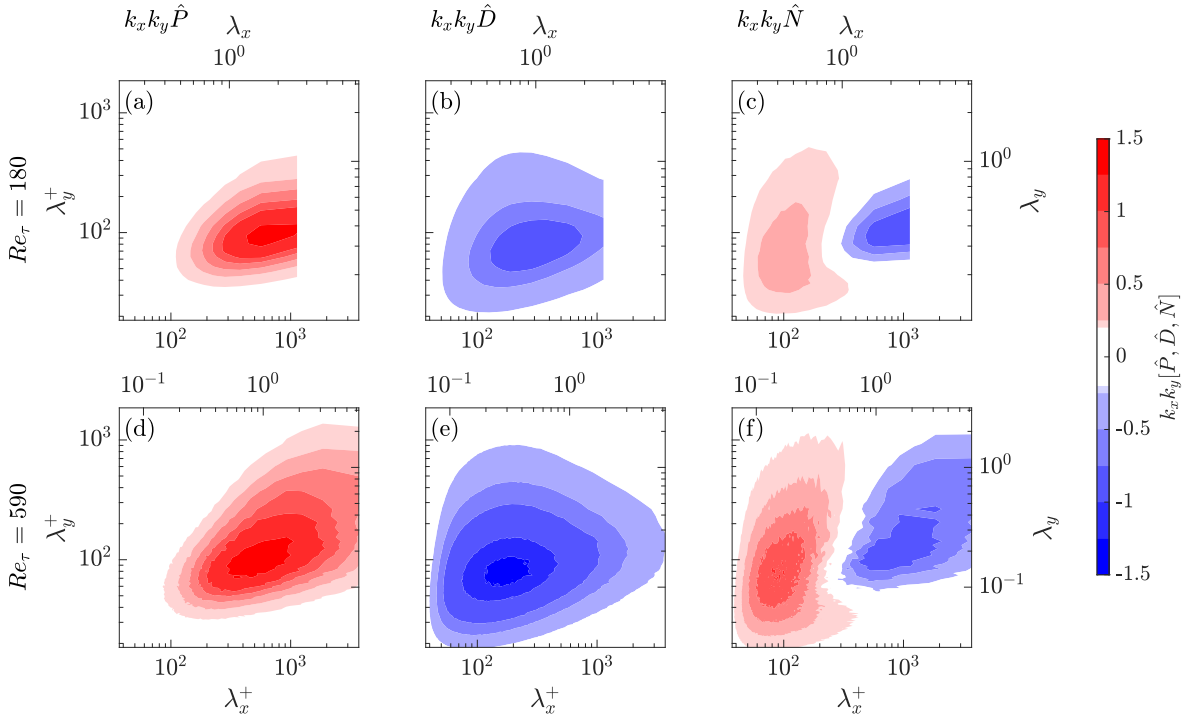

Figure 4.1: (a,d) Premultiplied production spectra $k_x k_y \hat{P}$; (b,e) premultiplied (negative) dissipation spectra $k_x k_y \hat{D}$; (c,f) premultiplied nonlinear energy transfer spectra $k_x k_y \hat{N}$. (a,b,c), $Re_\tau = 180$; (d,e,f), $Re_\tau = 590$.

This section revisits the wall-normal integrated energy transfer for a single mode, as stated in equation (4.3a) (Symon et al., 2021). Different from Symon et al. (2021), we use two full channel datasets, and visualise the premultiplied energy transfer spectra, as shown in figure 4.1. The relationship between wavenumber and wavelength is $\lambda = 2\pi/k$, where λ refers to wavelength and k refers to wavenumber. As for the production spectra $\hat{P}$ and dissipation spectra $\hat{D}$ (figures 4.1(a,b,d,e)), we see that the wall-normal integrated energy transfer spectra show relatively Re_τ-independent features at these two Reynolds numbers: their peaks are nearly aligned. The locations of the peaks are in line with the previous study that the production peak occurs at $\lambda_x^+ \approx 600$, $\lambda_y^+ \approx 100$ (at $z^+ \approx 15$) and the peak for dissipation caused by streamwise velocities occurs at $\lambda_x^+ \approx 200$, $\lambda_y^+ \approx 70$ (at $z^+ \approx 70$) (Lee & Moser, 2019). The Reynolds-Orr equation states that the energy source for turbulence is production and the energy sink is dissipation (Schmid &

Henningson, 2001). However, the energy source and sink are characterised by different structures, because the production and dissipation spectra are not identical as seen from figures 4.1(a,b,d,e). When viewed in terms of individual Fourier modes, equation (4.3a) states that the gap between production and dissipation is bridged by nonlinear energy transfer which is conservative as shown in equation (4.4). As for the nonlinear energy transfer spectra $\hat{N}$ (figures 4.1(c,f)), we see the same streamwise forward cascade in which energy is transferred from large streamwise scales to small streamwise scales at $Re_\tau = 180$ and 590.

Recall that $\hat{N}$ represents the net energy one mode receives from all other modes through nonlinear interactions. Observing figures 4.1(c,f), we see that there is a band of modes near $\lambda_x^+ \approx 300$ with near-zero net energy transfer $\hat{N}(k_x, k_y) \approx 0$. However, $\hat{N} = 0$ alone cannot distinguish these two possible cases: first, these modes do not participate in nonlinear interactions; second, these modes gain and lose approximately the same amount of energy resulting in a near-zero energy transfer. Similarly, for modes for which $\hat{N} \neq 0$, $\hat{N}$ only provides the net energy transfer for one mode without giving the detailed budget. We see the same streamwise forward cascade at $Re_\tau = 180$ and 590 (figures 4.1(c,f)) by examining $\hat{N}$. However, it is not the only piece of information we can obtain from the nonlinear interactions. In order to explore nonlinear interactions in more detail, we investigate the mode-to-mode nonlinear energy transfer using the variable $\hat{M}_{(s_x,s_y)(k_x,k_y)}$ defined in equation (4.6).

4.3.2 Energy transfer pathways

We first use two examples to interpret the introduced four-dimensional variable $\hat{M}_{(s_x,s_y)(k_x,k_y)}$ which represents energy transferred nonlinearly from mode (s_x, s_y) to mode (k_x, k_y), as shown in equation (4.6) and Appendix A.3. For each example, we first choose a streamwise wavenumber and a spanwise wavenumber for mode (k_x, k_y), which remains fixed. Then, we vary the streamwise and spanwise wavenumbers for mode (s_x, s_y). Both examples use the $Re_\tau = 180$ dataset. First, $\hat{M}$ is visualised with linear axes because modes containing zero wavenumbers cannot be shown on a premultiplied energy spectrum. Second, the premultiplied spectrum $s_x s_y \hat{M}$ is shown.

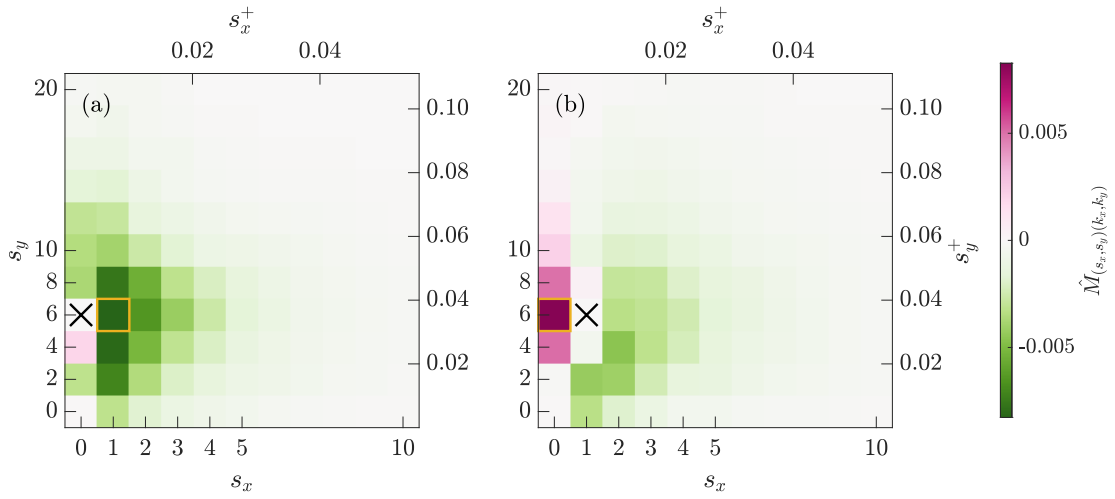

Figure 4.2: (a) $\hat{M}_{(s_x,s_y)(0,6)}$, the black cross marks the fixed mode $(0,6)$; (b) $\hat{M}_{(s_x,s_y)(1,6)}$, the black cross marks the fixed mode $(1,6)$. Modes marked in orange boxes are used to illustrate the property stated in equation (4.7). The data is calculated for the $Re_\tau = 180$ case.

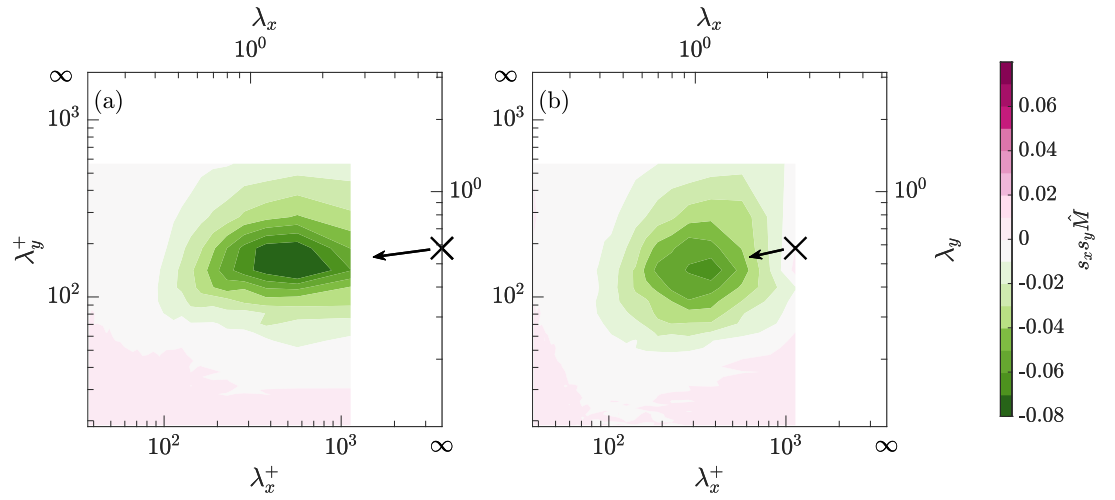

Figure 4.3: (a) The premultiplied spectrum $s_x s_y \hat{M}_{(s_x,s_y)(0,6)}$, the black cross marks the fixed mode $(0,6)$ corresponding to $(\lambda_x^+, \lambda_y^+) = (\infty, 188)$. (b) The premultiplied spectrum $s_x s_y \hat{M}_{(s_x,s_y)(1,6)}$, the black cross marks the fixed mode $(1,6)$ corresponding to $(\lambda_x^+, \lambda_y^+) = (1130, 188)$. The arrow in each figure marks the dominant energy transfer direction.

For the first example, we choose to fix mode $(0,6)$ corresponding to $(\lambda_x^+ = \infty, \lambda_y^+ = 188)$. This mode has significant production at $Re_\tau = 180$ which means that this mode gains significant energy from the mean flow. We would like to understand how this streamwise-constant mode redistributes energy to other modes. Figure 4.2(a) shows $\hat{M}_{(s_x,s_y)(0,6)}$ which quantifies the energy that mode $(0,6)$ marked by the black cross gains from modes in pink and loses to modes in green. We see that apart from gaining energy from the wider

mode $(0,4)$ (wider in the spanwise direction), it loses energy to all other modes, including the even wider mode $(0,2)$. The colour intensity tells us that local nonlinear energy transfer between mode $(0,6)$ and its neighbouring modes in Fourier space is strong (Domaradzki et al., 1994; Brasseur & Wei, 1994; Cho et al., 2018). In particular, mode $(0,6)$ loses the most energy to the next smallest streamwise scales with $s_x = 1$ outlined in orange, representing a forward energy cascade. This forward cascade can also be observed from the arrow in the premultiplied spectrum in figure 4.3(a).

For the second example, we choose to fix mode $(1,6)$ corresponding to $(\lambda_x^+ = 1130, \lambda_y^+ = 188)$. Figure 4.2(b) shows $\hat{M}_{(s_x,s_y)(1,6)}$. From the first example, we see that mode $(0,6)$ loses the most energy to this mode $(1,6)$. The two modes highlighted in orange boxes in figures 4.2(a,b) have the same magnitude but opposite signs, respecting equation (4.7). We see the similar forward energy cascade in which mode $(1,6)$ gains energy from the next largest streamwise scale with $s_x = 0$ and loses energy to the next smallest streamwise scale with $s_x = 2$ but larger spanwise scale with $s_y = 4$. In general, inspecting the spanwise wavenumbers, we observe that mode $(1,6)$ loses a significant amount of energy to scales with larger spanwise wavelengths $(s_y < 6)$. This corresponds to a spanwise inverse energy cascade in which energy is transferred from small spanwise scales to large spanwise scales (Cimarelli et al., 2013, 2016; Cho et al., 2018), though this inverse spanwise energy cascade is not obvious from the arrow in the premultiplied spectrum in figure 4.3(b).

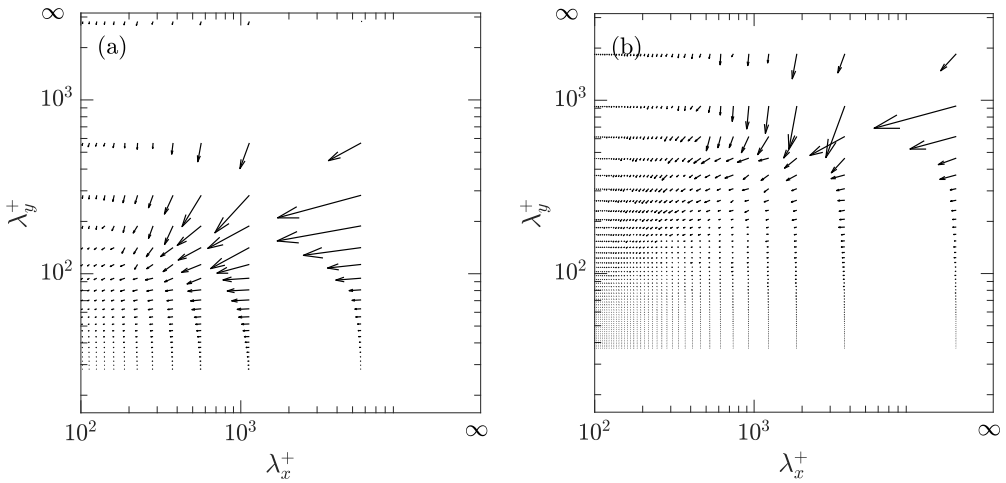

Figure 4.4: Dominant energy transfer pathways. (a) $Re_\tau = 180$; (b) $Re_\tau = 590$.

For each example, we obtain one dominant energy transfer pathway from the fixed mode (k_x,k_y) to the mode to which the fixed mode (k_x,k_y) loses the most energy (as shown by the arrows in figure 4.3). We can further change the fixed mode (k_x,k_y) to obtain more dominant energy transfer pathways in order to better visualise the nonlinear energy transfer in streamwise-spanwise wavenumber space, as shown in figure 4.4. For

both $Re_\tau = 180$ and 590, we see that there are large left-pointing arrows corresponding to the forward streamwise energy cascade and large bottom-pointing arrows corresponding to the forward spanwise energy cascade. It should be noted that each arrow in figure 4.4 only illustrates the dominant energy transfer pathway for each fixed (k_x, k_y) case without showing other less dominant energy transfer pathways. In addition, the energy transfer pathways describe only the statistical properties because the variable $\hat{M}$ is a time-averaged quantity (4.6).

The two examples (figure 4.2) illustrate the quantification of mode-to-mode nonlinear energy transfer in streamwise-spanwise wavenumber space. For mode $(0,6)$, we can further calculate how much energy mode $(0,6)$ gains in total due to nonlinear interactions by summing all the modes in pink in figure 4.2(a). Similarly, we can calculate how much energy mode $(0,6)$ loses in total due to nonlinear interactions by summing all the modes in green in figure 4.2(a). The next section aims to calculate the net energy transfer gain and loss due to nonlinear interactions for each mode in streamwise-spanwise wavenumber space.

4.3.3 Decomposition of net nonlinear energy transfer $\hat{N}$

With the introduced variable $\hat{M}$ (4.5), we can decompose $\hat{N}$ for a given mode (k_x, k_y) into positive and negative contributions:

$$\hat{N}^+(k_x,k_y) = \int_0^\infty \int_0^\infty \hat{M}_{(s_x,s_y)(k_x,k_y)} \{\hat{M} > 0\} \, \mathrm{d}s_x \mathrm{d}s_y \tag{4.9a}$$

$$\hat{N}^-(k_x,k_y) = \int_0^\infty \int_0^\infty \hat{M}_{(s_x,s_y)(k_x,k_y)} \{\hat{M} < 0\} \, \mathrm{d}s_x \mathrm{d}s_y \tag{4.9b}$$

where $\{\ \}$ is an indicator. An indicator is equal to 1 when the argument is true and 0 when the argument is false. The positive energy transfer $\hat{N}^+$ quantifies the total energy mode (k_x, k_y) gains from other modes. The negative energy transfer $\hat{N}^-$ quantifies the total energy mode (k_x, k_y) loses to other modes. According to equation (4.5), these two variables are linked to the net energy transfer $\hat{N}$ by

$$\hat{N}(k_x,k_y) = \hat{N}^+(k_x,k_y) + \hat{N}^-(k_x,k_y) \tag{4.10}$$

Although seeming straightforward, this decomposition cannot be attained without formulating the mode-to-mode nonlinear energy transfer $\hat{M}_{(s_x,s_y)(k_x,k_y)}$.

Figures 4.5(a)(b) quantify the energy transfer gain and loss for each mode at $Re_\tau = 180$. We see the dual characteristic of nonlinear energy transfer that each mode acts as an energy source and energy recipient. The difference between the energy transfer gain and loss for each mode results in the net nonlinear energy transfer spectrum $\hat{N}$, as shown

in figure 4.5(c) and respecting equation (4.10). Figure 4.5(c) is the same as figure 4.1(c). Here, we address one consideration raised at the end of §4.3.1. We see that the mode marked by the black cross where $\hat{N} \approx 0$ in figure 4.5(c) has non-negligible net energy loss and net energy gain as observed in the corresponding locations in figures 4.5(a)(b). This indicates that this mode gains and loses approximately equal amount of energy, resulting in near-zero net nonlinear energy transfer. It would be incorrect to infer that this mode does not participate in nonlinear interactions purely judging from the net nonlinear energy transfer spectrum $\hat{N}$.

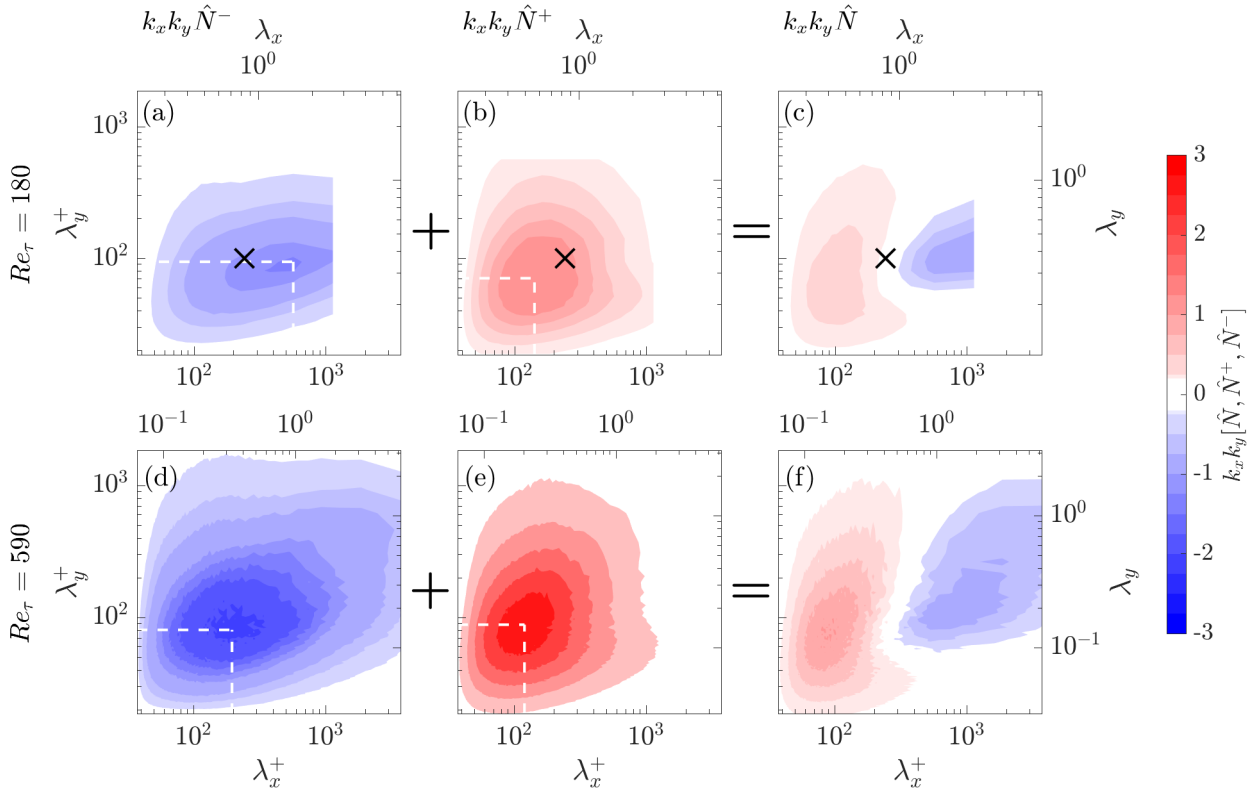

Figure 4.5: Decomposition of net nonlinear energy transfer: $\hat{N}^- + \hat{N}^+ = \hat{N}$. (a,d) Premultiplied negative nonlinear energy transfer spectra $k_x k_y \hat{N}^-$, dashed lines mark the peak; (b,e) Premultiplied positive nonlinear energy transfer spectra $k_x k_y \hat{N}^+$, dashed lines mark the peak; (c,f) Premultiplied net nonlinear energy transfer spectra $k_x k_y \hat{N}$. (a,b,c), $Re_\tau = 180$; (d,e,f), $Re_\tau = 590$. The black crosses in (a,b,c) mark a mode with $\hat{N} \approx 0$ for explanation purposes.

Now we answer the other question raised at the end of §4.3.1. As mentioned previously, the net energy transfer spectra $\hat{N}$ reveal the same streamwise forward cascade at $Re_\tau = 180$ and 590 (figures 4.5(c,f)). At $Re_\tau = 180$, we see that the negative energy transfer spectrum $\hat{N}^-$ peak is at $\lambda_x^+ \approx 600$, $\lambda_y^+ \approx 100$ and the positive energy transfer spectrum $\hat{N}^+$ peak is at $\lambda_x^+ \approx 150$, $\lambda_y^+ \approx 70$ indicated by the white dashed lines in figures 4.5(a,b). This indicates that large streamwise scales lose the most energy and small

streamwise scales gain the most energy. Thus, figures 4.5(a,b) illustrate the streamwise forward cascade, which aligns with the net energy transfer spectrum (figure 4.5(c)).

At $Re_\tau = 590$, we see that the negative energy transfer spectrum $\hat{N}^-$ peak is at $\lambda_x^+ \approx 200$, $\lambda_y^+ \approx 90$ and the positive energy transfer spectrum $\hat{N}^+$ peak is at $\lambda_x^+ \approx 150$, $\lambda_y^+ \approx 80$ indicated by the white dashed lines in figures 4.5(d,e). From $Re_\tau = 180$ to 590, there is a significant negative energy transfer spectrum peak shift to a much smaller λ_x^+. Figures 4.5(d,e) reveal that modes losing the most energy and modes gaining the most energy are of similar sizes, as the two peaks are near to each other. This is a new piece of information obtained from $\hat{N}^+$ and $\hat{N}^-$ as this wavenumber area responsible for the significant energy gain and loss cannot be seen from the net energy transfer spectrum (figure 4.5(f)). Note that the above discussions are for the whole channel since $\hat{M}$ is wall-normal integrated nonlinear energy transfer which hides the nonlinear energy transfer in the wall-normal direction.

4.3.4 Nonlinear energy transfer of three structures

Linear analysis explains the energy amplification mechanisms of different structures (Schmid & Henningson, 2001; Jovanović & Bamieh, 2005), leaving the nonlinear part relatively unexplored. Since nonlinear energy transfer is conservative, the nonlinear energy transfer among different structures should be interpreted as energy redistribution. In this section, we use $\hat{M}$ to investigate the energy redistribution of three different structures: streamwise streaks, oblique waves and Tollmien–Schlichting (TS) waves. Since streamwise streaks and TS waves are characterised by zero wavenumbers which cannot be shown on pre-multiplied energy transfer spectra using logarithmic axes, we first present the nonlinear energy transfer using $\hat{M}$ on linear axes. It should be noted that the original definition of TS waves refers to the velocity fluctuations based on the laminar profile. Here, the velocity fluctuations are based on the turbulent mean profile.

Following Jovanović & Bamieh (2005), streamwise streaks are characterised by $k_x \approx 0, k_y \approx O(1)$. Therefore, we define streamwise streaks as modes with $k_x = 0$ ($\lambda_x^+ = \infty$). We define the nonlinear energy transfer of streamwise streaks as:

$$\hat{M}_{(s_x,s_y)\to streaks},\ k_{x(streaks)} = 0\ (\lambda^+_{x(streaks)} = \infty) \tag{4.11}$$

Oblique waves are characterised by $k_x \approx O(1), k_y \approx O(1)$. Considering the geometry of the channel box used in this study, we define oblique waves as modes satisfying $k_y = 2k_x$ ($\lambda_x^+ = 2\lambda_y^+$). We define the nonlinear energy transfer of oblique waves as:

$$\hat{M}_{(s_x,s_y)\to obwaves},\ k_{y(obwaves)} = 2k_{x(obwaves)}\ (\lambda^+_{x(obwaves)} = 2\lambda^+_{y(obwaves)}) \tag{4.12}$$

TS waves are characterised by $k_x \approx O(1), k_y \approx 0$. Therefore, we define TS waves as modes with $k_y = 0$ ($\lambda_y^+ = \infty$). We define the nonlinear energy transfer of TS waves as:

$$\hat{M}_{(s_x,s_y)\to TSwaves},\ k_{y(TSwaves)} = 0\ (\lambda^+_{y(TSwaves)} = \infty) \tag{4.13}$$

Note that the purpose of this section is to discuss the above three distinct structures rather than discuss all modes in streamwise-spanwise wavenumber space.

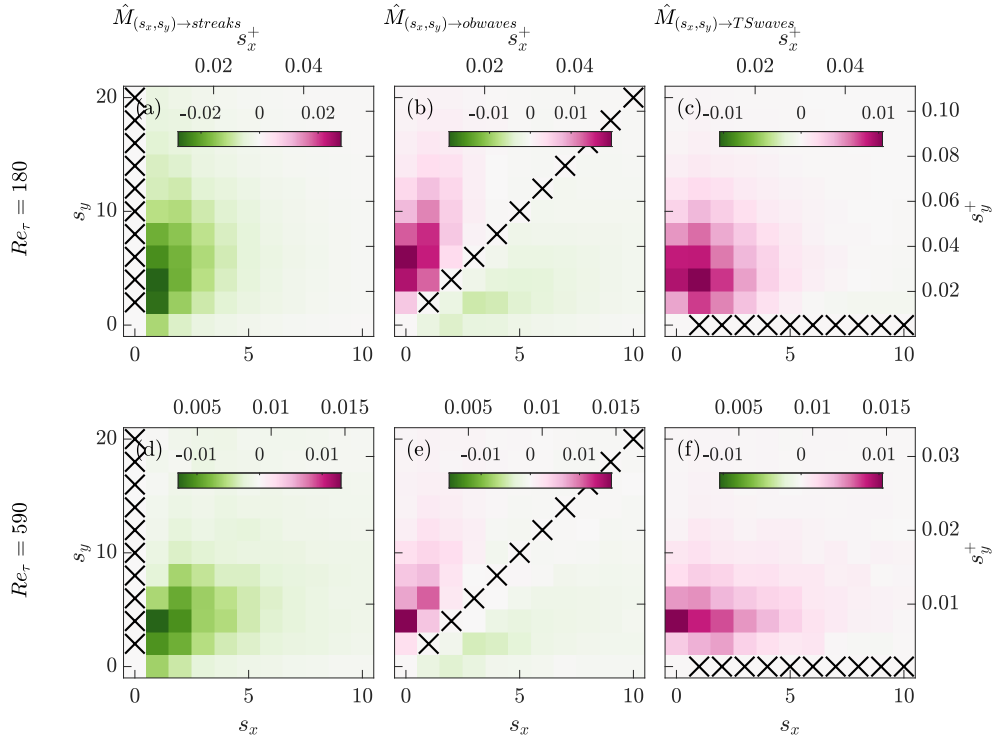

Figure 4.6: (a,d) $\hat{M}_{(s_x,s_y)\to streaks}$; (b,e) $\hat{M}_{(s_x,s_y)\to obwaves}$; (c,f) $\hat{M}_{(s_x,s_y)\to TSwaves}$ visualised using discrete modes. (a,b,c), $Re_\tau = 180$; (d,e,f), $Re_\tau = 590$. Black crosses mark the modes of the investigated structures.

Figure 4.6 shows the nonlinear energy transfer of the three different structures at $Re_\tau = 180$ and 590. As for the interpretation of each subplot, the specific structure (indicated by the black crosses) gains energy from modes in pink and loses energy to modes in green. We see that streamwise streaks (figures 4.6(a,d)) lose energy to smaller streamwise scales ($s_x > 0$), exhibiting a streamwise forward cascade. This could be linked to streak breakdown which is one phase of the self-sustaining process (SSP). Due to the instability of long streamwise streaks, they break down into smaller streamwise streaks (Hamilton et al., 1995). For oblique waves (figures 4.6(b,e)), we see that they generally gain energy from scales with larger aspect ratios s_y/s_x (which is equivalent to k_y/k_x) (Symon et al., 2021) and lose energy to scales with smaller aspect ratios, exhibiting a transverse cascade

(Lee & Moser, 2019; Symon et al., 2021). For TS waves (figures 4.6(c,f)), we see that they mainly gain energy from smaller spanwise scales, exhibiting a spanwise inverse cascade (Cimarelli et al., 2013, 2016; Cho et al., 2018). If we think of streamwise streaks with infinite aspect ratio $s_y/s_x \to \infty$ and TS waves with zero aspect ratio $s_y/s_x \to 0$, then we could conclude that there exists energy transfer from scales with large aspect ratio to scales with small aspect ratio. In terms of the shapes of scales, this transverse cascade refers to energy transfer from streamwise-elongated scales to spanwise-elongated scales. It is also worth noting that the transverse cascade of the three structures is not substantially influenced by the Reynolds number for this range.

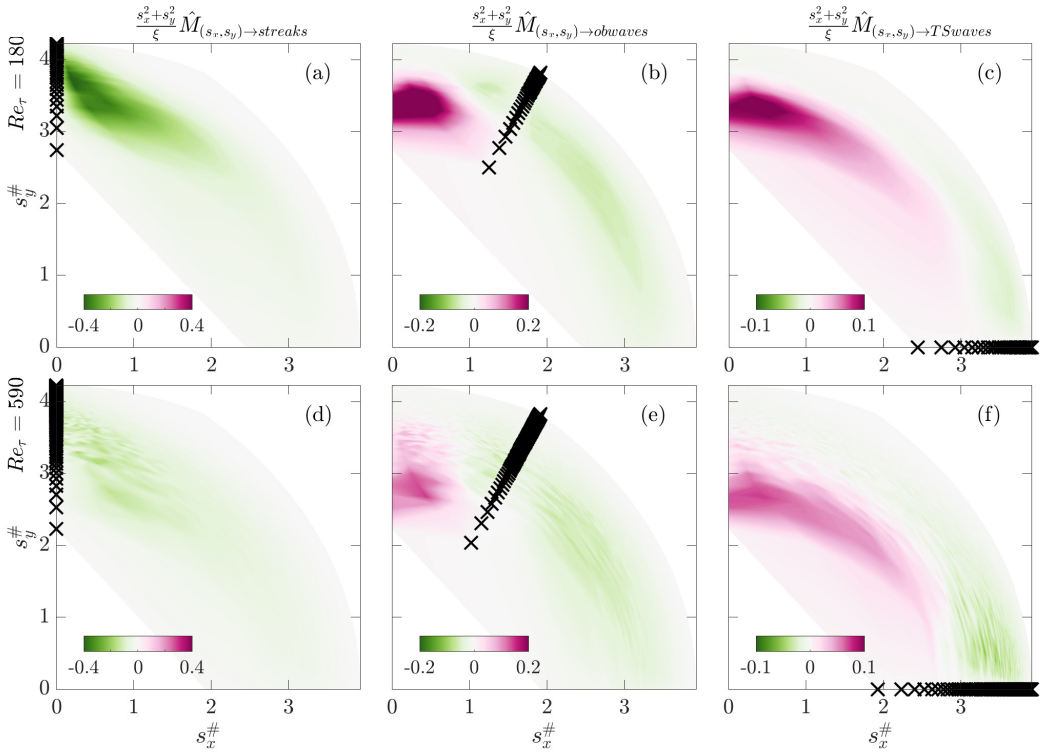

Figure 4.7: Log-polar premultipled energy spectra (a,d) $\frac{s_x^2+s_y^2}{\xi}\hat{M}_{(s_x,s_y)\to streaks}$; (b,e) $\frac{s_x^2+s_y^2}{\xi}\hat{M}_{(s_x,s_y)\to obwaves}$; (c,f) $\frac{s_x^2+s_y^2}{\xi}\hat{M}_{(s_x,s_y)\to TSwaves}$. (a,b,c), $Re_\tau = 180$; (d,e,f), $Re_\tau = 590$. Black crosses mark the modes of the investigated structures.

The above discussion tells us that the transverse energy cascade is related to s_y/s_x (which is equivalent to k_y/k_x). We can also visualise the nonlinear energy transfer spectrum on a log-polar coordinate in which s_y/s_x corresponds to a certain slope (Lee & Moser, 2019), as shown in figure 4.7. Following Lee & Moser (2019), $s_x^\# = \xi s_x/\sqrt{s_x^2+s_y^2}$, $s_y^\# = \xi s_y/\sqrt{s_x^2+s_y^2}$ and $\xi = \log(\sqrt{s_x^2+s_y^2}/k_{ref})$ with $k_{ref} = 50000$. From figure 4.7(a,d), the streamwise streaks located on the $a^\# = 0$ axis lose energy to other modes, corresponding to the finding that modes located on the $s_x^\# = 0$ axis have significant net negative

nonlinear energy transfer (Lee & Moser, 2019). From figures 4.7(b,e), the oblique waves located on the $s_y^\# = 2s_x^\#$ gain energy from modes satisfying $s_y^\# > 2s_x^\#$ and lose energy to modes satisfying $s_y^\# < 2s_x^\#$, corresponding to the transverse cascade mentioned previously. From figures 4.7(c,f), the TS waves located on the $s_y^\# = 0$ axis mainly gain energy but also lose a small amount of energy. We see that one advantage of using log-polar premultiplied spectra over the traditional premultiplied spectra is that we can visualise modes which contain one zero wavenumber (either $s_x = 0$ or $s_y = 0$).

Note that the above discussion only concerns the nonlinear energy transfer as one component in the energy transfer balance (4.3a). One should not interpret that energy merely originates from streamwise streaks, goes through oblique waves and finally dissipates at TS waves. Equation (4.3a) gives the energy transfer budget for each mode. To evaluate the overall energy transfer balance comprehensively, we need to consider the production and dissipation as well. Motivated by §4.3.3, we decompose the net nonlinear energy transfer of each structure into its positive and negative parts. According to equations (4.3a) and (4.10), for each structure, the energy transfer budget is

$$\hat{P} + \hat{D} + \hat{N}^+ + \hat{N}^- = 0 \tag{4.14}$$

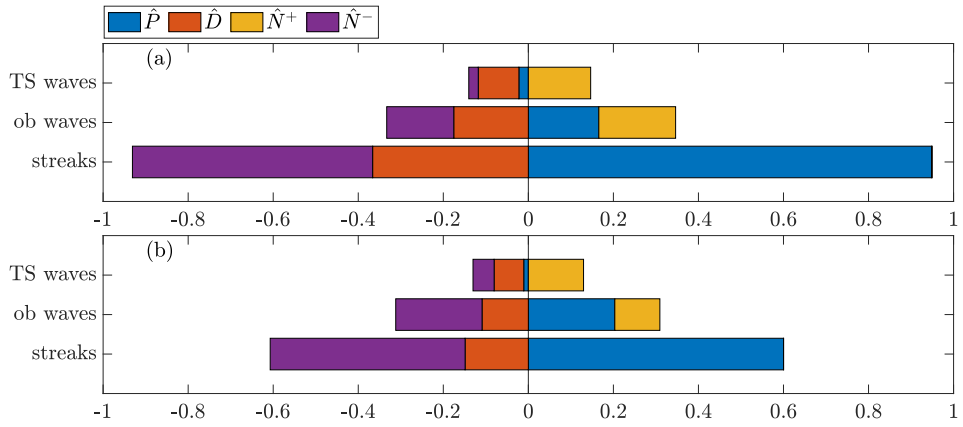

Figure 4.8: Energy budgets for the streamwise streaks, oblique waves and TS waves. (a) $Re_\tau = 180$; (b) $Re_\tau = 590$.

The energy budgets (4.3a) for the three structures are shown in figure 4.8. For the streamwise streaks, they receive a large amount of energy from the mean flow through production as seen from the blue bars and they lose a large amount of energy nonlinearly to other modes as seen from the purple bars. For the oblique waves, apart from gaining energy from the mean flow and dissipating energy, they gain and lose energy nonlinearly through interacting with other modes as seen from the purple and yellow bars. For the TS waves, the only energy gain is through nonlinear energy transfer as seen from the yellow

bars. The negative production in the TS waves reported in figure 4.8 is consistent with the negative production observed by Lee & Moser (2019). TS waves are characterised by zero spanwise wavenumbers, and as seen in figure 6 of Lee & Moser (2019), the region with zero spanwise wavenumber shows negative production values, particularly near the wall ($z^+ = 15$ and 30). Streamwise streaks and oblique waves gain energy from the mean flow (positive production), while TS waves lose energy to the mean flow (negative production). Dissipation occurs for all three structures as seen from the red bars. Although the values are different at the two Reynolds numbers, different types of energy transfer show similar trends in the three structures.

4.3.5 Forward cascade and inverse cascade

In this section, we use $\hat{M}$ to quantify the forward and inverse cascades between the large scales and small scales in the spirit of large-eddy simulation (LES). For channel flows, resolved scales could be set by modes belonging to a rectangular region determined by the conditions of $k_x \leq k_{xC}$ and $k_y \leq k_{yC}$, where k_{xC} and k_{yC} are cutoff wavenumbers. These cutoff wavenumbers are determined by the choice of a single variable n_C (Germano et al., 1991; Härtel et al., 1994; Domaradzki et al., 1994):

$$k_{xC} = \frac{2\pi n_C}{L_x}, \quad k_{yC} = \frac{2\pi n_C}{L_y} \tag{4.15a,b}$$

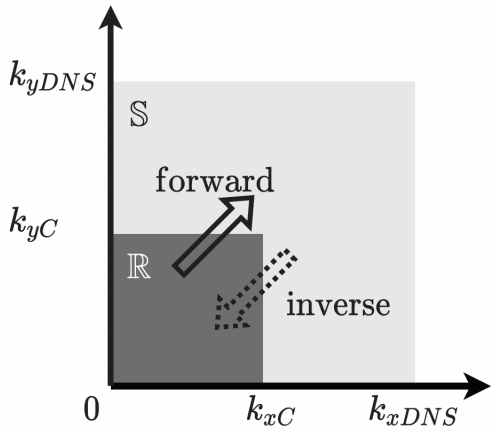

Figure 4.9: A sketch illustrating the forward cascade and inverse cascade between the resolved-scale region $\mathbb{R}$ marked in dark grey and the subgrid-scale region $\mathbb{S}$ marked in light grey. Region $\mathbb{R}$ contains the resolved scales and region $\mathbb{S}$ contains the subgrid scales. k_{xC} and k_{yC} are the cutoff wavenumbers. k_{xDNS} and k_{yDNS} are the maximum wavenumbers resolved by DNS.

One issue of subgrid scale energy transfer modelling with eddy viscosity is that it assumes the subgrid scales only dissipate energy and neglects the energy transferred from the subgrid scales to the resolved scales, also known as 'backscatter' (Piomelli et al., 1991). It is worth to note that both inverse energy cascade and backscatter are used to describe energy transfer from small scales to large scales. Backscatter is specific to LES and is used when energy transfer is discussed in Fourier space after selecting cutoff wavenumbers that separate resolved scales (large scales) from subgrid scales (small scales). Figure 4.9 illustrates the two-way energy transfer between the resolved scales and subgrid scales. We aim to quantify the forward cascade and inverse cascade using mode-to-mode nonlinear energy transfer $\hat{M}$.

Recall that $\hat{M}_{(s_x,s_y)(k_x,k_y)}$ represents energy transfer from mode (s_x,s_y) to mode (k_x,k_y). For the forward cascade, energy is transferred from the resolved scales in region $\mathbb{R}$ to the subgrid scales in region $\mathbb{S}$, as indicated by the solid arrow in figure 4.9. Similar to equations (4.9a) and (4.9b), for this forward cascade, we can calculate the energy lost by each mode (4.16b) in the resolved-scale region $\mathbb{R}$ and the energy gained by each mode (4.16a) in the subgrid-scale region $\mathbb{S}$:

$$\hat{N}_F^+(k_x,k_y,n_C) = \iint \hat{M}_{(s_x,s_y)(k_x,k_y)}\{\hat{M}>0,(s_x,s_y)\in\mathbb{R},(k_x,k_y)\in\mathbb{S}\}\,\mathrm{d}s_x\mathrm{d}s_y \tag{4.16a}$$

$$\hat{N}_F^-(k_x,k_y,n_C) = \iint \hat{M}_{(s_x,s_y)(k_x,k_y)}\{\hat{M}<0,(s_x,s_y)\in\mathbb{S},(k_x,k_y)\in\mathbb{R}\}\,\mathrm{d}s_x\mathrm{d}s_y \tag{4.16b}$$

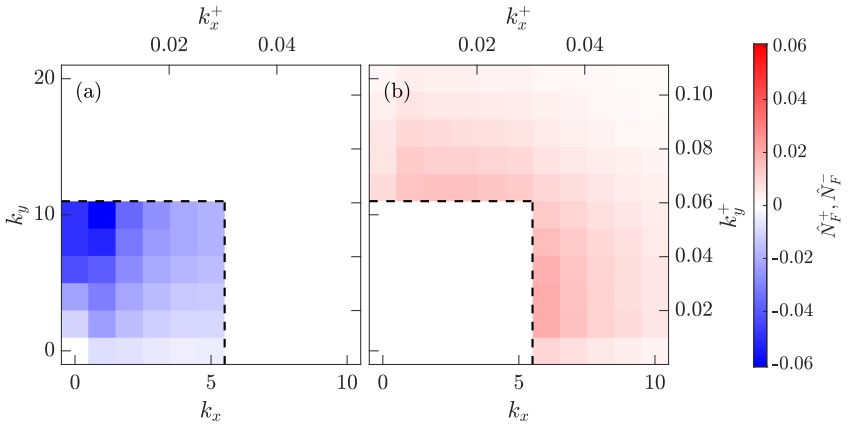

Figure 4.10: An example of the forward cascade, where $n_C = 5$ corresponding to $(\lambda_x^+ = 226, \lambda_y^+ = 113)$ at $Re_\tau = 180$. (a) $\hat{N}_F^-(k_x,k_y,5)$ shows the energy lost by resolved scales in region $\mathbb{R}$; (b) $\hat{N}_F^+(k_x,k_y,5)$ shows the energy gained by subgrid scales in region $\mathbb{S}$. Dashed lines mark the boundary between the resolved-scale region $\mathbb{R}$ and the subgrid-scale region $\mathbb{S}$. Note that the maximum wavenumbers in this figure are not the maximum wavenumbers resolved in the DNS.

Figure 4.10 shows an example of the forward cascade from the resolved scales to the subgrid scales at $Re_\tau = 180$. The choice of cutoff wavenumber $n_C = 5$ corresponds to the filtering width Δ_i satisfying $\Delta_i \approx 5\Delta x_i$ $(i = 1, 2)$ at $Re_\tau = 180$. Figure 4.10(a) shows that streamwise elongated modes with large k_y/k_x in region $\mathbb{R}$ lose the most energy. Figure 4.10(b) shows that modes gaining energy in region $\mathbb{S}$ do not show significant preference with respect to k_y/k_x.

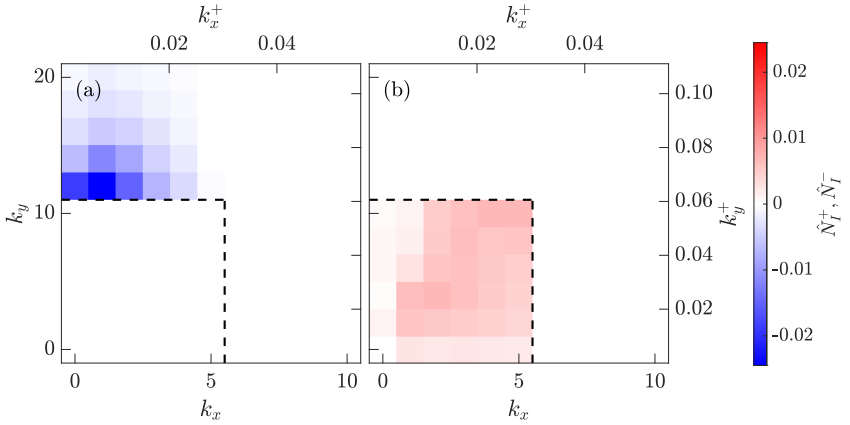

Figure 4.11: Inverse cascade example: $n_C = 5(\lambda_x^+ = 226, \lambda_y^+ = 113)$ at $Re_\tau = 180$. (a) $\hat{N}_I^-(k_x, k_y, 5)$ shows how subgrid scales in region $\mathbb{S}$ lose energy; (b) $\hat{N}_I^+(k_x, k_y, 5)$ shows how resolved scales in region $\mathbb{R}$ gain energy.

Figure 4.11 shows an example of the inverse cascade from the subgrid scales to the resolved scales at $Re_\tau = 180$. Figure 4.11(a) shows the asymmetry of modes losing energy in region $\mathbb{S}$: only streamwise elongated modes with large k_y/k_x lose energy. Figure 4.11(b) shows that modes gaining energy in region $\mathbb{R}$ do not show significant preference with respect to k_y/k_x.

We further quantify the forward cascade and inverse cascade between the resolved scales and subgrid scales determined by n_C:

$$N_F(n_C) = \iint_{\mathbb{S}} \hat{N}_F^+ \, \mathrm{d}k_x \mathrm{d}k_y \overset{(4.7)}{=} -\iint_{\mathbb{R}} \hat{N}_F^- \, \mathrm{d}k_x \mathrm{d}k_y \tag{4.17}$$

$$N_I(n_C) = \iint_{\mathbb{R}} \hat{N}_I^+ \, \mathrm{d}k_x \mathrm{d}k_y \overset{(4.7)}{=} -\iint_{\mathbb{S}} \hat{N}_I^- \, \mathrm{d}k_x \mathrm{d}k_y \tag{4.18}$$

The forward cascade and inverse cascade calculated using equations (4.17) and (4.18) for $Re_\tau = 180$ and 590 are shown in figures 4.12. A general criterion for LES is to resolve a sufficient amount of large scales which should contain 80% of the total kinetic energy (Pope, 2000). By checking the DNS datasets, we know that scales with $\lambda_x^+ = 2\lambda_y^+ > 162$ need to be resolved at $Re_\tau = 180$ and scales with $\lambda_x^+ = 2\lambda_y^+ > 232$ need to be resolved at $Re_\tau = 590$. Therefore, we need to consider the energy transfer when the

cut-off wavelengths satisfying $\lambda_{xC}^{+} = 2\lambda_{yC}^{+} < 162$ at $Re_\tau = 180$ and $\lambda_{xC}^{+} = 2\lambda_{yC}^{+} < 232$ at $Re_\tau = 590$. We see that the forward cascade is at least four times larger than the inverse cascade when $\lambda_{xC}^{+} < 250$, indicating that the net energy transfer is from the resolved scales to the subgrid scales and shown by the solid lines. This justifies why eddy viscosity considering only the forward cascade is used in LES (Pope, 2000). However, the inverse cascade is not negligible when $\lambda_{xC}^{+} > 100$, so the negligence of it has been proposed as a source of inaccuracy in LES (Anderson & Domaradzki, 2012; Cimarelli & De Angelis, 2014).

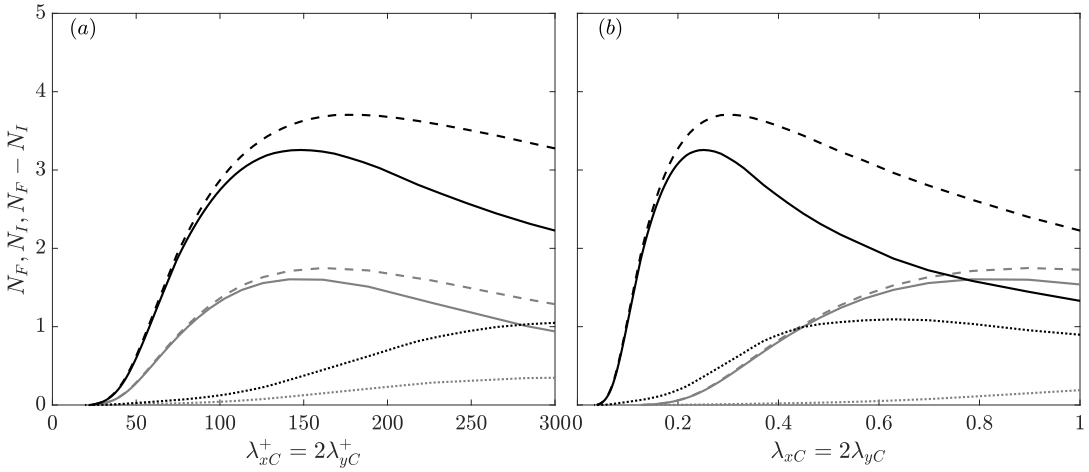

Figure 4.12: (a) Quantification of the energy transfer between the resolved scales and subgrid scales in inner units; (b) in outer units. Dashed lines, forward cascade N_F; dotted lines, inverse cascade N_I; solid lines, net energy cascade $N_F - N_I$. Grey colour, $Re_\tau = 180$; black colour, $Re_\tau = 590$.

When interpreting figure 4.12, two things should be noted. First, the results would be different if the aspect ratio between the streamwise and spanwise cutoff wavenumbers $k_{xC}/k_{yC} = \frac{1}{2}$ were changed. With the introduction of $\hat{M}$, experimenting with different aspect ratios of k_{xC}/k_{yC} could help identify an optimal value that minimises backscatter from subgrid scales to resolved scales. Second, the above results only represent the wall-normal integrated forward and inverse cascades. Due to the inhomogeneity in the wall-normal direction of wall-bounded flows, the forward cascade and inverse cascade would vary with wall-normal height.

Now, we compare the energy cascade calculated using $\hat{M}$ with the eddy viscosity method. The forward cascade from the resolved scales to the subgrid scales N_ν can be calculated using the linear eddy viscosity model (Pope, 2000):

$$N_\nu = \nu \tilde{S}^2 \tag{4.19}$$

where ν is the eddy viscosity. $\tilde{S}$ is the characteristic filtered rate of strain: $\tilde{S} = (2\tilde{S}_{ij}\tilde{S}_{ij})^{\frac{1}{2}}$. $\tilde{S}_{ij}$ is the filtered rate-of-strain tensor: $\tilde{S}_{ij} = \frac{1}{2}(\frac{\partial \tilde{u}_i}{\partial x_j} + \frac{\partial \tilde{u}_j}{\partial x_i})$. $\tilde{u}_i$ is the filtered velocity of the resolved scales.

We can use the Smagorinsky eddy viscosity (Smagorinsky, 1963):

$$\nu = (C_s D_z \Delta)^2 \tilde{S} \tag{4.20}$$

C_s is the Smagorinsky coefficient and is set to be $C_s = 0.067$ (Moin & Kim, 1982). D_z is the damping function which accounts for low-Reynolds-number subgrid scale stress (SGS) near the wall and is set to be $D_z = 1 - \exp(-z^+/25)$ (Moin & Kim, 1982). Since we do not apply filtering in the wall-normal direction, the characteristic length scale of the largest subgrid scale eddies Δ is set to be $\Delta = (\Delta_1 \Delta_2)^{\frac{1}{2}}$. After we have obtained the filtered velocity fields $\tilde{u}_i$ using the cutoff wavenumbers (4.15) in Fourier space, we calculate the forward cascade N_ν (4.19) and the Smagorinsky eddy viscosity ν (4.20) directly in physical space.

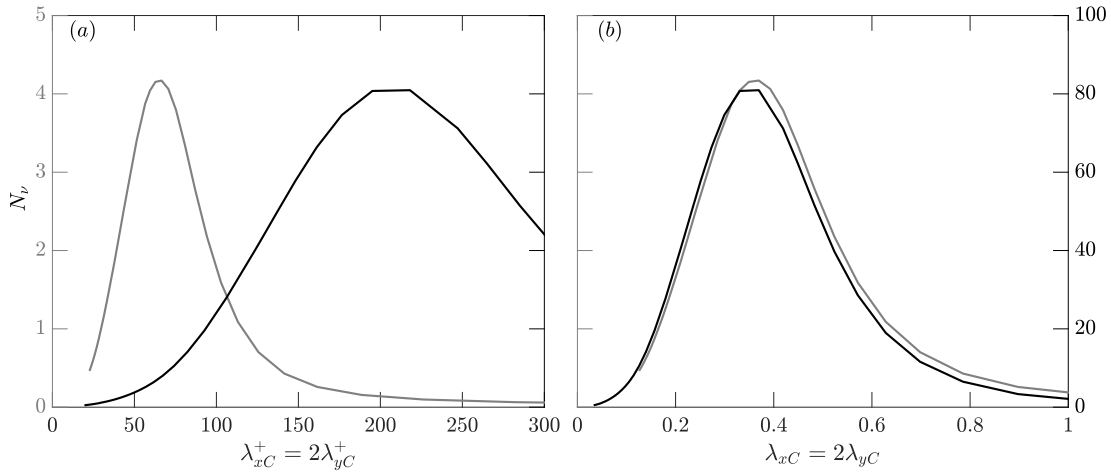

Figure 4.13: (a) Forward cascade N_ν predicted by the eddy viscosity (4.20) in inner units; (b) in outer units. $Re_\tau = 180$: grey colour, left axis; $Re_\tau = 590$: black colour, right axis.

Figure 4.13 shows the forward cascades from the resolved scales to subgrid scales predicted by the eddy viscosity (4.20) at $Re_\tau = 180$ and 590. We see that the forward cascade at $Re_\tau = 590$ is approximately 20 times higher than the forward cascade at $Re_\tau = 180$. The forward cascade predicted by the eddy viscosity (4.20) first increases as the cutoff wavelengths (λ_{xC} and λ_{yC}) decrease and then decreases to zero as the cutoff wavelengths approach the DNS grid sizes, aligning with the trends in figure 4.12. However, the values of the forward cascade predicted by the eddy viscosity (4.20) do not match that calculated using $\hat{M}$ (the solid lines in figure 4.12). Since $\hat{M}$ represents the wall-normal integrated

energy transfer and is a time-averaged variable, statistics of energy transfer has been averaged out in the wall-normal direction and the time domain. That is the main reason why $N_F - N_I$ in figure 4.12 is substantially smaller than N_ν in figure 4.13. Nevertheless, $\hat{M}$ could be extended to include the wall-normal coordinate and $N_F - N_I$ can be calculated at each wall-normal height before being time and wall-normal averaged.

4.4 Conclusions

Nonlinear energy transfer in turbulent channel flow has been investigated in Fourier space at $Re_\tau = 180$ and 590. We introduce a four-dimensional variable $\hat{M}_{(s_x,s_y)(k_x,k_y)}$ which describes the nonlinear energy transfer between any two modes in streamwise-spanwise wavenumber space, by analysing the individual triadic interactions of the nonlinear energy transfer term in the spectral turbulent kinetic energy (sTKE) equation.

We use this variable to explore three things. First, we decompose the net nonlinear energy transfer $\hat{N}$ into its positive and negative contributions: $\hat{N}^+$ and $\hat{N}^-$. This allows us to separately quantify the total energy gained and total energy lost by each mode. Second, we investigate the nonlinear energy transfer of streamwise streaks, oblique waves and TS waves. We observe that there exists energy transfer from streamwise-elongated structures to spanwise-elongated structures and that this transverse cascade is characterised by the aspect ratio k_y/k_x. Third, we quantify the forward cascade and inverse cascade between the resolved scales and subgrid scales in the spirit of LES. For both Reynolds numbers considered, the forward cascade is significantly larger than the inverse cascade when $\lambda_{xC}^+ < 250$, justifying why eddy viscosity only considers the forward cascade is used in LES. However, the inverse cascade is not negligible when $\lambda_{xC}^+ > 100$. We also compare the energy cascade calculated using $\hat{M}$ with the Smagorinsky eddy viscosity.

The pathways illustrated by $\hat{M}$ represent a nonlinear energy transfer network in two-dimensional Fourier space (Gürcan et al., 2020). A promising area for future work would be to extend mode-to-mode nonlinear energy transfer $\hat{M}_{(s_x,s_y)(k_x,k_y)}$ to include another dimension which is wall-normal coordinate to investigate the details of mode-to-mode nonlinear energy transfer at any wall-normal height.

Chapter 5

Coherent structures related to turbulent convection in channel flows

We study the coherent structures related to the turbulent convection term in the turbulent kinetic energy equation using conditional averaging in channel flows at friction Reynolds numbers $Re_\tau = 180$ and 590. Two types of conditional events are investigated: one is characterised by significant energy gain due to turbulent convection and the other is characterised by significant energy loss due to turbulent convection. Both types of events are associated with patterns composed of positive and negative turbulent convection areas aligned in the streamwise direction. The main difference between the two types of events is that positive and negative turbulent convection occur at different locations around quasi-streamwise vortices and hairpin vortices.

5.1 Introduction

Coherent structures exist in chaotic turbulence systems (Cantwell, 1981; Robinson, 1991; Jiménez, 2018). Developments in experimental techniques have enabled observations of coherent structures in wall-bounded flows, such as streamwise streaks (Kline et al., 1967) and hairpin vortices (Head & Bandyopadhyay, 1981; Zhou et al., 1999; Dennis & Nickels, 2011). Dynamic processes such as bursts have also been observed (Blackwelder & Kaplan, 1976). At the same time, advances in computational power have validated the observations of the coherent structures seen in experiments and provide more detailed

statistics and three-dimensional visualisations (Moin & Kim, 1985; Kim & Moin, 1986; Zhou et al., 1999; Adrian et al., 2000; Wu & Moin, 2009).

Coherent structures also play an important role in turbulent energy transfer. For wall-bounded flows, bursts composed of series of ejections and sweeps contribute significantly to turbulent production, though their time scales are relatively short (Wallace et al., 1972; Lu & Willmarth, 1973); the formation and breakdown of streamwise streaks are important to the self-sustaining process (SSP) in the near-wall region (Hamilton et al., 1995; Waleffe, 1997). Accordingly, manipulating coherent structures can change the dynamics of wall turbulence in order to suppress turbulence (Bae et al., 2021; Oehler & Illingworth, 2021) or reduce drag (Lim, 2003; Stone et al., 2004).

The well-known quadrant analysis (Wallace et al., 1972; Wallace, 2016) investigates the conditional events of the product of the streamwise fluctuation velocity u and wall-normal fluctuation velocity w, which is directly related to turbulent production, as shown in the turbulent kinetic energy (TKE) equation (Pope, 2000):

$$\frac{\mathrm{D}}{\mathrm{D}t}\left(\frac{1}{2}u_i u_i\right) = \overbrace{-uw\frac{\mathrm{d}U}{\mathrm{d}z}}^{\text{production}} \underbrace{-\frac{1}{Re_\tau}\frac{\partial u_i}{\partial x_j}\frac{\partial u_i}{\partial x_j}}_{\text{dissipation}} \overbrace{-u_j\frac{\partial\left(\frac{1}{2}u_i u_i\right)}{\partial x_j}}^{\text{turbulent convection}} \underbrace{-u_i\frac{\partial p}{\partial x_i}}_{\text{pressure diffusion}} \overbrace{+\frac{1}{Re_\tau}\frac{\partial^2\left(\frac{1}{2}u_i u_i\right)}{\partial x_j \partial x_j}}^{\text{viscous diffusion}} \tag{5.1}$$

When viewed in Fourier space, turbulent convection, which is often called nonlinear energy transfer is responsible for an energy cascade from large scales to small scales and a momentum cascade in the wall-normal direction (Lee & Moser, 2019). However, there has been no study focusing on the conditional events of the turbulent convection term in physical space:

$$N = -u_j\frac{\partial\left(\frac{1}{2}u_i u_i\right)}{\partial x_j} = -u_i u_j\frac{\partial u_i}{\partial x_j} \tag{5.2}$$

where the final identity follows from the continuity equation for an incompressible flow. This study investigates the conditional events of the turbulent convection term. At a particular instant in time, a point with a positive turbulent convection value implies that turbulent fluctuations gain energy due to turbulent convection at this point; and a point with a negative turbulent convection value implies that turbulent fluctuations lose energy due to turbulent convection at this point. Similar studies investigating the conditional events of the forward cascade and inverse cascade between resolved scales and subgrid scales in the spirit of large-eddy simulation (LES) have found that the energy transfer is associated with ejections, sweeps (Piomelli et al., 1996) and hairpin vortex packets (Carper & Porté-Agel, 2004; Natrajan & Christensen, 2006). This study aims to look at the coherent structures present in the conditional events related to turbulent convection in turbulent

channel flows at $Re_\tau = 180$ and 590. To account for the inhomogeneity in the wall-normal direction of wall turbulence, we investigate the conditional events at different wall-normal heights covering the near-wall, logarithmic and outer layer regions.

This chapter is organised as follows. §5.2 presents the conditional averaging method, swirling strength calculation method and investigated wall-normal heights. §5.3 presents the results of the velocity fields, turbulent convection fields and vorticity fields of the conditional events. §5.4 draws the conclusions.

5.2 Methods

5.2.1 Conditional averaging

At one specific wall-normal height z, we choose a point in the xy plane and record the time series of the turbulent convection values. We aim to select events with large absolute values of turbulent convection N (5.2). Then, we categorise these conditional events into positive turbulent convection events $\tilde{N}|_+$ and negative turbulent convection events $\tilde{N}|_-$:

$$\tilde{N}(z)|_+ = \{N(z;t) \mid |N(z;t)| > kN_{\mathrm{RMS}}(z) \cap N(z;t) > 0\} \tag{5.3a}$$

$$\tilde{N}(z)|_- = \{N(z;t) \mid |N(z;t)| > kN_{\mathrm{RMS}}(z) \cap N(z;t) < 0\} \tag{5.3b}$$

$\tilde{N}(z)|_+$ represents an individual positive turbulent convection event and $\tilde{N}(z)|_-$ represents an individual negative turbulent convection event at the wall-normal height z. $N_{\mathrm{RMS}}(z)$ is the root mean square (RMS) of the turbulent convection at the wall-normal height z. k represents a non-dimensional threshold value. If k is too small, then the selected flow snapshots do not capture strong turbulent convection events. Conversely, if k is too large, then the number of selected flow snapshots becomes insufficient and convergence cannot be achieved. Through a trial-and-error process, we set $k = 3$. According to the percolation analysis, $k = 3$ meets the criterion of $1 \lesssim k \lesssim 3$ suggested in Lozano-Durán et al. (2012).

Figure 5.1 shows an example of conditional events detection at $Re_\tau = 180$ at a wall-normal height of $z^+ = 15$. The significant positive and negative turbulent convection events are indicated by red and blue arrows, respectively.

After having gathered the conditional events, we take the ensemble average of the velocity fields of those conditional events to obtain the conditionally averaged velocity field $\tilde{u}_i$ (Antonia, 1981):

$$\tilde{u}_i = \frac{\Sigma u_i|_{\tilde{N}}}{\text{the number of conditional events}} \tag{5.4}$$

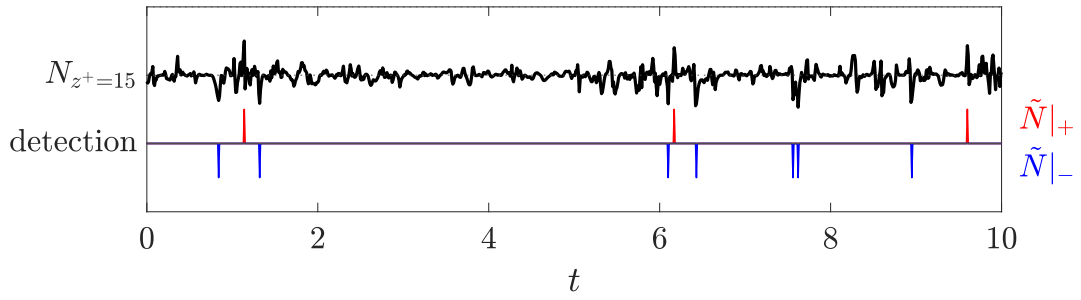

Figure 5.1: Conditional events detection at $Re_\tau = 180$. $N_{z^+=15}$ represents the turbulent convection N varying with respect to time at one point in the xy plane at $z^+ = 15.44$. Red arrows mark the selected positive turbulent convection events $\tilde{N}|_+$ and blue arrows mark the selected negative turbulent convection events $\tilde{N}|_-$.

5.2.2 Swirling strength calculation

Based on the conditionally averaged velocity field $\tilde{u}_i$, we can further investigate the vortical structures. We use the swirling strength λ_{ci} method, as it effectively captures local swirling motions and is insensitive to shear and strain (Chong et al., 1990; Zhou et al., 1999). Other vortex identification criteria, such as the Q criterion, could also be used, since both methods give similar vortical structures Zhou et al. (1999). For one point in the flow field, we first calculate its velocity tensor:

$$\left[\frac{\partial u_i}{\partial x_j}\right] = \begin{bmatrix} \frac{\partial u}{\partial x} & \frac{\partial u}{\partial y} & \frac{\partial u}{\partial z} \\ \frac{\partial v}{\partial x} & \frac{\partial v}{\partial y} & \frac{\partial v}{\partial z} \\ \frac{\partial w}{\partial x} & \frac{\partial w}{\partial y} & \frac{\partial w}{\partial z} \end{bmatrix} \tag{5.5}$$

Then, we calculate the eigenvalues of this velocity tensor:

$$\lambda_{cr} \pm \mathrm{i}\lambda_{ci} = \mathrm{eig}\left[\frac{\partial u_i}{\partial x_j}\right] \tag{5.6}$$

The imaginary part of this eigenvalue λ_{ci} is the swirling strength at this point. Note that if $\lambda_{ci} = 0$, then this point has zero local vorticity. After the swirling strength of every point in the flow field has been calculated, we plot the iso-surfaces of $|\lambda_{ci}|$ to visualise the vortical structures.

5.2.3 Wall-normal heights considered

The wall-normal heights in which conditional events are considered for the two datasets are summarised in table 5.1. Note that four additional wall-normal heights are investigated

at $Re_\tau = 590$ due to the longer outer layer when measured in viscous units.

$z^+_{Re_\tau=180}$	5	10	15	20	25	50	100	150	-	-	-	-
$z^+_{Re_\tau=590}$									200	300	400	500

Table 5.1: The wall-normal locations z^+ of the conditional events for the two datasets.

5.3 Results

By applying the conditional averaging criteria (5.3a) and (5.3b), we extract the conditional events from the DNS datasets. The numbers of conditional events for all cases are listed in table 5.2.

	z^+	5	10	15	20	25	50	100	150	200	300	400	500
$Re_\tau = 180$	$\tilde{N}\|_+$	4146	2464	1891	2198	2735	3416	3205	3192	–	–	–	–
	$\tilde{N}\|_-$	648	2738	2992	2577	2170	1701	1406	1027	–	–	–	–
$Re_\tau = 590$	$\tilde{N}\|_+$	2029	1038	958	1140	1320	1577	1530	1494	1504	1532	1615	1651
	$\tilde{N}\|_-$	625	1687	1719	1462	1224	1071	1069	1109	1097	1057	1002	926

Table 5.2: The numbers of conditional events at each wall-normal height.

5.3.1 Conditionally averaged velocity fields

This section shows the conditionally averaged velocity fields at $Re_\tau = 180$ and 590. Figures 5.2 and 5.3 show the conditionally averaged streamwise $\tilde{u}$ and wall-normal $\tilde{w}$ velocity fields at $Re_\tau = 180$, respectively. First, we detail the layout of each subfigure in figure 5.2. Figure 5.2(a) shows the conditionally averaged streamwise velocity fields in the streamwise-wall-normal plane (the xz plane). Each subfigure consists of two vertically stacked panels: the upper panel shows results from the positive turbulent convection event, while the lower panel shows results from the negative turbulent convection event. Labels for z^+ are displayed for the lower panel: from $z^+ = 0$ to $z^+ = 50$. The upper panel is also from $z^+ = 0$ to $z^+ = 50$. This layout applies to to all subfigures in figures 5.2, 5.3, 5.4, 5.5, 5.6, 5.7, 5.8 and 5.9. The magnitudes of the conditionally averaged spanwise velocity fields $\tilde{v}$ are negligible compared to $\tilde{u}$ and $\tilde{w}$. Theoretically, the conditionally averaged spanwise velocity $\tilde{v}$ should be zero from (5.3a) and (5.3b) because those turbulent convection events are statistically spanwise symmetrical, and this is borne out in the data. Therefore, $\tilde{v}$ is not shown.

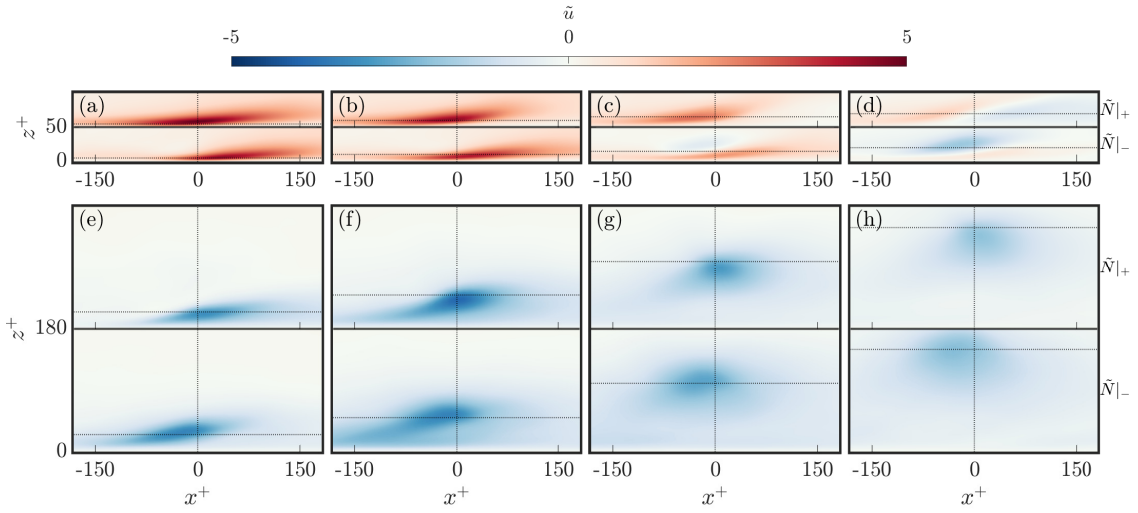

Figure 5.2: Conditionally averaged streamwise velocity fields $\tilde{u}$ at $Re_\tau = 180$. Subfigures (a) to (h) correspond to the conditional events at the wall-normal heights from $z^+ = 5$ to 150 as listed in table 5.1. The intersections of dashed lines mark the detection locations $x^+ = 0$. For each subfigure, the upper panel shows the result from the positive turbulent convection event $\tilde{N}|_+$ and the lower panel shows the result from the negative turbulent convection event $\tilde{N}|_-$. Labels for z^+ are displayed only on the lower panel.

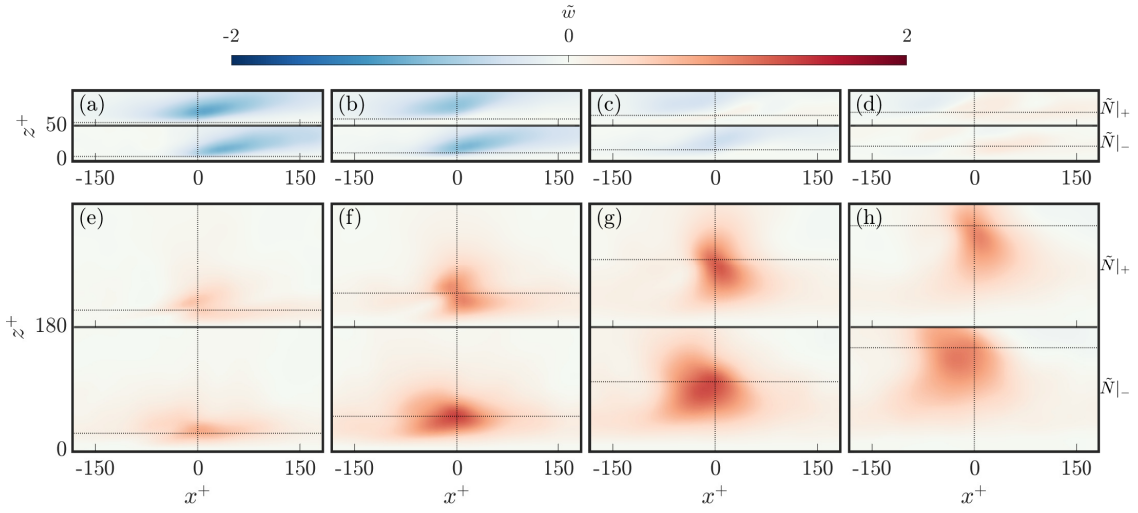

Figure 5.3: Conditionally averaged wall-normal velocity fields $\tilde{w}$ at $Re_\tau = 180$.

For each subplot corresponding to the conditional averaging at a specific wall-normal height, we see a similar pattern for both positive and negative turbulent convection events. In the near-wall region ($z^+ < 20$), positive streamwise fluctuation velocities are detected as shown in figures 5.2(a,b,c) and negative wall-normal fluctuation velocities are detected as shown in figures 5.3(a,b,c). The product $\tilde{u}\tilde{w}$ in this region ($\tilde{u} > 0, \tilde{w} < 0$) corresponds to sweeps or Q4 events (Wallace et al., 1972). Farther away from the wall ($z^+ > 20$), negative streamwise fluctuation velocities are detected as shown in figures 5.2(e,f,g,h) and

positive wall-normal fluctuation velocities are detected as shown in figures 5.3(e,f,g,h). The product $\tilde{u}\tilde{w}$ in this region $(\tilde{u} < 0, \tilde{w} > 0)$ corresponds to ejections or Q2 events (Wallace et al., 1972). The transition from sweeps to ejections occurs at $z^+ \approx 20$. The results could be related to the quadrant analysis that sweeps contribute most to the turbulent shear stress in the near-wall region and that ejections contribute most to the turbulent shear stress farther away from the wall (Wallace, 2016).

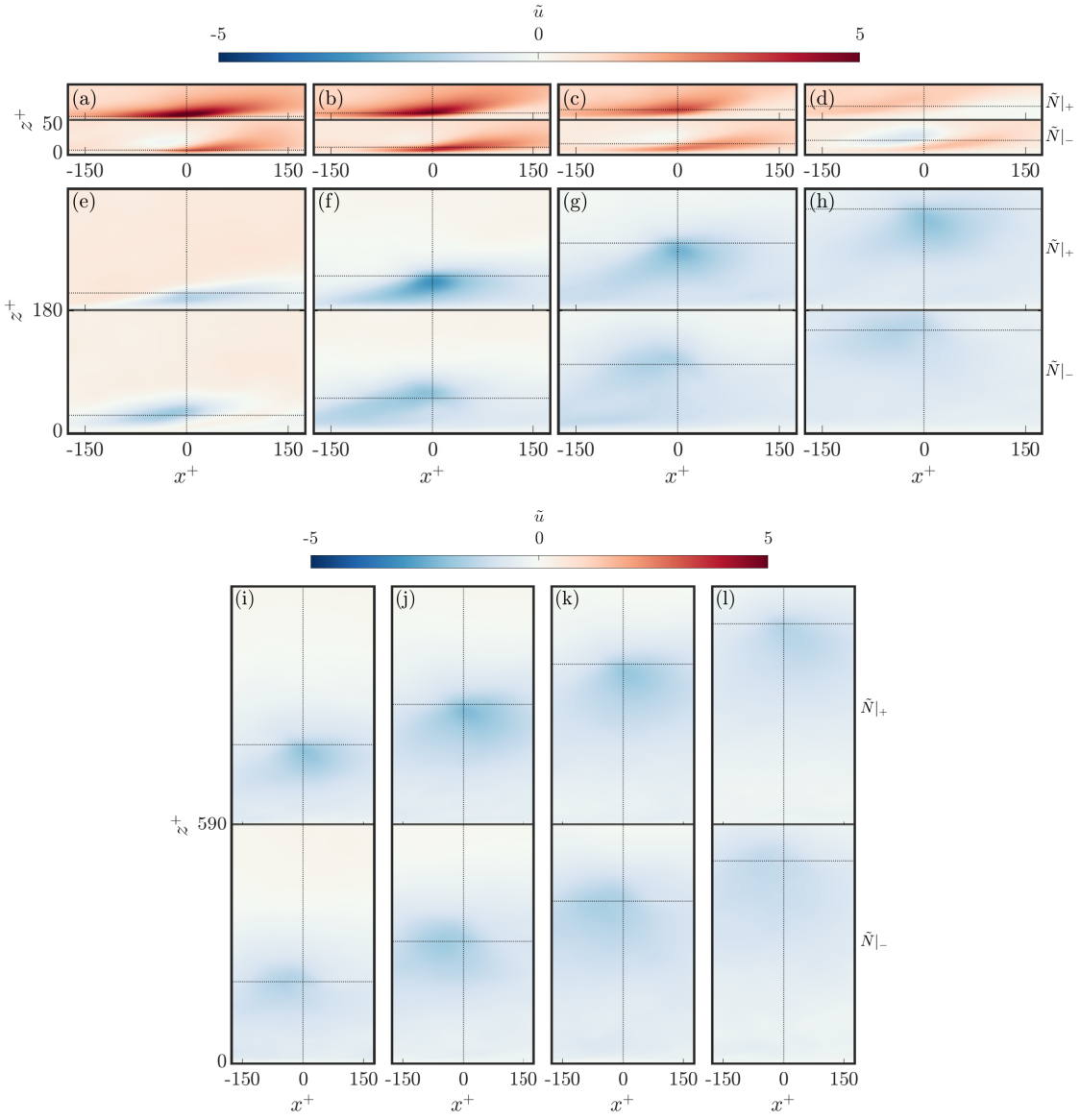

Figure 5.4: Conditionally averaged streamwise velocity fields $\tilde{u}$ at $Re_\tau = 590$. Subfigures (a) to (l) correspond to the conditional events detected at the wall-normal heights from $z^+ = 5$ to 500 as listed in table 5.1.

Figures 5.4 and 5.5 show $\tilde{u}$ and $\tilde{w}$ at $Re_\tau = 590$, respectively. According to figures 5.4(a-h) and 5.5(a-h), the same conclusions could be drawn for $Re_\tau = 590$ from $z^+ =$

5 to 150. We see that the shapes and magnitudes of the conditional velocity fields at $Re_\tau = 590$ are similar to those at $Re_\tau = 180$, potentially related to the Re-independent characteristics of the velocity profiles in the near-wall and log layers (Moser et al., 1999; Lee & Moser, 2019). According to figures 5.4(i-l) and 5.5(i-l), we see that ejections are related to turbulent convection events up to $z^+ = 500$ at $Re_\tau = 590$.

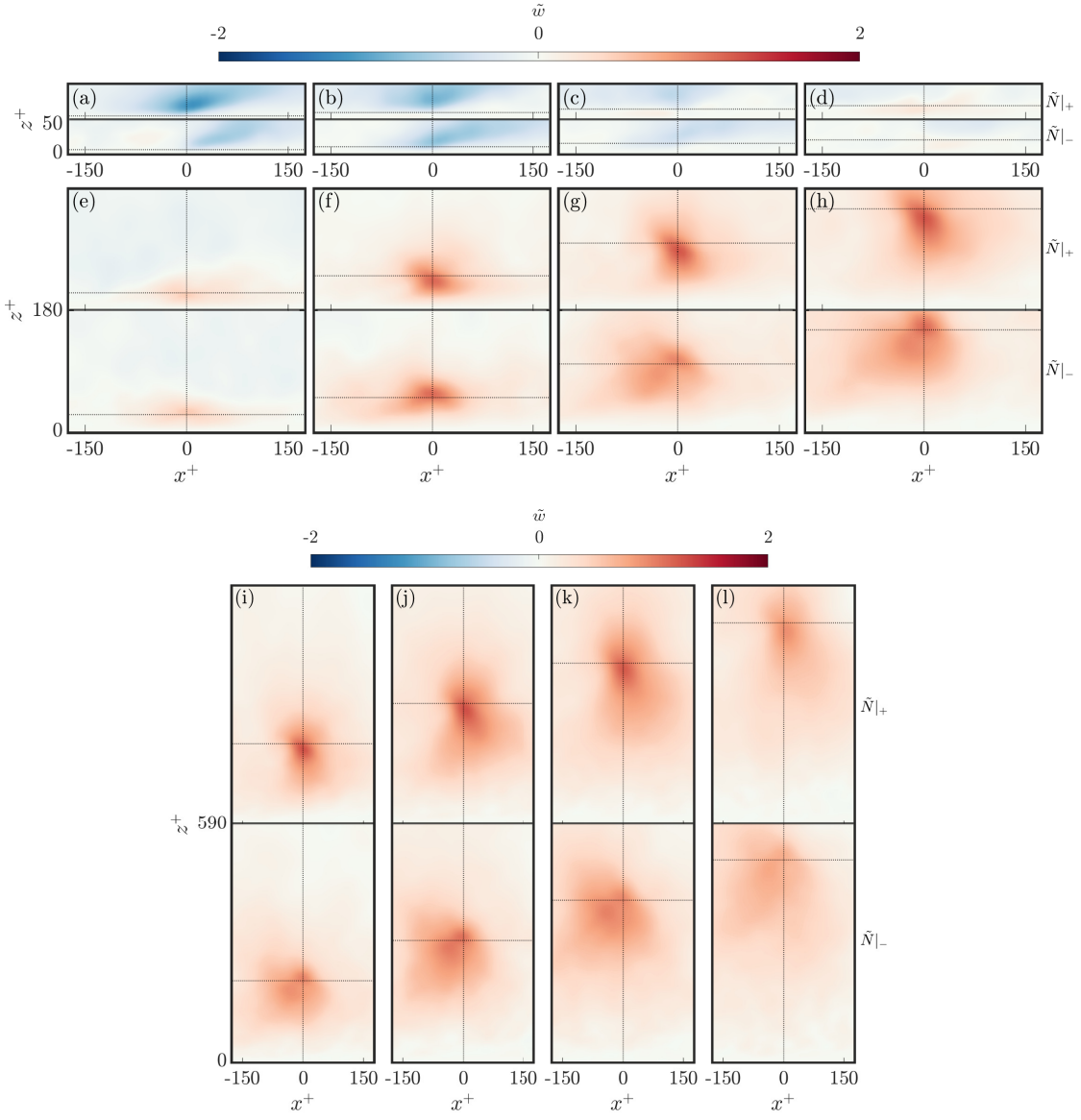

Figure 5.5: Conditionally averaged wall-normal velocity fields $\tilde{w}$ at $Re_\tau = 590$.

However, the colours in figures 5.2-5.5 only show the conditionally averaged velocity fields qualitatively. Therefore, we present the values of the corresponding velocity fields quantitatively in figures 5.6 and 5.7. The transition from sweeps (Q4 events) to ejections (Q2 events) occurs at $z^+ \approx 20$ for both positive and negative turbulent convection events. Apart from this same trend, we see that there are small differences in terms of the ve-

locity profile and magnitude between positive and negative turbulent convection events, indicating that differences exist. The differences are further discussed in the following sections.

Now we look at the values of the conditionally averaged velocity profiles as shown in figures 5.6 and 5.7. In terms of the different Reynolds numbers, we see that the velocity profiles at $Re_\tau = 180$ are nearly identical to that at $Re_\tau = 590$ in terms of the magnitudes and shapes, giving quantitative support for the Re-independent characteristics of velocity scaling in the near-wall and logarithmic regions (Moser et al., 1999; Lee & Moser, 2019). Despite the high similarity, the conditionally averaged velocity profiles at $Re_\tau = 180$ and 590 do not collapse on each other completely because they are obtained from the conditionally averaged events. The time-averaged velocity fields at $Re_\tau = 180$ and 590 will collapse in the near-wall and logarithmic regions (Moser et al., 1999; Lee & Moser, 2019). . In terms of the positive and negative turbulent convection events, the velocity profiles from both events are highly similar. However, subtle differences between the curves from the positive and negative events are still discernible. The differences can be further observed in the turbulent convection and vortical fields discussed in the subsequent sections.

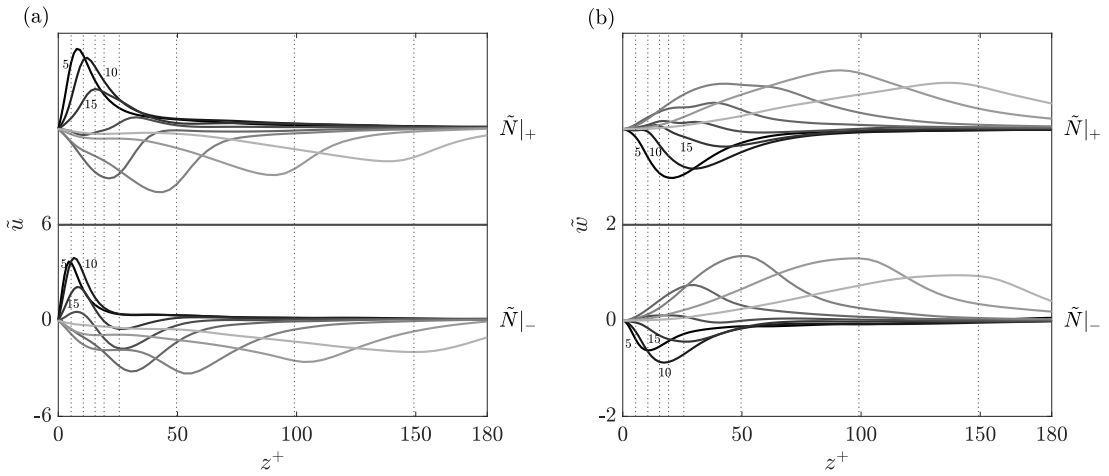

Figure 5.6: (a) Conditionally averaged streamwise velocity $\tilde{u}$; (b) wall-normal velocity $\tilde{w}$ at $Re_\tau = 180$. Solid lines show the velocity profiles at $x^+ = 0$ in figures 5.2 and 5.3. Solid lines with darker colours correspond to conditional averaged cases at lower wall-normal heights. Dashed lines mark the wall-normal heights of conditional averaged cases in table 5.1. For each subplot, the upper part shows the velocity profiles for positive turbulent convection events $\tilde{N}|_+$ and the lower part shows the velocity profiles for negative turbulent convection events $\tilde{N}|_-$. Labels for the Y-axes are only displayed for the lower panels.

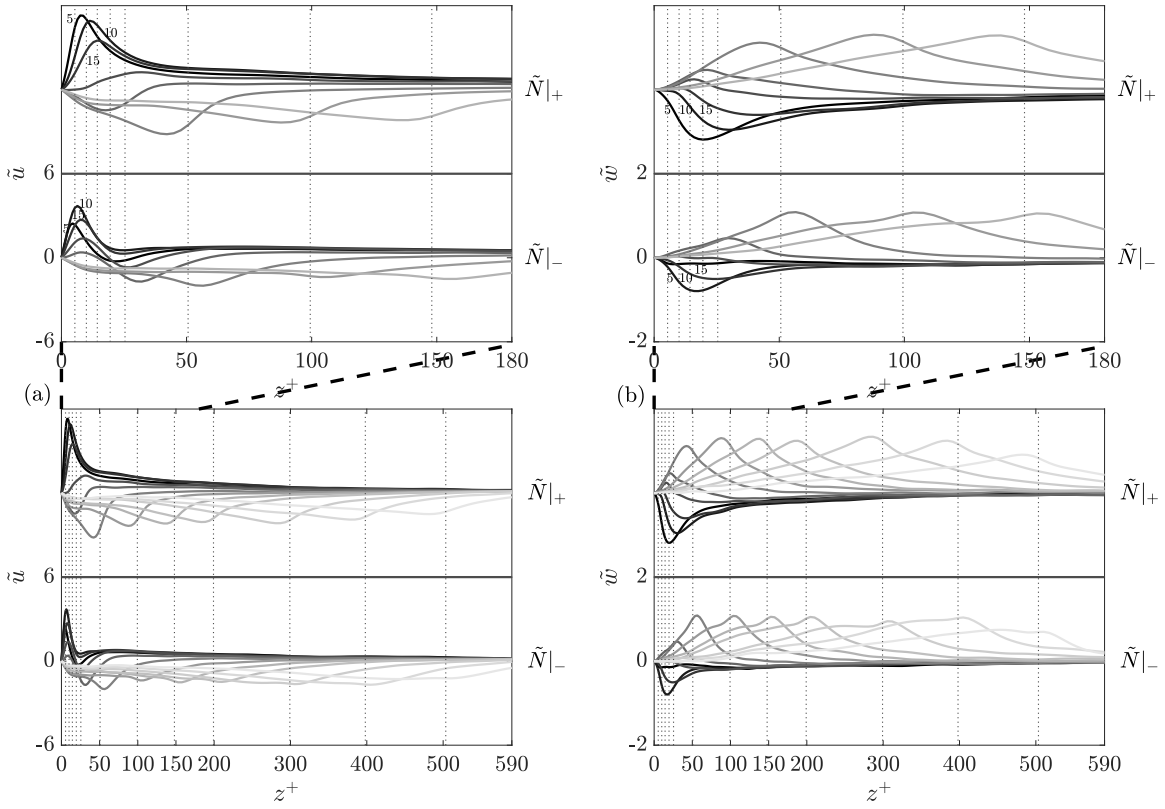

Figure 5.7: (a) Conditionally averaged streamwise velocity $\tilde{u}$; (b) wall-normal velocity $\tilde{w}$ at $Re_\tau = 590$. The upper plots show the wall-normal region $0 < z^+ < 180$.

5.3.2 Conditionally averaged turbulent convection fields

Since the conditional averaging is based on the turbulent convection term, it is of interest to also inspect the conditionally averaged turbulent convection fields. This section shows the conditionally averaged turbulent convection fields $\tilde{N}$ at $Re_\tau = 180$ and 590. $\tilde{N}$ is calculated from the conditionally averaged velocity fields $\tilde{u}_i$. For a fair comparison between $Re_\tau = 180$ and 590, we normalise the absolute turbulent convection values by a characteristic value. Production in equation (5.1) is the only energy source for turbulence and we can calculate the time-averaged bulk production at a specific Re_τ:

$$P_b(Re_\tau) = \frac{\overline{\iiint -uw\frac{\mathrm{d}U}{\mathrm{d}z}\,\mathrm{d}x\,\mathrm{d}y\,\mathrm{d}z}}{L_x L_y L_z} \tag{5.7}$$

P_b represents the total energy provided to fluctuations at a specific Re_τ and is therefore insensitive to the size of the simulation box. P_b increases as Re_τ increases. Therefore, we divide the absolute values of turbulent convection by P_b to obtain the normalised turbulent convection. The bulk production P_b has the same units as the turbulent convection N (5.2).

If a given point has a value (normalised turbulent convection) of 10, it means that the energy gained per unit volume at this point is 10 times the average production per unit volume.

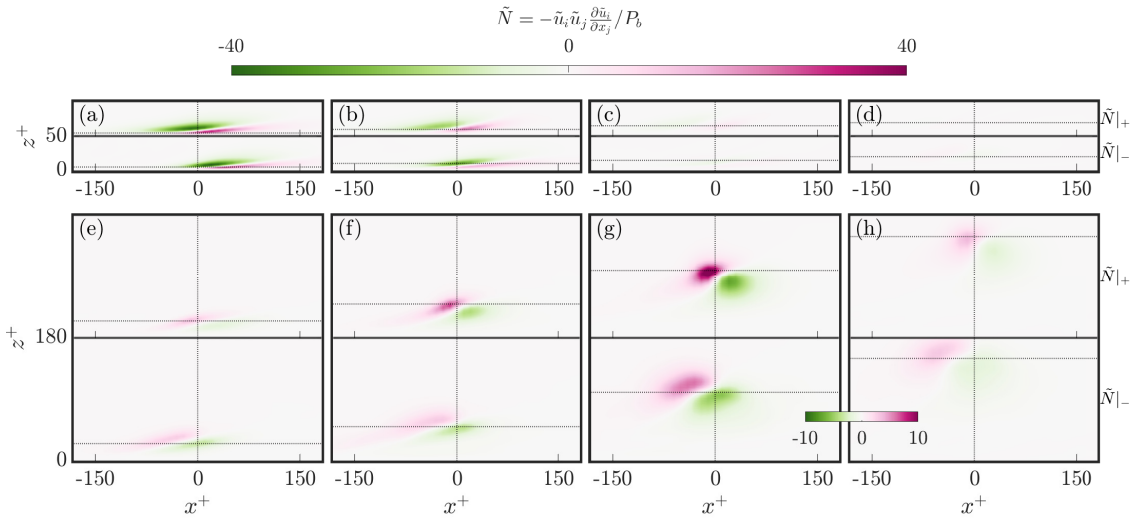

Figure 5.8: Normalised conditionally averaged turbulent convection fields $\tilde{N}$ at $Re_\tau = 180$. Subfigures (a) to (h) correspond to the conditional events detected at the wall-normal heights from $z^+ = 5$ to 150 as listed in table 5.1. For each subplot, the upper part is for positive turbulent convection event $\tilde{N}|_+$ and the lower part is for negative turbulent convection event $\tilde{N}|_-$. The colourmap limit is from -40 to 40 in subfigures (a) to (f); the colourmap limit is from -10 to 10 in subfigures (g,h).

Figure 5.8 shows the normalised turbulent convection $\tilde{N}$ at $Re_\tau = 180$. According to the colour scale, we see that turbulent convection is intense in the near-wall region (figures 5.8(a,b)) and fades away at $z^+ \approx 20$ (figures 5.8(c,d)). This could be related to the finding that the conditionally averaged velocities $\tilde{u}_i$ are near zero at $z^+ \approx 20$ where the transition from sweeps to ejections occurs as shown in figure 5.6. The intensity of turbulent convection grows again farther away from the wall (figures 5.8(e,f)) and decreases at $z^+ > 100$ (figures 5.8(g,h)). For positive turbulent convection events (the upper subplots in figures 5.8(a,b,e,f,g,h)), we see an expected region of positive turbulent convection (pink region) at the detection location since the conditional averaging criterion (5.3a) is based on positive turbulent convection. Interestingly, there is also a region of negative turbulent convection (green region) which is not expected merely according to the conditional averaging criterion (5.3a). For negative turbulent convection events (the lower subplots in figures 5.8(a,b,e,f,g,h)), we see an expected region of negative turbulent convection (green region) at the detection location since the conditional averaging criterion (5.3b) is based on negative turbulent convection. In addition, there is also a region of positive turbulent convection (pink region) which is not expected merely according to the conditional averaging criterion (5.3b). This feature will be further discussed at the end of

this section. In the near-wall region ($z^+ < 20$) as shown in figures 5.8(a,b), the region of negative turbulent convection occurs upstream of the region of positive turbulent convection in the streamwise direction. Farther away from the wall ($z^+ > 20$) as shown in figures 5.8(e,f,g,h), the region of positive turbulent convection occurs upstream of the region of negative turbulent convection in the streamwise direction. It is worth mentioning that the same conclusions in this study could be drawn if the conditionally averaged turbulent convection is directly extracted from the conditional events (rather than calculated from the conditionally averaged velocities).

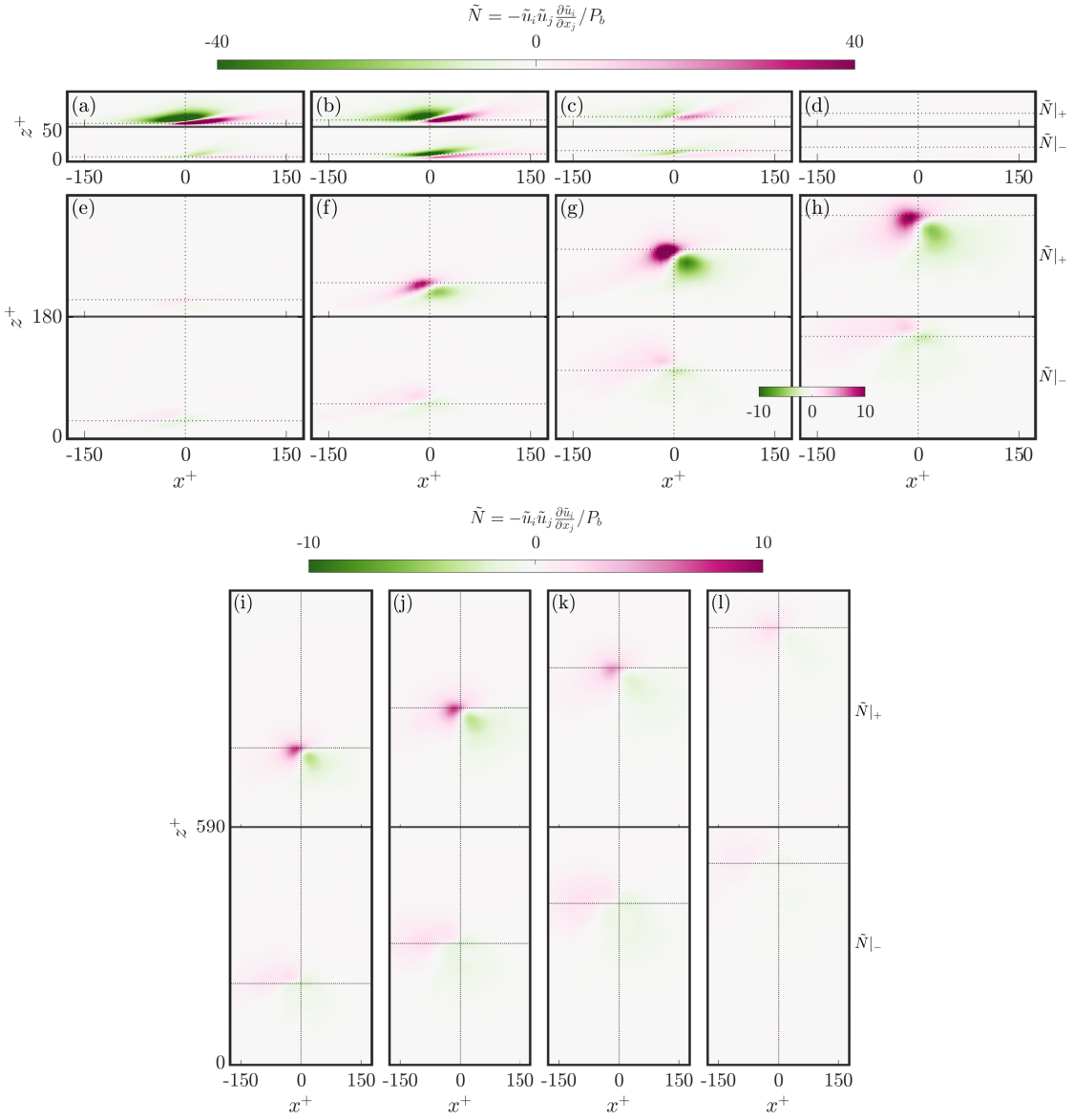

Figure 5.9: Normalised conditionally averaged turbulent convection fields $\tilde{N}$ at $Re_\tau = 590$. Subfigures (a) to (l) correspond to the conditional events detected at the wall-normal heights from $z^+ = 5$ to 500 as listed in Table 5.1. The colourmap limit is from -40 to 40 in subfigures (a) to (f); the colourmap limit is from -10 to 10 in subfigures (g) to (l).

Figure 5.9 shows the normalised $\tilde{N}$ at $Re_\tau = 590$. Except similar observations from $Re_\tau = 180$, more intense turbulent convection events occur in the near-wall region at $Re_\tau = 590$ compared to $Re_\tau = 180$ according to the colour scale (comparing figures 5.8(a,b) with figures 5.9(a,b)). The turbulent convection pattern can be observed up to $z^+ = 500$ (figures 5.9(i-l)) though they become substantially weaker, especially for the negative turbulent convection events. This could be related to the number of conditional events from table 5.2 that the number of positive turbulent convection events is significantly higher than the number of negative turbulent convection events from $z^+ = 200$ to 500.

Figures 5.10 and 5.11 further show the normalised conditionally averaged turbulent convection values at $Re_\tau = 180$ and 590. Each dot shows the value at the detection locations (the intersection of the dashed lines in figure 5.8 or 5.9). Magenta dots show the values for positive turbulent convection events (the upper part of each subfigure in figure 5.8 or 5.9) and green dots show the values for negative turbulent convection events (the lower part of each subfigure in figure 5.8 or 5.9).

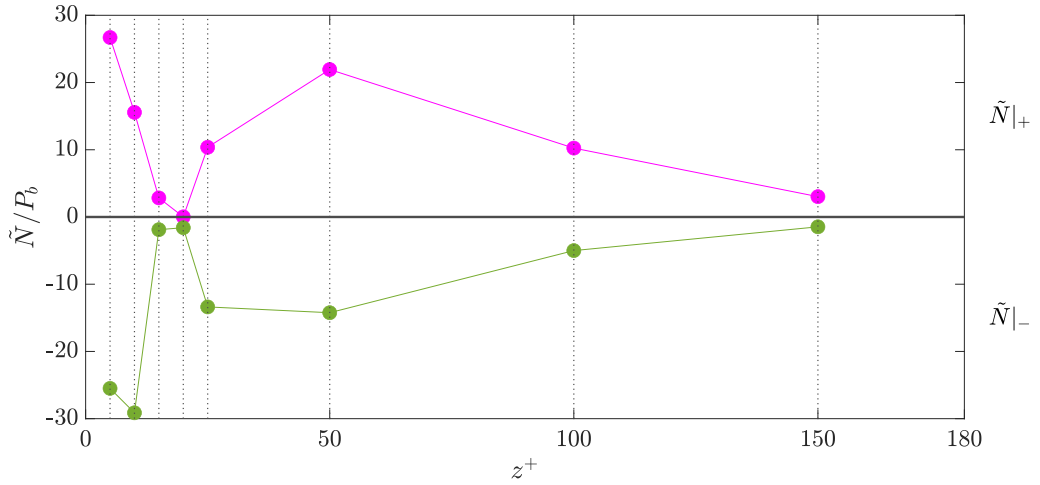

Figure 5.10: Normalised conditionally averaged turbulent convection values at the detection points indicated by the intersections of the dashed lines in figure 5.8 at $Re_\tau = 180$. The magenta line in the upper part shows the values for the positive turbulent convection events and the green line in the lower part shows the values for the negative turbulent convection events.

Figures 5.10 and 5.11 quantitatively reveal that the conditionally averaged turbulent convection at $Re_\tau = 590$ is more intense than that at $Re_\tau = 180$ in the near-wall region. In addition, we see that the largest values are attained in the near-wall region. The value decreases to zero at $z^+ \approx 20$ corresponding to the transition from sweeps to ejections. The value increases again and gradually decreases farther away from the wall at $z^+ > 100$. Apart from the similarities between the pink and green lines, differences also exist, cor-

responding to the differences between positive and negative turbulent convection events. Firstly, in the near-wall region at $z^+ < 20$, the intensity of negative turbulent convection is lower than that of positive turbulent convection, especially at $Re_\tau = 590$ as shown in figure 5.11. Secondly, farther away from the wall at $z^+ > 20$, the intensity of negative turbulent convection is lower than that of positive turbulent convection and nearly approaches zero, as can also be observed in figures 5.9(i-l).

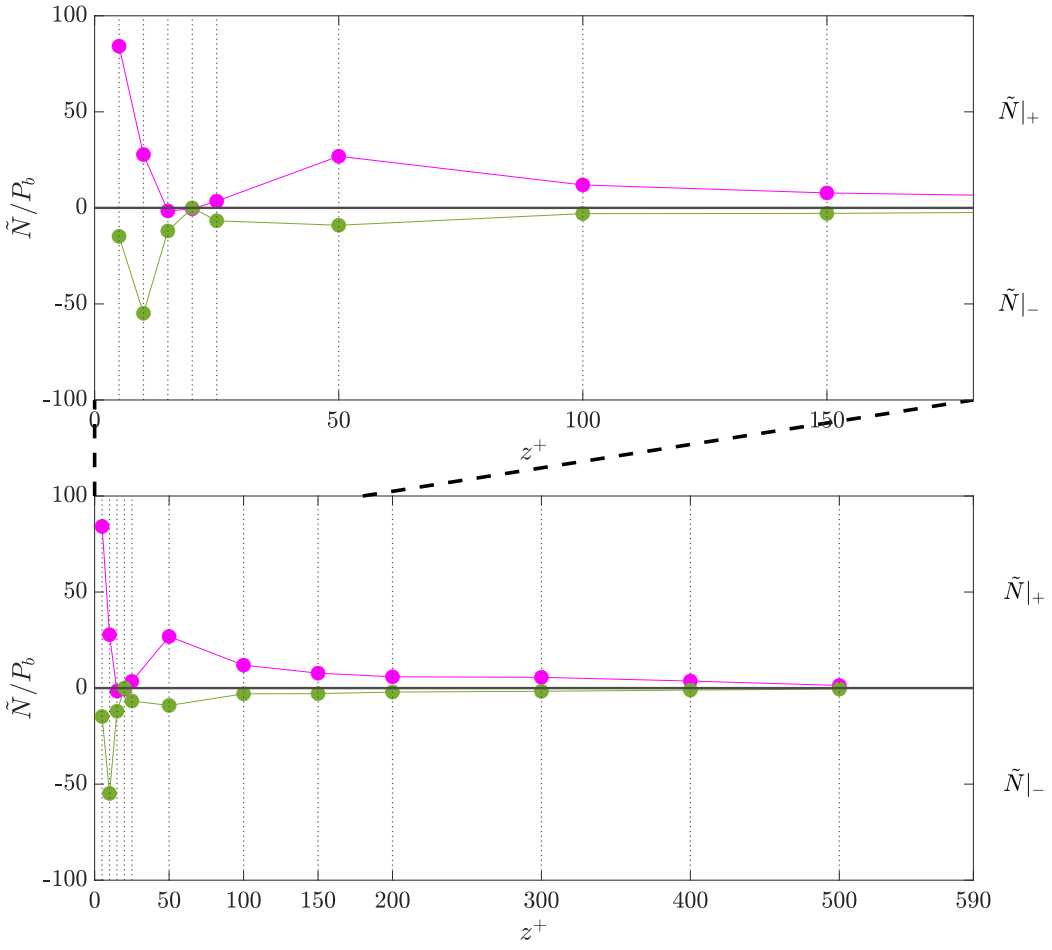

Figure 5.11: Normalised conditionally averaged turbulent convection values at the detection points indicated by the intersections of the dashed lines in figure 5.9 at $Re_\tau = 590$. The upper plot shows the wall-normal region $0 < z^+ < 180$.

For both Reynolds numbers, we see similar turbulent convection patterns as illustrated in figure 5.12. At a specific wall-normal height, a similar pattern is detected for both positive and negative turbulent convection events. This pattern is composed of a region of positive turbulent convection and a region of negative turbulent convection. This indicates that energy gain and energy loss due to turbulent convection occur in pairs (Piomelli et al., 1996). In the near-wall region $(z^+ < 20)$, the region of negative turbulent convection occurs upstream of the region of positive turbulent convection in the streamwise direction

and they present themselves as streamwise streak shapes with a small angle around 15° to the wall. The intensity is strong compared to the turbulent convection patterns farther away from the wall. Farther away from the wall ($z^+ > 20$), the region of positive turbulent convection occurs upstream of the region of negative turbulent convection in the streamwise direction, and the angle to the wall increases to around 30°. The intensity becomes slightly weaker. The intensity becomes significantly weaker in the outer-layer region $z^+ > 100$, and the patterns no longer present as streak shapes. The region of positive turbulent convection occurs upstream of the region of negative turbulent convection.

Note that the turbulent convection patterns described above apply to both positive and negative turbulent convection events. The similar patterns detected from both types of events suggest that positive and negative turbulent convection events are potentially related to the same structures. This drives us to investigate other physical quantities which may reveal the particular coherent structures.

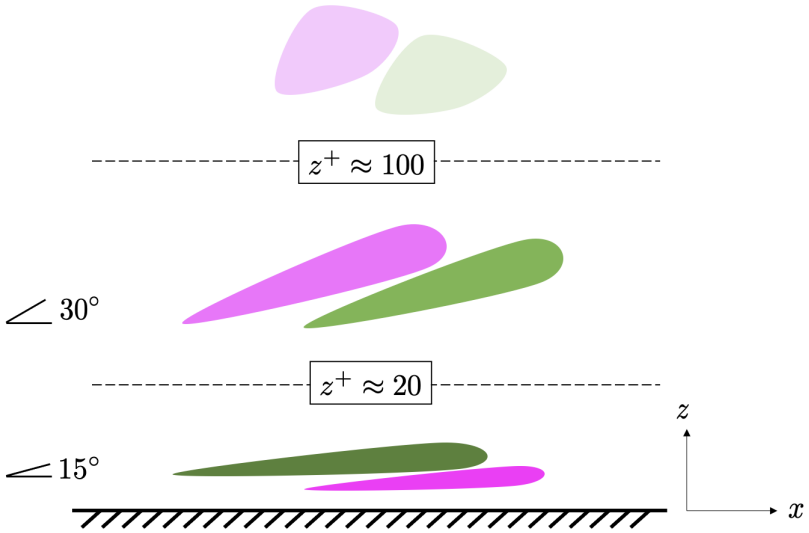

Figure 5.12: Cartoon of turbulent convection patterns along the wall-normal direction. Pink colour marks the regions of positive turbulent convection and green colour marks the regions of negative turbulent convection. The colour scale indicates the intensity of turbulent convection.

5.3.3 Conditionally averaged vorticity fields

As motivated by the previous section, we now seek to extract the coherent structures that correlate with turbulent convection events. We choose to look at vorticity fields because quasi-streamwise vortices and hairpin vortices are basic elements in wall turbulence (Theodorsen, 1952; Perry & Chong, 1982; Head & Bandyopadhyay, 1981; Wu & Moin, 2009) and they are important in the self-sustaining process (SSP) (Hamilton et al., 1995;

Waleffe, 1997). This section shows the conditionally averaged vorticity fields represented by swirling strength (Chong et al., 1990).

Dennis & Nickels (2011) nicely showed the 3-D vortical structures conditionally averaged on significant 2-D vorticity events in a boundary layer in experiments using PIV. Here, we follow their approach for visualising the vorticity fields and show the 3-D vortical structures conditionally averaged on turbulent convection events in channels in the DNS, as shown in figures 5.13 to 5.18. For each figure, the conditionally averaged vorticity fields are shown at five different angles to better visualise the 3-D characteristics. The vorticity iso-surfaces for the conditional averaged event at one wall-normal height are shown using the same colour. The vorticity iso-surfaces for the conditional averaged events at different wall-normal heights are displayed along the x^+ axis. A Gaussian smoothing method has been applied to the conditional averaged data to reduce the coarseness of the plots. Note that the smoothing retains the main features of the vortical structures and does not change the conclusions in this study.

Figures 5.13 and 5.14 show the swirling strength fields from positive and negative turbulent convection events at $Re_\tau = 180$, respectively. We see that at a specific wall-normal height, structures from the positive and negative turbulent convection events are similar, satisfying the deduction from the previous section that both events are related to the same structures. In the near-wall region $(z^+ < 20)$, a pair of quasi-streamwise vortices exhibit a small angle around 15° to the wall. From the hairpin vortex diagram, the legs of a hairpin vortex are composed of a pair of quasi-streamwise vortices (Adrian et al., 2000). Farther from the wall $(z^+ > 20)$, a hairpin structure with a head and a pair of necks exhibiting a larger angle around 45° to the wall and the structure becomes detached from the wall for $z^+ > 100$. The structures detected based on significant turbulent convection events are similar to those reported in previous studies (Head & Bandyopadhyay, 1981; Zhou et al., 1999; Adrian et al., 2000; Wu & Moin, 2009; Dennis & Nickels, 2011).

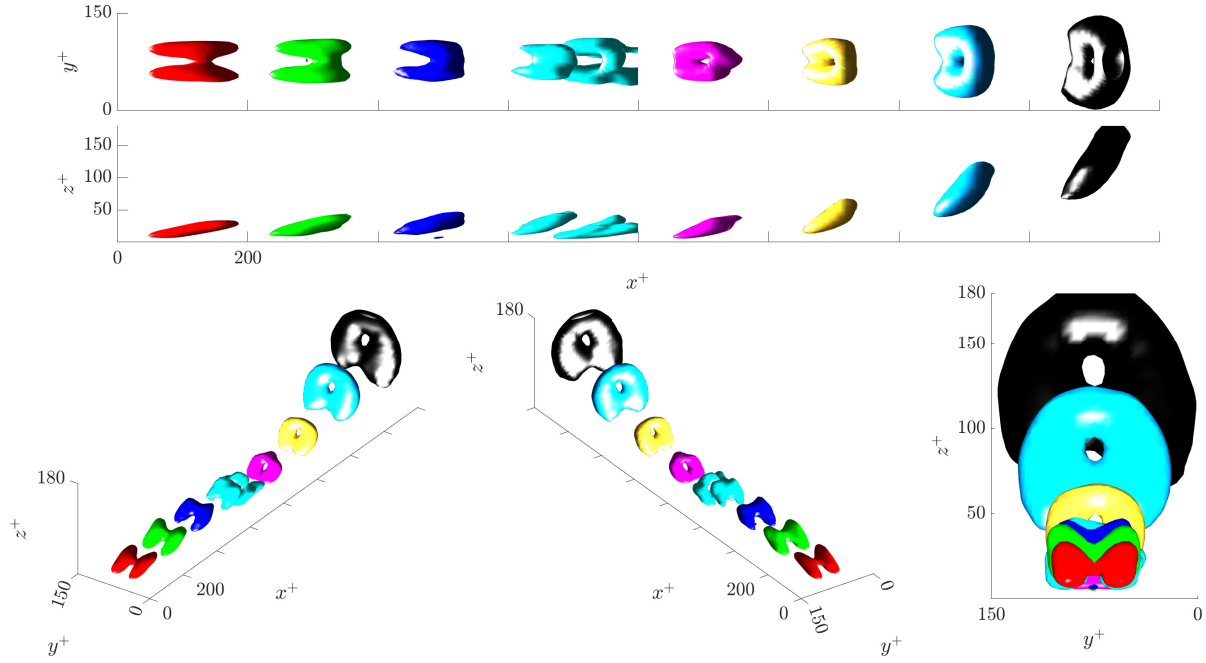

Figure 5.13: Swirling strength fields from positive turbulent convection events $\tilde{N}|_+$ at $Re_\tau = 180$. Iso-surfaces shown are for $\lambda_{ci,iso} = 0.5\lambda_{ci,max}$. The structures in red, green,..., black correspond to the conditional events from $z^+ = 5$ to 150 listed in table 5.1. Tick marks on the x^+ axis are one unit apart.

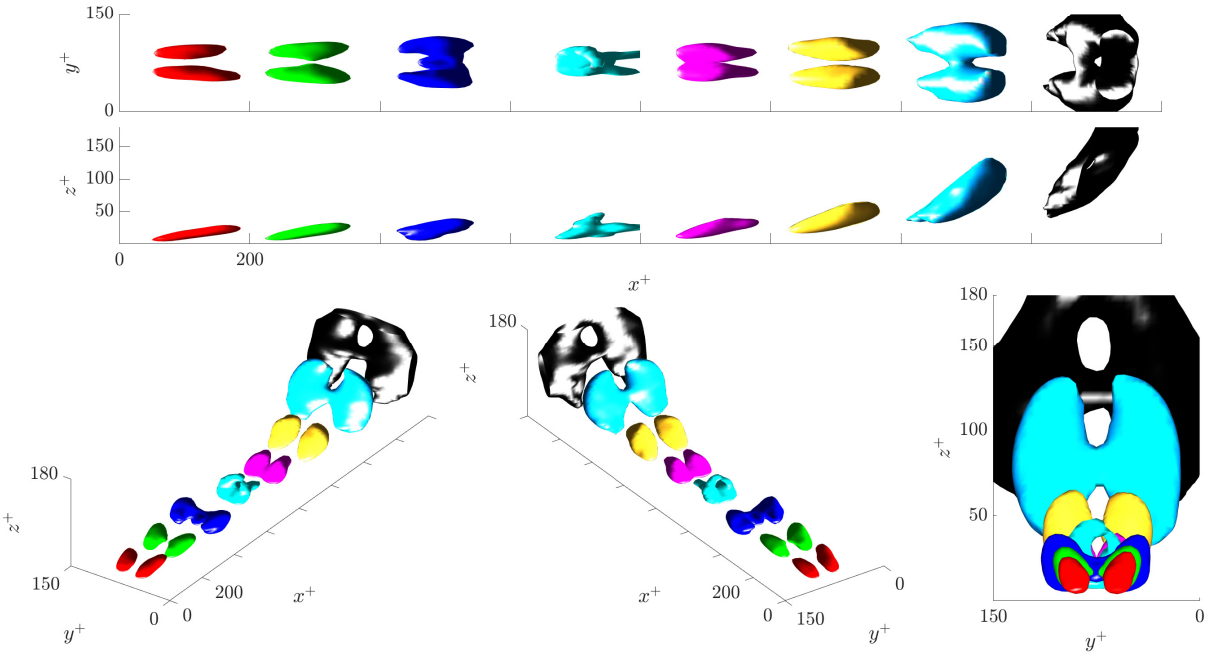

Figure 5.14: Swirling strength fields from negative turbulent convection events $\tilde{N}|_-$ at $Re_\tau = 180$. Iso-surfaces shown are for $\lambda_{ci,iso} = 0.5\lambda_{ci,max}$. The structures in red, green,..., black correspond to the conditional events from $z^+ = 5$ to 150 listed in table 5.1. Tick marks on the x^+ axis are one unit apart.

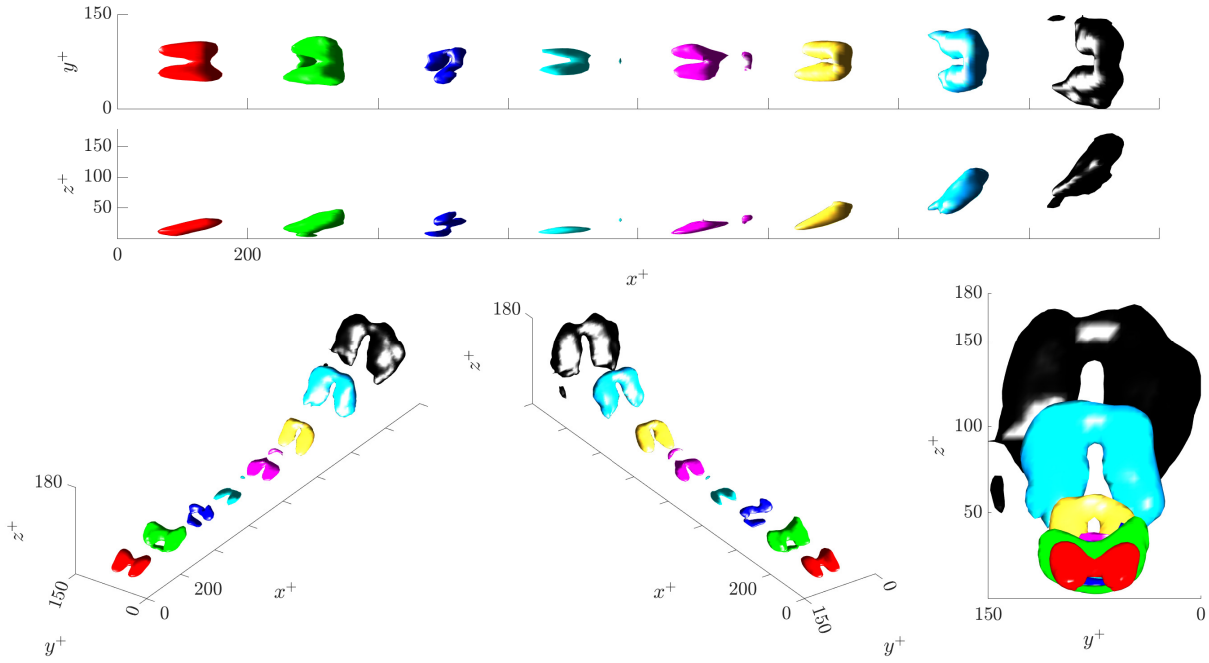

Figure 5.15: Swirling strength fields from positive turbulent convection events $\tilde{N}|_+$ at $Re_\tau = 590$. Iso-surfaces shown are for $\lambda_{ci,iso} = 0.5\lambda_{ci,max}$. The structures in red, green,..., black correspond to the conditional events from $z^+ = 5$ to 150 listed in table 5.1. Tick marks on the x^+ axis are one unit apart.

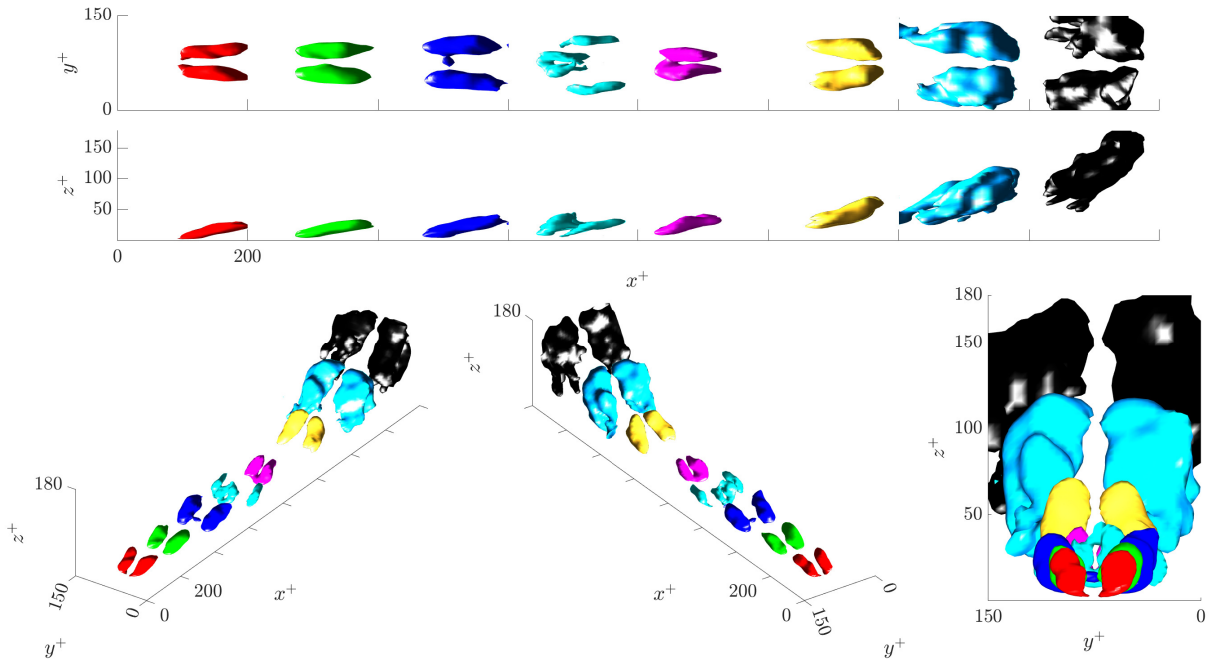

Figure 5.16: Swirling strength fields from negative turbulent convection events $\tilde{N}|_-$ at $Re_\tau = 590$. Iso-surfaces shown are for $\lambda_{ci,iso} = 0.5\lambda_{ci,max}$. The structures in red, green,..., black correspond to the conditional events from $z^+ = 5$ to 150 listed in table 5.1. Tick marks on the x^+ axis are one unit apart.

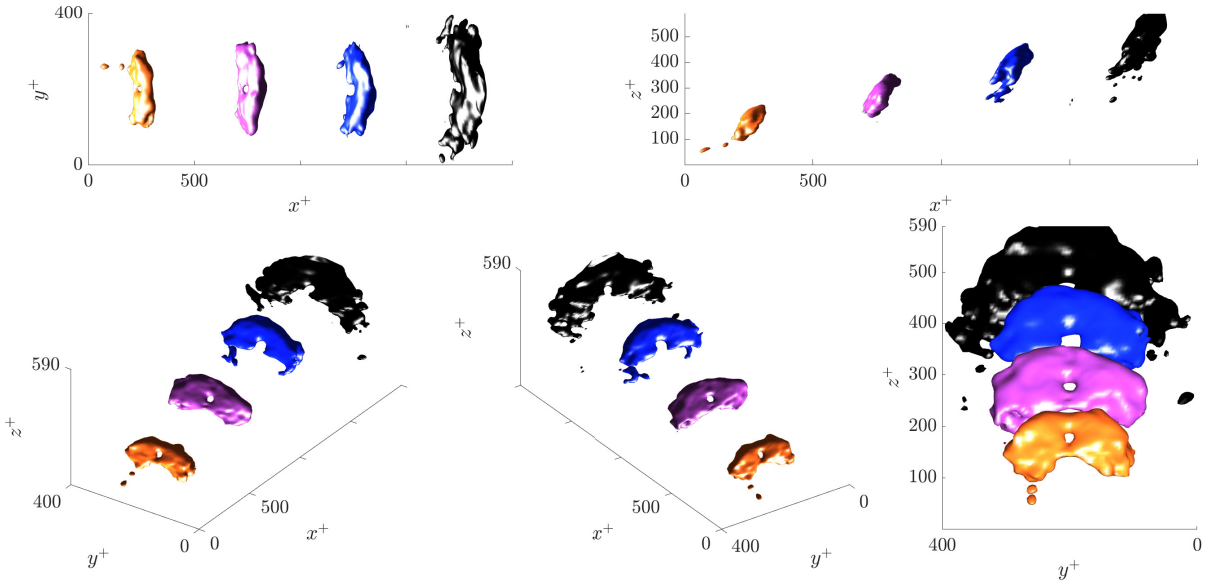

Figure 5.17: Swirling strength fields from positive turbulent convection events $\tilde{N}|_+$ at $Re_\tau = 590$. Iso-surfaces shown are for $\lambda_{ci,iso} = 0.5\lambda_{ci,max}$. The structures in orange, pink, blue and black correspond to the conditional events from $z^+ = 200$ to 500 listed in table 5.1. Tick marks on the x^+ axis are one unit apart.

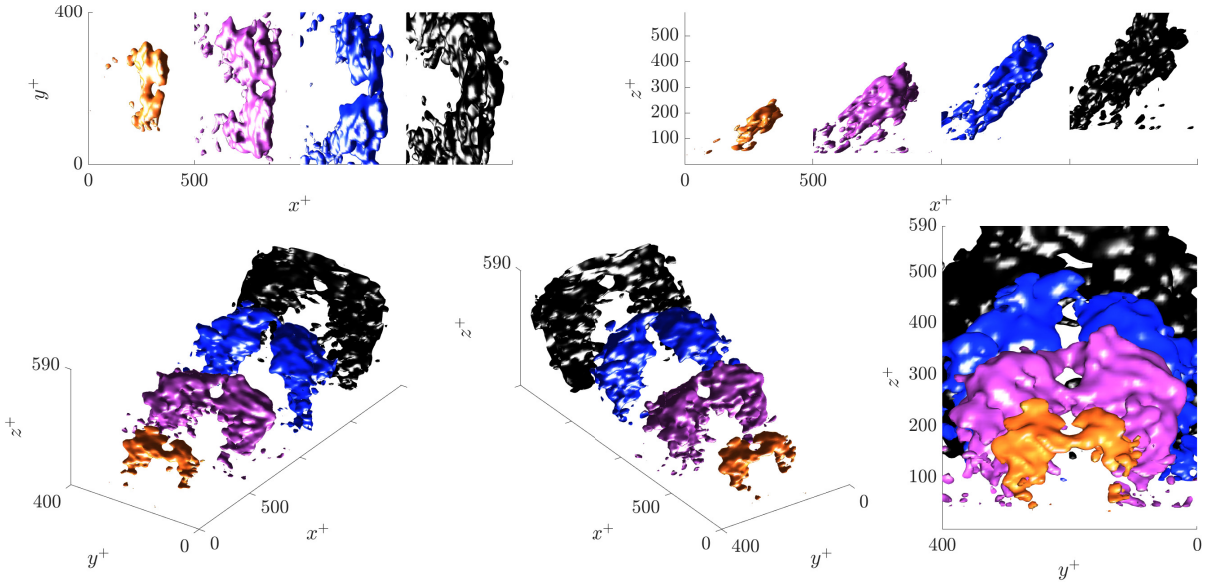

Figure 5.18: Swirling strength fields from negative turbulent convection events $\tilde{N}|_-$ at $Re_\tau = 590$. Iso-surfaces shown are for $\lambda_{ci,iso} = 0.5\lambda_{ci,max}$. The structures in orange, pink, blue and black correspond to the conditional events from $z^+ = 200$ to 500 listed in table 5.1. Tick marks on the x^+ axis are one unit apart.

Figures 5.15 and 5.17 show the swirling strength fields for positive turbulent convection events at $Re_\tau = 590$. Figures 5.16 and 5.18 show the swirling strength fields for

negative turbulent convection events at $Re_\tau = 590$. The layouts in figures 5.15 and 5.16 are the same as those in figures 5.13 and 5.14 for an easy comparison between $Re_\tau = 180$ and 590 from $z^+ = 5$ to 150. We see similar quasi-streamwise vortices, hairpin heads and necks at both Reynolds numbers. The results show the self-similarity of the coherent structures at these two Reynolds numbers (Robinson, 1991). Figures 5.17 and 5.18 show the vortical structures at wall-normal heights between $z^+ = 200$ and 500. We see hairpin heads with arch shapes from positive turbulent convection events. We see coarse hairpin heads and necks from negative turbulent convection events. The iso-contours are coarse because of the low occurrence of significant turbulent convection events between $z^+ = 200$ and 500. In addition, we can see that the size of a hairpin vortex increases as the wall-normal distance from the wall increases, in line with the attached eddy hypothesis (Townsend, 1976). The different sizes of the hairpin vortices detected along the wall-normal height support the existence of hairpin vortex packets that small hairpin vortices grow as they travel in the streamwise direction and generate new hairpin vortices upstream (Zhou et al., 1999; Adrian et al., 2000).

Displaying coherent structures is not the main purpose of this study. Robinson (1991) proposed that quasi-streamwise vortices in the near-wall region and hairpin vortices farther away from the wall are the basic elements in wall-bounded flows. The same coherent structures found in this study using conditional averaging ((5.3a) and (5.3b)) further indicate that those coherent structures are related to both positive and negative turbulent convection.

However, positive and negative turbulent convections are two different types of events. One is associated with gaining energy and the other is associated with losing energy. In addition, although the vortical structures between positive and negative turbulent convections are similar, differences in the conditionally averaged velocity profiles exist (figures 5.6 and 5.7). Therefore, we further plot them together in the xz plane to further analyse the similarities and differences, as shown in figures 5.19 and 5.20. We see that there is a phase difference in the streamwise direction between the structures from positive and negative turbulent convection events at both Reynolds numbers. In the near-wall region ($z^+ < 20$) as shown in figures 5.19(a,b) and 5.20(a,b), quasi-streamwise vortices from positive turbulent convection events are upstream of that from negative turbulent convection events in the streamwise direction. Farther away from the wall ($z^+ > 20$) as shown in figures 5.19(e,f,g,h), 5.20(e-i), hairpin heads from positive turbulent convection events are downstream of that from negative turbulent convection events in the streamwise direction.

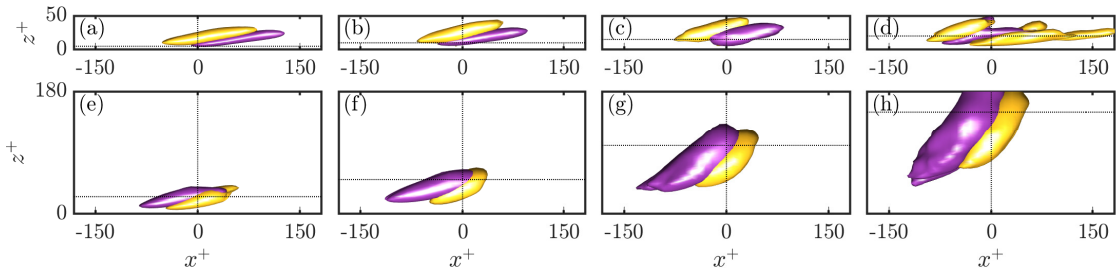

Figure 5.19: Swirling strength viewed in the xz plane at $Re_\tau = 180$. For each subfigure, the swirling strength in yellow is for $\tilde{N}|_+$ and the swirling strength in purple is for $\tilde{N}|_-$. Subfigures (a) to (h) correspond to the conditional events detected at the wall-normal heights from $z^+ = 5$ to 150 as listed in table 5.1.

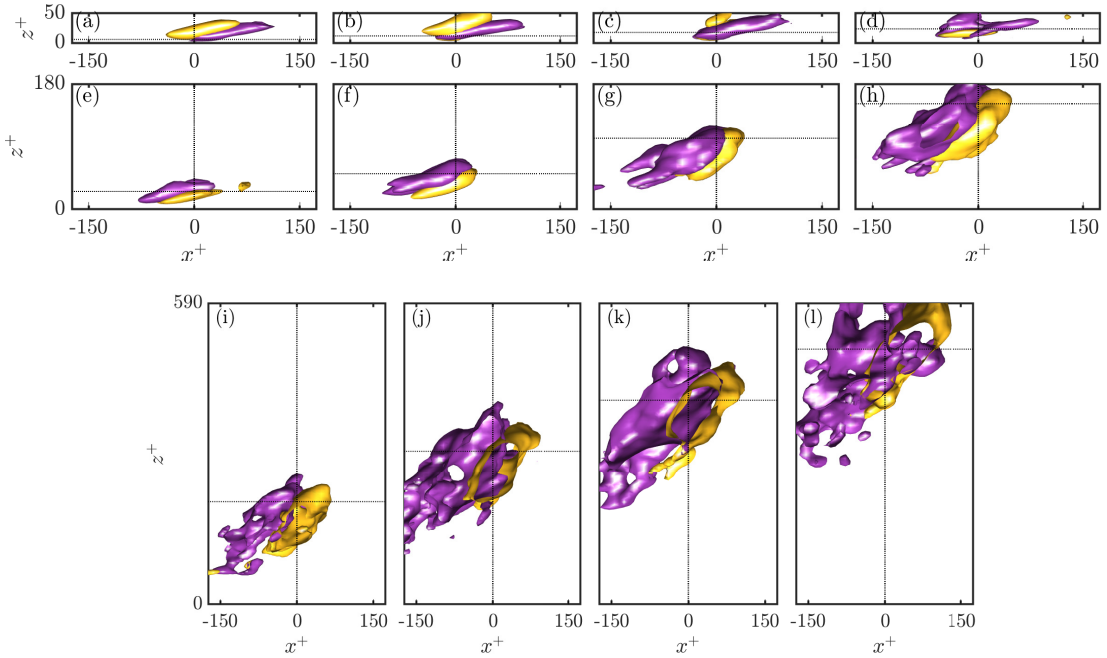

Figure 5.20: Swirling strength viewed in the xz plane at $Re_\tau = 590$. For each subfigure, the swirling strength in yellow is for $\tilde{N}|_+$ and the swirling strength in purple is for $\tilde{N}|_-$. Subfigures (a) to (l) correspond to the conditional events detected at the wall-normal heights from $z^+ = 5$ to 500 as listed in table 5.1.

We can see the relationship between turbulent convection and the detected vortical structures. For example, in figures 5.19(g) and 5.20(g), the detection points indicated by the intersection of the dashed lines are upstream of the yellow hairpin heads, indicating that positive turbulent convection is concentrated in the upstream region of the hairpin heads. The detection points are downstream of the purple hairpin heads, indicating that negative turbulent convection is concentrated in the downstream region of the hairpin heads. After we have analysed the vortical structures detected at other wall-normal

heights, we can sketch the relationship between turbulent convection and coherent structures as shown in figure 5.21. At $z^+ < 20$ (figure 5.21(a)), positive turbulent convection is concentrated below the quasi-streamwise vortices and negative turbulent convection is concentrated around the same height as the quasi-streamwise vortices. The region of negative turbulent convection is upstream of the region of positive turbulent convection in the streamwise direction. At $z^+ > 20$ (figure 5.21(b)), positive turbulent convection is concentrated upstream of hairpin heads and negative turbulent convection is concentrated downstream of hairpin heads. Hairpin heads at different wall-normal heights are found in this study (figures 5.19 and 5.20).

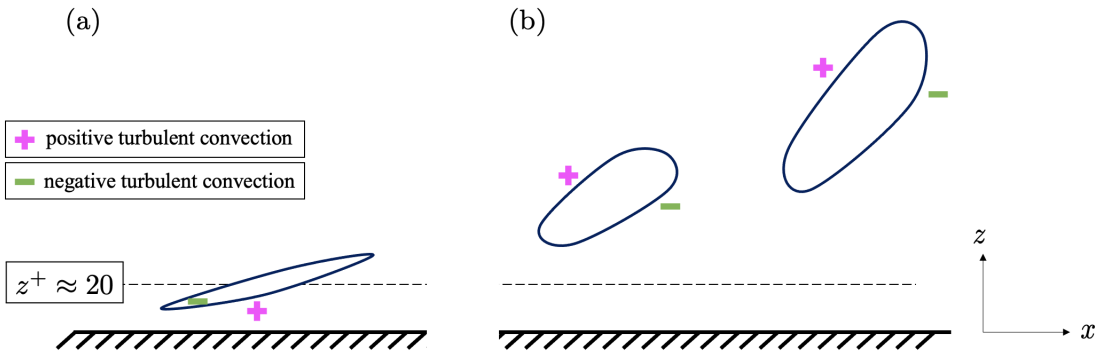

Figure 5.21: The relationship between turbulent convection (both positive and negative) and coherent structures. (a) Turbulent convection events at $z^+ < 20$ where quasi-streamwise vortices are detected; (b) turbulent convection events at $z^+ > 20$ where hairpin vortex heads are detected.

In this study, we do not detect the structures resembling a hairpin vortex diagram which is composed of a head, a pair of necks and a pair of legs. Nevertheless, the relationship illustrated in figure 5.21 is related to the relationship between interscale energy transfer in the spirit of LES and hairpin vortex packets (Piomelli et al., 1996; Carper & Porté-Agel, 2004; Natrajan & Christensen, 2006). For example, Natrajan & Christensen (2006) found that a forward cascade is concentrated around the upper trailing edge of a hairpin vortex and an inverse cascade is concentrated around the lower leading edge of the same hairpin vortex.

5.4 Conclusions

In this chapter, we explore the coherent structures related to the turbulent convection term in the turbulent kinetic energy equation using conditional averaging techniques at $Re_\tau = 180$ and 590. We pick out events with large absolute values of turbulent convection and categorise them according to the sign of the turbulent convection. Positive turbu-

lent convection events $\tilde{N}|_+$ are characterised by significant energy gain due to turbulent convection and negative turbulent convection events $\tilde{N}|_-$ are characterised by significant energy loss due to turbulent convection.

Both positive and negative turbulent convection events are associated with specific turbulent convection patterns: at $z^+ < 20$, a negative turbulent convection area is upstream of a positive turbulent convection area in the streamwise direction; at $z^+ > 20$, a positive turbulent convection area is upstream of a negative turbulent convection area in the streamwise direction.

Both positive and negative turbulent convection events are associated with the same vortical structures. In terms of the differences, positive and negative turbulent convection events are concentrated at different locations around quasi-streamwise vortices and hairpin vortex heads. Positive turbulent convection occurs below quasi-streamwise vortices and in the upstream region of hairpin heads; negative turbulent convection occurs at the same height as quasi-streamwise vortices and in the downstream region of hairpin heads.

Chapter 6

Nonlinear estimation in channel flows

We design a nonlinear estimator for channel flows at $Re_\tau = 180$ and 590. The nonlinear estimator uses a linear estimator structure based on the linearised Navier-Stokes equations and explicitly calculates the nonlinear forcing from the estimated velocities in physical space. The goal is to use the velocities at one wall-normal height to estimate the velocities at other wall-normal heights. The estimation performance is compared among the nonlinear estimator, the linear estimator and the linear estimator augmented with eddy viscosity. At $Re_\tau = 180$, the nonlinear estimator and the linear estimator augmented with eddy viscosity outperform the linear estimator in terms of estimating the velocity magnitudes, structures and energy transfer (production and dissipation) across the channel height. The limitations of using measurement data at one wall-normal height are discussed. At $Re_\tau = 590$, the nonlinear estimator does not work well with only one measurement plane, whereas the linear estimator augmented with eddy viscosity performs well. The performance of the nonlinear estimator at $Re_\tau = 590$ is significantly enhanced by providing multiple measurement planes.

6.1 Introduction

Flow estimation has a wide range of applications ranging from large-scale weather prediction (Richardson, 1922; Le Dimet & Talagrand, 1986) to micro-scale flow estimation in electronic chips (Fan et al., 2015). However, practical limitations hinder us from accessing the full information of a fluid flow. For example, particle image velocimetry

(PIV) only measures a limited number of 2-D planes in a 3-D flow field and few materials could be used to measure the temperature inside a combustion chamber. The goal of flow estimation is to predict unknown quantities using limited flow measurement data. To achieve this, one way is to build mathematical models based on the flow physics (Rowley & Dawson, 2017; Taira et al., 2017, 2020). As the Navier-Stokes equations governing the flow dynamics are nonlinear and pose significant challenges, a simple way is to use the Navier-Stokes equations linearised around the mean velocity field.

The linearised Navier-Stokes equations can explain important physical mechanisms in wall-bounded flows, such as transient energy growth and the lift-up mechanism caused by non-normality in the presence of the mean shear (Ellingsen & Palm, 1975; Landahl, 1980; Trefethen et al., 1993; Schmid & Henningson, 2001). The linearised Navier-Stokes equations have been used in both laminar flows (Gustavsson, 1991; Butler & Farrell, 1992; Reddy & Henningson, 1993; Jovanović & Bamieh, 2005) and fully developed turbulent flows (Del Alamo & Jimenez, 2006; Pujals et al., 2009; Hwang & Cossu, 2010a,b) for the fluctuation velocities following a Reynolds decomposition. More recently, a novel approach proposed by McKeon & Sharma (2010) does not assume small fluctuations to the linearised Navier-Stokes equations around the mean velocity profile in fully developed turbulent flows. From an input-output perspective, the nonlinear forcing is treated as an unknown input, and the leading output mode of the velocity field represents the structure that is most amplified by linear mechanisms. This linear method can extract low-rank features in fully developed turbulent flows and sheds light on reduced-order modelling (McKeon & Sharma, 2010; Sharma & McKeon, 2013; McKeon, 2017).

However, resolvent analysis implicitly assumes that the nonlinear forcing is white in space and time and does not model the 'shape' of the nonlinear forcing. This can cause problems in situations where the nonlinear forcing has a significant projection onto the suboptimal input modes (Symon et al., 2018; Rosenberg et al., 2019; Morra et al., 2021). It has been shown that the nonlinear forcing is structured (Chevalier et al., 2006; Morra et al., 2021; Nogueira et al., 2021) and embedding the knowledge of the nonlinear forcing into the linear resolvent model outperforms the pure linear resolvent model in terms of recovering flow statistics and structures (Zare et al., 2017; Illingworth et al., 2018; Madhusudanan et al., 2019; Towne et al., 2020; Amaral et al., 2021; Holford et al., 2023; Fan et al., 2024; Holford et al., 2024).

This chapter investigates channel flow estimation at $Re_\tau = 180$ and 590. Similar to Illingworth et al. (2018), we use a resolvent-based linear estimator with consideration of the nonlinear forcing. The goal is to use the velocity data coming from direct numeric simulations (DNS) at one wall-normal height to estimate the velocity field at other wall-normal heights. The key feature in this study is that we explicitly calculate the nonlinear

forcing from the estimated velocities in physical space, resembling closing the loop of the resolvent-based linear estimator. Estimation in this study is implemented using a filtering technique (Kalman filter) which involves predicting the flow states by marching the governing equations with measurement data (Hœpffner et al., 2005; Chevalier et al., 2006; Colburn et al., 2011; Illingworth et al., 2018; Oehler et al., 2018; Gong, 2021). We compare the estimation performance between the nonlinear estimator designed in this study, the linear estimator and the linear estimator augmented with an eddy viscosity (Illingworth et al., 2018). In addition, we discuss the limitations of using velocity measurement data at only one wall-normal height. Having looked at estimation using only one measurement plane, we proceed to explore estimation using multiple measurement planes distributed in the wall-normal direction at $Re_\tau = 180$ and 590.

The nonlinear estimator in this study shares some similarities with large-eddy simulation (LES). The main similarity is that both the nonlinear estimator and LES only resolve the large scales (the reasons for the nonlinear estimator only considering the large scales are described in §6.2.2). The main difference is that the nonlinear estimator requires continuous external information from measurement data, whereas LES is an autonomous simulation that does not need external input apart from the initial condition.

This chapter is organised as follows. In §6.2, we revisit the linear estimator (Illingworth et al., 2018) and introduce the nonlinear estimator. Then, we proceed to the discussion of the results. We compare the nonlinear estimator, linear estimator and linear estimator augmented with eddy viscosity at $Re_\tau = 180$ and 590. Specifically, §6.3 discusses the estimation with one measurement plane, and §6.4 discusses the estimation with multiple measurement planes. Conclusions are drawn in §6.5.

6.2 Model descriptions

6.2.1 Linear model

The equations of the fluctuation velocities u_i are obtained from the substitution of a Reynolds decomposition into the Navier-Stokes equations and subtracting the mean equations:

$$\frac{\partial u_i}{\partial t} = -u_j \frac{\partial U_i}{\partial x_j} - U_j \frac{\partial u_i}{\partial x_j} - \frac{\partial p}{\partial x_i} + \frac{1}{Re_\tau} \frac{\partial^2 u_i}{\partial x_j \partial x_j} + f_i \tag{6.1a}$$

$$\frac{\partial u_i}{\partial x_i} = 0 \tag{6.1b}$$

where $U_i = (U(z), 0, 0)$ represents the mean velocity profile, $f_i = -u_j \frac{\partial u_i}{\partial x_j} + \overline{u_j \frac{\partial u_i}{\partial x_j}}$ represents the nonlinear forcing term including the Reynolds stress.

Equations (6.1) can be rearranged to arrive at the Orr-Sommerfeld & Squire equations of the wall-normal velocity w and wall-normal vorticity $\eta = \frac{\partial u}{\partial y} - \frac{\partial v}{\partial x}$. Due to the homogeneity in the streamwise and spanwise directions for channel flows, 2-D Fourier transform in these two directions can be applied with the Chebyshev distribution in the wall-normal direction to arrive at the state-space model at streamwise wavenumber k_x and spanwise wavenumber k_y (Schmid & Henningson, 2001):

$$\frac{\mathrm{d}}{\mathrm{d}t}\hat{\boldsymbol{x}}(t) = \mathscr{A}\hat{\boldsymbol{x}}(t) + \mathscr{B}\hat{\boldsymbol{f}}(t) \tag{6.2a}$$

$$\hat{\boldsymbol{y}} = \mathscr{C}\hat{\boldsymbol{x}}(t) \tag{6.2b}$$

where $\hat{\boldsymbol{x}} = [\hat{w} \;\; \hat{\eta}]^T$; $\hat{\boldsymbol{y}} = [\hat{u} \;\; \hat{v} \;\; \hat{w}]^T$ and $\hat{\boldsymbol{f}} = [\hat{f}_x \;\; \hat{f}_y \;\; \hat{f}_z]^T$. In this chapter, variables with $\hat{}$ indicate that those variables are in Fourier space. The detailed information of (6.2) is described in Appendix B.1.

6.2.2 Linear estimator

The goal is to use limited velocity measurement data to estimate the velocities at other locations. To achieve this, we use a Kalman filter based on the linear model (6.2). Consider a linear state-space model with zero input:

$$\frac{\mathrm{d}}{\mathrm{d}t}\hat{\boldsymbol{x}}(t) = \mathscr{A}\hat{\boldsymbol{x}}(t) + \mathscr{B}\hat{\boldsymbol{d}}(t) \tag{6.3a}$$

$$\hat{\boldsymbol{y}}_{mea}(t) = \mathscr{C}_{mea}\hat{\boldsymbol{x}}(t) + \hat{\boldsymbol{n}}(t) \tag{6.3b}$$

where $\hat{\boldsymbol{d}}$ is the system process noise vector and $\hat{\boldsymbol{n}}$ is the measurement noise vector. There are two main differences between (6.2) and (6.3). First, $\hat{\boldsymbol{d}}(t)$ in (6.3) is Gaussian white noise whereas $\hat{\boldsymbol{f}}(t)$ in (6.2) is the nonlinear forcing. To comply with the Kalman filter setting, we treat the nonlinear forcing as white noise. Second, the output $\hat{\boldsymbol{y}}_{mea}(t)$ in (6.3) only consists of a small portion of the full state $\hat{\boldsymbol{x}}(t)$, corresponding to the estimation problem that we have the velocity measurement at only one wall-normal height among the full velocity states across the channel height. The extraction of the measurement data at a specific wall-normal height is implemented using Barycentric Lagrange interpolation (Berrut & Trefethen, 2004). If the state-space model (6.3) has n states, p disturbances and q measurements, then the corresponding matrices have the following dimensions: $\mathscr{A} \in \mathbb{C}^{n\times n}$; $\mathscr{B} \in \mathbb{C}^{n\times p}$; and $\mathscr{C}_{mea} \in \mathbb{C}^{q\times n}$.

The goal is to estimate the full state $\hat{\boldsymbol{x}}(t)$ according to the dynamics of the system

(6.3a) and the measurement data (6.3b). The equation of the estimated full state $\hat{\boldsymbol{x}}_{est}(t)$ is (Seron et al., 2012):

$$\frac{\mathrm{d}}{\mathrm{d}t}\hat{\boldsymbol{x}}_{est} = \mathscr{A}\hat{\boldsymbol{x}}_{est}(t) + \mathscr{L}[\hat{\boldsymbol{y}}_{mea}(t) - \mathscr{C}_{mea}\hat{\boldsymbol{x}}_{est}(t)] \tag{6.4}$$

where $\mathscr{L}$ is the Kalman filter gain obtained by solving a Riccati equation to minimise the difference between the estimated state and true state $\|\hat{\boldsymbol{x}}_{est}(t) - \hat{\boldsymbol{x}}(t)\|^2$. Measurement data either from experiments or DNS is supplied at a measurement sampling time ΔT_m. Therefore, the model in the continuous time domain (6.3) is transformed into the discrete time domain. The diagram for the linear estimator is shown in figure 6.1 and the details are described in Appendix B.2.

Figure 6.1: The diagram of the linear estimator. 'KF' represents Kalman filter which is implemented at measurement sampling time ΔT_m. The input is measurement $\hat{y}_{mea}$ and the output is estimation $\hat{x}_{est}$, according to (6.4).

The Kalman filter described above is implemented at a single wavenumber pair (k_x, k_y) in Fourier space. The same estimator could be applied at other wavenumber pairs. We choose to consider the energetically dominant wavenumber pairs corresponding to the large scales (Illingworth et al., 2018; Amaral et al., 2021; Arun et al., 2023). There are three reasons. First, large scales contain the most kinetic energy and further increasing the wavenumber pairs does not change the estimation results significantly. Second, considering a small number of wavenumber pairs reduces computational cost and storage, achieving the goal of reduced-order modelling. Third, we do not expect to obtain accurate estimation of small structures because they are not coherent across the channel height (Madhusudanan et al., 2019).

6.2.3 Nonlinear estimator

The idea of designing the nonlinear estimator is to explicitly calculate the nonlinear forcing from the estimated velocities, closing the loop of the resolvent-based linear estimator. We consider a linear state-space model with input $\hat{\boldsymbol{f}}(t)$.

$$\frac{\mathrm{d}}{\mathrm{d}t}\hat{\boldsymbol{x}}(t) = \mathscr{A}\hat{\boldsymbol{x}}(t) + \mathscr{B}\hat{\boldsymbol{d}}(t) + \mathscr{B}\hat{\boldsymbol{f}}(t) \tag{6.5a}$$

$$\hat{\boldsymbol{y}}_{mea}(t) = \mathscr{C}_{mea}\hat{\boldsymbol{x}}(t) + \hat{\boldsymbol{n}}(t) \tag{6.5b}$$

Different from the linear state-space model with zero input (6.3) in which we assume the disturbance $\hat{\boldsymbol{d}}(t)$ as unstructured nonlinear forcing, the input term $\hat{\boldsymbol{f}}(t)$ is the nonlinear forcing in the linear model (6.5). The equation of the estimated state $\hat{\boldsymbol{x}}_{est}$ is then (Seron et al., 2012):

$$\frac{\mathrm{d}}{\mathrm{d}t}\hat{\boldsymbol{x}}_{est} = \mathscr{A}\hat{\boldsymbol{x}}_{est}(t) + \mathscr{B}\hat{\boldsymbol{f}}(t) + \mathscr{L}[\hat{\boldsymbol{y}}_{mea}(t) - \mathscr{C}_{mea}\hat{\boldsymbol{x}}_{est}(t)] \tag{6.6}$$

We calculate the nonlinear forcing using the nonlinear dynamics $f_i = -u_j\frac{\partial u_i}{\partial x_j}$ in physical space, where the velocities u_i are obtained from the estimated velocities $\hat{x}_{est}$ in (6.6) using the inverse Fourier transform. With this idea, we come to the structure of the nonlinear estimator as illustrated in figure 6.2. Further details are given in Appendix B.3.

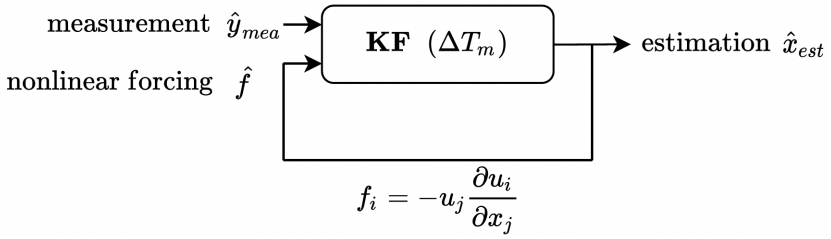

Figure 6.2: Block diagram of the nonlinear estimator. 'KF' represents Kalman filter which is implemented at measurement sampling time ΔT_m. The two inputs are the measurement $\hat{y}_{mea}$ and the nonlinear forcing $\hat{f}$; the output is the estimation $\hat{x}_{est}$, according to (6.6). The nonlinear forcing is obtained from the estimated velocities using $f_i = -u_j\frac{\partial u_i}{\partial x_j}$.

We tried the nonlinear estimator in figure 6.2 with measurement data provided every measurement sampling time step ΔT_m, as illustrated in figure 6.3(a). The results were all divergent even when measurement data at every wall-normal height were provided. Thus, the divergent problem is not primarily related to insufficient measurement data. So, we switched the attention to another variable crucial to the nonlinear estimation: the measurement sampling time ΔT_m which is also the marching time step for the Kalman filter.

One straightforward solution is to use high time-resolution DNS data with a much smaller measurement sampling time. However, at that time we did not have access to high time-resolution DNS data so the measurement sampling time ΔT_m had to be fixed. This also could be the case in an experiment (for example PIV) or even in a DNS that we could not obtain velocity measurements with high time-resolution due to technical constraints. Nevertheless, we could still decrease the marching time step for the Kalman filter state prediction from ΔT_m to ΔT_s, where $\Delta T_s \ll \Delta T_m$. In this case, at time t, we have the estimated velocities $\hat{x}_{est}|_t$; at time $t + \Delta T_m$ (because we do not change the measurement sampling time ΔT_m), the Kalman filter needs to give estimation according to the measurement at time $t + \Delta T_m$ and the previous nonlinear forcing at time $t + \Delta T_m - \Delta T_s$ with

the marching time step of ΔT_s. One question arises: how do we go from the estimated velocities $\hat{x}_{est}|_t$ at time t to the nonlinear forcing $\hat{f}|_{t+\Delta T_m-\Delta T_s}$ at time $t+\Delta T_m-\Delta T_s$?

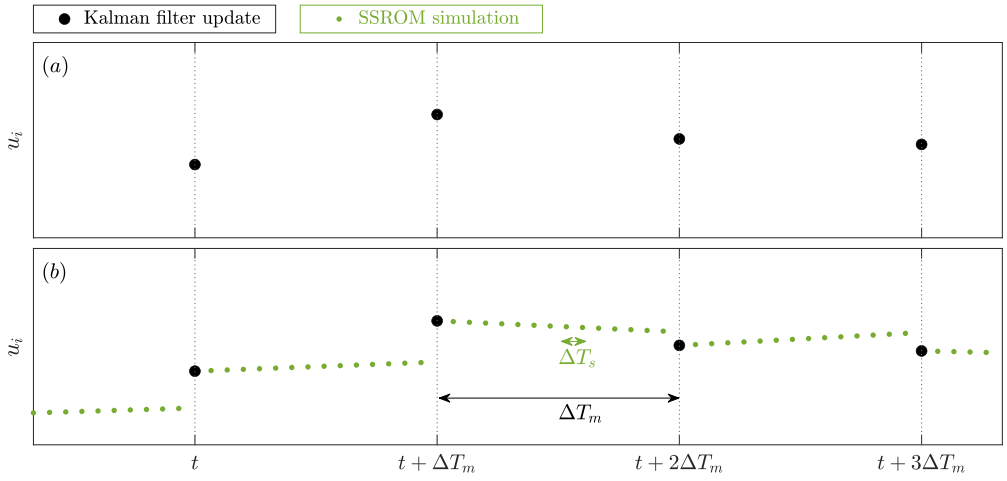

Figure 6.3: An illustration of the estimation process: (a) the nonlinear estimator in figure 6.2; (b) the revised nonlinear estimator in figure 6.4.

In light of the method of introducing the nonlinear dynamics back to the estimator as shown in figure 6.2, we combine the Orr-Sommerfeld & Squire state-space model (6.2) with this nonlinear dynamics feedback loop. We choose a time step ΔT_s which is much smaller than ΔT_m to discretise the state-space model 6.2. First, we use the nonlinear forcing at time t as input to drive the state-space model (6.2) to obtain the velocities at time $t+\Delta T_s$. Second, we use the nonlinear dynamics in physical space $f_i = -u_j \frac{\partial u_i}{\partial x_j}$ to calculate the nonlinear forcing at time $t+\Delta T_s$. Third, the nonlinear forcing at time $t+\Delta T_s$ serves as input to drive the state-space model (6.2) again to iterate the process until time $t+\Delta T_m-\Delta T_s$. These three steps resemble an autonomous simulation. We embed this autonomous simulation as shown by the green dots in figure 6.3(b) between two consecutive Kalman filter updates determined by the measurement sampling time ΔT_m. To align with the estimation process, we consider the same wavenumber pairs used in the Kalman filter estimation for this autonomous simulation. Since we only consider large scales in this simulation, we name this simulation as state-space reduced-order model (SSROM) simulation. Further details about the SSROM simulation are given in Appendix B.4.

The block diagram for the revised nonlinear estimator embedded with SSROM simulation is shown in figure 6.4. Further details are given in Appendix B.5. From the nonlinear estimator illustrated in figure 6.2 to the revised nonlinear estimator illustrated in figure 6.4, the stability of the estimator has greatly improved. Comparing the nonlinear estimators in figures 6.2 and 6.4, the main similarity is that they both explicitly calculate

the nonlinear forcing rather than treat it as an unknown forcing and use the structured nonlinear forcing to serve as input to the Kalman filters. The main difference is the marching time step for the state prediction. The nonlinear estimator in figure 6.2 marches forward in time at the measurement sampling time ΔT_m as shown in figure 6.3(a), which easily triggers divergence if ΔT_m is too big. The revised nonlinear estimator in figure 6.4 marches forward in time at a much smaller time step ΔT_s achieved by the inclusion of an autonomous simulation from the SSROM between two consecutive Kalman filter updates, as shown in figure 6.3(b).

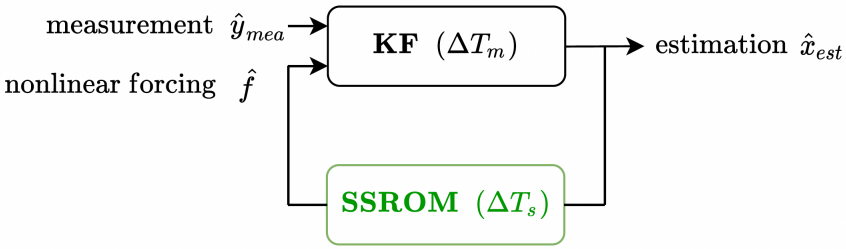

Figure 6.4: Block diagram of the revised nonlinear estimator. 'KF' represents Kalman filter which is used at every measurement sampling time ΔT_m with a marching time step of ΔT_s. The two inputs are measurement $\hat{y}_{mea}$ and nonlinear forcing $\hat{f}$; the output is estimation $\hat{x}_{est}$, according to (6.6). Between two consecutive Kalman filter updates, SSROM simulation running at ΔT_s $(\Delta T_s \ll \Delta T_m)$ is used to obtain the nonlinear forcing $\hat{f}$ for the next Kalman filter update.

6.3 Estimation using one measurement plane

Now we discuss the estimation results for the different estimators introduced previously. §6.3.1 and §6.3.2 discuss the estimation at $Re_\tau = 180$. §6.3.3 examines the effect of changing the location of the measurement plane at $Re_\tau = 180$. §6.3.4 discusses the estimation at $Re_\tau = 590$. To simplify the discussion, 'NE' refers to the nonlinear estimator in figure 6.4, 'LE' refers to the linear estimator in figure 6.1 and 'LEe' refers to the linear estimator augmented with eddy viscosity to be introduced in §6.3.2.

6.3.1 Comparison between NE and LE at $Re_\tau = 180$

We apply the nonlinear estimator (NE) and the linear estimator (LE) at $Re_\tau = 180$ and discuss the result comparison between these two estimators. The goal is to use the velocity data at a single wall-normal height to estimate the velocities at other wall-normal heights. Since the estimation is implemented in a channel, the measurement velocity at one wall-normal height is mirrored into the other half of the channel. To ensure a fair comparison, the same estimation setting is applied to NE and LE. The wavenumbers considered at

$Re_\tau = 180$ are $|k_x| \leq 10$ and $|k_y| \leq 20$, corresponding to structures with $\lambda_x^+ \geq 113$ and $\lambda_y^+ \geq 57$. In the wall-normal direction we use 129 Chebyshev points and convergence has been checked by doubling the number of Chebyshev points. The measurement data (velocities) come from $z^+ = 15$, where the turbulent kinetic energy reaches its maximum in the wall-normal direction. The measurement data comes from DNS and the temporal resolution is $\Delta T_m = 0.02$ which is small enough to resolve the frequency of the smallest scale according to Taylor's hypothesis. The SSROM simulation time step is set to be $\Delta T_s = 0.0005$. The estimation starts with zero initial condition. We present the estimation results starting from $t = 2(t^+ = 360)$ to $t = 3(t^+ = 540)$ to minimise the initial transient.

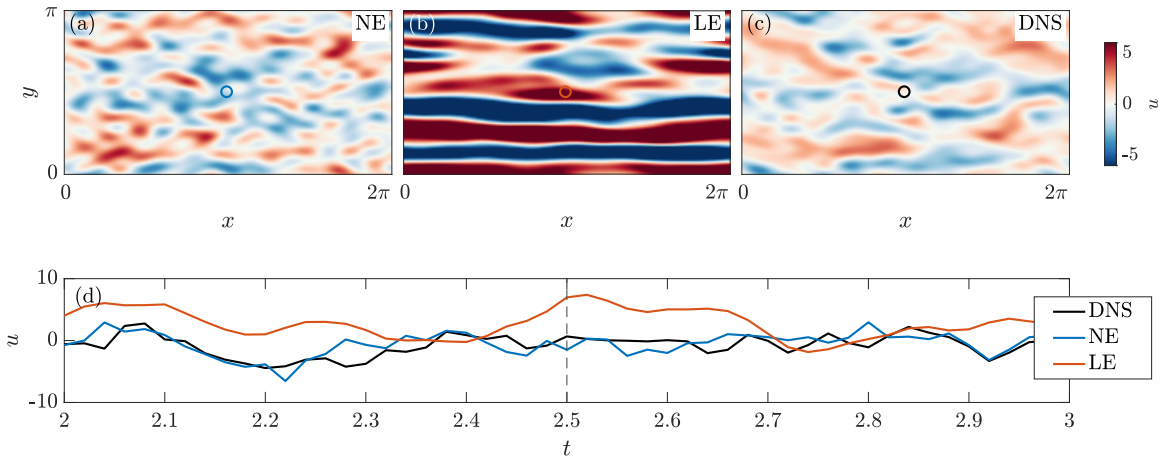

Figure 6.5: Streamwise velocity u for (a) NE, (b) LE and (c) DNS data in the xy plane at $z^+ = 50$. The measurement data comes from $z^+ = 15$. The circles in the middle of (a,b,c) denote the locations of the streamwise velocity plotted in (d). (d) Streamwise velocity varying with time at the centre of the xy plane at $z^+ = 50$. The vertical dashed line denotes the time instant for (a,b,c).

Figure 6.5 shows the estimated velocity field at $z^+ = 50$. The DNS velocity field in figure 6.5(c) only contains the large scales considered in the estimation. The estimated velocities from NE (figure 6.5(a)) are around the similar magnitudes of the DNS data (figure 6.5(c)). The estimated velocities from LE (figure 6.5(b)) are much overpredicted compared with the DNS data (figure 6.5(c)), which were also observed in previous studies (Illingworth et al., 2018; Amaral et al., 2021). The features related to the magnitudes can also be seen in figure 6.5(d). As for the structures, NE gives some correct large-scale structures at the corresponding locations in the DNS but it also generates small-scale structures that are non-existent in the DNS; LE only gives the large-scale structures.

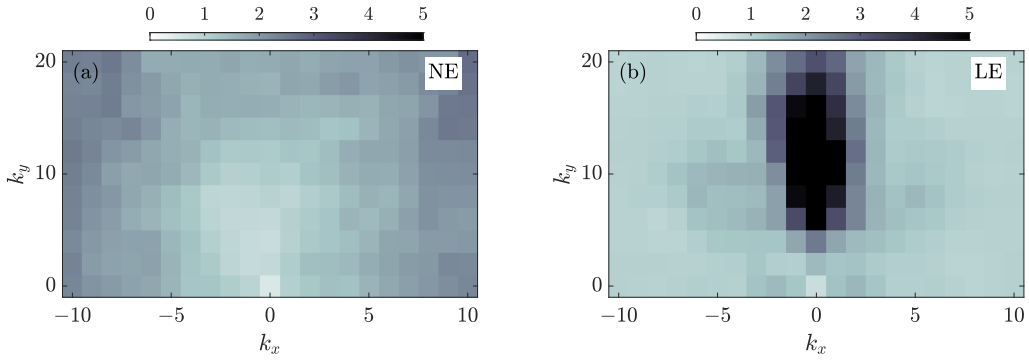

Figure 6.6: Error in Fourier space (6.7) for (a) NE and (b) LE at $z^+ = 50$.

Since the estimation is conducted in Fourier space, we evaluate the estimation performance at each wavenumber pair by defining the error (Illingworth et al., 2018):

$$\hat{\varepsilon}(k_x, k_y) = \frac{\sqrt{\int |\hat{u}_{est} - \hat{u}_{DNS}|^2 \mathrm{d}t}}{\sqrt{\int |\hat{u}_{DNS}|^2 \mathrm{d}t}} \tag{6.7}$$

Figure 6.6 shows the estimation error in Fourier space for NE and LE. In figure 6.6(a), we see that NE performs better for large streamwise scales with small k_x than small streamwise scales with large k_x. This corresponds to the observation of incorrect small scales from NE (6.5(a)). In figure 6.6(b), we see that LE has substantial errors for the streamwise-elongated scales ($k_x = 0$). This corresponds to the observation of large magnitudes of the large streamwise scales from LE (6.5(b)), which is also noted in the previous study that the error from the linear estimator is large for streamwise-elongated scales (Illingworth et al., 2018). Comparing figures 6.6(a,b), we see that NE performs better than LE at $z^+ = 50$.

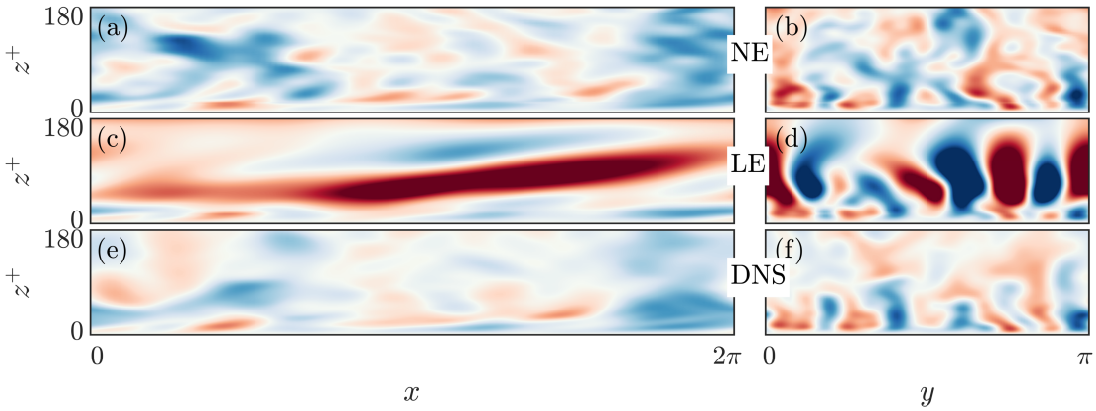

Figure 6.7: (a,c,e) Streamwise velocity field in the xz plane at $y = \frac{\pi}{2}$. (b,d,f) Streamwise velocity field in the yz plane at $x = \pi$. (a,b) NE; (c,d) LE and (e,f) the DNS data. The limits of the colour map are the same as that in figure 6.7.

Having looked at the estimated velocity field at $z^+ = 50$, we now look at the velocity

field across the wall-normal height at a particular instant in time, as shown in figure 6.7. We see that NE gives the correct shapes of the near-wall structures since the measurement plane is at $z^+ = 15$ and the shapes of the estimated velocity field far from the wall do not match the DNS (figures 6.7(a,b,e,f)). LE overpredicts the velocity magnitudes as observed from the colour scale and the shapes of the estimated velocity field do not match the DNS (figures 6.7(c,d,e,f)).

We quantify the estimation performance across the wall-normal height by defining the error and correlation (Chevalier et al., 2006; Colburn et al., 2011):

$$\varepsilon(z) = \frac{\sqrt{\iiint (u_{est} - u_{DNS})^2 \, \mathrm{d}x \, \mathrm{d}y \, \mathrm{d}t}}{\sqrt{\iiint u_{DNS}^2 \, \mathrm{d}x \, \mathrm{d}y \, \mathrm{d}t}} \tag{6.8a}$$

$$\mathrm{corr}(z) = \frac{\iiint u_{est} u_{DNS} \, \mathrm{d}x \, \mathrm{d}y \, \mathrm{d}t}{\sqrt{\iiint u_{est}^2 \, \mathrm{d}x \, \mathrm{d}y \, \mathrm{d}t} \sqrt{\iiint u_{DNS}^2 \, \mathrm{d}x \, \mathrm{d}y \, \mathrm{d}t}} \tag{6.8b}$$

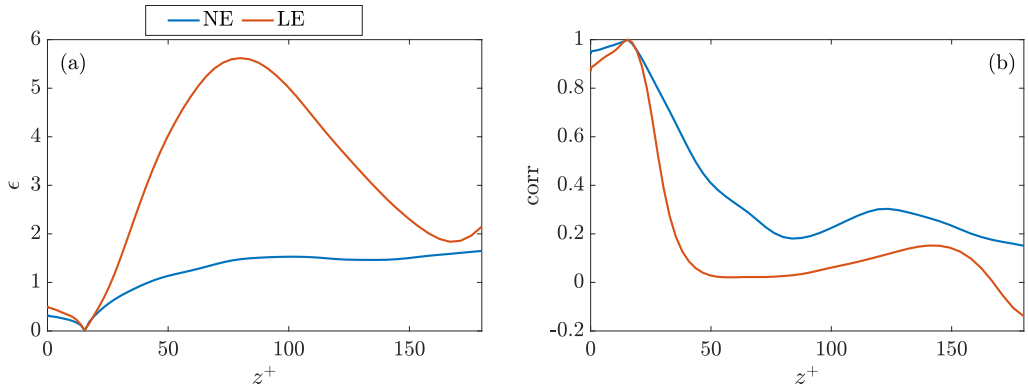

Figure 6.8: The error (6.8a) and correlation (6.8b) across the wall-normal height for NE and LE.

Equation (6.8a) quantifies the deviation between the estimated quantity and true quantity (DNS data). Correlation (6.8b) quantifies the phase alignment between the estimated quantity and true quantity. To fairly assess the estimation performance, it is crucial to consider both the error and correlation metrics together. Figure 6.8 shows the errors and correlations for NE and LE. An indicator of good estimation performance is a low error approaching zero and a high correlation approaching one. We see that both estimators perform the best at $z^+ = 15$ where the measurement data is provided, and the estimation performance deteriorates away from the measurement plane. This is expected and has been observed in previous studies (Chevalier et al., 2006; Colburn et al., 2011; Illingworth et al., 2018; Amaral et al., 2021; Arun et al., 2023; Ying et al., 2023). The big spike of the red line in figure 6.8(a) corresponds to the large magnitudes of the estimated

velocity from LE (figure 6.7(c,d)). As for NE, it has a lower error and higher correlation compared with LE, indicating that NE outperforms LE. As there is only one measurement plane provided to NE, the nonlinear forcing is only accurate near the measurement plane. Nevertheless, NE with partial knowledge of the nonlinear forcing outperforms LE.

For a statistically stationary flow, the Reynolds-Orr equation tells us that production P and dissipation D achieve a balance when considered over the entire domain Ω:

$$\int_\Omega \frac{\mathrm{D}}{\mathrm{D}t}\left(\frac{1}{2}u_i u_i\right)\mathrm{d}\Omega = \underbrace{\int_\Omega -u_i u_j \frac{\partial U_i}{\partial x_j}\mathrm{d}\Omega}_{\text{production}} + \underbrace{\int_\Omega -\frac{1}{Re}\frac{\partial u_i}{\partial x_j}\frac{\partial u_i}{\partial x_j}\mathrm{d}\Omega}_{\text{dissipation}} \tag{6.9}$$

The energy source for turbulence is production, and the energy sink for turbulence is dissipation. We can inspect the production and dissipation for NE and LE.

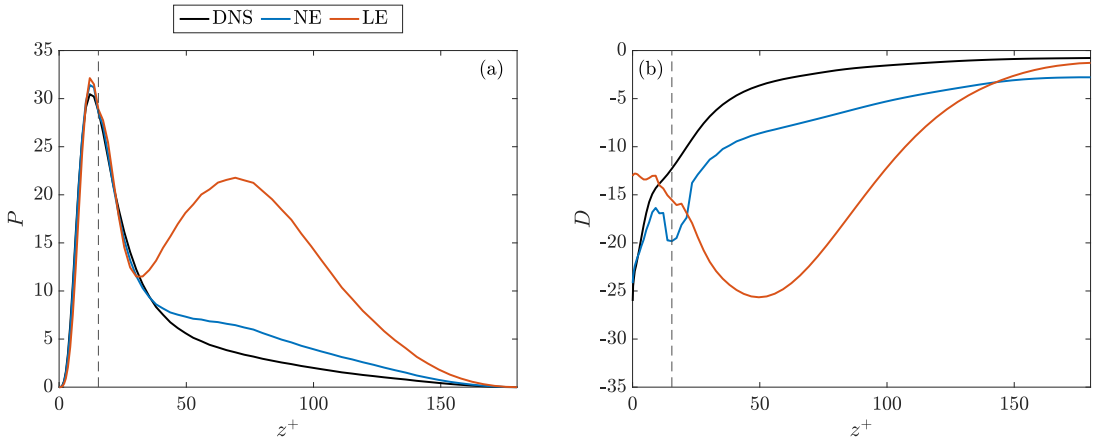

Figure 6.9: (a) Production P and (b) dissipation D across the wall-normal height. The black dashed line marks the measurement plane location $z^+ = 15$.

Figure 6.9 shows the production and dissipation as a function of wall-normal height. At each wall-normal height, the production and dissipation are averaged in the xy plane and in time. We see good agreement for production and dissipation between NE and DNS, except for the significant dissipation near the measurement plane (the blue plunge in figure 6.9(b)). It is suspected that the sudden change of dissipation from NE is caused by the sudden change of the velocities at the measurement plane since only one measurement plane data is provided. The sudden change of the velocities at the measurement plane will cause large velocity gradients $\frac{\partial u_i}{\partial x_j}$ contributing to the dissipation. For LE, substantial production and dissipation occur around $z^+ = 60$, corresponding to the large magnitudes of the estimated velocities (figures 6.7(c,d)). The strong estimated velocities are potentially due to the large 2-norm of the linearised Navier-Stokes operator compared to the operator embedded with eddy viscosity (to be introduced in the next section). LE gives accurate

dissipation at $z^+ > 120$ because both the estimated and true velocity fields are near zero in that region, resulting in a smaller error. LE gives fair production and dissipation at $z^+ < 30$ because LE provides a more precise estimated velocity field near the wall where the measurement is provided. We can further check the sum of production and dissipation across the wall-normal height, as shown in table 6.1. According to the normalisation of (6.1), the energy transfer is normalised by u_τ^3/h.

Table 6.1: Sum of energy transfer across the channel height of NE and LE.

	$\int P\,\mathrm{d}z$	$\int D\,\mathrm{d}z$	$\int (P+D)\,\mathrm{d}z$
DNS	5.31	-3.82	1.49
NE	6.36	-7.47	-1.11
LE	12.07	-12.99	-0.92

For the DNS, the sum of production and dissipation is greater than zero because only the large scales are considered in the estimation and the energy transfer is calculated for those large scales only. Since small scales are mainly responsible for dissipation, we expect that the dissipation calculated from the large scales will not counterbalance production. Compared with the DNS, we see that both NE and LE give excessive production and dissipation. The fact that the sum of production and dissipation for NE and LE is smaller than zero indicates that energy dissipates excessively in NE and LE. We do not expect that NE and LE conserve energy since the estimated velocities from the Kalman filters do not satisfy the Navier-Stokes equations because of the observation noise and the difference between estimation and observations (Wang & Zaki, 2021).

6.3.2 Comparison between NE and LEe at $Re_\tau = 180$

In the previous section, we see that NE outperforms LE, suggesting that closing the loop of the linear resolvent-based estimator in NE is helpful. As an alternative way of considering the nonlinear forcing, we can use LE augmented with eddy viscosity which considers the nonlinear effects of the small scales on the large scales (Del Alamo & Jimenez, 2006; Pujals et al., 2009; Illingworth et al., 2018; Madhusudanan et al., 2019; Towne et al., 2020; Amaral et al., 2021; Ying et al., 2023). We start by performing a triple decomposition of the instantaneous velocity field, $\mathscr{U}_i = U_i + u_i + u_i'$, where $\mathscr{U}$, U, u and u' represent the instantaneous velocity, time-averaged velocity, large-scale organised motion and small-scale fluctuation velocity, respectively. The nonlinear effect of the small scales on the large-scale organised motion is modelled by an eddy viscosity (Reynolds & Hussain,

1972). The equations of the large-scale organised motion are:

$$\frac{\partial u_i}{\partial t} = -u_j \frac{\partial U_i}{\partial x_j} - U_j \frac{\partial u_i}{\partial x_j} - \frac{\partial p}{\partial x_i} + \frac{1}{Re_\tau} \frac{\nu_T}{\nu} \frac{\partial^2 u_i}{\partial x_j \partial x_j} + f_i \tag{6.10a}$$

$$\frac{\partial u_i}{\partial x_i} = 0 \tag{6.10b}$$

with the eddy viscosity profile given by (Cess, 1958):

$$\nu_T(z) = \frac{\nu}{2}(1 + \frac{\kappa^2 Re_\tau^2}{9}(1-z^2)^2(1+2z^2)^2[1-\exp(\frac{(|z|)Re_\tau}{A})]^2)^{\frac{1}{2}} + \frac{\nu}{2}, \; z \in [-1,1] \tag{6.11}$$

where $\kappa = 0.426$ and $A = 25.4$, as they were the optimal values as a result of a least-square fit to experimental data at $Re_\tau = 2000$ (Del Alamo & Jimenez, 2006). The detailed expressions for the Orr-Sommerfeld and Squire operators are described in Appendix B.1.

Figure 6.10 compares the estimated velocity fields between NE and LEe (linear estimator augmented with eddy viscosity) at $z^+ = 50$. We see that the velocity magnitudes from LEe are similar to those from the DNS and LEe can give the correct large streamwise scales but small scales are missing (figure 6.12(b,c)). Figure 6.10(d) further indicates that NE and LEe can give velocity magnitudes comparable to the DNS.

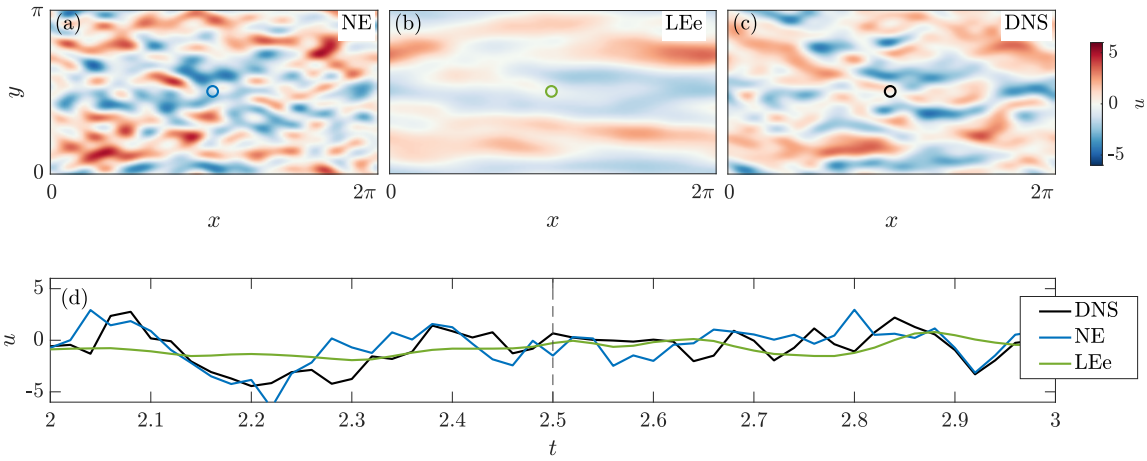

Figure 6.10: Streamwise velocity u from (a) NE, (b) LEe and (c) DNS data in the xy plane at $z^+ = 50$. The measurement data come from $z^+ = 15$. The circles in the middle of (a,b,c) denote the locations of the streamwise velocity plotted in (d). (d) Streamwise velocity varying with time at the centre of the xy plane at $z^+ = 50$. The vertical dashed line denotes the time instant for (a,b,c).

Figure 6.11 shows the error in Fourier space for NE and LEe at $z^+ = 50$. Both models perform well for the large streamwise scales with small k_x. From LE to LEe, we see an improvement in estimation performance at large streamwise scales, as noted in previous

work (Illingworth et al., 2018). This indicates that the eddy viscosity, which considers the nonlinear effect of the small scales on the large scales, improves estimation performance. However, both NE and LEe have relatively large errors at small streamwise scales with large k_x. The reasons are different: for NE, it gives the incorrect small scales because only partial knowledge of the nonlinear forcing around the measurement plane is accurate (figure 6.10(a)); for LEe, it gives zeros for the small scales because LEe identifies a lack of coherence of small scales (figure 6.10(b)) (Madhusudanan et al., 2019).

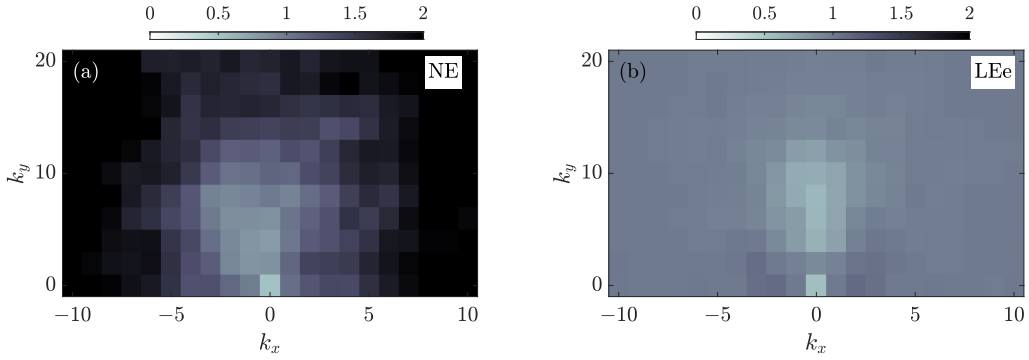

Figure 6.11: Error in Fourier space (6.7) for (a) NE and (b) LEe.

Figure 6.12 shows the velocity field across the wall-normal height for NE and LEe. Both models give the velocity magnitudes and structures comparable to the DNS near the measurement plane at $z^+ = 15$. Away from $z^+ = 15$, the estimated velocities from NE deviate from the DNS and the estimated velocities from LEe are near zero which is noted in Oehler et al. (2018).

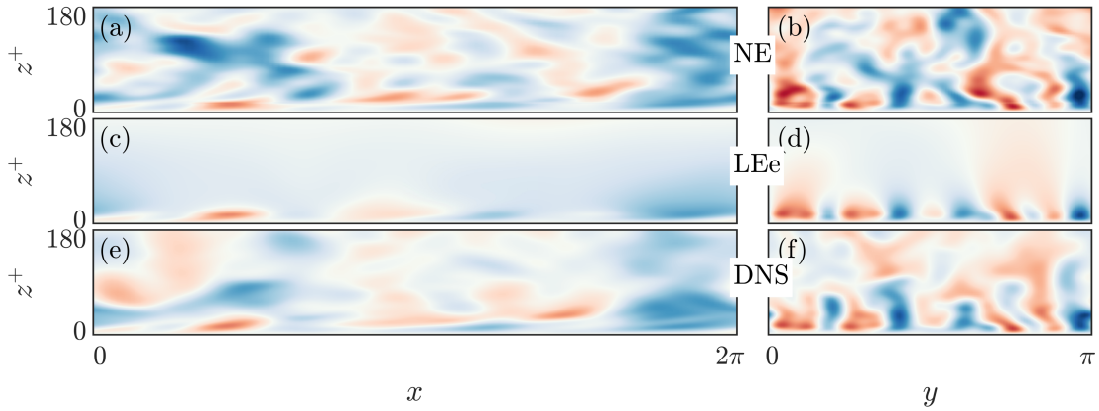

Figure 6.12: (a,c,e) Streamwise velocity field in the xz plane at $y = \frac{\pi}{2}$. (b,d,f) Streamwise velocity field in the yz plane at $x = \pi$. (a,b) NE; (c,d) LEe and (e,f) the DNS data. The limits of the colour map are the same as those in figure 6.7.

Figure 6.13 quantifies the estimation performance for NE and LEe across the wall-normal height. Both models perform best at $z^+ = 15$ where the measurement data is

provided, and the performance deteriorates away from the measurement plane. Looking at the error and correlation across the wall-normal direction, we see that LEe outperforms NE except in the near-wall region.

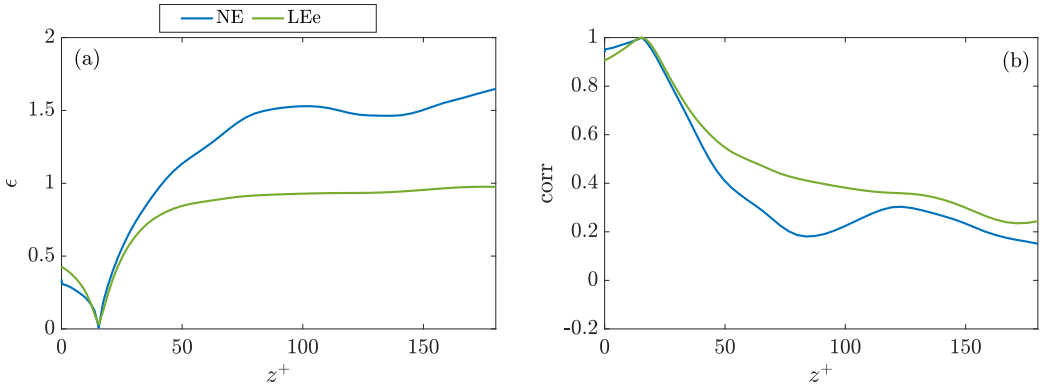

Figure 6.13: Error (6.8a) and correlation (6.8b) across the wall-normal height for NE and LEe.

We see that both NE and LEe outperform LE, indicating that considering the nonlinear forcing is important. The difference between NE and LE is the treatment of the nonlinear forcing in the state-space model (6.2). The nonlinear forcing in NE is structured since it is calculated from the estimated velocities, while the nonlinear forcing in LE is unstructured (McKeon & Sharma, 2010; Illingworth et al., 2018). It has been shown that the structured nonlinear forcing gives more accurate flow statistics even though only partial knowledge of the nonlinear forcing is available (Zare et al., 2017). The difference between LEe and LE is the Orr-Sommerfeld and Squire operators in the state-space model (6.2). Although LEe treats the nonlinear forcing as unstructured (Illingworth et al., 2018), the nonlinear effect of the small scales on the large scales is embedded in the state-space model (6.2) (Del Alamo & Jimenez, 2006; Pujals et al., 2009).

Here, we explain the strong velocity magnitudes obtained from LE rather than from LEe. The strong estimated velocities from LE are potentially due to the large 2-norm of the linearised Navier-Stokes operator compared to the operator embedded with eddy viscosity. The 2-norm of an operator (transfer function) $\mathscr{H}$ is defined as:

$$\|\mathscr{H}\|_2^2 = \sqrt{\frac{1}{2\pi}\int_{-\infty}^{\infty} \mathrm{Trace}[\mathscr{H}(\mathrm{i}\omega)^H \mathscr{H}(\mathrm{i}\omega)]\mathrm{d}\omega} \tag{6.12}$$

In this case, $\mathscr{H} = \mathscr{C}(\mathrm{i}\omega - \mathscr{A})^{-1}\mathscr{B}$. The 2-norms for both operators, without eddy viscosity and with eddy viscosity, are shown in figure 6.14. From the colour bar values, we can observe that the 2-norm of the operator used for LE (figure 6.14(a)) is significantly larger than that of the operator used for LEe (figure 6.14(b)).

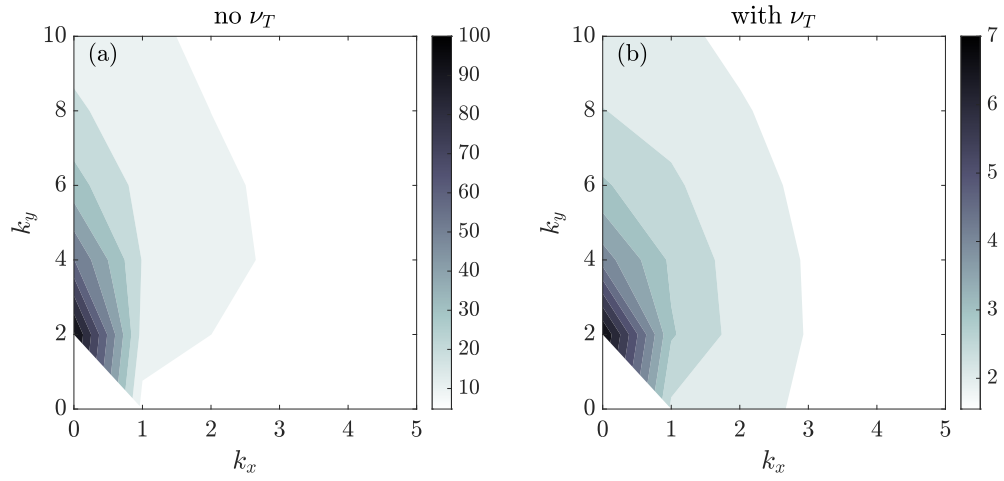

Figure 6.14: (a) The 2-norm of the linearised Navier-Stokes operators without eddy viscosity, (b) with eddy viscosity.

Figure 6.14 shows that the maximum amplification occurs at $k_x = 0$ and $k_y = 2$, corresponding to a streamwise-constant mode. We can further obtain the optimal velocity mode u_1 corresponding to this maximum amplification from the linearised Navier-Stokes operator without eddy viscosity. We achieve this by computing the solution $\mathscr{X}_\infty$ of the algebraic Lyapunov equation (Hwang & Cossu, 2010a):

$$\mathscr{A}\mathscr{X}_\infty + \mathscr{X}_\infty \mathscr{A}^H + \mathscr{B}\mathscr{B}^H = 0 \tag{6.13}$$

where H denotes conjugate transpose. Then, we calculate the output covariance matrix $\mathscr{C}\mathscr{X}_\infty \mathscr{C}^H$ to obtain the optimal velocity mode u_1.

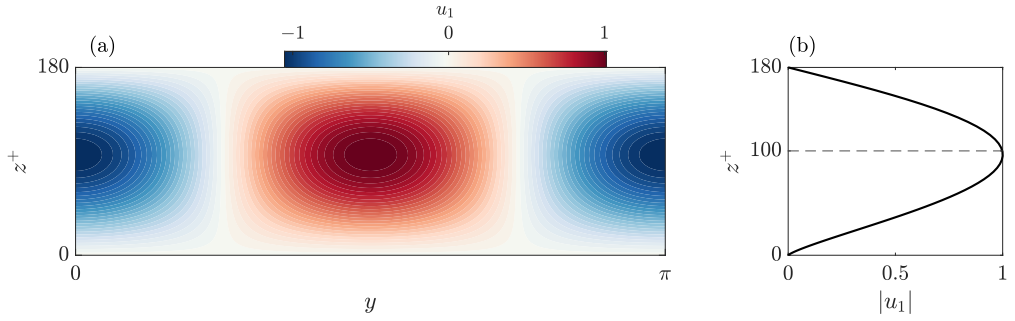

Figure 6.15: (a) The optimal output mode u_1 in the yz plane at $k_x = 0$ and $k_y = 2$. (b) The magnitude of u_1 at $y = \pi/2$ in (a). The values of u_1 has been normalised by its maximum absolute value.

Figure 6.15 reveals that the peak of the optimal streamwise velocity mode u_1 occurs at $z^+ \approx 100$, which could potentially be linked to the strong amplification phenomenon of the estimated velocity at $z^+ \approx 60$ in figure 6.7.

6.3.3 The effect of changing the measurement plane location on non-linear estimation at $Re_\tau = 180$

Previous studies show that using wall-shear stress as measurement only gives good velocity estimation up to the logarithmic region (Chevalier et al., 2006; Colburn et al., 2011; Suzuki & Hasegawa, 2017; Amaral et al., 2021) and is no better than using velocity as measurement (Oehler et al., 2018). Since we investigate using the velocity measurement only at $z^+ = 15$ in the previous sections, we would like to know the effect of changing the measurement plane location in the wall-normal direction, especially farther away from the wall. We change the measurement plane location from $z^+ = 15$ to $50, 75, 100, 125$ and 150, respectively. For each estimation case, we further evaluate the overall estimation performance by integrating the error and correlation in the wall-normal direction:

$$\varepsilon_{int} = \int_0^1 \varepsilon \, \mathrm{d}z, \quad \mathrm{corr}_{int} = \int_0^1 \mathrm{corr} \, \mathrm{d}z \tag{6.14a,b}$$

Figure 6.16 shows the estimation results with the measurement plane at different wall-normal heights. No matter where we put the measurement plane, the estimation performance deteriorates away from the measurement location and the overall performance does not change substantially as seen from the inset plots. When the measurement plane is placed farther away from the wall ($z^+ = 75, 100, 125, 150$), the error in the near-wall region increases significantly (figure 6.16(a)). The estimated statistics in the near-wall region could be improved by embedding the relationship between the inner layer and outer layer (Marusic et al., 2010; Baars et al., 2016).

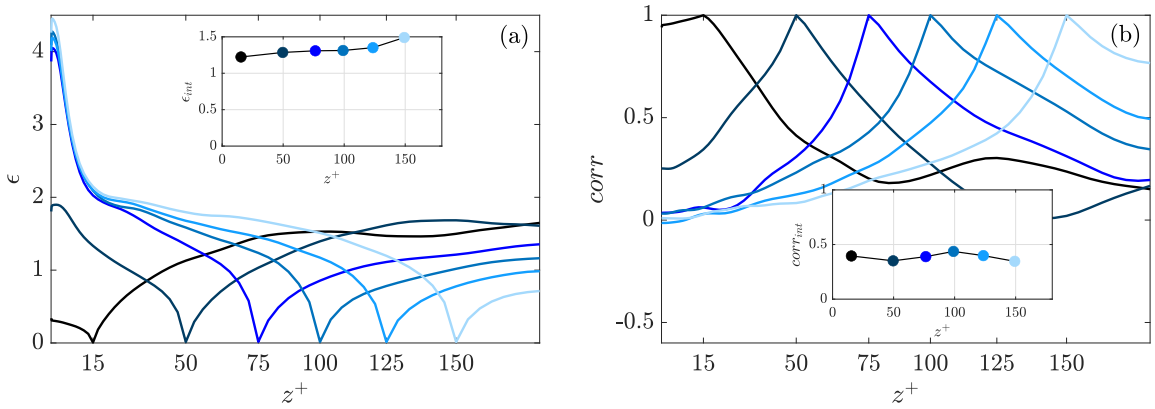

Figure 6.16: Error (6.8a) and correlation (6.8b) for NE when the measurement plane is at $z^+ = 15, 50, 75, 100, 125$ and 150, respectively. An estimation case with a measurement plane located farther away from the wall is indicated by a lighter blue colour. Inset plots show the integrated error and correlation (6.14).

6.3.4 Nonlinear estimation at $Re_\tau = 590$

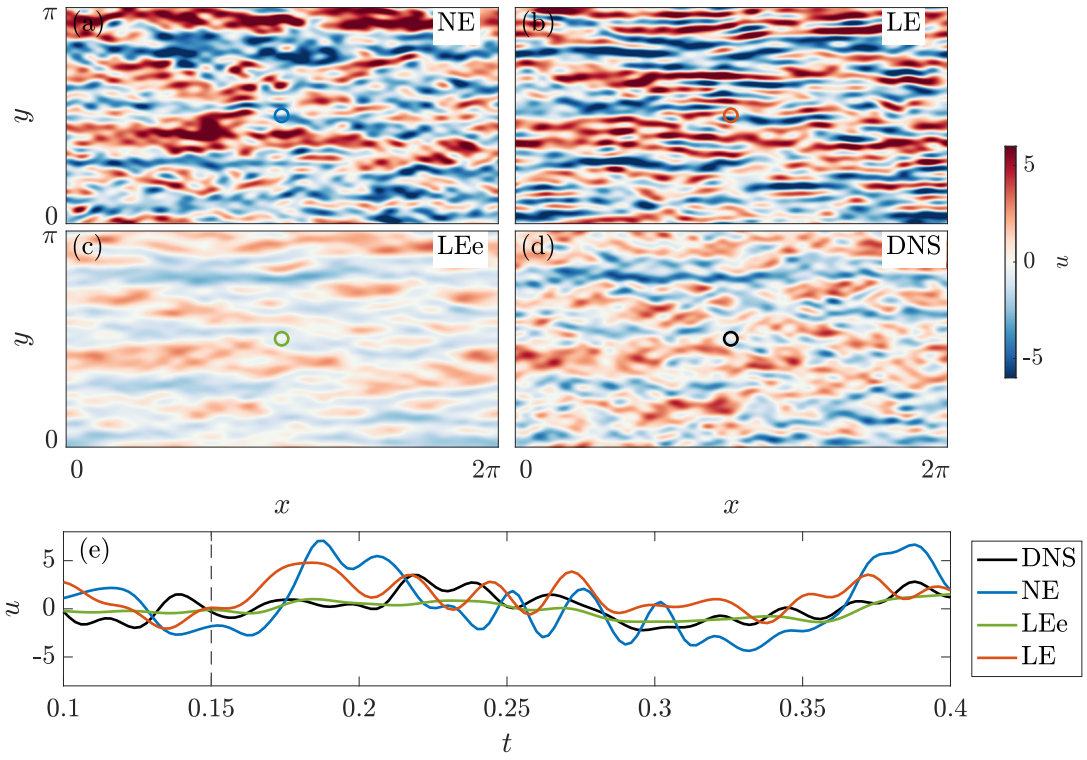

Figure 6.17: Streamwise velocity u from (a) NE, (b) LE, (c) LEe and (d) DNS data in the xy plane at $z^+ = 50$ and $Re_\tau = 590$. The measurement data come from $z^+ = 18$. The circles in the middle of (a,b,c,d) denote the locations of the streamwise velocity plotted in (e). (e) Streamwise velocity varying with time at the centre of the xy plane at $z^+ = 50$. The vertical dashed line denotes the time instant for (a,b,c,d).

Channel flow estimation has been investigated at high Reynolds numbers (Illingworth et al., 2018; Oehler et al., 2018; Amaral et al., 2021; Wang et al., 2022; Ying et al., 2023) and we wonder if the nonlinear estimator designed in this study can be applied at a higher Reynolds number. In this section, we apply the nonlinear estimator at $Re_\tau = 590$. As Re_τ increases, the influence of small-scale motions becomes more significant. Consequently, we increase the number of wavenumbers considered for $Re_\tau = 590$. The wavenumbers considered at $Re_\tau = 590$ are $|k_x| \leq 20$ and $|k_y| \leq 40$, corresponding to structures with $\lambda_x^+ \geq 185$ and $\lambda_y^+ \geq 93$. In the wall-normal direction we use 257 Chebyshev points and convergence has been checked by doubling the number of Chebyshev points. The measurement data (velocities) come from $z^+ = 18$, where the turbulent kinetic energy reaches its maximum in the wall-normal direction. The measurement data comes from DNS and the temporal resolution is $\Delta T_m = 0.002 (\Delta T_m^+ = 1.18)$ which is small enough to resolve the frequency of the smallest scale according to Taylor's hypothesis. The SSROM simulation time step is set to be $\Delta T_s = 0.00005$. The estimation starts with zero initial

condition. We present the estimation results starting from $t = 0.1(t^+ = 59)$ to $t = 0.4(t^+ = 236)$ to minimise the initial transient.

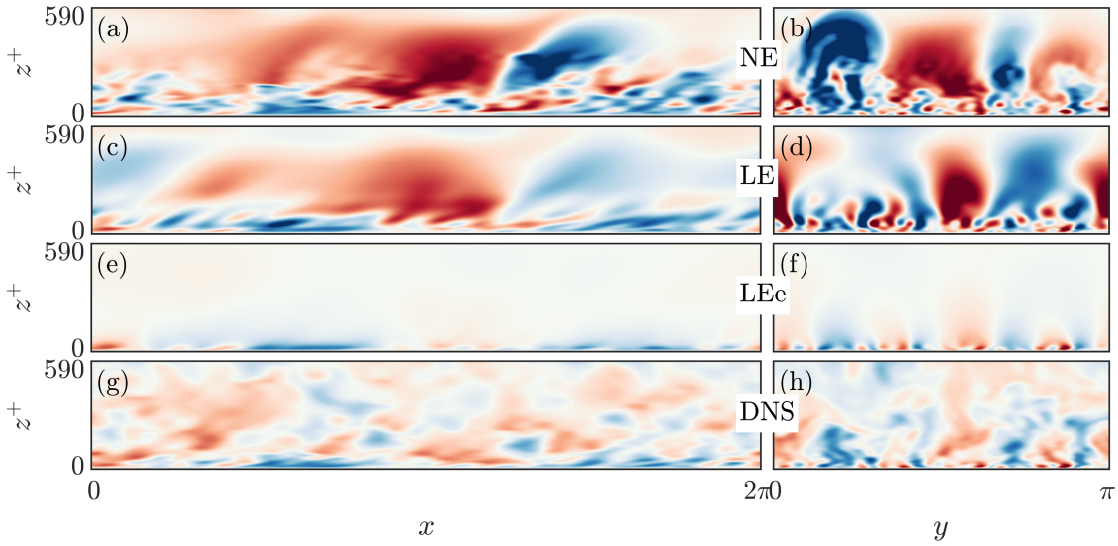

Figure 6.18: (a,c,e,g) Streamwise velocity field in the xz plane at $y = \frac{\pi}{2}$. (b,d,f,h) Streamwise velocity field in the yz plane at $x = \pi$. (a,b) NE; (c,d) LE; (e,f) LEe and (g,h) the DNS data. The limits of the colour map are the same as that in figure 6.18.

Figure 6.17 shows the estimation results using different estimators at $Re_\tau = 590$. From the colour scale in figures 6.17(a,b,c,d), we see that both NE and LE overpredict the velocity magnitudes; LEe underpredicts the velocity magnitudes. From the shapes of the structures, we see that NE tends to break the large-scale structures presented in the DNS into small-scale structures; LE only gives structures that are long in the streamwise direction and thin in the spanwise direction; LEe retains the shapes of the large-scale structures. Figure 6.17(e) further shows that the velocity from NE deviates from the DNS substantially.

From the previous section, we see that estimators using one measurement plane do not provide a good overall result across the channel height at $Re_\tau = 180$, irrespective of the location of the measurement plane. Therefore, we do not expect that estimators using only one measurement plane will work well across the channel height at $Re_\tau = 590$. Figure 6.18 shows the streamwise velocity fields across the wall-normal height. We see that all estimators cannot give the correct fields away from the near-wall region (the measurement plane is at $z^+ = 18$). NE and LE overpredict the values; the velocity magnitudes outside the near-wall region from LEe are approximately zero, which is also noted in Oehler et al. (2018). Further including small scales in the estimation does not show noticeable improvement. For the estimation with only one measurement plane provided, NE does not perform well. LEe performs well near the measurement plane and gives zero velocities at

wall-normal heights that do not share coherence with the measurement plane, indicating the effectiveness of the eddy viscosity at higher Reynolds numbers (Illingworth et al., 2018; Oehler et al., 2018).

6.4 Nonlinear estimation using multiple measurement planes

We have seen from the previous section that the performance of the nonlinear estimator deteriorates significantly away from the measurement plane with only one measurement plane provided. Due to the inhomogeneity caused by the wall in wall-bounded flows, the flow physics varies significantly in the wall-normal direction. It has been shown that the coherence between two wall-normal heights decreases as the two wall-normal heights are separated farther (Madhusudanan et al., 2019). This implies that even though we consider the effect of the nonlinear forcing in NE and LEe, the underlying physics forbids us from estimating the velocities that are not coherent with the measurement data (Illingworth et al., 2018). The failure to estimate the velocities away from the measurement plane can also be attributed to insufficient measurement data in the wall-normal direction. The OSS state-space model (6.2) contains a sufficient number of states (129 Chebyshev points at $Re_\tau = 180$) distributed in the buffer layer, log layer and outer layer in the wall-normal direction in order to describe the flow statistics comprehensively. Therefore, the nonlinear estimator with measurement data at only one wall-normal height is not able to estimate the velocities across the channel.

Arun et al. (2023) investigated channel flow estimation using multiple measurement planes in the wall-normal direction. Inspired by this, we increase the number of measurement planes provided to the nonlinear estimator. Specifically, §6.4.1 discusses the results at $Re_\tau = 180$ and §6.4.2 discusses the results at $Re_\tau = 590$.

6.4.1 At $Re_\tau = 180$

We test four cases with the number of measurement planes N_{mea} varying from 1 to 4. The details are listed in table 6.2.

Table 6.2: Wall-normal locations of the measurement planes for four cases.

N_{mea}	1	2	3	4
z^+_{mea}	15	15,50	15,50,100	15,50,100,150

Figure 6.19 shows the estimation performance of the four cases listed in table 6.2. As expected, NE gives the correct velocities at the measurement locations (Arun et al., 2023). However, even if the number of measurement planes increases, substantial error

still occurs when the estimation plane is far from the measurement plane, as seen in the cases with $N_{mea} = 1, 2, 3$.

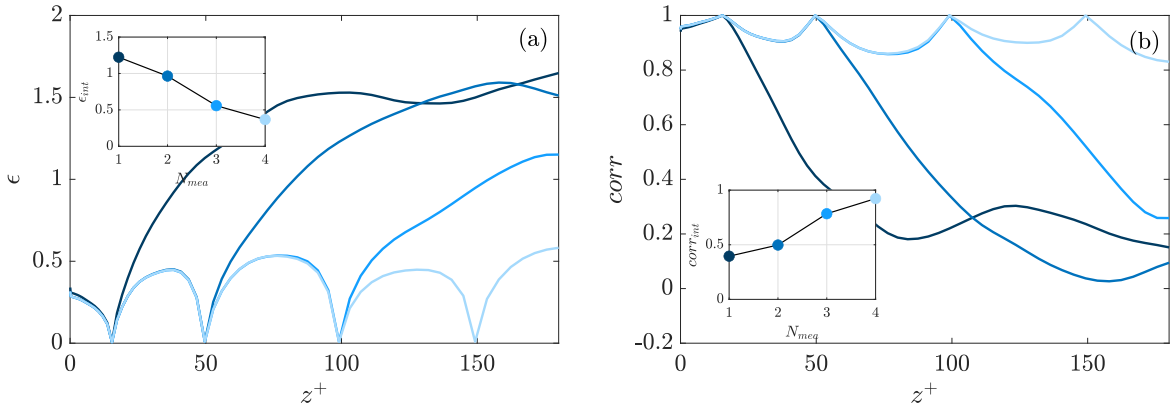

Figure 6.19: Error (6.8a) and correlation (6.8b) for NE with multiple measurement planes considered as listed in table 6.2. A case with a larger number of measurement planes is shown using a lighter blue colour. Inset plots show the integrated error and correlation (6.14).

As for the overall estimation performance indicated by ε_{int} and corr_{int} (6.14), we see that the overall estimation significantly improves with the inclusion of just a few more measurement planes (inset plots in figure 6.19). If the measurement planes are more evenly distributed in the wall-normal direction (for example the case with $N_{mea} = 4$), the error and correlation do not deteriorate significantly (the curves flatten out). In terms of achieving a good overall estimation performance, an open question concerns the number of measurement planes needed and the distribution of the measurement planes in the wall-normal direction. The visualisation of the estimated velocity fields for NE with multiple measurements are shown for the $Re_\tau = 590$ case in §6.4.2 and are not shown for the $Re_\tau = 180$ case because the results are similar.

6.4.2 At $Re_\tau = 590$

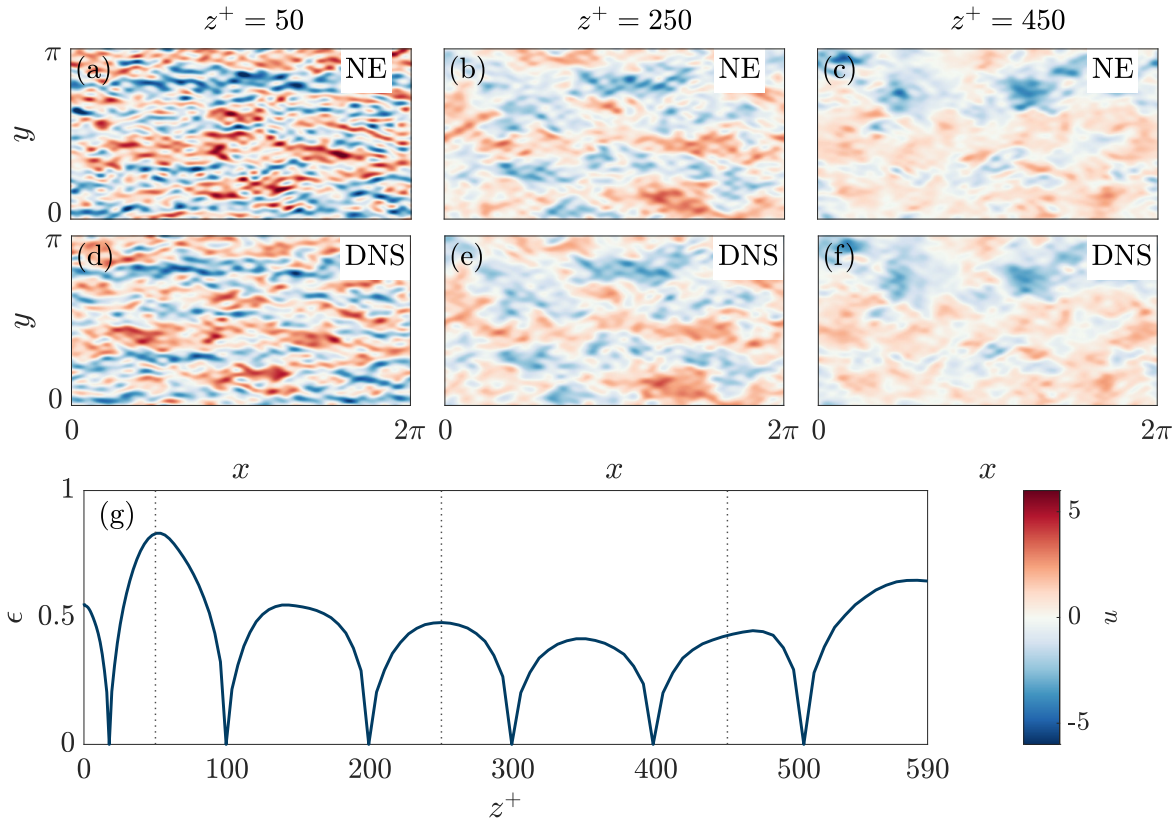

Figure 6.20: Results in xy plane of nonlinear estimation with six measurement planes at $z^+ = 18, 100, 200, 300, 400$ and 500. (a,b,c) The estimated velocity fields for NE; (d,e,f) The velocity fields from DNS. (a,d) $z^+ = 50$; (b,e) $z^+ = 250$; (c,f) $z^+ = 450$. (g) Error (6.8a) for NE. Three dotted lines mark $z^+ = 50, 250$ and 450.

From §6.4.1, we know that multiple measurement planes evenly distributed across the wall-normal height enhances the NE performance significantly. Therefore, we increase the number of measurement planes from one to six at $Re_\tau = 590$, with measurement planes at $z^+ = 18, 100, 200, 300, 400$ and 500. Figure 6.20 shows the estimated velocity fields at $z^+ = 50, 250, 450$ and the estimation error across the channel height (the correlation is similar to the error and is not shown). As expected, figure 6.20(g) shows that NE gives accurate estimation results at the measurement planes. At the three chosen wall-normal heights $z^+ = 50, 250$ and 450 (figure 6.20(a-f)), NE gives satisfactory estimation results for large-scale structures, though NE slightly overpredicts the velocity magnitudes at a few locations.

Figure 6.21 shows the estimated velocity fields across the channel height. Compared with the single measurement plane case in figure 6.18, increasing the number of measurement planes greatly improves the estimation performance across the channel height.

Even with the increased number of measurement planes, this number is still substantially smaller than the number of DNS gridpoints in the wall-normal direction.

The nonlinear estimator in this study can be related to large-eddy simulation (LES). Both LES and nonlinear estimation only consider the largest scales. The main difference is that LES is autonomous, whereas the nonlinear estimator requires external information continuously supplied (the measurement data). In LES, the energy transfer between the resolved scales and subgrid scales is modelled to improve accuracy. In light of this and the energy transfer in figure 6.9, a possible way to improve the nonlinear estimator would be to consider the energy transfer.

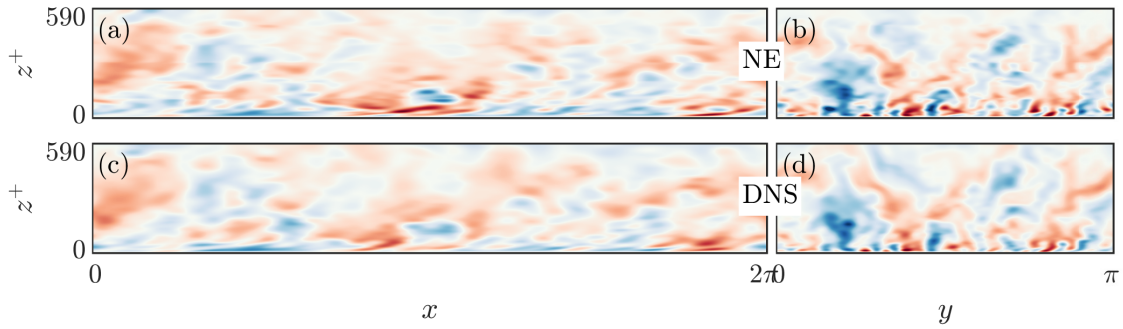

Figure 6.21: Results in xz and yz planes of nonlinear estimation with six measurement planes at $z^+ = 18, 100, 200, 300, 400$ and 500. (a,b) The estimated velocity fields for NE; (c,d) The velocity fields from DNS. (a,c) xz plane; (b,d) yz plane.

6.5 Conclusions

We investigate turbulent channel flow estimation at $Re_\tau = 180$ and 590. The nonlinear estimator designed in this study consists of two main parts. The linear part is based on the linearised Navier-Stokes equations with nonlinear forcing as input and velocity as output (Illingworth et al., 2018). The nonlinear part links the velocity back to the nonlinear forcing through the nonlinear dynamics $f_i = -u_j \frac{\partial u_i}{\partial x_j}$.

We compare the estimation performance between the nonlinear estimator (NE), linear estimator (LE) and linear estimator augmented with eddy viscosity (LEe). At $Re_\tau = 180$, NE and LEe outperform LE in terms of estimating the velocity magnitudes, structure shapes and energy transfer across the wall-normal height. We see that the overall estimation performance does not change substantially as the location of the measurement plane is varied. At $Re_\tau = 590$, NE does not work well using only one measurement plane. The performance of the nonlinear estimator can be significantly enhanced by including a few more measurement planes evenly distributed in the wall-normal direction.

The linear estimator augmented with eddy viscosity outperforms the nonlinear esti-

mator designed in this study in terms of the estimation performance, stability, simplicity and applicability to high Reynolds number flows. This has shown the usefulness of eddy viscosity although eddy viscosity only serves to dissipate energy. Apart from using the nonlinear estimation methodology in this study and eddy viscosity, there are other ways to consider the nonlinearity, such as using extended Kalman filter (Chevalier et al., 2006), ensemble Kalman filter (Colburn et al., 2011), inner-outer layer relationship (Baars et al., 2016), cross-spectral density (CSD) tensor (Towne et al., 2020) and so on. A promising future work would be to combine the advantages of different nonlinear estimation strategies.

The improved estimation performance of the proposed nonlinear estimator compared to the linear estimator highlights the significance of considering nonlinearity in fluid systems governed by the nonlinear Navier-Stokes equations. Since nonlinear mechanisms contribute to sustaining turbulence, flow control strategies could target either enhancing or disrupting nonlinear forcing, as demonstrated in several studies (Kim, 2011; Bae et al., 2021).

Chapter 7

Conclusions

7.1 Summary

This thesis focuses on the nonlinear energy transfer physics and nonlinear estimation of turbulent channel flows. The work comprises three parts: i) mode-to-mode nonlinear energy transfer in spectral space; ii) coherent structures related to nonlinear energy transfer (turbulent convection) in physical space; and iii) a flow estimation problem in which knowledge of the nonlinear forcing terms is included in the linear estimator. The results have been generated using direct numerical simulation (DNS) datasets at friction Reynolds numbers of $Re_\tau = 180$ and 590 (Chung et al., 2014).

In chapter 4, nonlinear energy transfer is investigated in spectral space. A mode (k_x, k_y) refers to a single Fourier mode with a specific streamwise wavelength and spanwise wavelength. In order to address the deficiency that we could previously only investigate the net nonlinear energy transfer $\hat{N}(k_x, k_y)$ for a given mode, we introduce a 4-D variable $\hat{M}_{(a,b)(k_x,k_y)}$ which quantifies the nonlinear energy transfer from a single mode (a,b) to another mode (k_x, k_y). Using this new quantity $\hat{M}$, three things are explored. First, we obtain two other values representing the net nonlinear energy gain $\hat{N}^+(k_x, k_y)$ and net nonlinear energy loss $\hat{N}^-(k_x, k_y)$ for a given mode, thus decomposing the net nonlinear energy transfer $\hat{N}$ into its positive $\hat{N}^+$ and negative $\hat{N}^-$ contributions. At $Re_\tau = 590$, both the net energy gain and loss spectra reveal a significant nonlinear interaction region at $\lambda_x^+ \approx 150, \lambda_y^+ \approx 100$, which cannot be observed from the net energy transfer spectrum alone. Second, the nonlinear energy transfer of streamwise streaks, oblique waves and Tollmien–Schlichting (TS) waves shows that a transverse energy cascade exists, for which the key parameter is the aspect ratio k_y/k_x. This transverse cascade refers to energy transfer from streamwise elongated modes to spanwise elongated modes and this transverse cascade is not substantially influenced by the Reynolds numbers considered. Third, we quantify the forward and inverse cascades between the resolved scales and

subgrid scales in the spirit of large-eddy simulation (LES). For both Reynolds numbers considered and when the cutoff wavelengths satisfy $\lambda_{xC}^{+} = 2\lambda_{yC}^{+} < 250$ (LES still needs to resolve a sufficient number of large scales), the forward cascade is at least four times greater than the inverse cascade. However, the inverse cascade is still not negligible for scales satisfying $\lambda_{xC}^{+} = 2\lambda_{yC}^{+} > 100$.

In chapter 5, nonlinear energy transfer is investigated in physical space. We use conditional averaging to extract two types of events. Positive nonlinear energy transfer events are characterised by significant energy gain due to nonlinear interactions and negative nonlinear energy transfer events are characterised by significant energy loss due to nonlinear interactions. The conditionally averaged velocity fields, nonlinear energy transfer fields and vorticity fields are similar for both types of events and for both Reynolds numbers considered. As for the conditionally averaged velocity fields, sweeps or Q4 events are observed in the near-wall region for $z^{+} < 20$, and ejections or Q2 events are observed farther away from the wall for $z^{+} > 20$. As for the conditionally averaged nonlinear energy transfer fields, the region of positive nonlinear energy transfer and the region of negative nonlinear energy transfer come in pairs. The two regions are adjacent to each other in the streamwise direction and their relative position switches at $z^{+} \approx 20$. As for the conditionally averaged vorticity fields, quasi-streamwise vortices are detected in the near-wall region for $z^{+} < 20$, and hairpin vortex heads are detected farther away from the wall for $z^{+} > 20$. The main difference between positive and negative nonlinear energy transfer events is that: positive nonlinear energy transfer is concentrated below quasi-streamwise vortices and in the upstream region of hairpin heads; negative nonlinear energy transfer is concentrated at the same height as quasi-streamwise vortices and in the downstream region of hairpin heads.

In chapter 6, we design a nonlinear estimator by embedding the nonlinear dynamics involving velocity and nonlinear forcing into the linear estimator based on the linearised Navier-Stokes equations. This idea is inspired by previous work on the channel flow estimation problem that the linear estimator augmented with eddy viscosity significantly outperforms the purely linear estimator (Illingworth et al., 2018). The goal is to use the velocity measurement data at one wall-normal height to estimate the velocities across the channel height. In terms of estimation performance concerning the velocity profile and energy transfer, both the nonlinear estimator and linear estimator augmented with eddy viscosity outperform the purely linear estimator at $Re_{\tau} = 180$, especially for the largest streamwise scales. The reasons for the better estimation performance over the purely linear estimator are different. The nonlinear estimator performs better because we calculate the structured nonlinear forcing to feed the estimator. The linear estimator augmented with eddy viscosity performs better because the nonlinear effect of the small scales on

the large scales is modelled, albeit crudely, by the eddy viscosity, though the nonlinear forcing is unstructured. However, the nonlinear estimator does not show superiority over the purely linear estimator at $Re_\tau = 590$ potentially because partial knowledge of the nonlinear forcing around the measurement plane is not sufficient to represent the nonlinearity in the flow. Nevertheless, the linear estimator augmented with eddy viscosity shows superiority and stability at high Reynolds numbers, indicating that a simple eddy viscosity model is a favourable model for flow estimation and control in high-Reynolds-number wall-bounded flows.

7.2 Future work

Applications to high Reynolds number cases

The flow dynamics at high Reynolds numbers differ from those at low Reynolds numbers. As the Reynolds number Re_τ increases, the influence of large scales on the total kinetic energy becomes more dominant, as observed in the one-dimensional premultiplied spectra and the scale decomposition of the streamwise turbulence intensity profile (Hutchins & Marusic, 2007; Smits et al., 2011). Additionally, results obtained at low Reynolds numbers are less applicable to real-world applications, such as gas turbine flows and weather predictions, where the Reynolds numbers are significantly higher. Chapters 4 and 5 can be directly extended to high-Reynolds-number flows since the relevant equations and methodology remain unchanged. However, in chapter 6, additional measurement planes would be required, or the structure of the estimator would need modification for high-Reynolds-number flow estimation. This is because the current nonlinear estimator lacks stability when applied to high-Reynolds-number flows.

Applications to boundary layer flows

There is a major difference in the methodology of the Fourier transform. In channel flows, a two-dimensional Fourier transform is applied in the streamwise and spanwise directions, whereas in boundary layer flows, only a one-dimensional Fourier transform is applied in the spanwise direction. This results in streamwise location dependence for boundary layer flows. It has been observed that differences exist in the largest scales between channel flows and boundary layer flows (Monty et al., 2009). Consequently, the peaks of the positive and negative nonlinear energy transfer ($\hat{n}^+$ and $\hat{n}^-$) may shift for boundary layer flows, in the context of chapter 4. Additionally, the sizes of the coherent structures related to significant turbulent convection could vary, in the context of chapter 5. Since the linearized Navier-Stokes equation operator for boundary layer flows differs from that for channel flows (Cossu et al., 2009), the estimation performance with respect

to the locations of the measurement planes could change, in the context of chapter 6.

Dynamics of mode-to-mode nonlinear energy transfer

In chapter 4, the discussions concerning mode-to-mode nonlinear energy transfer $\hat{M}_{(a,b)(k_x,k_y)}$ describe the statistical features because $\hat{M}$ is a time-averaged variable. More information about the dynamical features could be extracted from the time series of $\hat{M}(t)$. A straightforward first step would be to calculate the variance of $\hat{M}(t)$. A low variance indicates that a given energy transfer pathway from mode (a,b) to mode (k_x,k_y) does not change significantly with respect to time. A high variance indicates that a given energy transfer pathway from mode (a,b) to mode (k_x,k_y) changes its magnitude or even direction frequently with respect to time.

Mode-to-mode nonlinear energy transfer at different wall-normal heights

In chapter 4, the discussions concerning mode-to-mode nonlinear energy transfer $\hat{M}_{(a,b)(k_x,k_y)}$ describe the wall-normal integrated energy transfer since the wall-normal integrated energy transfer only involves production, dissipation and nonlinear energy transfer. However, nonlinear energy transfer in the wall-normal direction is hidden in $\hat{M}$. It has been shown that energy transfer occurs from the logarithmic region to the near-wall and outer-layer regions (Bolotnov et al., 2010; Lee & Moser, 2019). $\hat{M}$ could be extended to contain the wall-normal coordinate z, and this would require only a minor modification in the derivation of $\hat{M}$.

Componenetwise analysis of mode-to-mode nonlinear energy transfer

(Jovanović & Bamieh, 2005) investigates the linear amplification mechanisms from the streamwise, spanwise and wall-normal nonlinear forcing to the streamwise, spanwise and wall-normal velocities individually. Inspired by this concept, we decomposed the mode-to-mode nonlinear energy transfer into contributions from the streamwise, spanwise, and wall-normal velocities. Our exploration revealed that the primary contribution arises from the streamwise velocity component. However, further research is needed to explore the specifics of energy transfer from the streamwise components to the spanwise and wall-normal components.

Scale-dependent eddy viscosity

Eddy viscosity models the effects of small scales on large scales. However, there is one ambiguity of the Cess eddy viscosity ν_T (Cess, 1958) concerning what the large scales and small scales are. Gupta et al. (2021) designed a scale-dependent eddy viscosity which is a function of the size of a scale and this scale-dependent eddy viscosity is able to predict

more accurate turbulence features in channel flows. Inspired by this, mode-to-mode nonlinear energy transfer $\hat{M}_{(a,b)(k_x,k_y)}$ could be used to develop more accurate scale-dependent eddy-viscosity models. Similar to the nonlinear energy transfer of the three structures (streamwise streaks, oblique waves and TS waves) in chapter 4, this time (a,b) contains the specific small scales and (k_x,k_y) contains the specific large scales. Following this, the obtained scale-dependent eddy viscosity $\nu_T(k_x,k_y)$ which could be used to improve wavenumber-based estimation and control.

DNS experiments using mode-to-mode nonlinear energy transfer

The net nonlinear energy transfer $\hat{N}(k_x,k_y)$ and the mode-to-mode nonlinear energy transfer $\hat{M}_{(a,b)(k_x,k_y)}$ could be coded in DNS (rather than experiments) to amplify or cut off certain nonlinear energy transfer pathways. This could be used to study the nonlinear aspects of the self-sustaining process (SSP) in the near-wall region (Hamilton et al., 1995). Since $\hat{M}$ is a 4-D variable exhibiting a large number of energy transfer pathways, a sensible starting point would be to use minimal channels where the number of energetically dominant modes is fewer than that in a full channel, and the statistics are nonetheless accurate in the near-wall region (Chung et al., 2014).

Dynamic relationship between nonlinear energy transfer and coherent structures

The coherent structures presented in chapter 5 are ensemble-averaged from the nonlinear energy transfer events. Each conditional event corresponds to one time instant, so the dynamic processes before that time instant and after that time instant are still missing. We can further extract the events adjacent to the conditional events in time, though storage issues need to be considered. The relationship between the nonlinear energy transfer and the evolution of quasi-streamwise vortices and hairpin vortices could then be explored.

Nonlinear estimator in other types of fluid flows

The nonlinear estimator designed in chapter 6 is for channel flows. The key feature is that we introduce the nonlinear dynamics $f_i = -u_j \frac{\partial u_i}{\partial x_j}$ which is universal for any type of flow. Therefore, the same methodology of the Kalman filter embedded with an SSROM simulation could be applied to the estimation problem for other types of flows. A promising application is wake flows in which the number of energetically dominant modes is less than that in channel flows and it has been shown that the higher harmonic motions in the wake flows are slave to the fundamental frequency (Gong, 2021).

Nonlinear estimation with machine learning

An open question left in chapter 6 is how to place a fixed number of measurement planes

across the channel height in order to achieve a better overall estimation performance. Brute force searching at low Reynolds numbers could be a feasible solution given the computational power available today. With the rapid progress of high-performance computing and algorithms, machine learning has been widely used in physical problems (Karniadakis et al., 2021; Brunton et al., 2020). For flows at high Reynolds numbers, the question could be tackled using machine learning methods, such as the iterative-gradient minimisation algorithm (Chen & Rowley, 2011) and sparse identification of nonlinear dynamics (SINDy) algorithm (Loiseau et al., 2018).

Appendix A

Details of mode-to-mode nonlinear energy transfer

A.1 Definition of energy transfer in Fourier space

First, we define scalar product as: $\langle c_1, c_2 \rangle = c_1^* c_2$, where c_1 and c_2 are two complex numbers and $*$ denotes complex conjugate.

At one wall-normal height, the average energy transfer in the streamwise-spanwise plane is composed of contributions from different Fourier modes. For example, the average nonlinear energy transfer at one wall-normal height could be written as:

$$\frac{\iint -u_i u_j \frac{\partial u_i}{\partial x_j} \mathrm{d}x\mathrm{d}y}{L_x L_y} = \sum_{-\max k_x}^{\max k_x} \sum_{-\max k_y}^{\max k_y} \langle \hat{u}_i, \widehat{\frac{\partial u_i u_j}{\partial x_j}} \rangle \tag{A.1}$$

where L_x and L_y are the turbulence domain lengths in the streamwise and spanwise directions, respectively. We consider non-negative wavenumbers: $k_x \geq 0$ and $k_y \geq 0$.

We prove equation (A.1) by considering a general case shown below.

If $a = f(x,y),\ b = g(x,y) \in \mathbb{R}$, where $x \in [0, L_x],\ y \in [0, L_y]$, then:

$$\frac{\iint ab \ \mathrm{d}x \ \mathrm{d}y}{L_x L_y} = \sum_{-\max k_x}^{\max k_x} \sum_{-\max k_y}^{\max k_y} \langle \hat{a}, \hat{b} \rangle \quad k_x \in [0, \max k_x] \quad k_y \in [0, \max k_y]$$

Proof. In terms of the 2-D Fourier transform, a, b can be expressed as:

$$a = \sum_{-\max k_{xa}}^{\max k_{xa}} \sum_{-\max k_{ya}}^{\max k_{ya}} \hat{a} e^{\mathrm{i}(k_{xa}x + k_{ya}y)} \qquad b = \sum_{-\max k_{xb}}^{\max k_{xb}} \sum_{-\max k_{yb}}^{\max k_{yb}} \hat{b} e^{\mathrm{i}(k_{xb}x + k_{yb}y)}$$

A sufficient number of Fourier modes needs to be used to capture the smallest scales. In

addition, another property states that:

$$\iint e^{\mathrm{i}(k_x x + k_y y)} \mathrm{d}x\,\mathrm{d}y = 0 \quad (k_x \neq 0 \cup k_y \neq 0)$$

because of the periodicity. Then:

$$\begin{aligned}
\iint ab\,\mathrm{d}x\,\mathrm{d}y &= \iint \{\sum_{-\max k_{xa}}^{\max k_{xa}} \sum_{-\max k_{ya}}^{\max k_{ya}} \hat{a} e^{\mathrm{i}(k_{xa}x + k_{ya}y)}\} \{\sum_{-\max k_{xb}}^{\max k_{xb}} \sum_{-\max k_{yb}}^{\max k_{yb}} \hat{b} e^{\mathrm{i}(k_{xb}x + k_{yb}y)}\}\,\mathrm{d}x\,\mathrm{d}y \\
&= \sum_{-\max k_{xa}}^{\max k_{xa}} \sum_{-\max k_{ya}}^{\max k_{ya}} \sum_{-\max k_{xb}}^{\max k_{xb}} \sum_{-\max k_{yb}}^{\max k_{yb}} \iint \hat{a} e^{\mathrm{i}(k_{xa}x + k_{ya}y)} \hat{b} e^{\mathrm{i}(k_{xb}x + k_{yb}y)}\,\mathrm{d}x\,\mathrm{d}y \\
&= \sum_{-\max k_x}^{\max k_x} \sum_{-\max k_y}^{\max k_y} \iint \hat{a}^* e^{\mathrm{i}(-k_x x - k_y y)} \hat{b} e^{\mathrm{i}(k_x x + k_y y)}\,\mathrm{d}x\,\mathrm{d}y \\
&= \sum_{-\max k_x}^{\max k_x} \sum_{-\max k_y}^{\max k_y} \iint \hat{a}^* \hat{b}\,\mathrm{d}x\,\mathrm{d}y \\
&= L_x L_y \sum_{-\max k_x}^{\max k_x} \sum_{-\max k_y}^{\max k_y} \langle \hat{a}, \hat{b} \rangle
\end{aligned}$$

□

Equation A.1 could be written as:

$$\begin{aligned}
&\sum_{-\max k_x}^{\max k_x} \sum_{-\max k_y}^{\max k_y} \langle \hat{u}_i, \widehat{\frac{\partial u_i u_j}{\partial x_j}} \rangle \\
&= \underbrace{\hat{u}_i^{(0,0)} \widehat{\frac{\partial u_i u_j}{\partial x_j}}^{(0,0)}}_{\hat{N}(0,0)} \\
&+ \sum_{\min k_x}^{\max k_x} \{\underbrace{\hat{u}_i^{(-k_x,0)} \widehat{\frac{\partial u_i u_j}{\partial x_j}}^{(k_x,0)} + \hat{u}_i^{(k_x,0)} \widehat{\frac{\partial u_i u_j}{\partial x_j}}^{(-k_x,0)}}_{\hat{N}(k_x,0)}\} \\
&+ \sum_{\min k_y}^{\max k_y} \{\underbrace{\hat{u}_i^{(0,-k_y)} \widehat{\frac{\partial u_i u_j}{\partial x_j}}^{(0,k_y)} + \hat{u}_i^{(0,k_y)} \widehat{\frac{\partial u_i u_j}{\partial x_j}}^{(0,-k_y)}}_{\hat{N}(0,k_y)}\} \\
&+ \sum_{\min k_x}^{\max k_x} \sum_{\min k_y}^{\max k_y} \{\underbrace{\hat{u}_i^{(-k_x,-k_y)} \widehat{\frac{\partial u_i u_j}{\partial x_j}}^{(k_x,k_y)} + \hat{u}_i^{(k_x,k_y)} \widehat{\frac{\partial u_i u_j}{\partial x_j}}^{(-k_x,-k_y)} + \hat{u}_i^{(k_x,-k_y)} \widehat{\frac{\partial u_i u_j}{\partial x_j}}^{(-k_x,k_y)} + \hat{u}_i^{(-k_x,k_y)} \widehat{\frac{\partial u_i u_j}{\partial x_j}}^{(k_x,-k_y)}}_{\hat{N}(k_x,k_y)}\}
\end{aligned}$$

For a statistically steady flow: $\hat{N}(0,0) = 0$, because $\hat{u}_i^{(0,0)} = 0$.
Two things need to be emphasised here:

- $\hat{N}(k_x, k_y)$ is not the Fourier coefficient of nonlinear energy transfer $-u_i u_j \frac{\partial u_i}{\partial x_j}$. It represents the nonlinear energy transfer contribution from mode (k_x, k_y).
- $\hat{u}_i$ and $\widehat{\frac{\partial u_i u_j}{\partial x_j}}$ are the Fourier coefficients of u_i and $\frac{\partial u_i u_j}{\partial x_j}$, respectively. $\hat{u}_i^{(k_x,k_y)}$ refers to the Fourier coefficient of u_i at Fourier mode (k_x, k_y).

When calculating the 2-D Fourier transform in MATLAB, the Fourier coefficients are stored in a 2-D matrix, as illustrated in figure A.1. Since the values (for example velocities) in the physical space are all real numbers, any two blocks with the same colour are complex conjugates of each other.

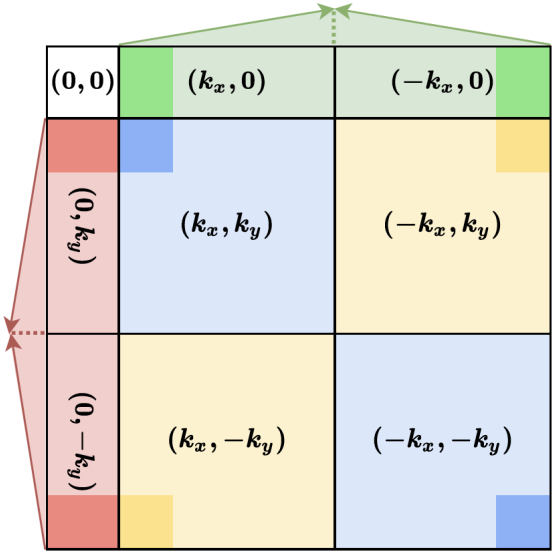

Figure A.1: The wavenumber frame for the 2-D Fourier transform using MATLAB command 'fft2'. $k_x, k_y \in \mathbb{R}^+$. The arrows indicate the directions in which the absolute values of the wavenumbers increase. The dark colours mark the regions containing small wavenumbers. This frame is the same as that in the Python NumPy library.

A.2 Spectral turbulent kinetic energy equation

Turbulent kinetic energy equation in physical space is (Pope, 2000):

$$\frac{\partial(\frac{1}{2}u_i u_i)}{\partial t} + U_j \frac{\partial(\frac{1}{2}u_i u_i)}{\partial x_j} = -u_i u_j \frac{\partial U_i}{\partial x_j} - \frac{1}{Re_\tau}\frac{\partial u_i}{\partial x_j}\frac{\partial u_i}{\partial x_j} - u_i u_j \frac{\partial u_i}{\partial x_j} - u_i \frac{\partial p}{\partial x_i} + \frac{1}{Re_\tau}\frac{\partial^2(\frac{1}{2}u_i u_i)}{\partial x_j \partial x_j} \tag{A.2}$$

The terms on the left-hand side of equation (A.2) represent the rate of change of turbulent kinetic energy and mean flow convection. The five terms on the right-hand side of equation (A.2) represent production, dissipation, turbulent convection, pressure diffusion and viscous diffusion, respectively.

From equation (A.2) and according to the scalar product definition, the spectral energy transfer budget at wavenumber (k_x, k_y) is:

$$\frac{\partial \hat{e}}{\partial t} + U_j \frac{\partial \hat{e}}{\partial x_j} = -\langle \hat{u}_i, \widehat{u_j \frac{\partial U_i}{\partial x_j}} \rangle - \frac{1}{Re_\tau} \langle \widehat{\frac{\partial u_i}{\partial x_j}}, \widehat{\frac{\partial u_i}{\partial x_j}} \rangle - \langle \hat{u}_i, \widehat{u_j \frac{\partial u_i}{\partial x_j}} \rangle - \langle \hat{u}_i, \widehat{\frac{\partial p}{\partial x_i}} \rangle + \frac{1}{Re_\tau} \frac{\partial^2 \hat{e}}{\partial x_j \partial x_j}$$

With the mean flow assumption $U_i = [U(z), 0, 0]$ for channel flows, the mean flow convection term at wavenumber (k_x, k_y) is:

$$U_j \frac{\partial \hat{e}}{\partial x_j} = \langle \hat{u}_i, \widehat{U_j \frac{\partial u_i}{\partial x_j}} \rangle = \mathrm{i} U k_x \hat{u}_i \hat{u}_i^*$$

where $\mathrm{i} = \sqrt{-1}$ is the imaginary unit. Then, by considering the conjugate wavenumber $(-k_x, -k_y)$, the mean flow convection at Fourier mode (k_x, k_y) is zero:

$$\langle \hat{u}_i, \widehat{U_j \frac{\partial u_i}{\partial x_j}} \rangle + \langle \hat{u}_i, \widehat{U_j \frac{\partial u_i}{\partial x_j}} \rangle^* = \mathrm{i} U k_x \hat{u}_i \hat{u}_i^* - \mathrm{i} U k_x \hat{u}_i \hat{u}_i^* = 0$$

Since mean flow convection is zero in Fourier space, spectral energy transfer at any wall-normal height at Fourier mode (k_x, k_y) for a channel flow could be written as (Bolotnov et al., 2010; Andrade et al., 2018; Lee & Moser, 2019):

$$\frac{\partial \hat{e}}{\partial t} = -\langle \hat{u}_i, \widehat{u_j \frac{\partial U_i}{\partial x_j}} \rangle - \frac{1}{Re_\tau} \langle \widehat{\frac{\partial u_i}{\partial x_j}}, \widehat{\frac{\partial u_i}{\partial x_j}} \rangle - \langle \hat{u}_i, \widehat{u_j \frac{\partial u_i}{\partial x_j}} \rangle - \langle \hat{u}_i, \widehat{\frac{\partial p}{\partial x_i}} \rangle + \frac{1}{Re_\tau} \frac{\partial^2 \hat{e}}{\partial x_j \partial x_j} \tag{A.3}$$

A.2.1 Integrating the pressure diffusion term

The pressure diffusion term at wavenumber (k_x, k_y) could be expressed as:

$$\langle \hat{u}_i, \widehat{\frac{\partial p}{\partial x_i}} \rangle = \mathrm{i} k_x \hat{p} \hat{u}^* + \mathrm{i} k_y \hat{p} \hat{v}^* + \frac{\partial \hat{p}}{\partial z} \hat{w}^* = -\hat{p} \underbrace{\{-\mathrm{i} k_x \hat{u}^* - \mathrm{i} k_y \hat{v}^* + \frac{\partial \hat{w}^*}{\partial z}\}}_{\text{continuity}} + \frac{\partial (\hat{p} \hat{w}^*)}{\partial z} = \frac{\partial (\hat{p} \hat{w}^*)}{\partial z}$$

where we use the continuity equation at wavenumber $(-k_x, -k_y)$.

Integrate this term across the channel height:

$$\int_{-1}^{1} \langle \hat{u}_i, \widehat{\frac{\partial p}{\partial x_i}} \rangle \mathrm{d}z = \int_{-1}^{1} \frac{\partial (\hat{p}\hat{w}^*)}{\partial z} \mathrm{d}z = \hat{p}\hat{w}^* |_{-1}^{1} = 0 \tag{A.4}$$

where we use the impermeability boundary condition: $\hat{w}^*(\pm 1) = 0$.

A.2.2 Integrating the viscous diffusion term

The viscous diffusion at mode (k_x, k_y) can be expressed as:

$$\frac{1}{Re_\tau} \frac{\partial^2 \hat{e}}{\partial x_j \partial x_j} = \frac{1}{Re_\tau} \langle \hat{u}_i, \widehat{\frac{\partial^2 u_i}{\partial x_j \partial x_j}} \rangle + \frac{1}{Re_\tau} \langle \widehat{\frac{\partial u_i}{\partial x_j}}, \widehat{\frac{\partial u_i}{\partial x_j}} \rangle$$

The first term on the right-hand side can be expressed as:

$$\langle \hat{u}_i, \widehat{\frac{\partial^2 u_i}{\partial x_j \partial x_j}} \rangle = \langle \hat{u}_i, \widehat{\frac{\partial^2 u_i}{\partial x^2}} \rangle + \langle \hat{u}_i, \widehat{\frac{\partial^2 u_i}{\partial y^2}} \rangle + \langle \hat{u}_i, \widehat{\frac{\partial^2 u_i}{\partial z^2}} \rangle = -k_x^2 \hat{u}_i \hat{u}_i^* - k_y^2 \hat{u}_i \hat{u}_i^* + \frac{\partial^2 \hat{u}_i}{\partial z^2} \hat{u}_i^*$$

The second term on the right-hand side can be expressed as:

$$\langle \widehat{\frac{\partial u_i}{\partial x_j}}, \widehat{\frac{\partial u_i}{\partial x_j}} \rangle = \langle \widehat{\frac{\partial u_i}{\partial x}}, \widehat{\frac{\partial u_i}{\partial x}} \rangle + \langle \widehat{\frac{\partial u_i}{\partial y}}, \widehat{\frac{\partial u_i}{\partial y}} \rangle + \langle \widehat{\frac{\partial u_i}{\partial z}}, \widehat{\frac{\partial u_i}{\partial z}} \rangle = k_x^2 \hat{u}_i \hat{u}_i^* + k_y^2 \hat{u}_i \hat{u}_i^* + \frac{\partial \hat{u}_i}{\partial z} \frac{\partial \hat{u}_i^*}{\partial z}$$

Then, add these two terms together to recover the viscous diffusion term:

$$\frac{\partial^2 \hat{e}}{\partial x_j \partial x_j} = \langle \hat{u}_i, \widehat{\frac{\partial^2 u_i}{\partial x_j \partial x_j}} \rangle + \langle \widehat{\frac{\partial u_i}{\partial x_j}}, \widehat{\frac{\partial u_i}{\partial x_j}} \rangle = \frac{\partial^2 \hat{u}_i}{\partial z^2} \hat{u}_i^* + \frac{\partial \hat{u}_i}{\partial z} \frac{\partial \hat{u}_i^*}{\partial z} = \frac{\partial \frac{\partial \hat{u}_i}{\partial z} \hat{u}_i^*}{\partial z}$$

Integrate this term across the channel height:

$$\frac{1}{Re_\tau} \int_{-1}^{1} \frac{\partial^2 \hat{e}}{\partial x_j \partial x_j} \mathrm{d}z = \frac{1}{Re_\tau} \int_{-1}^{1} \frac{\partial \frac{\partial \hat{u}_i}{\partial z} \hat{u}_i^*}{\partial z} \mathrm{d}z = \frac{1}{Re_\tau} \frac{\partial \hat{u}_i}{\partial z} \hat{u}_i^* |_{-1}^{1} = 0 \tag{A.5}$$

where we use the no-slip and the impermeability boundary condition: $\hat{u}_i^*(\pm 1) = 0$. Combining equations (A.3), (A.4) and (A.5), we arrive at the wall-normal integrated energy transfer balance (4.3a).

$$\overline{\frac{\partial \hat{E}(k_x, k_y)}{\partial t}} = \underbrace{-\overline{\langle \hat{u}, \frac{\mathrm{d}U}{\mathrm{d}z} \hat{w} \rangle_I}}_{\hat{P}(k_x,k_y)} \underbrace{- \frac{1}{Re_\tau} \overline{\langle \widehat{\frac{\partial u_i}{\partial x_j}}, \widehat{\frac{\partial u_i}{\partial x_j}} \rangle_I}}_{\hat{D}(k_x,k_y)} \underbrace{- \overline{\langle \hat{u}_i, \widehat{\frac{\partial u_i u_j}{\partial x_j}} \rangle_I}}_{\hat{N}(k_x,k_y)}$$

The sign $\langle\ ,\ \rangle_I$ in (4.3a) represents the inner product defined as $\langle \boldsymbol{c}_1, \boldsymbol{c}_2 \rangle_I = \frac{1}{2}\int_{-1}^{1} \boldsymbol{c}_1^* \boldsymbol{c}_2 \, \mathrm{d}z = \boldsymbol{c}_1^* W \boldsymbol{c}_2$. where $\boldsymbol{c}_1$ and $\boldsymbol{c}_2$ are two complex vectors. In this study, $\boldsymbol{c}_1$ and $\boldsymbol{c}_2$ store the variables on the Chebyshev grid points in the wall-normal direction, and W is a weight matrix derived from the Clenshaw–Curtis quadrature.

A.3 Full expression of $\hat{M}_{(s_x,s_y)(k_x,k_y)}$

Mode-to-mode nonlinear energy transfer $\hat{M}$ could be formulated at one wall-normal height. First, we look at $\hat{N}$:

$$\hat{N}(k_x,k_y) = -\langle \hat{u}_i^{(k_x,k_y)}, \widehat{\frac{\partial u_i u_j}{\partial x_j}}^{(k_x,k_y)} \rangle \overset{\text{continuity}}{=} -\langle \hat{u}_i^{(k_x,k_y)}, \widehat{u_j \frac{\partial u_i}{\partial x_j}}^{(k_x,k_y)} \rangle$$

If we assign $f_i = -u_j \frac{\partial u_i}{\partial x_j}$, $\hat{N}$ could be expressed according to three different cases:

$$\begin{aligned} \underset{(k_x,k_y\in\mathbb{R}^+)}{\hat{N}(k_x,k_y)} &= (\hat{f}_i^{(k_x,k_y)} \hat{u}_i^{(-k_x,-k_y)} + \hat{f}_i^{(-k_x,k_y)} \hat{u}_i^{(k_x,-k_y)} + \text{c.c.}) \\ &= 2\text{Real}\{\hat{f}_i^{(k_x,k_y)} \hat{u}_i^{(-k_x,-k_y)} + \hat{f}_i^{(-k_x,k_y)} \hat{u}_i^{(k_x,-k_y)}\} \end{aligned} \tag{A.6a}$$

$$\underset{(k_y\in\mathbb{R}^+)}{\hat{N}(0,k_y)} = (\hat{f}_i^{(0,k_y)} \hat{u}_i^{(0,-k_y)} + \text{c.c.}) = 2\text{Real}\{\hat{f}_i^{(0,k_y)} \hat{u}_i^{(0,-k_y)}\} \tag{A.6b}$$

$$\underset{(k_x\in\mathbb{R}^+)}{\hat{N}(k_x,0)} = (\hat{f}_i^{(k_x,0)} \hat{u}_i^{(-k_x,0)} + \text{c.c.}) = 2\text{Real}\{\hat{f}_i^{(k_x,0)} \hat{u}_i^{(-k_x,0)}\} \tag{A.6c}$$

where c.c. represents conjugate terms.

From the dyadic interactions in the wavenumber space, $\hat{f}_i^{(k_x,k_y)}$ could be expressed as:

$$\begin{aligned} \hat{f}_i^{(k_x,k_y)} = &- \sum_{s_x,s_y\in\mathbb{R}^+} (\hat{u}_j^{(k_x-s_x,k_y-s_y)} \widehat{\frac{\partial u_i}{\partial x_j}}^{(s_x,s_y)} + \hat{u}_j^{(k_x+s_x,k_y+s_y)} \widehat{\frac{\partial u_i}{\partial x_j}}^{(-s_x,-s_y)} + \hat{u}_j^{(k_x+s_x,k_y-s_y)} \widehat{\frac{\partial u_i}{\partial x_j}}^{(-s_x,s_y)} + \hat{u}_j^{(k_x-s_x,k_y+s_y)} \widehat{\frac{\partial u_i}{\partial x_j}}^{(s_x,-s_y)}) \\ &- \sum_{s_y\in\mathbb{R}^+} (\hat{u}_j^{(k_x,k_y-s_y)} \widehat{\frac{\partial u_i}{\partial x_j}}^{(0,s_y)} + \hat{u}_j^{(k_x,k_y+s_y)} \widehat{\frac{\partial u_i}{\partial x_j}}^{(0,-s_y)}) \\ &- \sum_{s_x\in\mathbb{R}^+} (\hat{u}_j^{(k_x-s_x,k_y)} \widehat{\frac{\partial u_i}{\partial x_j}}^{(s_x,0)} + \hat{u}_j^{(k_x+s_x,k_y)} \widehat{\frac{\partial u_i}{\partial x_j}}^{(-s_x,0)}) \end{aligned} \tag{A.7}$$

Substitute equation (A.7) into equation (A.6a):

$$
\begin{aligned}
\hat{N}(k_x,k_y) = \{ & \\
& -2\mathrm{Real}\{ \sum_{s_x,s_y\in\mathbb{R}^+} \overbrace{(\hat{u}_j^{(k_x-s_x,k_y-s_y)} \widehat{\frac{\partial u_i}{\partial x_j}}^{(s_x,s_y)} \hat{u}_i^{(-k_x,-k_y)} + \hat{u}_j^{(k_x+s_x,k_y+s_y)} \widehat{\frac{\partial u_i}{\partial x_j}}^{(-s_x,-s_y)} \hat{u}_i^{(-k_x,-k_y)}}^{\text{contribution from } (s_x,s_y)} \\
& \underbrace{+ \hat{u}_j^{(k_x+s_x,k_y-s_y)} \widehat{\frac{\partial u_i}{\partial x_j}}^{(-s_x,s_y)} \hat{u}_i^{(-k_x,-k_y)} + \hat{u}_j^{(k_x-s_x,k_y+s_y)} \widehat{\frac{\partial u_i}{\partial x_j}}^{(s_x,-s_y)} \hat{u}_i^{(-k_x,-k_y)})}_{\text{contribution from } (s_x,s_y)} \\
& - \sum_{s_y\in\mathbb{R}^+} \underbrace{(\hat{u}_j^{(k_x,k_y-s_y)} \widehat{\frac{\partial u_i}{\partial x_j}}^{(0,s_y)} \hat{u}_i^{(-k_x,-k_y)} + \hat{u}_j^{(k_x,k_y+s_y)} \widehat{\frac{\partial u_i}{\partial x_j}}^{(0,-s_y)} \hat{u}_i^{(-k_x,-k_y)})}_{\text{contribution from } (0,s_y)} \\
& - \sum_{s_x\in\mathbb{R}^+} \underbrace{(\hat{u}_j^{(k_x-s_x,k_y)} \widehat{\frac{\partial u_i}{\partial x_j}}^{(s_x,0)} \hat{u}_i^{(-k_x,-k_y)} + \hat{u}_j^{(k_x+s_x,k_y)} \widehat{\frac{\partial u_i}{\partial x_j}}^{(-s_x,0)} \hat{u}_i^{(-k_x,-k_y)})}_{\text{contribution from } (s_x,0)} \} \\
& -2\mathrm{Real}\{ \sum_{s_x,s_y\in\mathbb{R}^+} \overbrace{(\hat{u}_j^{(-k_x-s_x,k_y-s_y)} \widehat{\frac{\partial u_i}{\partial x_j}}^{(s_x,s_y)} \hat{u}_i^{(k_x,-k_y)} + \hat{u}_j^{(-k_x+s_x,k_y+s_y)} \widehat{\frac{\partial u_i}{\partial x_j}}^{(-s_x,-s_y)} \hat{u}_i^{(k_x,-k_y)}}^{\text{contribution from } (s_x,s_y)} \\
& \underbrace{+ \hat{u}_j^{(-k_x+s_x,k_y-s_y)} \widehat{\frac{\partial u_i}{\partial x_j}}^{(-s_x,s_y)} \hat{u}_i^{(k_x,-k_y)} + \hat{u}_j^{(-k_x-s_x,k_y+s_y)} \widehat{\frac{\partial u_i}{\partial x_j}}^{(s_x,-s_y)} \hat{u}_i^{(k_x,-k_y)})}_{\text{contribution from } (s_x,s_y)} \\
& - \sum_{s_y\in\mathbb{R}^+} \underbrace{(\hat{u}_j^{(-k_x,k_y-s_y)} \widehat{\frac{\partial u_i}{\partial x_j}}^{(0,s_y)} \hat{u}_i^{(k_x,-k_y)} + \hat{u}_j^{(-k_x,k_y+s_y)} \widehat{\frac{\partial u_i}{\partial x_j}}^{(0,-s_y)} \hat{u}_i^{(k_x,-k_y)})}_{\text{contribution from } (0,s_y)} \\
& - \sum_{s_x\in\mathbb{R}^+} \underbrace{(\hat{u}_j^{(-k_x-s_x,k_y)} \widehat{\frac{\partial u_i}{\partial x_j}}^{(s_x,0)} \hat{u}_i^{(k_x,-k_y)} + \hat{u}_j^{(-k_x+s_x,k_y)} \widehat{\frac{\partial u_i}{\partial x_j}}^{(-s_x,0)} \hat{u}_i^{(k_x,-k_y)})}_{\text{contribution from } (s_x,0)} \}
\end{aligned}
\tag{A.8}
$$

We see the contributions from modes (s_x,s_y), $(0,s_y)$ and $(s_x,0)$ to mode (k_x,k_y). Following this, we can form the terms $\hat{M}_{(s_x,s_y)(k_x,k_y)}$, $\hat{M}_{(0,s_y)(k_x,k_y)}$ and $\hat{M}_{(s_x,0)(k_x,k_y)}$, as shown in equations (A.11a), (A.11b) and (A.11c).

Substitute equation (A.7) into equation (A.6b):

$$
\begin{aligned}
\hat{N}(0,k_y) = -2\text{Real}\{ & \\
& \sum_{s_x,s_y\in\mathbb{R}^+} \overbrace{(\hat{u}_j^{(-s_x,k_y-s_y)} \widehat{\frac{\partial u_i}{\partial x_j}}^{(s_x,s_y)} \hat{u}_i^{(0,-k_y)} + \hat{u}_j^{(s_x,k_y+s_y)} \widehat{\frac{\partial u_i}{\partial x_j}}^{(-s_x,-s_y)} \hat{u}_i^{(0,-k_y)}}^{\text{contribution from } (s_x,s_y)} \\
& \underbrace{+ \hat{u}_j^{(s_x,k_y-s_y)} \widehat{\frac{\partial u_i}{\partial x_j}}^{(-s_x,s_y)} \hat{u}_i^{(0,-k_y)} + \hat{u}_j^{(-s_x,k_y+s_y)} \widehat{\frac{\partial u_i}{\partial x_j}}^{(s_x,-s_y)} \hat{u}_i^{(0,-k_y)})}_{\text{contribution from } (s_x,s_y)} \\
& - \sum_{s_y\in\mathbb{R}^+} \underbrace{(\hat{u}_j^{(0,k_y-s_y)} \widehat{\frac{\partial u_i}{\partial x_j}}^{(0,s_y)} \hat{u}_i^{(0,-k_y)} + \hat{u}_j^{(0,k_y+s_y)} \widehat{\frac{\partial u_i}{\partial x_j}}^{(0,-s_y)} \hat{u}_i^{(0,-k_y)})}_{\text{contribution from } (0,s_y)} \\
& - \sum_{s_x\in\mathbb{R}^+} \underbrace{(\hat{u}_j^{(-s_x,k_y)} \widehat{\frac{\partial u_i}{\partial x_j}}^{(s_x,0)} \hat{u}_i^{(0,-k_y)} + \hat{u}_j^{(s_x,k_y)} \widehat{\frac{\partial u_i}{\partial x_j}}^{(-s_x,0)} \hat{u}_i^{(0,-k_y)})}_{\text{contribution from } (s_x,0)} \}
\end{aligned}
\tag{A.9}
$$

We see the contributions from modes (s_x,s_y), $(0,s_y)$ and $(s_x,0)$ to mode $(0,k_y)$. Following this, we can form the terms $\hat{M}_{(s_x,s_y)(0,k_y)}$, $\hat{M}_{(0,s_y)(0,k_y)}$ and $\hat{M}_{(s_x,0)(0,k_y)}$, as shown in equations (A.11d), (A.11e) and (A.11f).

Substitute equation (A.7) into equation (A.6c):

$$
\begin{aligned}
\hat{N}(k_x,0) = -2\text{Real}\{ & \\
& \sum_{s_x,s_y\in\mathbb{R}^+} \overbrace{(\hat{u}_j^{(k_x-s_x,-s_y)} \widehat{\frac{\partial u_i}{\partial x_j}}^{(s_x,s_y)} \hat{u}_i^{(-k_x,0)} + \hat{u}_j^{(k_x+s_x,s_y)} \widehat{\frac{\partial u_i}{\partial x_j}}^{(-s_x,-s_y)} \hat{u}_i^{(-k_x,0)}}^{\text{contribution from } (s_x,s_y)} \\
& \underbrace{+ \hat{u}_j^{(k_x+s_x,-s_y)} \widehat{\frac{\partial u_i}{\partial x_j}}^{(-s_x,s_y)} \hat{u}_i^{(-k_x,0)} + \hat{u}_j^{(k_x-s_x,s_y)} \widehat{\frac{\partial u_i}{\partial x_j}}^{(s_x,-s_y)} \hat{u}_i^{(-k_x,0)})}_{\text{contribution from } (s_x,s_y)} \\
& - \sum_{s_y\in\mathbb{R}^+} \underbrace{(\hat{u}_j^{(k_x,-s_y)} \widehat{\frac{\partial u_i}{\partial x_j}}^{(0,s_y)} \hat{u}_i^{(-k_x,0)} + \hat{u}_j^{(k_x,s_y)} \widehat{\frac{\partial u_i}{\partial x_j}}^{(0,-s_y)} \hat{u}_i^{(-k_x,0)})}_{\text{contribution from } (0,s_y)} \\
& - \sum_{s_x\in\mathbb{R}^+} \underbrace{(\hat{u}_j^{(k_x-s_x,0)} \widehat{\frac{\partial u_i}{\partial x_j}}^{(s_x,0)} \hat{u}_i^{(-k_x,0)} + \hat{u}_j^{(k_x+s_x,0)} \widehat{\frac{\partial u_i}{\partial x_j}}^{(-s_x,0)} \hat{u}_i^{(-k_x,0)})}_{\text{contribution from } (s_x,0)} \}
\end{aligned}
\tag{A.10}
$$

We see the contributions from modes (s_x, s_y), $(0, s_y)$ and $(s_x, 0)$ to mode $(k_x, 0)$. Following this, we can form the terms $\hat{M}_{(s_x,s_y)(k_x,0)}$, $\hat{M}_{(0,s_y)(k_x,0)}$ and $\hat{M}_{(s_x,0)(k_x,0)}$, as shown in equations (A.11g), (A.11h) and (A.11i).

The mode-to-mode nonlinear transfer for nine different cases is summarised here:

$$\begin{aligned}
\hat{M}_{(s_x,s_y)(k_x,k_y)} = -2\text{Real}\{ & \\
& \hat{u}_j^{(k_x-s_x,k_y-s_y)} \widehat{\frac{\partial u_i}{\partial x_j}}^{(s_x,s_y)} \hat{u}_i^{(-k_x,-k_y)} + \hat{u}_j^{(k_x+s_x,k_y+s_y)} \widehat{\frac{\partial u_i}{\partial x_j}}^{(-s_x,-s_y)} \hat{u}_i^{(-k_x,-k_y)} + \\
& \hat{u}_j^{(k_x+s_x,k_y-s_y)} \widehat{\frac{\partial u_i}{\partial x_j}}^{(-s_x,s_y)} \hat{u}_i^{(-k_x,-k_y)} + \hat{u}_j^{(k_x-s_x,k_y+s_y)} \widehat{\frac{\partial u_i}{\partial x_j}}^{(s_x,-s_y)} \hat{u}_i^{(-k_x,-k_y)} + \\
& \hat{u}_j^{(-k_x-s_x,k_y-s_y)} \widehat{\frac{\partial u_i}{\partial x_j}}^{(s_x,s_y)} \hat{u}_i^{(k_x,-k_y)} + \hat{u}_j^{(-k_x+s_x,k_y+s_y)} \widehat{\frac{\partial u_i}{\partial x_j}}^{(-s_x,-s_y)} \hat{u}_i^{(k_x,-k_y)} + \\
& \hat{u}_j^{(-k_x+s_x,k_y-s_y)} \widehat{\frac{\partial u_i}{\partial x_j}}^{(-s_x,s_y)} \hat{u}_i^{(k_x,-k_y)} + \hat{u}_j^{(-k_x-s_x,k_y+s_y)} \widehat{\frac{\partial u_i}{\partial x_j}}^{(s_x,-s_y)} \hat{u}_i^{(k_x,-k_y)} \}
\end{aligned} \tag{A.11a}$$

$$\begin{aligned}
\hat{M}_{(0,s_y)(k_x,k_y)} = -2\text{Real}\{ & \\
& \hat{u}_j^{(k_x,k_y-s_y)} \widehat{\frac{\partial u_i}{\partial x_j}}^{(0,s_y)} \hat{u}_i^{(-k_x,-k_y)} + \hat{u}_j^{(k_x,k_y+s_y)} \widehat{\frac{\partial u_i}{\partial x_j}}^{(0,-s_y)} \hat{u}_i^{(-k_x,-k_y)} + \hat{u}_j^{(-k_x,k_y-s_y)} \widehat{\frac{\partial u_i}{\partial x_j}}^{(0,s_y)} \hat{u}_i^{(k_x,-k_y)} + \hat{u}_j^{(-k_x,k_y+s_y)} \widehat{\frac{\partial u_i}{\partial x_j}}^{(0,-s_y)} \hat{u}_i^{(k_x,-k_y)} \}
\end{aligned} \tag{A.11b}$$

$$\begin{aligned}
\hat{M}_{(s_x,0)(k_x,k_y)} = -2\text{Real}\{ & \\
& \hat{u}_j^{(k_x-s_x,k_y)} \widehat{\frac{\partial u_i}{\partial x_j}}^{(s_x,0)} \hat{u}_i^{(-k_x,-k_y)} + \hat{u}_j^{(k_x+s_x,k_y)} \widehat{\frac{\partial u_i}{\partial x_j}}^{(-s_x,0)} \hat{u}_i^{(-k_x,-k_y)} + \hat{u}_j^{(-k_x-s_x,k_y)} \widehat{\frac{\partial u_i}{\partial x_j}}^{(s_x,0)} \hat{u}_i^{(k_x,-k_y)} + \hat{u}_j^{(-k_x+s_x,k_y)} \widehat{\frac{\partial u_i}{\partial x_j}}^{(-s_x,0)} \hat{u}_i^{(k_x,-k_y)} \}
\end{aligned} \tag{A.11c}$$

$$\begin{aligned}
\hat{M}_{(s_x,s_y)(0,k_y)} = -2\text{Real}\{ & \\
& \hat{u}_j^{(-s_x,k_y-s_y)} \widehat{\frac{\partial u_i}{\partial x_j}}^{(s_x,s_y)} \hat{u}_i^{(0,-k_y)} + \hat{u}_j^{(s_x,k_y+s_y)} \widehat{\frac{\partial u_i}{\partial x_j}}^{(-s_x,-s_y)} \hat{u}_i^{(0,-k_y)} + \hat{u}_j^{(s_x,k_y-s_y)} \widehat{\frac{\partial u_i}{\partial x_j}}^{(-s_x,s_y)} \hat{u}_i^{(0,-k_y)} + \hat{u}_j^{(-s_x,k_y+s_y)} \widehat{\frac{\partial u_i}{\partial x_j}}^{(s_x,-s_y)} \hat{u}_i^{(0,-k_y)} \}
\end{aligned} \tag{A.11d}$$

$$\hat{M}_{(0,s_y)(0,k_y)} = -2\text{Real}\{\hat{u}_j^{(0,k_y-s_y)} \widehat{\frac{\partial u_i}{\partial x_j}}^{(0,s_y)} \hat{u}_i^{(0,-k_y)} + \hat{u}_j^{(0,k_y+s_y)} \widehat{\frac{\partial u_i}{\partial x_j}}^{(0,-s_y)} \hat{u}_i^{(0,-k_y)}\} \tag{A.11e}$$

$$\hat{M}_{(s_x,0)(0,k_y)} = -2\text{Real}\{\hat{u}_j^{(-s_x,k_y)} \widehat{\frac{\partial u_i}{\partial x_j}}^{(s_x,0)} \hat{u}_i^{(0,-k_y)} + \hat{u}_j^{(s_x,k_y)} \widehat{\frac{\partial u_i}{\partial x_j}}^{(-s_x,0)} \hat{u}_i^{(0,-k_y)}\} \tag{A.11f}$$

$$\hat{M}_{(s_x,s_y)(k_x,0)} = -2\text{Real}\{$$
$$\hat{u}_j^{(k_x-s_x,-s_y)}\widehat{\frac{\partial u_i}{\partial x_j}}^{(s_x,s_y)}\hat{u}_i^{(-k_x,0)} + \hat{u}_j^{(k_x+s_x,s_y)}\widehat{\frac{\partial u_i}{\partial x_j}}^{(-s_x,-s_y)}\hat{u}_i^{(-k_x,0)} + \hat{u}_j^{(k_x+s_x,-s_y)}\widehat{\frac{\partial u_i}{\partial x_j}}^{(-s_x,s_y)}\hat{u}_i^{(-k_x,0)} + \hat{u}_j^{(k_x-s_x,s_y)}\widehat{\frac{\partial u_i}{\partial x_j}}^{(s_x,-s_y)}\hat{u}_i^{(-k_x,0)}\} \tag{A.11g}$$

$$\hat{M}_{(0,s_y)(k_x,0)} = -2\text{Real}\{\hat{u}_j^{(k_x,-s_y)}\widehat{\frac{\partial u_i}{\partial x_j}}^{(0,s_y)}\hat{u}_i^{(-k_x,0)} + \hat{u}_j^{(k_x,s_y)}\widehat{\frac{\partial u_i}{\partial x_j}}^{(0,-s_y)}\hat{u}_i^{(-k_x,0)}\} \tag{A.11h}$$

$$\hat{M}_{(s_x,s_y)(k_x,0)} = -2\text{Real}\{\hat{u}_j^{(k_x-s_x,0)}\widehat{\frac{\partial u_i}{\partial x_j}}^{(s_x,0)}\hat{u}_i^{(-k_x,0)} + \hat{u}_j^{(k_x+s_x,0)}\widehat{\frac{\partial u_i}{\partial x_j}}^{(-s_x,0)}\hat{u}_i^{(-k_x,0)}\} \tag{A.11i}$$

A.4 Proof of $\hat{M}_{(s_x,s_y)(k_x,k_y)} = -\hat{M}_{(k_x,k_y)(s_x,s_y)}$

Note that $\hat{M}_{(s_x,s_y)(k_x,k_y)} = -\hat{M}_{(k_x,k_y)(s_x,s_y)}$ only satisfies for wall-normal integrated $\hat{M}$. Two identities described below are used.

First, for three complex variables a, b and c: $\text{Real}\{abc\} = \text{Real}\{a^*b^*c^*\}$.

Second, for any set of triadic interaction, there exists a relationship that involves swapping the Fourier modes between the second and the third terms.

$$-\int \hat{u}_j^{(k_x-s_x,k_y-s_y)}\widehat{\frac{\partial u_i}{\partial x_j}}^{(s_x,s_y)}\hat{u}_i^{(-k_x,-k_y)}\mathrm{d}z = \int \hat{u}_j^{(k_x-s_x,k_y-s_y)}\widehat{\frac{\partial u_i}{\partial x_j}}^{(-k_x,-k_y)}\hat{u}_i^{(s_x,s_y)}\mathrm{d}z$$

Proof.

$$\begin{aligned}
&\int \hat{u}_j^{(k_x-s_x,k_y-s_y)}\widehat{\frac{\partial u_i}{\partial x_j}}^{(s_x,s_y)}\hat{u}_i^{(-k_x,-k_y)}\mathrm{d}z + \int \hat{u}_j^{(k_x-s_x,k_y-s_y)}\widehat{\frac{\partial u_i}{\partial x_j}}^{(-k_x,-k_y)}\hat{u}_i^{(s_x,s_y)}\mathrm{d}z \\
&= \int \hat{u}_j^{(k_x-s_x,k_y-s_y)}\frac{\partial \hat{u}_i^{(s_x,s_y)}\hat{u}_i^{(-k_x,-k_y)}}{\partial x_j}\mathrm{d}z \\
&= \int (\hat{u}_j^{(k_x-s_x,k_y-s_y)}\frac{\partial \hat{u}_i^{(s_x,s_y)}\hat{u}_i^{(-k_x,-k_y)}}{\partial x_j} + \frac{\partial \hat{u}_j^{(k_x-s_x,k_y-s_y)}}{\partial x_j}\hat{u}_i^{(s_x,s_y)}\hat{u}_i^{(-k_x,-k_y)})\mathrm{d}z \\
&= \int \frac{\partial(\hat{u}_j^{(k_x-s_x,k_y-s_y)}\hat{u}_i^{(s_x,s_y)}\hat{u}_i^{(-k_x,-k_y)})}{\partial x_j}\mathrm{d}z \\
&= \hat{u}_j^{(k_x-s_x,k_y-s_y)}\hat{u}_i^{(s_x,s_y)}\hat{u}_i^{(-k_x,-k_y)}|_{-1}^{1} \\
&= 0
\end{aligned}$$

We use the continuity equation and the boundary conditions at the walls. □

We consider three different cases. For each case, we list the terms in $\hat{M}_{(s_x,s_y)(k_x,k_y)}$ in the left column and the terms in $\hat{M}_{(k_x,k_y)(s_x,s_y)}$ in the right column. Then we compare the left and right columns. For simplicity, we use Fourier modes to represent the terms. For example, $(k_x-s_x,k_y-s_y)(s_x,s_y)(-k_x,-k_y)$ means the term $\hat{u}_j^{(k_x-s_x,k_y-s_y)}\frac{\partial \hat{u}_i}{\partial x_j}^{(s_x,s_y)}\hat{u}_i^{(-k_x,-k_y)}$. The first identity indicates $(k_x-s_x,k_y-s_y)(s_x,s_y)(-k_x,-k_y)=(s_x-k_x,s_y-k_y)(-s_x,-s_y)(k_x,k_y)$ and the second identity indicates $(k_x-s_x,k_y-s_y)(s_x,s_y)(-k_x,-k_y)=-(k_x-s_x,k_y-s_y)(-k_x,-k_y)(s_x,s_y)$.

- $k_x,k_y,s_x,s_y\in\mathbb{R}^+$, according to equation (A.11a):

$\hat{M}_{(s_x,s_y)(k_x,k_y)}$	$\hat{M}_{(k_x,k_y)(s_x,s_y)}$
①$(k_x-s_x,k_y-s_y)(s_x,s_y)(-k_x,-k_y)$	$-$①$(s_x-k_x,s_y-k_y)(k_x,k_y)(-s_x,-s_y)$
②$(k_x+s_x,k_y+s_y)(-s_x,-s_y)(-k_x,-k_y)$	$-$②$(s_x+k_x,s_y+k_y)(-k_x,-k_y)(-s_x,-s_y)$
③$(k_x+s_x,k_y-s_y)(-s_x,s_y)(-k_x,-k_y)$	$-$⑤$(s_x+k_x,s_y-k_y)(-k_x,k_y)(-s_x,-s_y)$
④$(k_x-s_x,k_y+s_y)(s_x,-s_y)(-k_x,-k_y)$	$-$⑥$(s_x-k_x,s_y+k_y)(k_x,-k_y)(-s_x,-s_y)$
⑤$(-k_x-s_x,k_y-s_y)(s_x,s_y)(k_x,-k_y)$	$-$③$(-s_x-k_x,s_y-k_y)(k_x,k_y)(s_x,-s_y)$
⑥$(-k_x+s_x,k_y+s_y)(-s_x,-s_y)(k_x,-k_y)$	$-$④$(-s_x+k_x,s_y+k_y)(-k_x,-k_y)(s_x,-s_y)$
⑦$(-k_x+s_x,k_y-s_y)(-s_x,s_y)(k_x,-k_y)$	$-$⑦$(-s_x+k_x,s_y-k_y)(-k_x,-k_y)(s_x,-s_y)$
⑧$(-k_x-s_x,k_y+s_y)(s_x,-s_y)(k_x,-k_y)$	$-$⑧$(-s_x-k_x,s_y+k_y)(k_x,-k_y)(s_x,-s_y)$

- $k_x=0$ $k_y,s_x,s_y\in\mathbb{R}^+$, according to equation (A.11d):

$\hat{M}_{(s_x,s_y)(0,k_y)}$	$\hat{M}_{(0,k_y)(s_x,s_y)}$
①$(-s_x,k_y-s_y)(s_x,s_y)(0,-k_y)$	$-$①$(s_x,s_y-k_y)(0,k_y)(-s_x,-s_y)$
②$(s_x,k_y+s_y)(-s_x,-s_y)(0,-k_y)$	$-$②$(s_x,s_y+k_y)(0,-k_y)(-s_x,-s_y)$
③$(s_x,k_y-s_y)(-s_x,s_y)(0,-k_y)$	$-$③$(-s_x,s_y-k_y)(0,k_y)(s_x,-s_y)$
④$(-s_x,k_y+s_y)(s_x,-s_y)(0,-k_y)$	$-$④$(-s_x,s_y+k_y)(0,-k_y)(s_x,-s_y)$

  $\hat{M}_{(s_x,s_y)(k_x,0)}$ and $\hat{M}_{(k_x,0)(s_x,s_y)}$ could be listed similarly.

- $k_x,a=0$ $k_y,s_y\in\mathbb{R}^+$, according to equation (A.11e):

$\hat{M}_{(0,s_y)(0,k_y)}$	$\hat{M}_{(0,k_y)(0,s_y)}$
①$(0,k_y-s_y)(0,s_y)(0,-k_y)$	$-$①$(0,s_y-k_y)(0,k_y)(0,-s_y)$
②$(0,k_y+s_y)(0,-s_y)(0,-k_y)$	$-$②$(0,s_y+k_y)(0,-k_y)(0,-s_y)$

$\hat{M}_{(s_x,0)(k_x,0)}, \hat{M}_{(k_x,0)(s_x,0)}; \hat{M}_{(s_x,0)(0,k_y)}, \hat{M}_{(0,k_y)(s_x,0)}$ could be listed similarly.

Combining these three cases, we prove that the nonlinear energy transfer from mode (s_x, s_y) to mode (k_x, k_y) equals the opposite of the nonlinear energy transfer from mode (k_x, k_y) to mode (s_x, s_y):

$$\hat{M}_{(s_x,s_y)(k_x,k_y)} = -\hat{M}_{(k_x,k_y)(s_x,s_y)} \quad k_x, k_y, s_x, s_y \in \{\mathbb{R}^+ \cup 0\} \tag{A.12}$$

In addition, there is no nonlinear energy transfer from one mode to itself. This could be proved by setting $s_x = k_x$ and $s_y = k_y$ in equation (A.12).

$$\hat{M}_{(k_x,k_y)(k_x,k_y)} = 0 \tag{A.13}$$

Again, properties (A.12) and (A.13) are for wall-normal integrated $\hat{M}$.

A.5 The number of independent wall-normal integrated $\hat{M}_{(s_x,s_y)(k_x,k_y)}$

Assume that the streamwise wavenumber considered is $k_x = [0 : \Delta k_x : \max k_x]$ (starting from 0 and ending at $\max k_x$ with an interval of Δk_x) and the number of discrete k_x is N_{k_x}; the spanwise wavenumber considered is $k_y = [0 : \Delta k_y : \max k_y]$ and the number of discrete k_y is N_{k_y}. Then, the number of different wavenumber (k_x, k_y) excluding mode $(0,0)$ is $(N_{k_x}N_{k_y} - 1)$. Then, the number of $\hat{M}_{(s_x,s_y)(k_x,k_y)}$ is $(N_{k_x}N_{k_y} - 1)^2$. However, from the properties of the wall-normal integrated $\hat{M}$ as shown in (4.7) and (4.8), this number overcounts the independent wall-normal integrated $\hat{M}$.

From equation (4.8), we know that $\hat{M}_{(s_x,s_y)(k_x,k_y)} = 0$ if $(s_x, s_y) = (k_x, k_y)$. So, we can exclude the wavenumber pair $(s_x, s_y)(k_x, k_y)$ when $(s_x, s_y) = (k_x, k_y)$. The number of independent wall-normal integrated $\hat{M}_{(s_x,s_y)(k_x,k_y)}$ reduces to $(N_{k_x}N_{k_y} - 1)(N_{k_x}N_{k_y} - 2)$.

From Equation (4.7), we know that $\hat{M}_{(s_x,s_y)(k_x,k_y)} = -\hat{M}_{(k_x,k_y)(s_x,s_y)}$. This means that for every wavenumber pair $(s_x, s_y)(k_x, k_y)$, there is an reversed wavenumber pair $(k_x, k_y)(s_x, s_y)$ which shares the wall-normal integrated $\hat{M}$ with the same magnitude but the opposite sign. So, the number of independent wall-normal integrated $\hat{M}_{(s_x,s_y)(k_x,k_y)}$ further reduces to:

$$\frac{(N_{k_x}N_{k_y} - 1)(N_{k_x}N_{k_y} - 2)}{2} \tag{A.14}$$

Appendix B

Details of the estimation models

B.1 State-space form of the linear model

The detailed expressions for matrices $\mathscr{A}$, $\mathscr{B}$ and $\mathscr{C}$ of the state-space model (6.2) are:

$$\mathscr{A} = \begin{bmatrix} \Delta^{-1}\mathscr{L}_{OS} & 0 \\ -\mathrm{i}k_y \frac{\mathrm{d}U}{\mathrm{d}z} & \mathscr{L}_{SQ} \end{bmatrix} \tag{B.1a}$$

$$\mathscr{B} = \begin{bmatrix} -\mathrm{i}k_x\Delta^{-1}D & -\mathrm{i}k_y\Delta^{-1}D & -k^2\Delta^{-1} \\ -\mathrm{i}k_y & -\mathrm{i}k_x & 0 \end{bmatrix} \tag{B.1b}$$

$$\mathscr{C} = \frac{1}{k^2}\begin{bmatrix} \mathrm{i}k_x D & -\mathrm{i}k_y \\ \mathrm{i}k_y D & \mathrm{i}k_x \\ k^2 & 0 \end{bmatrix} \tag{B.1c}$$

with boundary conditions $\hat{\boldsymbol{w}}(t) = \frac{\partial\hat{\boldsymbol{w}}}{\partial z}(t) = \hat{\boldsymbol{\eta}}(t) = 0$ at the two walls. $\mathrm{i} = \sqrt{-1}$ is the imaginary unit. D is the differentiation matrix in the wall-normal direction; $k^2 = k_x^2 + k_y^2$; $\Delta = \mathscr{D}^2 - k^2$ is the Laplacian operator; and $\mathscr{L}_{OS}$ and $\mathscr{L}_{SQ}$ are the Orr-Sommerfeld and Squire operators, respectively:

$$\mathscr{L}_{OS} = -\mathrm{i}k_x U\Delta + \mathrm{i}k_x\frac{\mathrm{d}^2U}{\mathrm{d}z^2} + \frac{1}{Re_\tau}\Delta^2 \tag{B.2a}$$

$$\mathscr{L}_{SQ} = -\mathrm{i}k_x U + \frac{1}{Re_\tau}\Delta \tag{B.2b}$$

The operators are discretised using the Chebyshev polynomial in the wall-normal direction (Trefethen, 2000). The boundary conditions at the walls are implemented following Trefethen (2000); Weideman & Reddy (2000). The integration in the wall-normal direction is implemented using Clenshaw-Curtis quadrature (Trefethen, 2000).

The linear model (6.2) is a building block for the linear and nonlinear estimators.

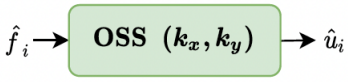

Figure B.1: The Orr-Sommerfeld & Squire state-space model (6.2) maps the nonlinear forcing $\hat{f}_i$ to the velocities $\hat{u}_i$ at a single wavenumber pair (k_x, k_y) in Fourier space.

For the linear model with eddy viscosity (6.10), $\mathscr{L}_{OS}$ and $\mathscr{L}_{SQ}$ change to:

$$\mathscr{L}_{OS} = -\mathrm{i}k_x U\Delta + \mathrm{i}k_x \frac{\mathrm{d}^2 U}{\mathrm{d}z^2} + \frac{1}{Re_\tau}\frac{\nu_T}{\nu}\Delta^2 + 2\frac{1}{Re_\tau}\frac{1}{\nu}\frac{\mathrm{d}\nu_T}{\mathrm{d}z}D\Delta + \frac{1}{Re_\tau}\frac{1}{\nu}\frac{\mathrm{d}^2\nu_T}{\mathrm{d}z^2}(D^2+k^2) \tag{B.3a}$$

$$\mathscr{L}_{SQ} = -\mathrm{i}k_x U + \frac{1}{Re_\tau}\frac{\nu_T}{\nu}\Delta + \frac{1}{Re_\tau}\frac{1}{\nu}\frac{\mathrm{d}\nu_T}{\mathrm{d}z}D \tag{B.3b}$$

B.2 More details about the linear estimator

The linear estimator (6.4) is implemented at one wavenumber pair (k_x, k_y). For the wavenumber range considered, multiple Kalman filters at different wavenumber pairs are implemented in parallel. Algorithm 1 details the processes of the linear estimation and the structure of the linear estimator is illustrated in figure B.2.

Algorithm 1: Linear Estimation

Input: measurement data y_{mea}, considered wavenumber pairs, measurement sampling time ΔT_m

Output: estimated velocities $\hat{x}_{est}$

Kalman filter estimation (every measurement sampling time ΔT_m):

- obtain the measurement data y_{mea} in physical space
- take the 2-D Fourier transform to get $\hat{y}_{mea}$ in wavenumber space
- **for** *every* (k_x, k_y) *considered* **do**
  - use the Kalman filter to get the estimated velocities $\hat{x}_{est}$ in wavenumber space:

$$\frac{\mathrm{d}}{\mathrm{d}t}\hat{\boldsymbol{x}}_{est} = \mathscr{A}\hat{\boldsymbol{x}}_{est}(t) + \mathscr{L}[\hat{\boldsymbol{y}}_{mea}(t) - \mathscr{C}_{mea}\hat{\boldsymbol{x}}_{est}(t)]$$

  `/* the marching time step for Kalman filter is` ΔT_m `*/`

- take the inverse 2-D Fourier transform to get x_{est} in physical space

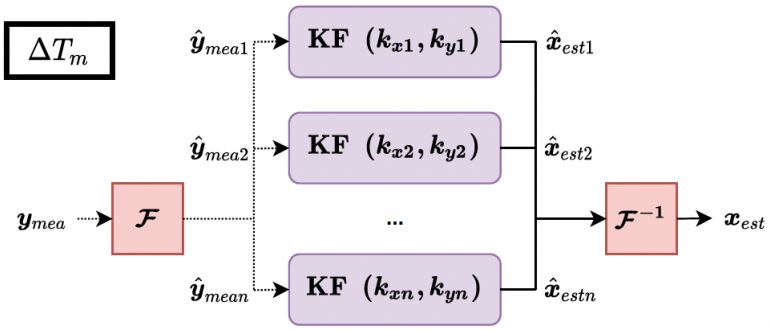

Figure B.2: The structure of the linear estimator corresponding to the diagram in figure 6.1. $\mathscr{F}$ represents the Fourier transform and $\mathscr{F}^{-1}$ represents the inverse Fourier transform. Each Kalman filter (KF) receives the measurement $\hat{\boldsymbol{y}}_{mea}$ and outputs the estimated full state $\hat{\boldsymbol{x}}_{est}$. Each Kalman filter is implemented in Fourier space at measurement sampling time ΔT_m.

B.3 More details about the nonlinear estimator

The main idea of the nonlinear estimator is that we close the loop of the linear estimator in figure B.2 by considering the nonlinear dynamics in physical space $f_i = -u_j \frac{\partial u_i}{\partial x_j}$. Algorithm 2 details the processes of the nonlinear estimation and the structure of the nonlinear estimator is illustrated in figure B.3. Since estimation processes at different wavenumbers are independent, parallel programming could be used to accelerate the computation (Kepner, 2009).

Algorithm 2: Nonlinear Estimation

Input: measurement data y_{mea}, considered wavenumber pairs, measurement sampling time ΔT_m

Output: estimated velocities $\hat{x}_{est}$

Kalman filter estimation (every measurement sampling time ΔT_m):

- obtain the measurement data y_{mea} and nonlinear forcing f_i in physical space
- take the 2-D Fourier transform to get $\hat{y}_{mea}$ and $\hat{f}_i$ in wavenumber space
- **for** *every* (k_x, k_y) *considered* **do**
  - use the Kalman filter to get the estimated velocities $\hat{x}_{est}$ in wavenumber space:

$$\frac{\mathrm{d}}{\mathrm{d}t}\hat{\boldsymbol{x}}_{est} = \mathscr{A}\hat{\boldsymbol{x}}_{est}(t) + \mathscr{B}\hat{\boldsymbol{f}}(t) + \mathscr{L}[\hat{\boldsymbol{y}}_{mea}(t) - \mathscr{C}_{mea}\hat{\boldsymbol{x}}_{est}(t)]$$

  `/* the marching time step for Kalman filter is` ΔT_m `*/`
- take the inverse 2-D Fourier transform to get x_{est} in physical space
- use the nonlinear dynamic to get the nonlinear forcing f_i in physical space:

$$f_i = -u_j \frac{\partial u_i}{\partial x_j}$$

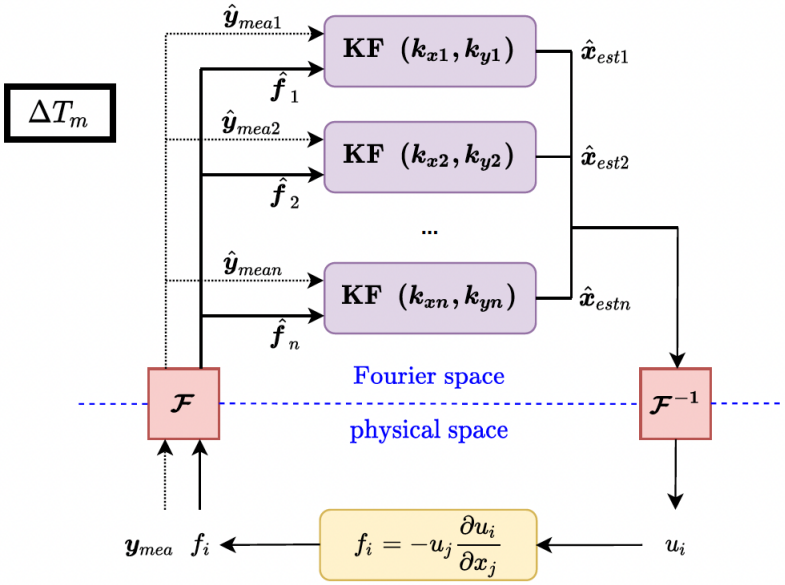

Figure B.3: The structure of the nonlinear estimator corresponding to the diagram in figure 6.2. For each Kalman filter at a single wavenumber pair (k_x, k_y), it receives the nonlinear forcing $\hat{\boldsymbol{f}}$ and measurement data $\hat{\boldsymbol{y}}_{mea}$, and outputs the estimated full velocity state $\hat{\boldsymbol{x}}_{est}$. The nonlinear forcing is explicitly calculated from the previously estimated velocities in physical space. Each Kalman filter is implemented in Fourier space at measurement sampling time ΔT_m.

B.4 State-space reduced-order model simulation

The state-space reduced-order model (SSROM) serves for autonomous simulations and is a key component of the revised nonlinear estimator 6.4. The basic idea is to use nonlinear forcing $\hat{f}_i$ to drive the OSS state-space model in figure B.1 to obtain velocities $\hat{u}_i$ in Fourier space and to use the nonlinear dynamics $f_i = -u_j \frac{\partial u_i}{\partial x_j}$ to link the velocities u_i back to nonlinear forcing f_i in physical space. To comply with the estimation setting in which we only consider the large scales, this autonomous simulation model only considers the same large scales as well. Since the total number of wavenumber pairs considered is much smaller than that considered in a DNS, we call this autonomous simulation model 'state-space reduced-order model (SSROM) simulation'. Algorithm 3 details the processes of the SSROM simulation and the structure of the SSROM simulation is illustrated in figure B.4.

The stability of the SSROM simulation is determined by the simulation time step ΔT_s. For a certain range of wavenumbers considered, ΔT_s needs to be set small enough to avoid divergence. In this study, ΔT_s needs to be set small enough for the SSROM simulation to 'survive' the measurement sampling time ΔT_m for a smooth implementation of the

nonlinear estimation.

Algorithm 3: State-Space Reduced-Order Model (SSROM) Simulation

Input: initial velocity fields u_{i0}, considered wavenumber pairs, SSROM simulation time step ΔT_s, total simulation time T_{end}

Output: simulated velocities u_i

SSROM simulation (running at ΔT_s):

- create a counter: $n_{SSROM} = 0$
- use the nonlinear dynamic to get the initial nonlinear forcing f_{i0} in physical space:

$$f_{i0} = -u_{j0}\frac{\partial u_{i0}}{\partial x_{j0}}$$

- **while** $n_{SSROM} < \frac{T_{end}}{\Delta T_s}$ **do**
  - take the 2-D Fourier transform to get the nonlinear forcing $\hat{f}_i$ in wavenumber space
  - **for** *every* (k_x, k_y) *considered* **do**
    - use the Orr-Sommerfeld & Squire state-space model to get the velocity $\hat{u}_i$ in wavenumber space
    - `/* the marching time step for the OSS state-space model is` ΔT_s `*/`
  - take the inverse 2-D Fourier transform to get the velocities u_i in physical space
  - use the nonlinear dynamic to get the nonlinear forcing f_i in physical space:

$$f_i = -u_j\frac{\partial u_i}{\partial x_j}$$

  - $n_{SSROM} = n_{SSROM} + 1$

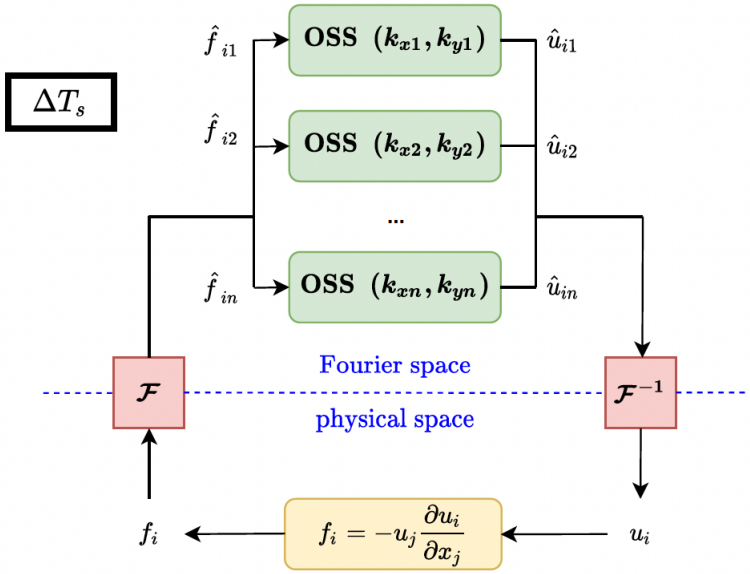

Figure B.4: The structure of state-space reduced-order model (SSROM) simulation. The upper part above the blue dashed line is implemented in Fourier space and the lower part below the blue dashed line is implemented in physical space. The SSROM simulation is implemented at the simulation time step ΔT_s.

B.5 More details about the revised nonlinear estimator

The nonlinear estimator illustrated in figure B.3 gives divergent estimation results easily if the measurement sampling time ΔT_m is not small enough. To overcome this problem, we embed the SSROM simulation running at a time step of ΔT_s ($\Delta T_s \ll \Delta T_m$) between two consecutive Kalman filter updates separated by measurement sampling time ΔT_m. Algorithm 4 details the processes of the revised nonlinear estimation and the structure of the revised nonlinear estimator is illustrated in figure B.5.

The time step for the SSROM simulation ΔT_s needs to be small enough so that the SSROM simulation can 'survive' the measurement sampling time ΔT_m. A general tip for selecting an appropriate ΔT_s is to run several SSROM simulations with different time steps and to pick out the cases without divergence. In addition, the divergence problem is related to how much external information is provided to the estimator. If the number of measurement planes increases, the occurrence of divergence will greatly decrease.

Algorithm 4: Revised Nonlinear Estimation (Kalman Filter Estimation Embedded with SSROM Simulation)

Input: measurement data y_{mea}, considered wavenumber pairs, measurement sampling time ΔT_m, SSROM simulation time step ΔT_s

Output: estimated velocities $\hat{x}_{est}$

Kalman filter estimation (every measurement sampling time ΔT_m):

obtain the measurement data y_{mea} and nonlinear forcing f_i in physical space

take the 2-D Fourier transform to get $\hat{y}_{mea}$ and $\hat{f}_i$ in wavenumber space

for *every* (k_x, k_y) *considered* **do**

use the Kalman filter to get the estimated velocities $\hat{x}_{est}$ in wavenumber space:

$$\frac{\mathrm{d}}{\mathrm{d}t}\hat{\boldsymbol{x}}_{est} = \mathscr{A}\hat{\boldsymbol{x}}_{est}(t) + \mathscr{B}\hat{\boldsymbol{f}}(t) + \mathscr{L}[\hat{\boldsymbol{y}}_{mea}(t) - \mathscr{C}_{mea}\hat{\boldsymbol{x}}_{est}(t)]$$

`/* the marching time step for Kalman filter is` ΔT_s `and Kalman filter is used every measurement sampling time` ΔT_m `*/`

take the inverse 2-D Fourier transform to get x_{est} in physical space

use the nonlinear dynamic to get the nonlinear forcing f_i in physical space:

$$f_i = -u_j \frac{\partial u_i}{\partial x_j}$$

create a counter for SSROM simulation: $n_{SSROM} = 0$

SSROM simulation (running at ΔT_s):

while $n_{SSROM} < \frac{\Delta T_m}{\Delta T_s}$ **do**

take the 2-D Fourier transform to get the nonlinear forcing $\hat{f}_i$ in wavenumber space

for *every* (k_x, k_y) *considered* **do**

use the Orr-Sommerfeld & Squire state-space model to get the velocity $\hat{u}_i$ in wavenumber space

`/* the marching time step for the OSS state-space model is` ΔT_s `*/`

take the inverse 2-D Fourier transform to get the velocities u_i in physical space

use the nonlinear dynamic to get the nonlinear forcing f_i in physical space:

$$f_i = -u_j \frac{\partial u_i}{\partial x_j}$$

$n_{SSROM} = n_{SSROM} + 1$

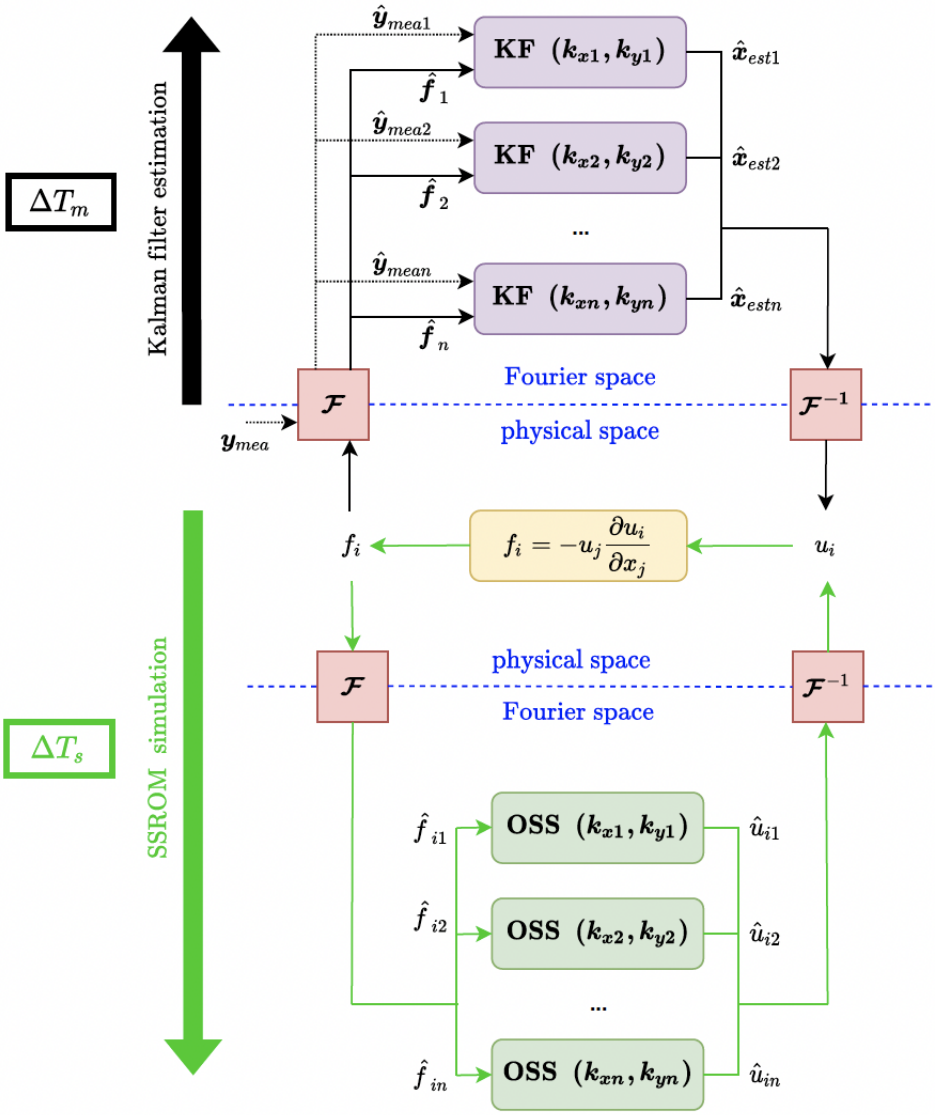

Figure B.5: The structure of the revised nonlinear estimator, which is composed of the linear resolvent-based estimator (6.5) and SSROM simulation. Black lines illustrate the Kalman filter estimation part which is the same as the model in figure B.2. Kalman filter is used every measurement sampling time ΔT_m. Green lines illustrate the SSROM simulation part which is implemented at the simulation time step ΔT_s. $\Delta T_s \ll \Delta T_m$ to avoid divergence.

Bibliography

Adrian, R. J., Meinhart, C. D., & Tomkins, C. D. (2000). Vortex organization in the outer region of the turbulent boundary layer. *J. Fluid Mech.*, *422*, 1–54.

Adrian, R. J., & Moin, P. (1988). Stochastic estimation of organized turbulent structure: homogeneous shear flow. *J. Fluid Mech.*, *190*, 531–559.

Åkervik, E., Ehrenstein, U., Gallaire, F., & Henningson, D. S. (2008). Global two-dimensional stability measures of the flat plate boundary-layer flow. *Eur. J. Mech. B Fluids*, *27*(5), 501–513.

Alexakis, A., Mininni, P., & Pouquet, A. (2005). Imprint of large-scale flows on turbulence. *Phys. Rev. Lett.*, *95*(26), 264503.

Alfonsi, G., & Primavera, L. (2007). The structure of turbulent boundary layers in the wall region of plane channel flow. *Proc. R. Soc. A: Math. Phys. Eng. Sci.*, *463*(2078), 593–612.

Amaral, F. R., Cavalieri, A. V., Martini, E., Jordan, P., & Towne, A. (2021). Resolvent-based estimation of turbulent channel flow using wall measurements. *J. Fluid Mech.*, *927*, A17.

Anderson, B. W., & Domaradzki, J. A. (2012). A subgrid-scale model for large-eddy simulation based on the physics of interscale energy transfer in turbulence. *Phys. Fluids*, *24*(6).

Andersson, P., Berggren, M., & Henningson, D. S. (1999). Optimal disturbances and bypass transition in boundary layers. *Phys. Fluids*, *11*(1), 134–150.

Andrade, J. R., Martins, R. S., Mompean, G., Thais, L., & Gatski, T. B. (2018). Analyzing the spectral energy cascade in turbulent channel flow. *Phys. Fluids*, *30*(6).

Antonia, R. (1981). Conditional sampling in turbulence measurement. *Annu. Rev. Fluid Mech.*, *13*(1), 131–156.

Arun, R., Bae, H. J., & McKeon, B. J. (2023). Towards real-time reconstruction of velocity fluctuations in turbulent channel flow. *Phys. Rev. Fluids*, *8*(6), 064612.

Aubry, N., Holmes, P., Lumley, J. L., & Stone, E. (1988). The dynamics of coherent structures in the wall region of a turbulent boundary layer. *J. Fluid Mech.*, *192*, 115–173.

Baars, W. J., Hutchins, N., & Marusic, I. (2016). Spectral stochastic estimation of high-reynolds-number wall-bounded turbulence for a refined inner-outer interaction model. *Phys. Rev. Fluids*, *1*(5), 054406.

Bae, H. J., Lozano-Duran, A., & McKeon, B. J. (2021). Nonlinear mechanism of the self-sustaining process in the buffer and logarithmic layer of wall-bounded flows. *J. Fluid Mech.*, *914*, A3.

Bagheri, S., Brandt, L., & Henningson, D. S. (2009). Input–output analysis, model reduction and control of the flat-plate boundary layer. *J. Fluid Mech.*, *620*, 263–298.

Bamieh, B., & Dahleh, M. (2001). Energy amplification in channel flows with stochastic excitation. *Phys. Fluids*, *13*(11), 3258–3269.

Beneddine, S., Sipp, D., Arnault, A., Dandois, J., & Lesshafft, L. (2016). Conditions for validity of mean flow stability analysis. *J. Fluid Mech.*, *798*, 485–504.

Berrut, J.-P., & Trefethen, L. N. (2004). Barycentric lagrange interpolation. *SIAM review*, *46*(3), 501–517.

Bewley, T. R., Moin, P., & Temam, R. (2001). Dns-based predictive control of turbulence: an optimal benchmark for feedback algorithms. *J. Fluid Mech.*, *447*, 179–225.

Blackwelder, R., & Kaplan, R. (1976). On the wall structure of the turbulent boundary layer. *J. Fluid Mech.*, *76*(1), 89–112.

Bolotnov, I. A., Lahey Jr, R. T., Drew, D. A., Jansen, K. E., & Oberai, A. A. (2010). Spectral analysis of turbulence based on the dns of a channel flow. *Comput. Fluids*, *39*(4), 640–655.

Brasseur, J. G., & Wei, C.-H. (1994). Interscale dynamics and local isotropy in high reynolds number turbulence within triadic interactions. *Phys. Fluids*, *6*(2), 842–870.

Brunton, S. L., & Noack, B. R. (2015). Closed-loop turbulence control: Progress and challenges. *Appl. Mech. Rev.*, *67*(5), 050801.

Brunton, S. L., Noack, B. R., & Koumoutsakos, P. (2020). Machine learning for fluid mechanics. *Annu. Rev. Fluid Mech.*, *52*, 477–508.

Butler, K. M., & Farrell, B. F. (1992). Three-dimensional optimal perturbations in viscous shear flow. *Phys. Fluids A*, *4*(8), 1637–1650.

Butler, K. M., & Farrell, B. F. (1993). Optimal perturbations and streak spacing in wall-bounded turbulent shear flow. *Phys. Fluids A*, *5*(3), 774–777.

Candès, E. J., & Wakin, M. B. (2008). An introduction to compressive sampling. *IEEE Signal Process. Mag.*, *25*(2), 21–30.

Cantwell, B. J. (1981). Organized motion in turbulent flow. *Annu. Rev. Fluid Mech.*, *13*(1), 457–515.

Carper, M. A., & Porté-Agel, F. (2004). The role of coherent structures in subfilter-scale dissipation of turbulence measured in the atmospheric surface layer. *J. Turbulence*, *5*(1), 040.

Cess, R. (1958). A survey of the literature on heat transfer in turbulent tube flow. *Res. Rep*, 8–0529.

Chen, K. K., & Rowley, C. W. (2011). H2 optimal actuator and sensor placement in the linearised complex ginzburg–landau system. *J. Fluid Mech.*, *681*, 241–260.

Cheung, L. C., & Zaki, T. A. (2014). An exact representation of the nonlinear triad interaction terms in spectral space. *J. Fluid Mech.*, *748*, 175–188.

Chevalier, M., Hœpffner, J., Bewley, T. R., & Henningson, D. S. (2006). State estimation in wall-bounded flow systems. part 2. turbulent flows. *J. Fluid Mech.*, *552*, 167–187.

Cho, M., Hwang, Y., & Choi, H. (2018). Scale interactions and spectral energy transfer in turbulent channel flow. *J. Fluid Mech.*, *854*, 474–504.

Chong, M. S., Perry, A. E., & Cantwell, B. J. (1990). A general classification of three-dimensional flow fields. *Phys. Fluids A*, *2*(5), 765–777.

Chung, D., Monty, J., & Ooi, A. (2014). An idealised assessment of townsend's outer-layer similarity hypothesis for wall turbulence. *J. Fluid Mech.*, *742*.

Cimarelli, A., & De Angelis, E. (2014). The physics of energy transfer toward improved subgrid-scale models. *Phys. Fluids*, *26*(5).

Cimarelli, A., De Angelis, E., & Casciola, C. (2013). Paths of energy in turbulent channel flows. *J. Fluid Mech.*, *715*, 436–451.

Cimarelli, A., De Angelis, E., Jimenez, J., & Casciola, C. M. (2016). Cascades and wall-normal fluxes in turbulent channel flows. *J. Fluid Mech.*, *796*, 417–436.

Colburn, C., Cessna, J., & Bewley, T. (2011). State estimation in wall-bounded flow systems. part 3. the ensemble kalman filter. *J. Fluid Mech.*, *682*, 289–303.

Cossu, C., Pujals, G., & Depardon, S. (2009). Optimal transient growth and very large–scale structures in turbulent boundary layers. *J. Fluid Mech.*, *619*, 79–94.

Dar, G., Verma, M. K., & Eswaran, V. (2001). Energy transfer in two-dimensional magnetohydrodynamic turbulence: formalism and numerical results. *Phys. D: Nonlinear Phenom.*, *157*(3), 207–225.

Davies, S. J., & White, C. M. (1928). An experimental study of the flow of water in pipes of rectangular section. *Proc. R. soc. Lond. Ser. A-Contain. Pap. Math. Phys. Character*, *119*(781), 92–107.

Del Alamo, J. C., & Jimenez, J. (2006). Linear energy amplification in turbulent channels. *J. Fluid Mech.*, *559*, 205–213.

Dennis, D. J., & Nickels, T. B. (2011). Experimental measurement of large-scale three-dimensional structures in a turbulent boundary layer. part 1. vortex packets. *J. Fluid Mech.*, *673*, 180–217.

Domaradzki, J. A. (1992). Nonlocal triad interactions and the dissipation range of isotropic turbulence. *Phys. Fluids A*, *4*(9), 2037–2045.

Domaradzki, J. A., Liu, W., Härtel, C., & Kleiser, L. (1994). Energy transfer in numerically simulated wall-bounded turbulent flows. *Phys. Fluids*, *6*(4), 1583–1599.

Domaradzki, J. A., & Rogallo, R. S. (1990). Local energy transfer and nonlocal interactions in homogeneous, isotropic turbulence. *Phys. Fluids A*, *2*(3), 413–426.

Dotto, A., Lengani, D., Simoni, D., & Tacchella, A. (2021). Dynamic mode decomposition and koopman spectral analysis of boundary layer separation-induced transition. *Phys. Fluids*, *33*(10).

Dunn, D. C., & Morrison, J. F. (2003). Anisotropy and energy flux in wall turbulence. *J. Fluid Mech.*, *491*, 353–378.

Dunn, D. C., & Morrison, J. F. (2005). Analysis of the energy budget in turbulent channel flow using orthogonal wavelets. *Comput. Fluids*, *34*(2), 199–224.

Eckart, C., & Young, G. (1936). The approximation of one matrix by another of lower rank. *Psychometrika*, *1*(3), 211–218.

Ellingsen, T., & Palm, E. (1975). Stability of linear flow. *Phys. Fluids*, *18*(4), 487–488.

Ertesvåg, I. S., & Magnussen, B. F. (2000). The eddy dissipation turbulence energy cascade model. *Combust. Sci. Technol.*, *159*(1), 213–235.

Fan, Y., Arwatz, G., Van Buren, T., Hoffman, D., & Hultmark, M. (2015). Nanoscale sensing devices for turbulence measurements. *Exp. Fluids*, *56*, 1–13.

Fan, Y., Kozul, M., Li, W., & Sandberg, R. D. (2024). Eddy-viscosity-improved resolvent analysis of compressible turbulent boundary layers. *Journal of Fluid Mechanics*, *983*, A46.

Farrell, B. F., Gayme, D. F., & Ioannou, P. J. (2017). A statistical state dynamics approach to wall turbulence. *Philos. Transact. A Math. Phys. Eng. Sci.*, *375*(2089), 20160081.

Farrell, B. F., & Ioannou, P. J. (1993). Stochastic forcing of the linearized navier–stokes equations. *Phys. Fluids A*, *5*(11), 2600–2609.

Farrell, B. F., & Ioannou, P. J. (1998). Perturbation structure and spectra in turbulent channel flow. *Theor. Comput. Fluid Dyn.*, *11*(3-4), 237–250.

Ferziger, J. H., Perić, M., & Street, R. L. (2019). *Computational methods for fluid dynamics*. springer.

Gad-el Hak, M. (1996). Modern developments in flow control.

Germano, M., Piomelli, U., Moin, P., & Cabot, W. H. (1991). A dynamic subgrid-scale eddy viscosity model. *Phys. Fluids A*, *3*(7), 1760–1765.

Gong, J. (2021). *Modelling and estimation in cylinder wakes* (Unpublished doctoral dissertation). University of Melbourne.

Gong, J., Monty, J. P., & Illingworth, S. J. (2020). Model-based estimation of vortex shedding in unsteady cylinder wakes. *Phys. Rev. Fluids*, *5*(2), 023901.

Guezennec, Y. (1989). Stochastic estimation of coherent structures in turbulent boundary layers. *Phys. Fluids A*, *1*(6), 1054–1060.

Gupta, V., Madhusudanan, A., Wan, M., Illingworth, S. J., & Juniper, M. P. (2021). Linear-model-based estimation in wall turbulence: improved stochastic forcing and eddy viscosity terms. *J. Fluid Mech.*, *925*, A18.

Gürcan, Ö. D., Li, Y., & Morel, P. (2020). Turbulence as a network of fourier modes. *Mathematics*, *8*(4), 530.

Gustavsson, L. H. (1991). Energy growth of three-dimensional disturbances in plane poiseuille flow. *J. Fluid Mech.*, *224*, 241–260.

Hamilton, J. M., Kim, J., & Waleffe, F. (1995). Regeneration mechanisms of near-wall turbulence structures. *J. Fluid Mech.*, *287*, 317–348.

Härtel, C., Kleiser, L., Unger, F., & Friedrich, R. (1994). Subgrid-scale energy transfer in the near-wall region of turbulent flows. *Phys. Fluids*, *6*(9), 3130–3143.

Hasselmann, K., Munk, W., & MacDonald, G. (1963). Bispectra of ocean waves. In *Symposium on time series analysis* (pp. 125–139).

Head, M., & Bandyopadhyay, P. (1981). New aspects of turbulent boundary-layer structure. *J. Fluid Mech.*, *107*, 297–338.

Henningson, D. S., & Reddy, S. C. (1994). On the role of linear mechanisms in transition to turbulence. *Phys. Fluids*, *6*(3), 1396–1398.

Hernández, C. G., Yang, Q., & Hwang, Y. (2022a). Generalised quasilinear approximations of turbulent channel flow. part 1. streamwise nonlinear energy transfer. *J. Fluid Mech.*, *936*, A33.

Hernández, C. G., Yang, Q., & Hwang, Y. (2022b). Generalised quasilinear approximations of turbulent channel flow. part 2. spanwise triadic scale interactions. *J. Fluid Mech.*, *944*, A34.

Hœpffner, J., Chevalier, M., Bewley, T. R., & Henningson, D. S. (2005). State estimation in wall-bounded flow systems. part 1. perturbed laminar flows. *J. Fluid Mech.*, *534*, 263–294.

Holford, J. J., Lee, M., & Hwang, Y. (2023). Optimal white-noise stochastic forcing for linear models of turbulent channel flow. *J. Fluid Mech.*, *961*, A32.

Holford, J. J., Lee, M., & Hwang, Y. (2024). A data-driven quasi-linear approximation for turbulent channel flow. *J. Fluid Mech.*, *980*, A12.

Hutchins, N., & Marusic, I. (2007). Evidence of very long meandering features in the logarithmic region of turbulent boundary layers. *J. Fluid Mech.*, *579*, 1–28.

Hwang, Y., & Cossu, C. (2010a). Amplification of coherent streaks in the turbulent couette flow: an input–output analysis at low reynolds number. *J. Fluid Mech.*, *643*, 333–348.

Hwang, Y., & Cossu, C. (2010b). Linear non-normal energy amplification of harmonic and stochastic forcing in the turbulent channel flow. *J. Fluid Mech.*, *664*, 51–73.

Ilak, M., & Rowley, C. W. (2008). Modeling of transitional channel flow using balanced proper orthogonal decomposition. *Phys. Fluids*, *20*(3).

Illingworth, S. J., Monty, J. P., & Marusic, I. (2018). Estimating large-scale structures in wall turbulence using linear models. *J. Fluid Mech.*, *842*, 146–162.

Jeun, J., Nichols, J. W., & Jovanović, M. R. (2016). Input-output analysis of high-speed axisymmetric isothermal jet noise. *Phys. Fluids*, *28*(4).

Jiménez, J. (2018). Coherent structures in wall-bounded turbulence. *J. Fluid Mech.*, *842*, P1.

Jiménez, J., & Moin, P. (1991). The minimal flow unit in near-wall turbulence. *J. Fluid Mech.*, *225*, 213–240.

Jiménez, J., & Pinelli, A. (1999). The autonomous cycle of near-wall turbulence. *J. Fluid Mech.*, *389*, 335–359.

Jin, B., Illingworth, S. J., & Sandberg, R. D. (2022). Optimal sensor and actuator placement for feedback control of vortex shedding. *J. Fluid Mech.*, *932*, A2.

Jin, B., Symon, S., & Illingworth, S. J. (2021). Energy transfer mechanisms and resolvent analysis in the cylinder wake. *Phys. Rev. Fluids*, *6*(2), 024702.

Jovanović, M. R., & Bamieh, B. (2005). Componentwise energy amplification in channel flows. *J. Fluid Mech.*, *534*, 145–183.

Kaiser, E., Kutz, J. N., & Brunton, S. L. (2018). Sparse identification of nonlinear dynamics for model predictive control in the low-data limit. *Proc. Math. Phys. Eng. Sci. A*, *474*(2219), 20180335.

Kalman, R. E. (1960). A new approach to linear filtering and prediction problems.

Karban, U., Martini, E., Cavalieri, A. V., & Jordan, P. (2023). Modal decomposition of nonlinear interactions in wall turbulence. *arXiv preprint arXiv:2301.01078*.

Karniadakis, G. E., Kevrekidis, I. G., Lu, L., Perdikaris, P., Wang, S., & Yang, L. (2021). Physics-informed machine learning. *Nat. Rev. Phys.*, *3*(6), 422–440.

Kepner, J. (2009). *Parallel matlab for multicore and multinode computers*. SIAM.

Kim, E., & Choi, H. (2017). Linear proportional–integral control for skin-friction reduction in a turbulent channel flow. *J. Fluid Mech.*, *814*, 430–451.

Kim, J. (2011). Physics and control of wall turbulence for drag reduction. *Philos. Transact. A Math. Phys. Eng. Sci.*, *369*(1940), 1396–1411.

Kim, J., & Bewley, T. R. (2007). A linear systems approach to flow control. *Annu. Rev. Fluid Mech.*, *39*, 383–417.

Kim, J., & Moin, P. (1986). The structure of the vorticity field in turbulent channel flow. part 2. study of ensemble-averaged fields. *J. Fluid Mech.*, *162*, 339–363.

Kline, S. J., Reynolds, W. C., Schraub, F., & Runstadler, P. (1967). The structure of turbulent boundary layers. *J. Fluid Mech.*, *30*(4), 741–773.

Kolmogorov, A. N. (1941). The local structure of turbulence in incompressible viscous fluid for very large reynolds numbers. *Cr Acad. Sci. URSS*, *30*, 301–305.

Landahl, M. (1980). A note on an algebraic instability of inviscid parallel shear flows. *J. Fluid Mech.*, *98*(2), 243–251.

Le Clainche, S., Rosti, M., & Brandt, L. (2022). A data-driven model based on modal decomposition: application to the turbulent channel flow over an anisotropic porous wall. *J. Fluid Mech.*, *939*, A5.

Le Dimet, F.-X., & Talagrand, O. (1986). Variational algorithms for analysis and assimilation of meteorological observations: theoretical aspects. *Tellus A: Dyn. Meteorol. Oceanogr.*, *38*(2), 97–110.

Lee, M., & Moser, R. D. (2019). Spectral analysis of the budget equation in turbulent channel flows at high reynolds number. *J. Fluid Mech.*, *860*, 886–938.

Lele, S. K. (1992). Compact finite difference schemes with spectral-like resolution. *J. Comput. Phys.*, *103*(1), 16–42.

Lim, J. (2003). *A linear control in turbulent boundary layers* (Unpublished doctoral dissertation). Ph. D. dissertation, University of California at Los Angeles.

Liu, C., & Gayme, D. F. (2021). Structured input–output analysis of transitional wall-bounded flows. *J. Fluid Mech.*, *927*, A25.

Loiseau, J.-C., Noack, B. R., & Brunton, S. L. (2018). Sparse reduced-order modelling: sensor-based dynamics to full-state estimation. *J. Fluid Mech.*, *844*, 459–490.

Lozano-Durán, A., Flores, O., & Jiménez, J. (2012). The three-dimensional structure of momentum transfer in turbulent channels. *J. Fluid Mech.*, *694*, 100–130.

Lozano-Durán, A., & Jiménez, J. (2014). Effect of the computational domain on direct simulations of turbulent channels up to $Re_\tau = 4200$. *Phys. Fluids*, *26*(1), 011702.

Lu, S., & Willmarth, W. (1973). Measurements of the structure of the reynolds stress in a turbulent boundary layer. *J. Fluid Mech.*, *60*(3), 481–511.

Luhar, M., Sharma, A. S., & McKeon, B. (2015). A framework for studying the effect of compliant surfaces on wall turbulence. *J. Fluid Mech.*, *768*, 415–441.

Lumley, J. L. (1964). Spectral energy budget in wall turbulence. *Phys. Fluids*, *7*(2), 190–196.

Lumley, J. L. (1973). Drag reduction in turbulent flow by polymer additives. *J. Polym. Sci. Macromol. Rev.*, *7*(1), 263–290.

Madhusudanan, A., Illingworth, S. J., & Marusic, I. (2019). Coherent large-scale structures from the linearized navier–stokes equations. *J. Fluid Mech.*, *873*, 89–109.

Mansour, N. N., Kim, J., & Moin, P. (1988). Reynolds-stress and dissipation-rate budgets in a turbulent channel flow. *J. Fluid Mech.*, *194*, 15–44.

Marusic, I., Mathis, R., & Hutchins, N. (2010). Predictive model for wall-bounded turbulent flow. *Science*, *329*(5988), 193–196.

Marusic, I., & Monty, J. P. (2019). Attached eddy model of wall turbulence. *Annu. Rev. Fluid Mech.*, *51*, 49–74.

McKeon, B. (2017). The engine behind (wall) turbulence: perspectives on scale interactions. *J. Fluid Mech.*, *817*, P1.

McKeon, B. J., & Sharma, A. S. (2010). A critical-layer framework for turbulent pipe flow. *Journal of Fluid Mechanics*, *658*, 336–382.

Meneveau, C., & Sreenivasan, K. (1991). The multifractal nature of turbulent energy dissipation. *J. Fluid Mech.*, *224*, 429–484.

Millikan, C. B. (1938). A critical discussion of turbulent flows in channels and circular tubes. *Proc. Fifth Intern. Congr. Appl. Mech., Cambridge*, 386–392.

Mizuno, Y. (2016). Spectra of energy transport in turbulent channel flows for moderate reynolds numbers. *J. Fluid Mech.*, *805*, 171–187.

Mizuno, Y., Duke, D., Atkinson, C., & Soria, J. (2011). Investigation of wall-bounded turbulent flow using dynamic mode decomposition. In *J. phys. conf. ser.* (Vol. 318, p. 042040).

Moarref, R., Jovanović, M., Tropp, J., Sharma, A., & McKeon, B. (2014). A low-order decomposition of turbulent channel flow via resolvent analysis and convex optimization. *Phys. Fluids*, *26*(5).

Moarref, R., Sharma, A. S., Tropp, J. A., & McKeon, B. J. (2013). Model-based scaling of the streamwise energy density in high-reynolds-number turbulent channels. *J. Fluid Mech.*, *734*, 275–316.

Moin, P., & Kim, J. (1982). Numerical investigation of turbulent channel flow. *J. Fluid Mech.*, *118*, 341–377.

Moin, P., & Kim, J. (1985). The structure of the vorticity field in turbulent channel flow. part 1. analysis of instantaneous fields and statistical correlations. *J. Fluid Mech.*, *155*, 441–464.

Monty, J., Hutchins, N., Ng, H., Marusic, I., & Chong, M. (2009). A comparison of turbulent pipe, channel and boundary layer flows. *J. Fluid Mech.*, *632*, 431–442.

Morinishi, Y., Lund, T. S., Vasilyev, O. V., & Moin, P. (1998). Fully conservative higher order finite difference schemes for incompressible flow. *J. Comput. Phys.*, *143*(1), 90–124.

Morra, P., Nogueira, P. A., Cavalieri, A. V., & Henningson, D. S. (2021). The colour of forcing statistics in resolvent analyses of turbulent channel flows. *J. Fluid Mech.*, *907*, A24.

Moser, R. D., Kim, J., & Mansour, N. N. (1999). Direct numerical simulation of turbulent channel flow up to $Re_\tau = 590$. *Phys. Fluids*, *11*(4), 943–945.

Natrajan, V. K., & Christensen, K. T. (2006). The role of coherent structures in subgrid-scale energy transfer within the log layer of wall turbulence. *Phys. Fluids*, *18*(6).

Nogueira, P. A., Morra, P., Martini, E., Cavalieri, A. V., & Henningson, D. S. (2021). Forcing statistics in resolvent analysis: application in minimal turbulent couette flow. *J. Fluid Mech.*, *908*, A32.

Oehler, S., Garcia-Gutiérrez, A., & Illingworth, S. (2018). Linear estimation of coherent structures in wall-bounded turbulence at reτ= 2000. In *Journal of physics: Conference series* (Vol. 1001, p. 012006).

Oehler, S. F., & Illingworth, S. J. (2021). Linear control of coherent structures in wall-bounded turbulence at reτ= 2000. *Int. J. Heat Fluid Flow*, *87*, 108735.

Orr, W. M. (1907). The stability or instability of the steady motions of a perfect liquid and of a viscous liquid. part ii: A viscous liquid. In *Proceedings of the royal irish academy. section a: Mathematical and physical sciences* (Vol. 27, pp. 69–138).

Orszag, S. A. (1971). Accurate solution of the orr–sommerfeld stability equation. *J. Fluid Mech.*, *50*(4), 689–703.

Park, J. S., & Graham, M. D. (2015). Exact coherent states and connections to turbulent dynamics in minimal channel flow. *J. Fluid Mech.*, *782*, 430–454.

Perry, A., & Chong, M. (1982). On the mechanism of wall turbulence. *J. Fluid Mech.*, *119*, 173–217.

Piomelli, U., Cabot, W. H., Moin, P., & Lee, S. (1991). Subgrid-scale backscatter in turbulent and transitional flows. *Phys. Fluids A*, *3*(7), 1766–1771.

Piomelli, U., Yu, Y., & Adrian, R. J. (1996). Subgrid-scale energy transfer and near-wall turbulence structure. *Phys. Fluids*, *8*(1), 215–224.

Pope, S. B. (2000). *Turbulent flows*. Cambridge university press.

Prandtl, L. (1925). 7. bericht über untersuchungen zur ausgebildeten turbulenz. *ZAMM-Journal of Applied Mathematics and Mechanics/Zeitschrift für Angewandte Mathematik und Mechanik*, *5*(2), 136–139.

Pujals, G., García-Villalba, M., Cossu, C., & Depardon, S. (2009). A note on optimal transient growth in turbulent channel flows. *Phys. Fluids*, *21*(1).

Ran, W., Zare, A., & Jovanović, M. R. (2021). Model-based design of riblets for turbulent drag reduction. *J. Fluid Mech.*, *906*, A7.

Reddy, S. C., & Henningson, D. S. (1993). Energy growth in viscous channel flows. *J. Fluid Mech.*, *252*, 209–238.

Reynolds, W., & Hussain, A. (1972). The mechanics of an organized wave in turbulent shear flow. part 3. theoretical models and comparisons with experiments. *J. Fluid Mech.*, *54*(2), 263–288.

Richardson, L. F. (1922). *Weather prediction by numerical process*. University Press.

Robinson, S. K. (1991). Coherent motions in the turbulent boundary layer. *Annu. Rev. Fluid Mech.*, *23*(1), 601–639.

Romanov, V. A. (1973). Stability of plane-parallel couette flow. *Functional analysis and its applications*, *7*(2), 137–146.

Rosenberg, K., Symon, S., & McKeon, B. J. (2019). Role of parasitic modes in nonlinear closure via the resolvent feedback loop. *Phys. Rev. Fluids*, *4*(5), 052601.

Rowley, C. W., & Dawson, S. T. (2017). Model reduction for flow analysis and control. *Annu. Rev. Fluid Mech.*, *49*, 387–417.

Schmid, P. J. (2007). Nonmodal stability theory. *Annu. Rev. Fluid Mech.*, *39*, 129–162.

Schmid, P. J., & Henningson, D. S. (1994). Optimal energy density growth in hagen–poiseuille flow. *J. Fluid Mech.*, *277*, 197–225.

Schmid, P. J., & Henningson, D. S. (2001). Stability and transition in shear flows.

Schoppa, W., & Hussain, F. (2002). Coherent structure generation in near-wall turbulence. *J. Fluid Mech.*, *453*, 57–108.

Seron, M. M., Braslavsky, J. H., & Goodwin, G. C. (2012). *Fundamental limitations in filtering and control*. Springer Science & Business Media.

Sharma, A., & McKeon, B. J. (2013). On coherent structure in wall turbulence. *J. Fluid Mech.*, *728*, 196–238.

Smagorinsky, J. (1963). General circulation experiments with the primitive equations: I. the basic experiment. *Monthly weather review*, *91*(3), 99–164.

Smits, A. J., McKeon, B. J., & Marusic, I. (2011). High–reynolds number wall turbulence. *Annu. Rev. Fluid Mech.*, *43*, 353–375.

Smyth, W. (1992). Spectral transfers in two-dimensional anisotropic flow. *Phys. Fluids A*, *4*(2), 340–349.

Sommerfield, A. (1908). Ein beitrag zur hydrodynamischen erklarung der turbulenten flussigkeisbewegung. *Atti Congr. Int. Math. 4th Rome*.

Squire, H. B. (1933). On the stability for three-dimensional disturbances of viscous fluid flow between parallel walls. *Proc. R. soc. Lond. Ser. A-Contain. Pap. Math. Phys. Character*, *142*(847), 621–628.

Stone, P. A., Roy, A., Larson, R. G., Waleffe, F., & Graham, M. D. (2004). Polymer drag reduction in exact coherent structures of plane shear flow. *Phys. Fluids*, *16*(9), 3470–3482.

Strang, G. (1988). Linear algebra and its applications, thomson learning. *Inc., United States*.

Suzuki, T., & Hasegawa, Y. (2017). Estimation of turbulent channel flow at based on the wall measurement using a simple sequential approach. *J. Fluid Mech.*, *830*, 760–796.

Symon, S., Illingworth, S. J., & Marusic, I. (2021). Energy transfer in turbulent channel flows and implications for resolvent modelling. *J. Fluid Mech.*, *911*, A3.

Symon, S., Rosenberg, K., Dawson, S. T., & McKeon, B. J. (2018). Non-normality and classification of amplification mechanisms in stability and resolvent analysis. *Phys. Rev. Fluids*, *3*(5), 053902.

Taira, K., Brunton, S. L., Dawson, S. T., Rowley, C. W., Colonius, T., McKeon, B. J., ... Ukeiley, L. S. (2017). Modal analysis of fluid flows: An overview. *AIAA*, *55*(12), 4013–4041.

Taira, K., Hemati, M. S., Brunton, S. L., Sun, Y., Duraisamy, K., Bagheri, S., ... Yeh, C.-A. (2020). Modal analysis of fluid flows: Applications and outlook. *AIAA*, *58*(3), 998–1022.

Tardu, S. (2017). *Wall turbulence control*. John Wiley & Sons.

Tardu, S. F. (2001). Active control of near-wall turbulence by local oscillating blowing. *J. Fluid Mech.*, *439*, 217–253.

Tennekes, H., & Lumley, J. L. (1972). *A first course in turbulence*. MIT press.

Theodorsen, T. (1952). Mechanisms of turbulence. In *Proceedings of the 2nd midwestern conference on fluid mechanics, 1952*.

Towne, A., Lozano-Durán, A., & Yang, X. (2020). Resolvent-based estimation of space–time flow statistics. *J. Fluid Mech.*, *883*, A17.

Townsend, A. (1976). *The structure of turbulent shear flow*. Cambridge university press.

Trefethen, L. N. (1999). Computation of pseudospectra. *Acta numerica*, *8*, 247–295.

Trefethen, L. N. (2000). *Spectral methods in matlab*. SIAM.

Trefethen, L. N., Trefethen, A. E., Reddy, S. C., & Driscoll, T. A. (1993). Hydrodynamic stability without eigenvalues. *Science*, *261*(5121), 578–584.

Tu, J. H., Griffin, J., Hart, A., Rowley, C. W., Cattafesta, L. N., & Ukeiley, L. S. (2013). Integration of non-time-resolved piv and time-resolved velocity point sensors for dynamic estimation of velocity fields. *Exp. Fluids*, *54*, 1–20.

Vassilicos, J. C. (2015). Dissipation in turbulent flows. *Annu. Rev. Fluid Mech.*, *47*, 95–114.

Waleffe, F. (1992). The nature of triad interactions in homogeneous turbulence. *Phys. Fluids A*, *4*(2), 350–363.

Waleffe, F. (1995). Hydrodynamic stability and turbulence: Beyond transients to a self-sustaining process. *Studies in applied mathematics*, *95*(3), 319–343.

Waleffe, F. (1997). On a self-sustaining process in shear flows. *Phys. Fluids*, *9*(4), 883–900.

Wallace, J. M. (2016). Quadrant analysis in turbulence research: history and evolution. *Annu. Rev. Fluid Mech.*, *48*, 131–158.

Wallace, J. M., Eckelmann, H., & Brodkey, R. S. (1972). The wall region in turbulent shear flow. *J. Fluid Mech.*, *54*(1), 39–48.

Wang, M., & Zaki, T. A. (2021). State estimation in turbulent channel flow from limited observations. *J. Fluid Mech.*, *917*, A9.

Wang, Q., Wang, M., & Zaki, T. A. (2022). What is observable from wall data in turbulent channel flow? *J. Fluid Mech.*, *941*, A48.

Webber, G., Handler, R., & Sirovich, L. (2002). Energy dynamics in a turbulent channel flow using the karhunen-loéve approach. *Int. J. Numer. Meth. Fluids*, *40*(11), 1381–1400.

Weideman, J. A., & Reddy, S. C. (2000). A matlab differentiation matrix suite. *ACM Transactions on Mathematical Software (TOMS)*, *26*(4), 465–519.

Williamson, C. H. (1996). Vortex dynamics in the cylinder wake. *Annu. Rev. Fluid Mech.*, *28*(1), 477–539.

Wu, X., & Moin, P. (2009). Direct numerical simulation of turbulence in a nominally zero-pressure-gradient flat-plate boundary layer. *J. Fluid Mech.*, *630*, 5–41.

Ying, A., Liang, T., Li, Z., & Fu, L. (2023). A resolvent-based prediction framework for incompressible turbulent channel flow with limited measurements. *J. Fluid Mech.*, *976*, A31.

Zare, A., Jovanović, M. R., & Georgiou, T. T. (2017). Colour of turbulence. *J. Fluid Mech.*, *812*, 636–680.

Zhou, J., Adrian, R. J., Balachandar, S., & Kendall, T. M. (1999). Mechanisms for generating coherent packets of hairpin vortices in channel flow. *J. Fluid Mech.*, *387*, 353–396.

Zhou, K., Doyle, J. C., & Glover, K. (1996). *Robust and optimal control*. Upper Saddle River: Prentice Hall.